To the Graduate Council:

I am submitting herewith a dissertation written by James Henry Miller entitled "Methylsilane Derived SiC Particle Coatings Produced By Fluid-Bed Chemical Vapor Deposition." I have examined the final electronic copy of this dissertation for form and content and recommend that it be accepted in partial fulfillment of the requirements for the degree of Doctor of Philosophy, with a major in Materials Science and Engineering

Peter K. Liaw
Major Professor

We have read this dissertation
and recommend its acceptance:

C. Stuart Daw

John D. Landes

Philip D. Rack

Theodore M. Besmann

Acceptance for the Council:

Linda Painter
Interim Dean of Graduate Studies

(Original signatures are on file with the official student records.)

METHYLSILANE DERIVED SiC PARTICLE COATINGS PRODUCED BY FLUID-BED CHEMICAL VAPOR DEPOSITION

A Dissertation
Presented for the
Doctor of Philosophy
Degree
The University of Tennessee, Knoxville

James Henry Miller
December 2006

Dedication

This dissertation is dedicated to two long time University of Tennessee, Materials Science & Engineer professors who recently passed away: Dr. W. T. Becker and Dr. R. A. Buchanan.

Acknowledgements

There are many people to whom I owe thanks for their help, guidance, advice, support, and encouragement. First of all I wish to express my love and appreciation to my wife. Without her patients, support and encouragement, this work would not have been done. My six month old son does not know it yet, but I look forward to telling him some day that he was the source of my motivation to finally finish this work. I also want to thank my Father W. H. Miller, Jr., his wife P. H. Miller, my mother K. S. Wiesehuegel, her husband R. E. Wiesehuegel, and my sister B. S. Miller for their encouragement and patients.

I wish to express my sincere appreciation to Drs. D. F. Williams and K. Pasamehmetoglu for their efforts in providing and maintaining the funding for this research.

Thanks are also due to my committee Drs. P. K. Liaw (Chair), T. M. Besmann, C. S. Daw, J. D. Landes, and P. D. Rack for their teaching, guidance, advice, and encouragement.

In addition, I wish to express my continued gratitude to R. A. Lowden and T. M. Besmann for their mentoring and support.

This research was sponsored by the U.S. Department of Energy through the Office of Nuclear Energy–Advanced Fuel Cycle Initiative Program under contract DE-AC05-00OR22725 with UT‑Battelle, LLC. The work was performed at the Oak Ridge National Laboratory under the auspices of the Materials Science and Technology Division.

Abstract

This report describes the research effort that was undertaken to develop and understand processing techniques for the deposition of both low and high density SiC coatings from a non-halide precursor, in support of the Generation IV Gas-Cooled Fast Reactor (GFR) fuel development program.

The research was conducted in two phases. In the first phase, the feasibility of producing both porous SiC coatings and dense SiC coatings on surrogate fuel particles by fluidized bed chemical vapor deposition (FBCVD) using gas mixtures of methylsilane and argon was demonstrated. In the second phase, a combined experimental and modeling effort was carried out in order to gain an understanding of the deposition mechanisms that result in either porous or dense SiC coatings, depending on the coating conditions. For this second phase effort, a simplified (compared to the fluid bed) single-substrate chemical vapor deposition (CVD) system was employed.

Based on the experimental and modeling results, the deposition of SiC from methylsilane is controlled by the extent of gas-phase reaction, and is therefore highly sensitive to temperature. The results show that all SiC coatings are due to the surface adsorption of species that result from gas-phase reactions. The model terms these gas-borne species embryos, and while the model does not include a prediction of coating morphology, a comparison of the model and experimental results indicates that the morphology of the coatings is controlled by the nucleation and growth of the embryos. The coating that results from small embryos (embryos with only two Si-C pairs) appears relatively dense and continuous, while the coating that results from larger embryos becomes less continuous and more nodular as embryo size increases. At some point in the growth of embryos they cease to behave as molecular species and instead behave as particles that grow by either agglomeration or by incorporation of molecular species on their surface. As these particles adhere to the substrate surface and become fixed in place by surface deposition in the interstices between adjacent particles, a low density coating consisting of these particles results.

Table of Contents

1 Introduction 1
1.1 Coated Particle Fuel 1
1.2 History of Gas-Cooled Reactors 2
1.3 Gas-Cooled Fast Reactor Fuel Concept 2
1.4 Coating Development Research 3
2 Background and Literature Review 5
2.1 FBCVD of SiC Containment Coatings from Methylsilane 5
2.2 Gas-phase Decomposition of Methylsilane 6
2.3 Surface Decomposition CVD of SiC From Methylsilane 7
2.4 Modeling of FBVCD 8
3 Particle Coating Investigation 11
3.1 System Description 11
3.2 Coating Procedure 11
3.3 Fluid Bed Thermal Profile 13
3.4 Coating Experiments and Characterization 13
3.5 SiC Buffer and Seal Coatings 15
3.6 Multilayer Particle Coatings for Fuel Applications 16
3.7 Particle Coating Conclusions 16
4 Single Substrate Experiments 17
4.1 Coating System 17
4.2 Coating Procedure 17
4.3 Coating Experiments 18
4.4 Surface Deposition Zone 19
4.5 Transition Zone 21
4.6 Homogeneous Nucleation Zone 22
5 Deposition Model 23
5.1 Model Reactions 23
5.2 Kinetic Calculations 25
5.3 Kinetic Parameters 25
5.4 Surface Deposition Premise 26
5.5 Surface Concentration 27
5.6 Gas-phase Reaction Premise 30
5.7 Thermal Model 31
5.8 Surface Temperature Determination 33
5.9 Model Specifics 34
5.10 Embryo Surface Reaction Activation Energy 45
6 Modeling Results 47
6.1 Predicted Species Concentration Profiles 47
6.2 Predicted Molar Amount Profiles 47
6.3 Predicted Reaction Rate Profiles 49
6.4 Predicted Species Production Rates 51
6.5 Embryo Growth Mode 52
6.6 Embryo Size Prediction 53

7 Discussion 55
7.1 Surface Deposition Zone 55
7.2 Transition Zone 56
7.3 Homogeneous Nucleation Zone 56
8 Conclusions 59
9 Recommendations 61
References 63
Appendix 67
Vita 167

List of Tables

Table 2.1. Arrehnius Parameters and Efficiency Of Reactions 2.1-2.3 68
Table 2.2. Methylsilane Decomposition Scheme Proposed By Nuedorfl (25)..... 68
Table 3.1. Summary List of Particle Coating Experiments 69
Table 3.2. Experimental Conditions of the X-Ray Measurements RTXRD..... 70
Table 4.1. Summary of Coating Experiments..... 71
Table 5.1. Summary of Kinetic Parameters Used In Model Calculations..... 72

List of Figures

Figure 1.1. The anatomy of a typical TRISO coated particle. 73
Figure 1.2. Schematic of GFR dispersion fuel concept. 73
Figure 2.1. Calculated CVD phase diagram for the CH_3SiH_3-(Ar-H_2) system. From Angelini (16-17)..... 74
Figure 2.2. FBCVD-Model-predicted temperature, void fraction, and hydrogen fraction. Six frames of three pictures each. Each frame represents a different time step in the FBCVD simulation..... 75
Figure 2.3. Time-averaged centerline temperature profiles of the gas and solids as a function of axial position along the height of the conical coating chamber. 76
Figure 3.1. Schematic the FBCVD furnace showing the configuration of the reactant and exhaust gas lines. 77
Figure 3.2. Cutaway drawing of FBCVD reactor. 78
Figure 3.3. Enlarged schematic of spouting bed, graphite cone, and water-cooled injector. 79
Figure 3.4. Schematic cut away view of the particle bed, coating chamber, and water-cooled gas injector showing the manner in which the fluid bed thermal profile measurements were made. 80
Figure 3.5. Thermocouple readings as a function of axial position inside a fluidized particle bed at four nominal coating temperatures. 81
Figure 3.6. SEM micrographs of fracture surfaces of SiC coatings produced over the range of temperatures. 82
Figure 3.7. SEM photographs of the fracture surfaces of crushed particles from the second set of coating experiments (900-1,200°C). 83
Figure 3.8. Particle XRD patterns for the SiC coatings produced over the range of coating temperature. 84
Figure 3.9. Particle XRD patterns of both annealed and un-annealed 900 °C SiC coatings along with the pattern for the 1200°C SiC coating and reference patterns for cubic SiC, ZrO_2, and graphite for comparison. 85
Figure 3.10. SEM micrographs of fracture surface of un-annealed and annealed 1173 K SiC coatings. 86
Figure 3.11. Low magnification optical photographs of SiC seal coated particles. 86
Figure 3.12. Low magnification optical photographs of SiC buffer coated particles. 87
Figure 3.13. SEM micrographs of fracture surface of SiC buffer and TRISO-type carbon buffer coatings. 87
Figure 3.14. SEM micrographs of fracture surface of SiC seal and TRISO-type MTS derived SiC coatings. 88
Figure 3.15. Particle XRD patterns of the annealed SiC seal coating, the SiC buffer coating, the TRISO-type MTS-SiC, and the reference patterns for cubic SiC, ZrO_2, and graphite for comparison. 89
Figure 3.16. SEM photographs of a dual layer SiC coated particle. 90
Figure 3.17. Low magnification optical photographs of dual layer SiC coated particles. 90

Figure 3.18. SEM photographs of the fracture surface of a three layer SiC coated particle. 91
Figure 3.19. Low magnification optical photographs of the three layer SiC coated particles 91
Figure 4.1. Coating chamber and substrate configuration used in coating experiments. 92
Figure 4.2. Photographs of specimens coated a variety of temperatures and methylsilane flow rates. 93
Figure 4.3. A photograph of AFCI-SiC-2 accompanied by SEM photographs showing the coating surface morphology in the three deposition mode zones. 94
Figure 4.4. Photographs showing the sectioning details of AFCI-SiC-11. MS = methylsilane. 95
Figure 4.5. Photographs showing the sectioning details of AFCI-SiC-14. MS = methylsilane 95
Figure 4.6. Photographs showing the sectioning details of AFCI-SiC-12. MS = methylsilane. 96
Figure 4.7. Photographs showing the sectioning details of AFCI-SiC-10. MS = methylsilane. 96
Figure 4.8. Photographs showing the sectioning details of AFCI-SiC-15. MS = methylsilane. 97
Figure 4.9. Photographs of specimen segment AFCI-SiC-14C showing locations where and SEM micrographs (also shown) were taken from for coating thickness measurements. 97
Figure 4.10. A typical SEM micrograph from sample AFCI-SiC-14C showing the approximate locations where length measurements were made. Length data obtained from this micrograph are also shown. 98
Figure 4.11. Coating thickness as a function of axial position for sample AFCI-SiC-11. The points are the average coating thickness and the error bars are the standard deviations. 98
Figure 4.12. Coating thickness as a function of axial position for sample AFCI-SiC-14. The points are the average coating thickness and the error bars are the standard deviations. 99
Figure 4.13. Coating thickness as a function of axial position for sample AFCI-SiC-12. The points are the average coating thickness and the error bars are the standard deviations. 99
Figure 4.14. Coating thickness as a function of axial position for sample AFCI-SiC-10. The points are the average coating thickness and the error bars are the standard deviations. 100
Figure 4.15. Coating thickness as a function of axial position for sample AFCI-SiC-15. The points are the average coating thickness and the error bars are the standard deviations. 100
Figure 4.16. Experimental deposition rate verses axial position for specimens coated at 600°C (AFCI-SiC-11 and 14) 101
Figure 4.17. Experimental deposition rate verses axial position for specimens coated at 625°C (AFCI-SiC-10, 12, and 15). 101

Figure 4.18. SEM micrographs, taken at a magnification of 5,000x, of the coating surface taken every two millimeters (in order left to right, top to bottom) in the transition zone of specimen number AFCI-SiC-10. 102
Figure 4.19. SEM micrographs, taken at a magnification of 5,000x, of the coating surface taken every two millimeters (in order left to right, top to bottom) in the transition zone of specimen number AFCI-SiC-1. 103
Figure 4.20. SEM micrographs, taken at a magnification of 5,000x, of the coating surface taken every two millimeters (in order left to right, top to bottom) in the transition zone of specimen number AFCI-SiC-4. 104
Figure 4.21. SEM micrographs, taken at a magnification of 10,000x, of the coating surface taken every two millimeters (in order left to right, top to bottom) in the transition zone of specimen number AFCI-SiC-10. 105
Figure 4.22. SEM micrographs, taken at a magnification of 10,000x, of the coating surface taken every two millimeters (in order left to right, top to bottom) in the transition zone of specimen number AFCI-SiC-1. 106
Figure 4.23. SEM micrographs, taken at a magnification of 10,000x, of the coating surface taken every two millimeters (in order left to right, top to bottom) in the transition zone of specimen number AFCI-SiC-4. 107
Figure 4.24. A photograph of specimen number AFCI-SiC-10 with SEM micrographs of selected areas in the homogeneous nucleation zone. 108
Figure 4.25. A photograph of specimen number AFCI-SiC-1 with SEM micrographs of selected areas in the homogeneous nucleation zone. 108
Figure 4.26. A photograph of specimen number AFCI-SiC-4 with SEM micrographs of selected areas in the homogeneous nucleation zone. 109
Figure 4.27. SEM micrographs taken near the down stream end of homogeneous nucleation zone of specimens AFCI-SiC-10, 4, and 1 respectively 109
Figure 5.1. Schematic of a portion of the concentric annulus substrate demonstrating how this geometry is treated by the model as individual axial segments. 110
Figure 5.2. Photograph of the concentric annulus substrate with the thermocouple positions shown. 111
Figure 5.3. Temperature measurements for the 600°C nominal case showing the six types of temperature measurements that were made. 112
Figure 5.4. Temperature measurements and curve fits that represent the surface temperature as a function of axial position of the concentric annulus. 112
Figure 5.5. Plot of the coefficients of the curve fits of surface temperature as a function of axial position ($T_S=ax^2+bx+c$). The curve fits for the coefficients as a function of nominal temperature are also shown. 113
Figure 5.6. Measured surface temperature and calculated gas temperature as a function of axial position. 113
Figure 5.7. Block flow diagram of the model calculation sequence. 114
Figure 5.8. Typical rates of Reactions 5.2-5.5 demonstrating methylsilylene production via Reaction 5.2 is the rate limiting step. 115
Figure 5.9. Typical rates of Reactions 5.7-5.10 demonstrating radical production via Reaction 5.7 is the rate limiting step. 115

Figure 5.10. Model predicted coating thickness profile for AFCI-SiC-11 with a photograph of the specimen shown at the approximate scale of the x-axis for comparison. 116
Figure 5.11. Model predicted coating thickness profile for AFCI-SiC-14 with a photograph of the specimen shown at the approximate scale of the x-axis for comparison. 116
Figure 5.12. Model predicted coating thickness profile for AFCI-SiC-10 with a photograph of the specimen shown at the approximate scale of the x-axis for comparison. 117
Figure 5.13. Model predicted coating thickness profile for AFCI-SiC-12 with a photograph of the specimen shown at the approximate scale of the x-axis for comparison. 117
Figure 5.14. Model predicted coating thickness profile for AFCI-SiC-15 with a photograph of the specimen shown at the approximate scale of the x-axis for comparison. 118
Figure 6.1. Model-predicted concentration profile for AFCI-SiC-8 with a photograph of the specimen shown at the approximate scale of the x-axis for comparison. 119
Figure 6.2. Model-predicted concentration profile for AFCI-SiC-11 with a photograph of the specimen shown at the approximate scale of the x-axis for comparison. 120
Figure 6.3. Model-predicted concentration profile for AFCI-SiC-14 with a photograph of the specimen shown at the approximate scale of the x-axis for comparison. 121
Figure 6.4. Model-predicted concentration profile for AFCI-SiC-12 with a photograph of the specimen shown at the approximate scale of the x-axis for comparison. 122
Figure 6.5. Model-predicted concentration profile for AFCI-SiC-10 with a photograph of the specimen shown at the approximate scale of the x-axis for comparison. 123
Figure 6.6. Model-predicted concentration profile for AFCI-SiC-15 with a photograph of the specimen shown at the approximate scale of the x-axis for comparison. 124
Figure 6.7. Model-predicted concentration profile for AFCI-SiC-1 with a photograph of the specimen shown at the approximate scale of the x-axis for comparison. 125
Figure 6.8. Model-predicted concentration profile for AFCI-SiC-4 with a photograph of the specimen shown at the approximate scale of the x-axis for comparison. 126
Figure 6.9. Model-predicted profile of the molar amounts of species for AFCI-SiC-8 with a photograph of the specimen shown at the approximate scale of the x-axis for comparison. 127
Figure 6.10. Model-predicted profile of the molar amounts of species for AFCI-SiC-11 with a photograph of the specimen shown at the approximate scale of the x-axis for comparison. 128

Figure 6.11. Model-predicted profile of the molar amounts of species for AFCI-SiC-14 with a photograph of the specimen shown at the approximate scale of the x-axis for comparison. 129
Figure 6.12. Model-predicted profile of the molar amounts of species for AFCI-SiC-12 with a photograph of the specimen shown at the approximate scale of the x-axis for comparison. 130
Figure 6.13. Model-predicted profile of the molar amounts of species for AFCI-SiC-10 with a photograph of the specimen shown at the approximate scale of the x-axis for comparison. 131
Figure 6.14. Model-predicted profile of the molar amounts of species for AFCI-SiC-15 with a photograph of the specimen shown at the approximate scale of the x-axis for comparison. 132
Figure 6.15. Model-predicted profile of the molar amounts of species for AFCI-SiC-1 with a photograph of the specimen shown at the approximate scale of the x-axis for comparison. 133
Figure 6.16. Model-predicted profile of the molar amounts of species for AFCI-SiC-4 with a photograph of the specimen shown at the approximate scale of the x-axis for comparison. 134
Figure 6.17. Model-predicted reaction rate profile for AFCI-SiC-8 with a photograph of the specimen shown at the approximate scale of the x-axis for comparison. 135
Figure 6.18. Model-predicted reaction rate profile for AFCI-SiC-11 with a photograph of the specimen shown at the approximate scale of the x-axis for comparison. 136
Figure 6.19. Model-predicted reaction rate profile for AFCI-SiC-14 with a photograph of the specimen shown at the approximate scale of the x-axis for comparison. 137
Figure 6.20. Model-predicted reaction rate profile for AFCI-SiC-12 with a photograph of the specimen shown at the approximate scale of the x-axis for comparison. 138
Figure 6.21. Model-predicted reaction rate profile for AFCI-SiC-10 with a photograph of the specimen shown at the approximate scale of the x-axis for comparison. 139
Figure 6.22. Model-predicted reaction rate profile for AFCI-SiC-15 with a photograph of the specimen shown at the approximate scale of the x-axis for comparison. 140
Figure 6.23. Model-predicted reaction rate profile for AFCI-SiC-1 with a photograph of the specimen shown at the approximate scale of the x-axis for comparison. 141
Figure 6.24. Model-predicted reaction rate profile for AFCI-SiC-4 with a photograph of the specimen shown at the approximate scale of the x-axis for comparison. 142
Figure 6.25. Model-predicted species rates of production as a function of axial position for AFCI-SiC-8 with a photograph of the specimen shown at the approximate scale of the x-axis for comparison. 143

Figure 6.26. Model-predicted species rates of production as a function of axial position for AFCI-SiC-11 with a photograph of the specimen shown at the approximate scale of the x-axis for comparison. 144
Figure 6.27. Model-predicted species rates of production as a function of axial position for AFCI-SiC-14 with a photograph of the specimen shown at the approximate scale of the x-axis for comparison. 145
Figure 6.28. Model-predicted species rates of production as a function of axial position for AFCI-SiC-12 with a photograph of the specimen shown at the approximate scale of the x-axis for comparison. 146
Figure 6.29. Model-predicted species rates of production as a function of axial position for AFCI-SiC-10 with a photograph of the specimen shown at the approximate scale of the x-axis for comparison. 147
Figure 6.30. Model-predicted species rates of production as a function of axial position for AFCI-SiC-15 with a photograph of the specimen shown at the approximate scale of the x-axis for comparison. 148
Figure 6.31. Model-predicted species rates of production as a function of axial position for AFCI-SiC-1 with a photograph of the specimen shown at the approximate scale of the x-axis for comparison. 149
Figure 6.32. Model-predicted species rates of production as a function of axial position for AFCI-SiC-4 with a photograph of the specimen shown at the approximate scale of the x-axis for comparison. 150
Figure 6.33. Model-predicted embryo reaction rates as a function of axial position for AFCI-SiC-8 with a photograph of the specimen shown at the approximate scale of the x-axis for comparison. 151
Figure 6.34. Model-predicted embryo reaction rates as a function of axial position for AFCI-SiC-11 with a photograph of the specimen shown at the approximate scale of the x-axis for comparison. 151
Figure 6.35. Model-predicted embryo reaction rates as a function of axial position for AFCI-SiC-14 with a photograph of the specimen shown at the approximate scale of the x-axis for comparison. 152
Figure 6.36. Model-predicted embryo reaction rates as a function of axial position for AFCI-SiC-12 with a photograph of the specimen shown at the approximate scale of the x-axis for comparison. 152
Figure 6.37. Model-predicted embryo reaction rates as a function of axial position for AFCI-SiC-10 with a photograph of the specimen shown at the approximate scale of the x-axis for comparison. 153
Figure 6.38. Model-predicted embryo reaction rates as a function of axial position for AFCI-SiC-15 with a photograph of the specimen shown at the approximate scale of the x-axis for comparison. 153
Figure 6.39. Model-predicted embryo reaction rates as a function of axial position for AFCI-SiC-1 with a photograph of the specimen shown at the approximate scale of the x-axis for comparison. 154
Figure 6.40. Model-predicted embryo reaction rates as a function of axial position for AFCI-SiC-4 with a photograph of the specimen shown at the approximate scale of the x-axis for comparison. 154

Figure 6.41. Model-predicted profile of the average size of embryos for AFCI-SiC-8 with a photograph of the specimen shown at the approximate scale of the x-axis for comparison. 155
Figure 6.42. Model-predicted profile of the average size of embryos for AFCI-SiC-11 with a photograph of the specimen shown at the approximate scale of the x-axis for comparison. 155
Figure 6.43. Model-predicted profile of the average size of embryos for AFCI-SiC-14 with a photograph of the specimen shown at the approximate scale of the x-axis for comparison. 156
Figure 6.44. Model-predicted profile of the average size of embryos for AFCI-SiC-12 with a photograph of the specimen shown at the approximate scale of the x-axis for comparison. 156
Figure 6.45. Model-predicted profile of the average size of embryos for AFCI-SiC-10 with a photograph of the specimen shown at the approximate scale of the x-axis for comparison. 157
Figure 6.46. Model-predicted profile of the average size of embryos for AFCI-SiC-15 with a photograph of the specimen shown at the approximate scale of the x-axis for comparison. 157
Figure 6.47. Model-predicted profile of the average size of embryos for AFCI-SiC-1 with a photograph of the specimen shown at the approximate scale of the x-axis for comparison. 158
Figure 6.48. Model-predicted profile of the average size of embryos for AFCI-SiC-4 with a photograph of the specimen shown at the approximate scale of the x-axis for comparison. 158
Figure 7.1. Predicted embryo growth mode rates and average size plot with SEM micrographs of selected areas shown for comparison for specimen AFCI-SiC-10. 159
Figure 7.2. Predicted embryo growth mode rates and average size plot with SEM micrographs of selected areas shown for comparison for specimen AFCI-SiC-1.. 160
Figure 7.3. Predicted embryo growth mode rates and average size plot with SEM micrographs of selected areas shown for comparison for specimen AFCI-SiC-4.. 161
Figure 7.4. Schematic drawing of a typical gas-borne aggregate. 162
Figure 7.5. Predicted embryo growth mode rates as a function of time of flight in the reactor for specimen AFCI-SiC-10. 162
Figure 7.6. Predicted embryo growth mode rates as a function of time of flight in the reactor for specimen AFCI-SiC-1. 163
Figure 7.7. Predicted embryo growth mode rates as a function of time of flight in the reactor for specimen AFCI-SiC-4. 163
Figure 7.8. Predicted embryo growth mode rates as a function of axial position with SEM micrographs of selected areas shown for comparison for specimen AFCI-SiC-10. 164
Figure 7.9. Predicted embryo growth mode rates as a function of axial position with SEM micrographs of selected areas shown for comparison for specimen AFCI-SiC-1. 165

Figure 7.10. Predicted embryo growth mode rates as a function of axial position with SEM micrographs of selected areas shown for comparison for specimen AFCI-SiC-4. 166

1 Introduction

The Generation IV Gas-Cooled Fast Reactor (GFR) Fuel Development program is investigating the use of coated particle dispersion fuel as one of the GFR fuel concepts. The concept calls for bi-layer, all ceramic fuel particle coatings. Processing techniques for the production of these particle coatings is the subject of the research described here. In the following sections coated particle nuclear reactor fuel (CPF) will be described, and the history of the gas-cooled reactors that employ CPF will be briefly reviewed. Then the GFR CPF concept will be discussed, and finally the research carried out in this work will be introduced.

1.1 Coated Particle Fuel

Coated particle dispersion fuel is not a new idea. Bi-layer isotropic (BISO) and Tri-layer isotropic (TRISO) coated fuel particles dispersed in a graphite matrix have a long history in thermal gas-cooled reactors (1-13). BISO CPF for thermal-spectrum reactors consists of fuel kernels that are coated with successive layers of low density and high density carbon. TRISO coated particle fuel is an extension of BISO fuel particles. TRISO particles have the BISO carbon coatings plus a SiC layer followed by another dense carbon layer. The fuel kernels are small diameter spheres (≈ 0.3-0.5 mm) consisting of carbides or oxides of uranium, and they are produced by sol-gel methods. The TRISO coatings are applied via fluidized bed chemical vapor deposition (FBCVD). The TRISO coating system consists of consecutive layers of low density pyrolytic carbon, high density pyrolytic carbon, SiC, and a final layer of high density pyrolytic carbon (11-12). Photographs of typical TRISO coated particles are shown in Figure 1.1[1].

The low-density carbon, or buffer layer is approximately fifty percent dense with predominantly open porosity. Its job is to provide void volume for the retention of fission-product gases, to protect subsequent layers from fission recoil, and to provide compliance to relieve stresses due to thermal expansion mismatch and radiation induced volume changes of the kernel and coatings.

The inner dense carbon layer protects the kernel from chlorine attack during the deposition of the SiC layer, and in service it protects the SiC coating from corrosive interactions with various fission products.

The SiC coating provides the primary containment of the fuel materials and fission products.

The outer dense carbon layer provides a bonding surface for the graphite matrix within which the coated particles are suspended in the final fuel form, as well as serving as a secondary containment layer for particles with defective SiC layers. In addition, due to the difference in thermal expansion between carbon and SiC, the outer dense carbon layer serves to put the SiC in residual compression, thereby improving integrity of the SiC layer.

[1] All tables and figures are located in the appendix.

1.2 History of Gas-Cooled Reactors

Development of coated particle fuel began in the 1950s and saw significant emphasis through the 1960s, and 70s. The primary coated particle fueled High Temperature Gas-Cooled Reactor (HTGR) programs in the United States were the Peach Bottom HTGR, the Fort St. Vrain (FSV) HTGR, and the large commercial HTGR.

The Peach Bottom HTGR was a BISO fueled reactor project that was initiated in 1958, and produced the first electricity by a HTGR in 1967. The Fort St. Vrain HTGR was a TRISO fueled reactor project that was started in 1965, and the first electricity was produced in late 1976. After the completion of the FSV reactor, work began of the design of large (2,240 megawatt) commercial HTGR power plants. Unfortunately due to changes in national priorities, the work related to large commercial HTGRs declined in the late 1970s. Interest in HTGRs continued in Europe and smaller scale collaborative (with European partners) efforts in the United States continued through 1980s and 90s.

In recent years, due to the emphasis on the hydrogen economy, the interest in gas-cooled reactors has re emerged. Gas-cooled reactors operate at higher temperatures ($\approx$ 800°C) than typical water cooled power reactors ($\approx$ 300°C), and with the higher temperatures, gas-cooled reactors can be used in the co-production of hydrogen and electricity. A subset of gas-cooled reactors that are currently of interest are Gas-Cooled Fast Reactors (GFRs). GFRs will utilize high operating temperatures ($\approx$ 850°C), and will also employ a fast neutron energy spectrum. These characteristics will make GFRs capable of power production and hydrogen production, and due to the fast neutron spectrum, they will also be capable of fuel breeding and actinide burning. GFR technology development and reactor design is the focus of the Generation IV (Gen. IV) Gas-Cooled Reactor program (15).

1.3 Gas-Cooled Fast Reactor Fuel Concept

There are several fuel forms under consideration for use in Gen. IV GFRs. The leading candidate is a refractory matrix dispersion fuel. The dispersion fuel concept calls for coated fuel particles dispersed in a refractory matrix, which is encased in a metallic cladding. The concept is schematically shown in Figure1.2. As shown in the figure, fuel kernels are coated with a porous buffer layer whose purpose is to provide void volume for gaseous fission products and compliance to alleviate thermal and irradiation induced volume change stresses. Following the porous layer, an impermeable containment or pressure vessel coating is applied. The containment layer does just what the name implies. It retains the fuel material and the resulting fission products inside the particle. These bi-layer coated particles are then dispersed in a ceramic matrix whose purpose is to provide additional containment and to transfer heat from the fuel material. This fuel composite is then encased in a metallic cladding that is in direct contact with the helium or CO_2 reactor coolant.

The refractory matrix dispersion fuel concept is very similar to the HTGR TRISO CPF system. Unfortunately, since GFRs operate at faster neutron energy spectrum, and higher levels of fuel burn-up than thermal gas-cooled reactors, HTGR fuel (TRISO coated particles dispersed in a graphite matrix) is unsuitable for use in GFR applications. The two main barriers to the use of TRISO CPF in GFR applications are the neutron irradiation induced volume change of the dense carbon layers, and the moderating

properties of the carbon coatings and matrix material. In order to be a viable GFR fuel, the carbon coatings need to be minimized or replaced with a higher atomic number, high thermal stability ceramic material, and for reasons of compatibility, the replacement coatings ideally need to be the same material as the refractory matrix. Several matrix materials are under consideration, but due a significant history of in-reactor use, SiC is the leading candidate.

The long history of coating development for thermal gas cooled reactors has resulted in a relatively mature technology for the production of SiC particle coatings with desirable properties. For optimum performance in thermal gas cooled reactors, the coating needs to be fine grained equiaxed cubic SiC. TRISO-type SiC development demonstrated that fine grained equiaxed SiC was better for fission product retention due to reduced diffusion rates compared to SiC coatings with columnar through-thickness grains (grain boundary diffusion). In addition, it was found that cubic SiC exhibited better irradiation performance than the many hexagonal polytypes of SiC due to the isotropy of the cubic structure which provided for isotropic volume changes during irradiation (12).

Unfortunately, the mature TRISO-type SiC technology can not be transferred to the GFR application. The TRISO-type SiC is produced by FBCVD employing gas mixtures of methyltrichlorosilane (MTS) in hydrogen. Recall that the GFR CPF concept calls for SiC coatings to be applied directly onto the fuel kernel. The hydrochloric acid reaction product of SiC formation from MTS would corrode the fuel kernel if it were in direct contact with the kernel. Therefore, new processing techniques are needed to produce porous SiC buffer coatings and impermeable SiC containment (seal) coatings from non-halide precursors.

Various non-halide precursors for the deposition SiC by FBCVD were evaluated by Federer, and methylsilane was found to be most favorable choice (14). In addition, Angelini, in his research into the coating of nuclear waste ceramics, demonstrated that the production of dense impermeable SiC coatings from methylsialne was indeed feasible (16-17). Therefore, an investigation into the deposition of SiC coatings from methylsilane with goal of developing processing techniques for producing the bi-layer buffer and seal coated GFR fuel particles was undertaken.

This report describes the research effort that was carried out to develop and understand processing techniques for the deposition of SiC buffer and seal coatings from methylsilane by FBCVD.

1.4 Coating Development Research

This research was conducted in two phases. In the first phase, the feasibility of producing both porous SiC buffer coatings and dense SiC seal coatings on surrogate fuel particles was demonstrated. The SiC coatings were produced by FBCVD from the decomposition of methylsilane. Partially-crystalline SiC with densities ranging from less than 40% to greater than 90% of theoretical density were produced, and the variation in coating density was found to be due only to a change in coating temperature.

During the particle coating phase of this research, the mechanisms responsible for the wide range of coating density with varied deposition temperature were not investigated. The deposition mechanisms were studied in the second phase of the project.

In this second phase, a combined experimental and modeling effort was carried out. Owing to the complexity of the fluid bed, a single-substrate chemical vapor deposition (CVD) approach was instead used. The fluid bed was replaced with a cylindrical graphite substrate, and coating experiments were carried out at varied coating temperature and varied methylsilane/argon coating gas mixtures.

To determine the local conditions that were responsible for the varied coating properties, the single-substrate geometry and the experimental coating conditions were modeled. The model divides the single substrate system into segments, and the gas temperature, the gas composition, and the progress of several gas-phase and surface reactions are calculated in each segment. The calculated outlet characteristics of each segment become the inlet conditions for the next segment as the model evaluates local conditions in a stepwise fashion along the length of the substrate.

In the following chapters, the relevant literature will be reviewed, and then both the particle coating and single substrate research phases will be described in detail. Following that will be a discussion of the key results of the combined experimental and modeling efforts. Finally, the conclusions drawn from this research will be presented, as well as, some recommendations for future research.

2 Background and Literature Review

There is little information in the literature related to the CVD of SiC from methylsilane. The research most applicable to the coating of particles by FBCVD is Angelini's work on the CVD of SiC from methylsilane and the coating of nuclear waste ceramics (16-17). There is also some research that relates to basic chemistry studies of both surface and gas-phase decomposition of methylsilane (18-32). In addition, there is some relevant on-going FBCVD modeling activities associated with TRISO CPF (33-35).

2.1 FBCVD of SiC Containment Coatings from Methylsilane

The most relevant research concerning the deposition of SiC from methylsilane was Angelini's work on the FBCVD of SiC containment coatings on simulated nuclear waste particles (16-17). Angelini coupled thermodynamic and experimental evaluations of the CVD of SiC from methylsilane. The goal of that work was to demonstrate that nuclear waste ceramics could be coated with leach-resistant SiC coatings. In that work, Angelini carried out thermodynamic equilibrium calculations of the methylsilane-argon-hydrogen system. The CVD phase diagrams that resulted from those calculations were used to direct a set of experiments with varied reactant gas mixtures at various temperatures.

Angelini's equilibrium calculations were performed with the computer software SOLGASMIX-PV. The calculated CVD phase diagram for the methylsilane-argon-hydrogen system is shown in Figure 2.1. The CVD phase diagram shows that single phase SiC is predicted to form in a small region of high temperature and low hydrogen content in the diluent gas, while co-deposition of SiC and Si is predicted to occur over the remaining wide range of conditions considered.

Angelini followed the equilibrium analysis with an experimental evaluation over a range of gas composition and temperature that was similar to that used in the thermodynamic calculations. The experiments involved applying SiC coatings to pyrocarbon-coated Al_2O_3 microspheres with a pre-SiC diameter of approximately 750 μm. The SiC coatings were deposited via FBCVD. The experimental evaluation included coating runs at temperatures ranging from 600-1200°C, with diluent gas compositions of 100% Ar, 8% H_2 in Ar, 77% H_2 in Ar, and 100% H_2. It is important to note that FBCVD is highly non uniform; therefore the coating temperatures that are quoted are average or nominal values taken from either thermocouple or pyrometer measurements.

Based on the theoretical and experimental evaluation of the methylsilane-argon-hydrogen system, the following conclusions were made. SiC coatings produced by FBCVD from methylsilane at temperatures in range the between 700°C and 800°C are amorphous regardless of hydrogen concentration in the diluent. At temperatures of 900°C and higher, as-deposited coatings are at least partially crystalline and the amount of free silicon present increases with increasing hydrogen content in the diluent. Free silicon is not detectable by x-ray diffraction in any coatings deposited with 100% argon diluent.

Angelini further concluded that the deposition of SiC from methylsilane is characterized by a competition between surface deposition (surface adsorption of

molecular species) and by adherence of SiC particles that nucleated homogeneously in the gas-phase. The relative contributions of surface deposition and gas-phase nucleation depend on both temperature and hydrogen concentration in the diluent. When the diluent is pure argon, surface deposition is more favored in the temperature range below 800°C. Above 800°C, the amount of deposition due to homogeneous nucleation increases, and becomes the dominant mode at temperatures of 1000°C and higher. When the diluent is pure hydrogen, homogeneous nucleation does not play a significant role until the temperature reaches 1000°C.

In addition, it was concluded that coating density was a function of deposition mechanism. Coatings that were deposited primarily by surface molecular adsorption and subsequent reaction exhibited high density (near 100% of theoretical density), while coatings that were deposited primarily by agglomeration and adherence of homogeneously-nucleated particles were found to possess low density (near 70% of theoretical density). Therefore, since the deposition mechanism was a function of gas composition and deposition temperature, the SiC coating density could be controlled by the proper choice of deposition conditions.

Angelini's final conclusion was that the coating of nuclear waste ceramics with high-density impermeable SiC by FBCVD from the decomposition of methylsilane was feasible (16-17).

2.2 Gas-phase Decomposition of Methylsilane

There are several papers reporting the primary gas-phase decomposition of methylsilane (25-30). All of these papers report on efforts to determine the relative contributions of competing reaction rates based on measurements of concentrations of reactant and/or product gases. The conclusion of these papers is that Reactions 2.1-2.3 shown below are the only significant contributors to the primary decomposition of methylsilane, and further that Reaction 2.1 is the dominant reaction.

$$CH_3SiH_3 \rightarrow CH_3SiH + H_2 \qquad (2.1)$$

$$CH_3SiH_3 \rightarrow CH_4 + SiH_2 \qquad (2.2)$$

$$CH_3SiH_3 \rightarrow H_2Si = CH_2 + H_2 \qquad (2.3)$$

Sawrey (23-28) conducted reaction-rate experiments under shock tube conditions (625 kPa) in the temperature range of 850-975°C. Experiments were done with both deuterated and normal methylsilane (Reactions 2.1, 2.1a, 2.2, 2.2a, 2.3, and 2.3a), so that hydrogen evolution from either the methyl group or the silane group of the methylsilane molecule could be distinguished. The Arrhenius parameters for the rate constants and the efficiencies of Reactions 2.1-2.3 resulting from Sawrey's experiments are shown in Table 2.1. Recall that the Arrhenius parameters are the pre-exponential factor (A-values) and activation energies (Ea) in the Arrhenius equation, Equation 2.4. The Arrhenius equation gives the variation of the reaction rate constant, k, with temperature, T. In Equation 2.4, R is the ideal gas constant.

$$CH_3SiD_3 \rightarrow CH_3SiD + D_2 \quad (2.1a)$$

$$CH_3SiD_3 \rightarrow CH_4 + SiD_2 \quad (2.2a)$$

$$CH_3SiD_3 \rightarrow D_2Si = CH_2 + HD \quad (2.3a)$$

$$k = Ae^{\frac{-E_a}{RT}} \quad (2.4)$$

Sawery's results indicate that the dominant primary decomposition reaction is the production of CH_3SiH (mehtylsilylene) and H_2, Reaction 2.1. The scission of the Si-C bond to produce CH_4 and SiH_2, Reaction 2.2, is only a small contributor. The production of the CH_3SiH isomer $H_2Si{=}CH_2$ is also shown to be a minor contributor (26-28).

Neudorfl (25) reviewed the work of Sawrey (26-28) and also conducted independent experiments into the primary decomposition of methylsilane. Neudorfl studied the decomposition of methylsilane as a function of pressure (4–53 kPa) and temperature (340-440°C) in a hot wall vacuum furnace (25). Concentrations of selected reactant and product gases were measured so that rate constants for decomposition reactions could be determined. Neudorfl's results agreed well with those of Sawrey (26-28) and lead to the conclusion that Reaction 2.1, the production of CH_3SiH and H_2, was the dominant primary gas-phase decomposition step. Neudorfl further concluded that the gas-phase decomposition of methylsilane ultimately resulted in the production of dimethyldisilane [DMDS, $(CH_3SiH_2)_2$] and hydrogen gas, along with small amounts of dimethylsilane [DMS, $(CH_3)_2SiH_2$] and an uncharacterized surface deposit through a radical chain-reaction mechanism, Reactions 2.5-2.11 (shown in Table 2.2). The reaction scheme and the resulting Arrhenius parameters for the rate constants they measured are shown in Table 2.2.

2.3 Surface Decomposition CVD of SiC From Methylsilane

Limited research has been reported regarding the CVD of SiC from methylsilane (19-23, 31-32). In general, the conclusion of these studies is that either methylsilane itself or an intermediate reaction product formed in the gas-phase becomes adsorbed onto the surface of the substrate. Then, surface reactions and molecular rearrangements occur, and hydrogen is evolved and SiC is formed. The most relevant of these studies are the work of Johnson (31) and Ohshita (32).

Johnson (31) conducted low-pressure (7 Pa) cold wall CVD experiments in the temperature range of 600-1150°C with the single source precursor methylsilane. Partial pressure analyses based on mass spectrometry were used to determine the dominant decomposition channels. Johnson concluded that methylsilane was first physisorbed onto the substrate (single crystal silicon), and then the rate-limiting step was the evolution of hydrogen to form either chemisorbed CH_3SiH or its isomer $H_2Si{=}CH_2$ via Reaction 2.1 or 2.3. Both CH_3SiH and $H_2Si{=}CH_2$ are believed to be highly reactive intermediates capable of forming SiC films (23, 31). Based on Sawrey's results (26-28), Johnson assumed that Reaction 2.1 was the dominant reaction. Johnson further demonstrated through a heat

transfer analysis of the experimental system that the reaction to form CH_3SiH occurred almost exclusively on the surface and that gas-phase reactions under these conditions were negligible. Johnson reported the activation energy of the surface reaction (Reaction 2.1) was found to be 222 kJ/mol.

Ohshita (32) investigated SiC CVD using methylsilane diluted in hydrogen (1% methylsilane) with a macro/microcavity technique. Ohshita's goal was to determine CVD conditions that resulted in good step coverage for electronic applications. The experimental setup consisted of two parallel silicon wafers, 400 micrometers apart, heated by an infrared (IR) lamp (the macrocavity). One of the silicon wafers had one micrometer wide by one micrometer deep grooves cut into its surface (the microcavity). The dilute source gas diffused between the wafers and deposited SiC onto the surfaces.

Ohshita found that deposition rates were high, and step coverage was poor near the entrance of the macrocavity. Then, the deposition rate decreased to a constant but lower value with improved step coverage along the length of the macrocavity. Based on these results, it was concluded that two reaction mechanisms were taking place. Near the entrance of the macrocavity, the SiC coating was reported to result from the highly active reaction product, CH_3SiH, that formed from the gas-phase, Reaction 2.1. It was postulated that the active CH_3SiH was depleted by deposition near the entrance of the macrocavity and that SiC deposition along the remaining length of the macrocavity was due to adsorption of the less reactive methylsilane (CH_3SiH_3) precursor. The sticking coefficients and activation energies of both the highly active CH_3SiH and less active CH_3SiH_3 were calculated based on the microcavity step coverage results. The sticking coefficient of the CH_3SiH intermediate was reported to be near one, and the sticking coefficient of the methylsilane molecule itself was reported to be between 4×10^{-5} and 10^{-4} The activation energies for the deposition SiC from the intermediate CH_3SiH and the methylsilane source precursor were reported to be 213 kJ/mol and 180 kJ/mol, respectively (32).

2.4 Modeling of FBVCD

The Advanced Gas-Cooled Reactor Program (AGR) is an ongoing effort to further develop and improve TRISO CPF. The AGR program includes a significant FBCVD modeling effort (33-35), and some key results of that work merit review here.

The overall objective of the AGR modeling work is to develop and validate a computational model of the hydrodynamics, heat, and mass transfer occurring within the FBCVD reactor during the coating of TRISO CPF. The main computational tool used to implement the model is the general-purpose MFIX (Multiphase Flow with Interface eXchange) multiphase fluid-dynamics code (http://www.mfix.org), which has been specifically adapted to the spouted-bed configuration used for the coating reactor (33-35).

2.4.1 Reaction Zone

The results of the AGR modeling effort that are of relevance here are the general characteristics of the FBCVD process. Specifically, AGR modeling results show that the deposition reaction can occur in a relatively small reaction zone within the core of the fluid bed. This result is shown schematically in Figure 2.2.

Figure 2.2 is a representation of the hydrodynamics, heat transfer, and carbon formation during inner pyrolytic carbon (IPyC) deposition. In IPyC deposition, solid carbon and hydrogen gas are the products of the decomposition of an acetylene and propylene gas mixture. The solid carbon is deposited within a conical shaped coating chamber where the particle charge is fluidized by a stream of gas (a mixture of active and inert gas) that is injected into the bottom of the conical chamber.

Figure 2.2 is made up of six frames of three pictures each. Each frame represents a different time step in the FBCVD simulation. The six frames in Figure 2.2 span approximately one tenth of a second. The three pictures within each frame are the simulated void fraction, temperature, and H_2 concentration respectively within the fluidized bed. The color scheme for the void fraction is blue = 0.8 and red = 1.0 (blue for solids and red for gas). The color scheme for temperature is blue = 27°C and red = 1227°C. The color scheme for hydrogen mole fraction is blue = 0 and red = .03 (red for high and blue for low).

Considering the void fraction as a function of time (the right-most picture in each frame) the figure shows that a gas bubble forms near the inlet of the conical coating chamber, and a portion of the particle charge is carried with this bubble up and out of the fluid bed forming a spout of gas and particles. The particles, then, fall back to the surface of the fluid bed where they circulate back to the bottom of the cone as the bubbling process repeats itself. Looking at the temperature distribution as a function of time (the center picture in each frame) shows that as the gas bubble makes its way through the fluid bed, that the gas temperature increases, but does not appear to reach the ambient bed temperature until after it passes completely through the fluid bed of particles. Now, examining the hydrogen concentration as a function of time (the right most picture in each frame) it is clear from the hydrogen concentration pictures that the acetylene and propylene active gases react to form the carbon coating and hydrogen product gas in a relatively small reaction zone in and adjacent to the expanding gas bubble.

2.4.2 Gas and Solids Temperatures

Another relevant result of the AGR modeling effort is the temperature difference within the fluid bed between the coating gases and the solids onto which the coatings are deposited. The time-averaged temperatures of the gas and solids within the fluid bed are shown in Figure 2.3 (34). This figure resulted from a simulation of inert gas passing through a fluid bed of particles with an ambient bed temperature of 1300°C. The blue line in the figure is the gas temperature profile assuming that the gas flows through an empty conical chamber with a wall temperature of 1300°C. The red and black lines in the figure are centerline gas and solids temperatures assuming that the gas passes through the bed of particles inside a conical coating chamber whose wall temperature is 1300°C.

The characteristic to note here is the difference in between the gas and solids temperatures, the red and black lines. The figure shows that the gas enters the cone at low temperature, and, then, the gas and solids temperatures converge approximately 2 cm from the inlet. For the purposes of comparison, the conical portion of the coating chambers shown in Figure 2.2 is approximately 6 cm tall.

Considering Figure 2.2 shows gas temperature as a function of time, and Figure 2.3 shows the time-averaged gas and solids temperatures, they show that the gas and

solids temperatures are likely different during the entire time that the reaction zone or bubble passes through the fluid bed.

3 Particle Coating Investigation

An experimental evaluation of the FBCVD of SiC by the decomposition of methylsilane was conducted. Based on Angelini's (16-17) findings, it was clear that the temperature profile of the reactant gas as it approached and passed through the fluidized bed controlled the resulting coating structure. Therefore, an experimental plan was devised and carried out where the coating gas composition and the kernel batch size and make up were held constant, while the thermal condition of the fluidized bed was varied. Following are the results of that study.

3.1 System Description

A schematic of the FBCVD system is shown in Figure 3.1. The furnace was configured such that argon, hydrogen, and methylsilane gases, as well as methyltrichlorosilane (MTS) vapor could be input to the furnace. Gas flows were controlled by mass flow controllers (MFCs), and MTS vapor was carried to the furnace by hydrogen, which bubbled at a constant rate through the MTS liquid. Each MFC could be purged before and after a run through the use of the three-way valves located upstream of the MFC, and additional three-way valves between the MFCs and the furnace allowed reactant gases to either flow through or bypass the furnace. When coating with MTS, the furnace exhaust passed through a scrubber to neutralize the HCl reaction product prior to going into the building exhaust system.

A sectional cutaway view of the furnace itself is shown in Figure 3.2, and an enlarged sectional view of the coating chamber is shown in Figure 3.3. The figures show that the furnace consists of a water-cooled gas injector that is connected to a conically shaped graphite coating chamber via a ball and socket joint. The conical coating chamber, or cone, is surrounded by a graphite heating element, which is contained within a water-cooled furnace shell. The reactant gases pass through the water-cooled injector and into the bottom of the graphite cone. The particles are fluidized and coated inside the cone, and the reaction product gases exit the furnace through an exhaust port in the top of the furnace. The temperature of the top surface of the fluidized bed is measured using a hand-held optical pyrometer looking down from the top of the furnace through a sight glass.

3.2 Coating Procedure

The procedure for conducting particle coating runs consisted of loading the particle charge into the furnace under inert fluidization, raising the temperature of the furnace to the desired level, establishing the desired methylsilane flow rate, holding the temperature and gas flow rates constant for the desired run time, discontinuing the methylsilane gas flow, lowering the furnace temperature to room temperature (turning off furnace power), and then unloading the coated particle charge.

The particle loading was accomplished by pouring the particle charge through a funnel that was inserted through the top sight glass port while inert fluidization gas was flowing and the furnace was at room temperature. The particle charge was 20 g of 0.5 mm yttria-stabilized zirconia (YTZ) microspheres. The microspheres were commercially

available YTZ spherical grinding media (95%ZrO_2, 5% Y_2O_3) purchased from TOSOH USA, INC.

The choice of surrogate microspheres was based on the physical properties of the surrogates compared to that of uranium-containing kernels that will ultimately be used in the final fuel form. There were two commercially available choices for surrogate kernels, hafnia and zirconia. The hafnia microspheres had a similar density compared with the uranium bearing kernels (hafnia-9.7 g/cm^3, zirconia-5.9 g/cm^3, U-bearing 11 g/cm^3), while the zirconia had a similar coefficient of thermal expansion compared to uranium bearing kernels (hafnia-6.5 x 10^{-6}/°C, zirconia-10 x 10^{-6}/°C, U-bearing11 x 10^{-6}/°C). Based in these property comparisons, the hafnia appears to be a more representative surrogate in terms of fluidization, while the zirconia is better in terms of residual thermal stresses. Since this study is focused on process development, the hafnia microspheres would seem to be a better choice of surrogates for U-bearing kernels, but unfortunately the commercially available hafnia microspheres where both more expensive and they exhibited poor sphericity compared to the zirconia kernels. For these reasons, this study was conducted using the zirconia microspheres.

After the particle charge was loaded and the sight glass was re-installed, the furnace was brought up the desired temperature. The temperature was measured using a handheld optical pyrometer (Spectrodyne Inc. Model DPF 2000 disappearing filament optical pyrometer with telephoto lens calibrated by the Oak Ridge National Laboratory Metrology Laboratory in compliance with ANSI/NCSL Z540.1-1999 R2002) focused on the top surface of the particle bed. It is important to note that the only the top-surface temperature of the fluidized bed is measured in preparation for a coating run, and the coating temperature reported herein is the top surface temperature of the fluid bed.

The furnace temperature was controlled by a second optical pyrometer (Ircon "Modline" spot pyrometer) that was focused on the outside of the conical coating chamber. Controlling the temperature on the outside of the coating chamber was necessary because of soot formation during deposition that obscured the view of the particle bed. (For the benefit of readers who are familiar with TRISO coating it should be noted that this sooting phenomenon during SiC coating does not occur in the TRISO-type MTS-derived SiC coating process, but due to the propensity for gas-phase nucleation, sooting similar to that observed during TRISO-type carbon deposition occurs during SiC deposition from methylsilane.) Therefore, the temperature of the coating chamber was noted when the particle bed temperature was at the desired value under inert fluidization, and this noted value of the coating chamber temperature was used as the set point for thermal control during the coating run.

Once the furnace temperature had reached the desired steady state value, the flow of methylsilane (CH_3SiH_3 UHP, 99.98%, Voltaix, Inc.) was initiated. The flow rates of inert and methylsilane gases were controlled via MKS Instruments model 1179 Mass-Flo® Controllers (calibrated using a Ritter Apparatebau GmbH & Co. KG drum-type gas meter model TG5/5-ER under calibration certificate Nr. 0.525.ICO). The methylsilane flow was routed directly to the exhaust (bypassing the furnace) until the flow reached a steady state value at the desired set point. Then the methylsilane flow was diverted to the furnace thus starting the coating run.

Temperature and gas flows were maintained at the set points until the desired run time has elapsed, at which point the flow of methylsilane was switched to bypass mode thus ending the coating run. The furnace power was then turned off, and the furnace was allowed to cool to room temperature. The particle charge remained fluidized by inert gas during the furnace cool down.

When the furnace had cooled to room temperature, the inert fluidization gas was turned off, and the particles drained by gravity into the catch cup on the bottom of the furnace.

3.3 Fluid Bed Thermal Profile

As mentioned above, a pyrometer measurement of the temperature of the top surface of the fluid bed is made to set the control temperature of a coating run, and that top surface temperature measurement is referred to in this report as the "coating temperature" for particle coating. From the background discussion presented above, the thermal profile of the fluid bed is both complex and important to the coating process. The thermal profile of the fluid bed was measured at nominal coating temperatures of 900°C, 1,000°C, 1,100°C, and 1,200°C using a thermocouple (Omega Engineering Type K) that was inserted into a bed of particles, as shown in Figure 3.4. Temperature readings were taken at several axial locations within the fluid bed at each coating temperature. During these measurements, the particle bed (20g of 500 μm diameter ZrO_2) was fluidized with 5,000 cm^3/min of argon.

The results of the thermal profile measurements are presented in Figure 3.5. The figure demonstrates that the fluid bed exhibits a significant thermal gradient between the inlet and exit of the particle bed. The thermocouple readings range from approximately 300°C to 500°C at the inlet and from 650°C to 1,050°C at the exit of the fluid bed, depending on the coating temperature. No effort was made to determine the relationship between these thermocouple measurements and either the gas temperature or the solids temperature. These results are presented to expose some of the complexity inherent in FBCVD.

3.4 Coating Experiments and Characterization

Coating experiments were carried out at bed temperatures of 900°C, 1,000°C, 1,100°C, and 1,200°C. A summary list of conditions and results of coating experiments is given in Table 3.1. The kernel batch size was held constant at 20g of 500 μm diameter ZrO_2 and the coating gas consisted of two volume percent methylsilane in argon with a total gas flow of 2,000 cm^3/min. Coatings produced in this experimental series were subjected to scanning electron microscopy (SEM) using a Hitachi Model S4700 SEM.

Photographs of the fracture surfaces of crushed particles produced during this series of experiments are shown in Figure 3.6. The SEM photographs demonstrate that coatings with an apparently high density could be made in the 900°C to 1,000°C range, and coatings with apparently low density could be made in the 1,100°C to 1,200°C range. The coating thickness produced in this series of experiments was too low to do meaningful characterization, so a follow-on set of coating runs was conducted to produce coated particle batches with increased coating thickness for characterization.

The follow-on set of coating experiments was performed over the same temperature range of 900°C to 1,200°C. In this series of experiments the run time was extended to produce thicker coatings to facilitate limited characterization. Also, the total gas flow was increased to 5,000 cm^3/min in order to maintain fluidization of particles with significantly thicker coatings. The flow rate of methylsilane was kept the same as the previous set of experiments, which reduced the volume fraction of methylsilane in argon to 0.8%. A summary list of conditions and results of coating experiments is given in Table 3.1.

SEM images of fracture surfaces of crushed coatings over the range of coating temperatures are shown in Figure 3.7. Bulk densities of the coatings are also shown on the figure. The figure shows again that low temperature coatings have little porosity, and high density. Then as temperature increases, the amount of porosity increases, resulting in decreased coating density.

The bulk densities shown in Figure 3.7 were calculated by diameter and mass differences of coated and uncoated kernels. One thousand bare kernels and 1,000 coated particles from each coating run were weighed. The diameters of fifty particles from each batch of 1,000 were measured from 50X photographs using the image analysis software Image J (47). The bulk density of the coatings was calculated, based on the averages of these measurements.

In addition to SEM, X-ray diffraction (XRD) was performed on samples of particles coated at each temperature. A monolayer of coated particles was embedded into a film of petroleum jelly that was applied to the goniometer sample holder. Diffraction scans were made under the conditions detailed in Table 3.2. The diffraction patterns from these samples are shown in Figure 3.8. Reference patterns (44-46) for cubic SiC, ZrO_2, and graphite are presented along with the diffraction patterns for the coatings. The patterns for the coatings show diffraction peaks that correspond to cubic silicon carbide, but the peaks are diffuse (spread out rather than sharp) indicating that the coatings consist of small crystallites in an amorphous matrix. The patterns show that as the coating temperature is increased, the diffraction peak width stays roughly constant, and that the peak intensity increases. The observation that the width of the diffraction peaks stays constant with increasing coating temperature indicates that the average size of the individual crystallites is constant with increasing coating temperature. The increase in diffraction peak intensity (height) leads to the conclusion that the volume fraction of crystallites (degree of crystallinity) does increase at higher coating temperatures. A detailed analysis to determine the size and volume fraction of the crystallites was not done.

The diffraction patterns gave no indication of crystalline free silicon in any of the coatings. The peaks that correspond to the ZrO_2 are due to the ZrO_2 kernels that were used as substrates. The slight amorphous hump (located at approximately 26 degrees) corresponding to graphite is present because a layer of carbon buffer coating was applied prior to the SiC to alleviate the thermal expansion mismatch between the ZrO_2 and SiC. This was necessary because thermal stresses present in earlier experiments where SiC was applied to bare ZrO_2 kernels caused the SiC coating to spall.

The effect of annealing on the level of crystallinity present in the low temperature coatings was evaluated. A sample of the 900°C batch was annealed at 1,500°C in

hydrogen for 30 minutes and re-analyzed by XRD. The particle diffraction patterns for both the un-annealed and annealed coatings are shown in Figure 3.9. The pattern for the un-annealed high temperature (1,200°C) coating and reference patterns for cubic SiC, ZrO_2, and graphite are presented also for comparison (44-46). The patterns demonstrate that the annealing step significantly increased the degree of crystallinity (volume fraction of crystallites) of the low temperature coating. Samples of the higher temperature coatings were not annealed because the low temperature coating represented the worst case.

SEM micrographs of fracture surfaces of crushed particles for both un-annealed and annealed coatings are shown in Figure 3.10. The photographs show little effect of annealing on the appearance of the coating fracture surface. No evidence of cracking or increased porosity was observed.

3.5 SiC Buffer and Seal Coatings

The ultimate goal of this experimental work was to develop both low density SiC buffer coatings and high density (impermeable) SiC seal coatings from non-halide precursors. Based on the results for coatings produced over the temperature range presented here, the low temperature, high density (1,000°C) coatings are promising candidates for the SiC seal coatings, and the high temperature, low density (1,200°C) coatings are promising candidates for SiC buffer coatings. Low magnification photographs of the low temperature, high density SiC seal coated particles are presented in Figure 3.11, and low magnification photographs of the high temperature, low density SiC buffer coated particles are presented in Figure 3.12. The consistency of both the seal and buffer coatings is apparent in these photographs.

The standard for comparison for the potential SiC buffer and seal coatings will be the TRISO-type acetylene-derived carbon buffer and MTS-derived SiC coatings, respectively. The TRISO-type carbon buffer coatings are near 50% of theoretical density and contain mostly open porosity (8-12). SiC buffer coatings have been produced in this work that are 33% dense. The porosity in these SiC coatings has not been characterized, but based on the similarity of the apparent deposition mode (the adherence of particle agglomerates that originated in the gas-phase), it is likely that a significant amount of open porosity exists in these SiC buffer coatings.

SEM micrographs of the fracture surfaces of both a TRISO-type carbon buffer coating and a SiC buffer coating produced in this study are presented in Figure 3.13. The micrographs show that both coatings consist of small homogeneously nucleated particles that adhere to the substrate. Although the particles that make up the SiC buffer coating are smaller than that of the carbon buffer coating, Figure 3.13 shows that the morphology of the SiC buffer coating produced in this study is similar to that of the TRISO-type carbon buffer coating.

A comparison of the coating fracture surfaces of non-halide SiC seal coating and MTS-derived TRISO-type SiC is shown in Figure 3.14. Figure 3.14 contains SEM micrographs of the fracture surfaces of a crushed SiC seal coating and a MTS-derived TRISO-type SiC. In addition to SEM, a sample of TRISO-type SiC produced by FBCVD at 1,500°C in a hydrogen/MTS gas mixture was subjected to XRD for comparison with the non-halide SiC coatings. The resulting pattern is shown in Figure 3.15 along with

those of the annealed seal coating and the un-annealed buffer coating. The patterns for the buffer and seal coatings show that they are not as crystalline as the MTS-derived SiC, but that the same SiC phase is present.

3.6 Multilayer Particle Coatings for Fuel Applications

The concept for all CPFs calls for multilayer coatings that work together to provide containment for the fissile and fertile species and the fission reaction products. Processing of multilayer coated particles was also examined. Both two layer and three layer variants were produced. Figure 3.16 shows both low magnification and higher magnification SEM images of a dual layer coated particle, while Figure 3.17 presents optical microscopy images of the dual layer coated particles. The first layer in the dual layer scenario is the high temperature, low density SiC buffer coating, and the second layer is the low temperature, high density SiC seal coating. These dual layer coated particles were produced in a continuous process where the processing conditions were adjusted during the run to transition between the buffer and seal coatings.

Three layer particle coatings were also produced in a continuous manner by changing processing conditions during the run. Figure 3.18 presents SEM photographs detailing the three layer coatings, and Figure 3.19 shows low magnification optical photographs of these three layer coated particles. The first two layers on the three layer coating scenario are the SiC buffer and seal coatings. The third layer is a MTS-derived SiC over-coating. The rationale for exploring the addition of MTS-derived SiC to the dual layer non-halide SiC coated particle is two fold. First, the deposition rate for MTS-derived SiC is higher than that of the methylsilane SiC seal coating, so the thought is to seal the particle with the non-halide SiC to protect the kernel from chlorine attack (HCl is a product of the MTS-SiC reaction) and apply the needed thickness of SiC for containment using the faster MTS-SiC processing. The second reason is the fact that MTS-derived SiC is a long used, well understood, and trusted particle coating, and its use as the primary containment layer would eliminate the need to qualify the non-halide SiC for duty as the containment layer.

3.7 Particle Coating Conclusions

The ultimate goal of this research is to work toward the development of particle coatings that would be suitable for use in GFR fuel applications. The results of the particle coating study are very encouraging. A range of new processing conditions was explored and non-halide derived SiC buffer and seal coatings were developed, but the deposition mechanisms responsible for producing both buffer and seal coatings by only varying the temperature merit further investigation.

Based on the literature review and the particle coating experiments it is hypothesized that the difference in observed coating morphology as a function of fluid bed temperature is due to a competition between surface and gas-phase reactions. Surface adsorption of either methylsilane or the CH_3SiH intermediate has been reported (18-32). The adhesion of particles that originated as a result of gas-phase nucleation has also been a proposed deposition mechanism (16-17). Determining the dominant reaction mechanisms merits study.

4 Single Substrate Experiments

In an effort to gain a better understanding of the deposition mechanisms, a combined experimental and modeling approach was carried out. Due to the complexity of the fluid bed environment, a series of coating experiments was carried out using a cylindrical graphite substrate in place of the fluidized bed of zirconia particles. (Graphite was chosen to replace zirconia because it is readily available and relatively inexpensive, and since this study deals with relatively thick coatings, the difference in the substrate surface between the zirconia and the graphite was assumed to be insignificant.) In addition, the single substrate geometry was modeled to illustrate the local conditions and the resulting reaction mechanisms. The following sections detail the single substrate coating system and coating results. Then the model and the results it generated will be discussed.

4.1 Coating System

A concentric annulus geometry was chosen for the experimental apparatus because it provides efficient heating of the reactant gas, and a relatively long time of flight of reactant gas over the surface of the substrate. These characteristics combined with the propensity for gas-phase decomposition of methylsilane allow the local deposition conditions to vary along the length of the substrate. Therefore, one coating experiment yields a variety of coating properties.

The single substrate coating experiments were carried out in the same furnace system as the particle coating experiments (Figures 3.1-3.2). For the single substrate coating runs, the particle coating chamber was replaced with the single substrate geometry, as shown in Figure 4.1. The figure shows that the substrate was a 1.9 cm diameter by fifteen cm long graphite cylinder, which was placed inside a 2.5 cm diameter conical-bottom coating chamber that was made to interface with the existing water cooled gas injector used for particle coating (ball and socket joint). The bottom end of the cylindrical substrate was beveled so that it would be self centering via three point contact in the conical bottom of the coating chamber. The beveled end also allowed gas flow from the inlet of the coating chamber into the annular gas space between the cylindrical substrate and the coating chamber. The top of the substrate was held in place by three tapered graphite pins that were press fit around the circumference of the upper end of the substrate. The substrate was loaded into the coating chamber and the alignment pins were pressed in by hand prior to installing the coating chamber into the furnace.

4.2 Coating Procedure

The procedure for coating the graphite substrates consisted of installing the pre-assembled coating chamber and substrate in the furnace, initiating the inert gas flow, bringing the furnace up to the desired coating temperature, establishing the flow of methylsilane, maintaining the temperature and flow rates through the desired run time, ceasing the flow of methylsilane, lowering the furnace temperature to ambient, and then unloading the coated substrate.

The pre-assembly of the coating chamber and substrate consisted of sliding the graphite substrate (Grapftek LLC grade GR008G superfine grain, high density extruded graphite rod) into the coating chamber and inserting the press-fit graphite alignment pins. The coating chamber/substrate assembly was then installed in the furnace.

Once the furnace was re-assembled with the substrate in place, the furnace was brought up to the coating temperature. The temperature was measured using a thermocouple (Omega Engineering Type C) that was inserted into a blind hole that was drilled along the centerline of the cylindrical substrate. The tip of the thermocouple was located at the 55 mm axial position, and the temperature was controlled at this location using a Honeywell Inc. Model UDC3300 controller.

The flow rates of the inert and methylsilane gases were controlled via MKS Instruments model 1179 Mass-Flo® Controllers. The inert gas flow was initiated prior to heating the furnace and was maintained until after the coating run when the furnace had cooled to room temperature. The flow of methylsilane (CH_3SiH_3 UHP, 99.98%, Voltaix, Inc.) was initiated after the furnace temperature had reached steady state at the desired set point. The temperature and gas flow rates were maintained constant at the desired set points until the run time had elapsed, at which point the methylsilane flow was turned off, the furnace power was turned off, and the furnace was allowed to cool to room temperature. After the furnace had cooled to room temperature, it was disassembled and the substrate was removed from the coating chamber.

4.3 Coating Experiments

A total of fifteen coating experiments were carried out in this study. The details of which are presented in Table 4.1. The table shows that coating experiments were carried out in the temperature range from 575°C to 700°C. The coating temperature range was chosen based on the thermal profile measurements conducted in the particle coating experiments, as described in the particle coating section of this document. The single substrate coating temperature was measured by a thermocouple that was inserted into a blind hole that was drilled into the substrate along its centerline.

Dilute mixtures of methylsilane in argon were used in all of the coating runs with total gas flow rates in the 900 to 1,000 cm^3/min range. The argon to methylsilane volume ratios varied from six to forty two. The gas flows rates were controlled via electronic mass flow controllers.

Photographs of several coated specimens are shown in Figure 4.2. The figure shows specimens that were coated over a variety of temperatures and methylsilane flow rates (the total gas flow rate was approximately1,000 cm^3/min for all of the specimens). The photographs are in order of increasing temperature and then increasing methylsilane flow rate from top to bottom.

Figure 4.2 shows that the coating temperature has a significant effect on coating appearance, while the flow rate of methylsilane only seems to affect the amount of coating and not its appearance. At the low coating temperature of 575°C (AFCI-SiC-8), the lower half of the specimen is uncoated and the coating on the upper half is grey and continuous. Specimens AFCI-SiC-11 and 14, which were coated at 600°C, have a short uncoated region near the inlet end of the specimen (left side of the photograph), and the coating transitions from grey to brown near the upper end of the specimen. Considering

the specimens coated at 625°C (AFCI-SiC-12, 10, and 15), the transition from the grey to the brown coating occurs near the mid point of the specimen and the brown coating continues to the outlet end. Then when the coating temperature is increased to 650°C and 700°C (AFCI-SiC-1 and 4 respectively), the transition from grey to brown occurs even closer to the inlet.

Figure 4.3 shows the reason for the change in appearance of the coating along the length of the specimens. Figure 4.3 contains a photograph of a coated specimen that exhibits the transition in coating appearance, as well as SEM (Hitachi model S4700 SEM) photographs of the surface morphology of three axial locations on the specimen. The figure shows that the grey deposit is a continuous coating that is due to molecular surface deposition (surface deposition zone). Then moving axially along the specimen, the coating becomes more nodular in appearance due to a mixed mode of deposition where surface deposition and adherence of homogeneously nucleated particles are both active (transition zone). Then at larger axial distances from the inlet, the transition from heterogeneous to homogeneous nucleation becomes complete and the coating appears to be completely made up of particles that originated in the gas-phase (homogeneous nucleation zone).

It should be noted that characterization of coatings was limited to SEM examination of the specimens and coating thickness determination in the surface deposition zone. Based on the characterization results of the particle coating experiments, the coating is assumed to be mostly amorphous SiC with the coating envelope density varying from approximately 90% of theoretical for the surface deposited coating to 50% of theoretical for coatings that consist of particles that nucleated homogenously. Since the purpose of this research is to investigate the deposition mechanisms, the detailed characterization of the coatings, beyond that mentioned above was deemed unnecessary.

In the next few sections the three zones of coating appearance will be discussed in more detail. The surface deposition zone will be first, followed by the transition zone, and finally the homogeneous nucleation.

4.4 Surface Deposition Zone

To compliment the modeling, coating thickness data as a function of axial position in the surface deposition zone was needed. The experiments demonstrated that the critical temperature range for surface deposition was from 575°C to 650°C. Unfortunately, the deposition rate at 575°C was so low that it made producing coatings thick enough to be effectively measured impossible. An attempt was made to measure coating thickness from a specimen coated at 650°C. Sample AFCI-SiC-1 was produced at 650°C, but the coating was too thin in the surface deposition zone to get meaningful measurements. An attempt was made to produce a sample with a thicker coating by increasing the run time (AFCI-SiC-13), but the deposition rate in the homogenous nucleation zone was so high that the coating in that zone completely filled the annular gas flow path and fused the substrate inside the coating chamber. As a result, coating thickness profiles were only determined for specimens coated at 600°C and 625°C.

The coating thickness was measured at several axial locations on samples AFCI-SiC-11, 12, 10, 14, and 15 (in order of increasing temperature and methylsilane flow

rate). The total gas flow for all of these coating experiments was 1,000 cm^3/min, and the coating times were sufficiently long to produce adequate coating thickness for measurement. The coated specimens were cut in half lengthwise with one half dedicated to coating thickness measurements and the other half kept for surface examination by SEM.

The coating thickness was measured from SEM photographs of polished cross sections that were cut from each specimen at several locations along the length of the surface deposition zone. Figures 4.4-4.8 are photographs of specimens AFCI-SiC-11, 14, 12, 10, and 15 respectively. The photographs show the section locations and polished surfaces from which the coating thickness measurements were made. The coating thickness was measured on SEM micrographs that were taken at least four locations on each sample segment. Figure 4.9 presents a picture of a typical specimen segment (AFCI-SiC-14C) along with the four SEM micrographs taken from the locations shown.

The coating thickness was measured using the image analysis software Image J (47). Figure 4.10 demonstrates how the coating thickness measurements were made. The linear scale for each measurement was set using the scale marker on the SEM micrograph. Then linear measurements of the coating thickness were made manually with the computer mouse at approximately ten locations on each micrograph. The red lines on Figure 4.10 represent the linear measurements made, and the table of measurements shown in the figure are the actual measurements from specimen segment AFCI-SiC-14C. The measurement results for each sample segment were averaged to give the average coating thickness for that segment. Therefore, the average coating thickness for each segment is the average of approximately forty individual measurements taken from four different SEM photographs.

The results of the coating thickness measurements as functions of position are shown graphically for samples ten, eleven, twelve, fourteen, and fifteen in Figures 4.11-4.15. Also shown for reference in each figure is a photograph of the associated specimen scaled approximately to match the scale of the x-axis of the plot. Note that the error bars on the plots of coating thickness verses position are the standard deviation of the thickness measurements.

The experimental deposition rates are plotted as a function of deposition temperature in Figures 4.16 and 4.17. Note that the deposition rate is the coating thickness divided by the run time. Figure 4.16 is a plot of deposition rate verses axial position for the specimens coated at an average temperature of 600°C, and Figure 4.17 is a similar plot for specimens coated at an average temperature of 625°C.

One of the motivations for determining the coating rates was to try to establish the deposition reaction activation energy so that it could be used in conjunction with the kinetic modeling. Unfortunately, the deposition rate data from the experiments carried out here does not lend itself to activation energy determination. In order to determine the activation energy of the deposition reaction, experiments need to be carried out over a range of temperatures, but each individual experiment needs to be isothermal. Also, the reactant gas composition needs to be constant and known for each experiment. As will be demonstrated in the modeling chapter, the gas and surface temperatures vary slightly over the length of the specimen, and gas-phase reactions over the length of the specimen

cause the gas composition to change significantly. Therefore, the experimental activation energy in the surface deposition zone was not determined.

4.5 Transition Zone

The transition zones for coatings produced at 625°C, 650°C, and 700°C (run numbers AFCI-SiC-10, 1, and 4) were examined using SEM. Figure 4.18 presents a series of SEM micrographs that were taken every two millimeters in the transition zone of specimen AFCI-SiC-10, which was coated at 625°C. Figures 4.19 and 4.20 are the corresponding series of SEM micrographs for specimens AFCI-SiC-1 (650°C) and 4 (700°C) respectively. Figures 4.21-4.23 are repeats of Figures 4.19-4.20 at a higher SEM magnification.

The lower magnification series of micrographs for coatings deposited at 625°C, 650°C, and 700°C (Figures 4.18-4.20), all show a similar trend. The surface deposited coating (the first micrograph in each series) is somewhat nodular and the average nodule size is roughly the same for the three coating temperatures. Then looking at successive photographs in each series, the nodules become smaller and have more distinct boundaries until the last photo is reached where the coating consists of irregularly shaped aggregates with a "snowflake-like" appearance. From these lower magnification micrographs, the transition from heterogeneous to homogeneous nucleation appears to not be a strong function of temperature. There is the peculiar observation that the intermediate temperature case (650°C) has a significantly shorter transition zone. This short transition may be due to the low methylsilane flow rate that was used in coating that specimen.

Looking at the higher magnification series of micrographs for each of the three deposition temperatures, shown in Figures 4.21-4.23, the observation that there is little effect of temperature on the transition behavior is seen again. The higher magnification does a better job of demonstrating how the transition occurs. Starting on the surface deposition end of the transition and stepping towards the homogeneous nucleation zone it is seen that the smooth features become rough on their surface and then the roughness becomes small nodules. These small nodules become more plentiful and ultimately grow in length and reduce in diameter to form dendrite-like structures with open space between the dendritic branches.

These series of pictures fit well with the theory that the deposition in the transition zone is a competition between surface deposition and homogeneous nucleation. In the surface deposition zone the coating is smooth and continuous, and then as homogeneous nucleation occurs, particles that nucleated in the gas stick to the surface. These surface bound nuclei are covered up by more surface deposition leaving a surface that appears slightly rough when compared to the surface deposition zone. As homogeneous nucleation becomes more prevalent, there is less surface deposition occurring to overcoat and fill in between the surface bound nuclei. This phenomenon provides for the appearance of dendrite-like structures with many branches and significant open space between the branches.

4.6 Homogeneous Nucleation Zone

Regardless of deposition temperature, the coating in the homogeneous nucleation zone consists exclusively of dendrite-like or snowflake-like aggregates. Figures 4.24, 4.25, and 4.26 show SEM micrographs of the coating surface at a few axial locations within the homogeneous nucleation zone for each of the three deposition temperature cases (AFCI-SiC-10, 1, and 4 respectively). Figure 4.24, which is for the 625°C case, illustrates that there is little change in the dendrite-like branch size or length as axial position is increased. This same trend is seen in Figure 4.26, which is for the 700°C case, run number AFCI-SiC-4. Looking at the 650°C case (Figure 4.25), there is an increase in dentrite-like feature appearance. The average size diameter of the dendrite branches increases with axial displacement. The reason this increase in feature size is evident only in the intermediate temperature case may be due to a competition between reaction rate increase with increased temperature and coating gas consumption. One would expect the nucleation and growth rates of gas borne particles to increase with increasing temperature, but in the high temperature case, the coating gas may be consumed by reaction at low axial displacement. This would have the effect of stopping the growth of the gas borne particles, meaning that the particles that become surface bound on the down stream end of the substrate had formed and stopped growing at a lower axial position.

Figure 4.27 presents SEM images of the surfaces of each of the three temperature cases. Theses micrographs were taken near the down stream end of each of the three specimens, and they illustrate the peak in feature size at the intermediate temperature of 650°C.

5 Deposition Model

A model of the deposition of SiC from the decomposition of methylsilane in the concentric annulus configuration has been developed. The model was constructed in a spreadsheet. In the model, the annular geometry is divided into axial segments as shown in Figure 5.1. The change in gas composition due to the chemical reactions, and the change in gas temperature due to heat transfer with the surface of the substrate and the inner wall of the coating chamber are calculated in each segment. The calculated conditions at the end of each segment become the initial conditions for the next segment. Therefore, the local conditions of temperature and gas composition are tracked in a stepwise fashion along the entire length of the substrate. The major assumptions of the model are:

- Each segment contains a fixed number of moles of gas (N_T).
- The volume of each element is defined as the volume occupied by N_T moles of gas at the segment temperature, under ideal gas assumptions.
- The initial composition of the gas is based on the experimental flow rates that are being modeled.
- The gas enters the first model segment at room temperature.
- Since only dilute mixtures of methylsilane are used, the thermal properties of the gas are assumed to be equal to that of the argon diluent.
- The gas temperature in each model segment is assumed to be constant through out the segment (no radial or axial gradients within the segment)
- The gas temperature in each segment is calculated based on heat transfer in the previous segment
- The surface temperatures of both the substrate and the inner diameter of the coating chamber are assumed to be equal and constant within each model segment.
- The rates of the chemical reactions are assumed to be constant through out each model segment.
- The amounts of the various species in each segment are calculated based on the extent of chemical reaction in the previous segment.
- The model calculates a radial concentration gradient within a segment based on the rates of depletion from surface deposition and diffusion of species to the surface.

In the following sections the model will be described in detail. A discussion of the reaction scheme employed in the model is first. Then, the assumptions that go into the reaction kinetics computations will be presented. After that, the determination of the temperature distribution will be discussed. Then finally, the model calculations will be stepped through in detail as they are carried out in the model.

5.1 Model Reactions

A reaction scheme was developed for the model that includes both surface deposition and gas-phase reactions. The model envisions surface deposition by

adsorption of methylsilane, adsorption of methylsilane decomposition products, and adsorption of embryos (molecules that are larger than methylsilane). The gas-phase reactions in the model include the initial decomposition of methylsilane followed by the formation of embryos by the combination of methylsilane and its decomposition products. The molecules that are larger than methylsilane are referred to as embryos because they are believed to be the initial stage of homogeneous nucleation of SiC particles.

The model reaction scheme assumes that the following ten reactions take place. The first is the adsorption of methylsilane (CH_3SiH_3) onto the surface of the substrate (Reaction 5.1).

$$CH_3SiH_3 \rightarrow Surface \tag{5.1}$$

The second is the gas-phase decomposition of methylsilane to form methylsilylene (CH_3SiH) and hydrogen (Reaction 5.2).

$$CH_3SiH_3 \rightarrow CH_3SiH + H_2 \tag{5.2}$$

Reaction 5.3 is methylsilylene surface adsorption.

$$CH_3SiH \rightarrow Surface \tag{5.3}$$

The combination of methylsilylene and methylsilane to form an embryo is given in Reaction 5.4, and the combination of methylsilylene and an embryo to form a larger embryo is presented in Reaction 5.5.

$$CH_3SiH + CH_3SiH_3 \rightarrow Embryo \tag{5.4}$$

$$CH_3SiH + Embryo \rightarrow Embryo \tag{5.5}$$

The model allows for embryos to adsorb onto the surface (Reaction 5.6), evolve hydrogen to form a radical (Reaction 5.7), or combine with either methylsilylene or a radical to form a larger embryo (Reactions 5.5 and 5.10). Note that the term "radical" is used here to refer to all molecules larger than methylsilane that have unused bonds and are likely to be highly reactive. The radicals formed by the decomposition of embryos can adsorb onto the surface (Reaction 5.8), or combine with either methylsilane or an embryo to form larger embryos (Reactions 5.9 and 5.10).

$$Embryo \rightarrow Surface \tag{5.6}$$

$$Embryo \rightarrow Radical + H_X \tag{5.7}$$

$$Radical \rightarrow Surface \tag{5.8}$$

$$Radical + CH_3SiH_3 \rightarrow Embryo \quad (5.9)$$

$$Radical + Embryo \rightarrow Embryo \quad (5.10)$$

Recall from the background discussion that the reaction between methylsilane and methylsilylene results in the formation of dimethyldisilane ($(CH_3SiH_2)_2$) (25). For the purposes of this calculation, the formation of dimethyldisilane is considered the initial step in embryo formation.

Of these ten reactions, only Reactions 5.1-5.4 have an explicit basis in the literature of methylsilane CVD (16-32). Detailed studies of the formation of homogeneously nucleated SiC particles from the decomposition of methylsilane have not been done and are outside the scope of this work. But based on the experimental results, homogeneous particle formation obviously occurs. Therefore, Reactions 5.5-5.10 were conceived to account for the observed gas-phase nucleation. The basis for this is that each of the Reactions 5.5-5.10 is assumed to be analogous to one of the Reactions 5.1-5.4.

5.2 Kinetic Calculations

The deposition model assumes all reactions are first order and follow the Arrhenius relation, Equations 5.11 and 5.12 (37)

$$r = \frac{d[B]}{dt} = k[B] \quad (5.11)$$

$$k = AExp^{\left(-E_A/RT\right)} \quad (5.12)$$

where [B] is the molar concentration of species B, k is the rate constant, A is the pre-exponential factor, E_A is the activation energy, R is the ideal gas constant, and T is the absolute temperature.

The kinetic theory of gases is used in conjunction with activation energy data from the literature and from the experimental results to model the reactions listed above. In the following sections, the manner in which the kinetic theory is employed in the model is first described in general form, and then the key results from the general treatment are presented as they are applied to the specific reactions considered by the model.

5.3 Kinetic Parameters

The limited kinetic data found in the literature was used in the model calculations. A summary of the kinetic parameters used in the model is given in Table 5.1. The first thing to note about Table 5.1 is that all but one of the pre-exponential factors are calculated based on the kinetic theory of gases. Pre-exponential factors for some of these reactions are available in the literature (16-32), but they are based on experiments done

outside the temperature range of this study. The pre-exponential factor for the uni-molecular decomposition of methylsilane (Reaction 5.2) is from Neudorfl (25).

The activation energies for reactions 5.1-5.4 are from the literature (25, 32). The activation energies for reactions 5.5-5.10 are assumed to be equal to the activation energys of the Reactions 5.1-5.4 respectively.

The activation energy for the surface adsorption of embryos (Reaction 5.6) is based on experimental data generated in this research and will be discussed later.

5.4 Surface Deposition Premise

The deposition of molecular species onto a surface (Reaction 5.13) is assumed to be the result thermally activated collisions of molecules with a surface.

$$B \rightarrow Surface \tag{5.13}$$

From kinetic theory, the number of collisions of B molecules with a surface, per surface area, per time is given by Equation 5.14 (37).

$$Z_{Wall} = \left(\frac{\kappa T}{2\pi m_B} \right)^{1/2} \frac{n_B}{V} \tag{5.14}$$

Where κ is Boltzman's constant, m_B is the mass of a B molecule, n_B is number of B molecules, and V is the volume.

Assuming that the adsorption is thermally activated with activation energy E_A, the number of B molecules adsorbed onto the surface, per time, per surface area is given by Equation 5.15 (37).

$$n_{Ad} = Z_{Wall} Exp^{\left(-E_A/RT\right)} = \left(\frac{\kappa T}{2\pi m_B} \right)^{1/2} \frac{n_B}{V} Exp^{\left(-E_A/RT\right)} \tag{5.15}$$

Converting n_{Ad} to a molar basis and multiplying by the ratio of the surface area to the volume (A_S/V) and dividing by Avogadro's number (A_V) yields the rate of change of concentration of B due to surface adsorption, as shown in Equations 5.16 and 5.17.

$$\frac{d[B]_{Surf}}{dt} = \frac{n_{Ad}}{A_V} \frac{A_S}{V} \tag{5.16}$$

$$\frac{d[B]_{Surf}}{dt} = \left(\frac{\kappa T}{2\pi m_B} \right)^{1/2} \frac{A_S}{V} Exp^{\left(-E_A/RT\right)} [B]_{Surf} \tag{5.17}$$

Note that Equation 5.17 has the Arrhenius form with the pre-exponential factor given by:

$$A = \left(\frac{\kappa T}{2\pi m_B} \right)^{1/2} \frac{A_S}{V} \tag{5.18}$$

The surface reactions considered by the model are methylisane adsorption (Reaction 5.1), methylsilylene adsorption (Reaction 5.3), embryo adsorption (Reaction 5.6), and radical adsorption (Reaction 5.8). The rates of these reactions are calculated for each segment in the model via the application of Equations 5.11, 5.12, and 5.18.

5.5 Surface Concentration

Diffusion effects on the concentration of embryos at the surface were considered in the model calculations. The diffusion calculation assumes that a finite number of embryos are present in each model segment. The diffusion flux rate at the surface is assumed equal to the rate of surface adsorption of embryos via Reaction 5.6. The diffusion geometry is as shown in Figure 5.1, with diffusion occurring along the y-axis which originates on the centerline of the annular flow gap. Diffusion is assumed to occur towards both the substrate surface and the inner surface of the coating chamber. This geometry is similar to the classic example of solute diffusion out of both sides of a slab of material (41).

The general solution for the concentration profile as function of both space and time, [B](y,t), of a finite amount of a diffusing species in fixed volume is given by Equation 5.19 (41).

$$[B](y,t) = A_0 + \sum_{n=1}^{\infty} \left(A_{1,n} \sin(\lambda_n y) + A_{2,n} \cos(\lambda_n y) \right) Exp^{\left(-\lambda^2 D_{AB} t\right)} \tag{5.19}$$

In Equation 5.19, A_0, $A_{1,n}$, $A_{2,n}$, and λ_n, are constants whose values are determined by the boundary conditions. D_{AB} is the diffusion coefficient of species B in species A, A_S is surface area, and t is time. Notice also that Equation 5.19 is an infinite summation in n. The concentration profile can be approximated by the first term in the summation for values of x (distance along the axis of the annulus) greater than approximately $3(Dt)^{1/2}$, which in this case is approximately one centimeter (41). The result of including only the first term in the summation is shown in Equation 5.20.

$$[B](y,t) = A_0 + \left(A_1 \sin(\lambda y) + A_2 \cos(\lambda y) \right) Exp^{\left(-\lambda^2 D_{AB} t\right)} \tag{5.20}$$

Applying the boundary conditions of concentration symmetry about the x-axis and zero solute concentration after infinite time, Equation 5.20 simplifies to Equation 5.21.

$$[B](y,t) = \left([B]_0 \cos(\lambda y) \right) Exp^{\left(-\lambda^2 D_{AB} t\right)} \tag{5.21}$$

The diffusion coefficient used in the model was calculated based on kinetic theory and is shown in Equation 5.22 (39).

$$D_{AB} = \frac{2}{3}\sqrt{\frac{\kappa T}{\pi}}\frac{\sqrt{\frac{1}{2}\left(\frac{1}{m_A}+\frac{1}{m_B}\right)}}{\pi\left(\frac{1}{2}\left(d_A+d_B\right)\right)^2}\frac{V}{N_T A_V} \tag{5.22}$$

In Equation 5.22, κ is Boltzmann's constant, T is the absolute temperature, m_A and m_B are the molecular masses of species A and B, d_A and d_B are the molecular diameters of species A and B, N_T is the total number of moles present in the volume, V, and A_V is Avogadro's number.

In order to determine the value of λ, it needs to be noted that the diffusive flux (J_{Surf}) of species B at the surface (Equation 5.23) is equal to the surface adsorption rate (Equation 5.24).

$$J_{Surf} = -D_{AB}\frac{\partial[B]_{Surf}}{\partial y} \tag{5.23}$$

$$J_{Surf} = r_{Surf}\frac{V}{A_S} \tag{5.24}$$

In Equation 5.24, V is the volume, and A_S is the surface area. Noting that r_{Surf} is the surface adsorption reaction rate given by Equation 5.11, Equation 5.24 can be rewritten as shown in Equation 5.25.

$$J_{Surf} = k_{Surf}[B]_{Surf}\frac{V}{A_S} \tag{5.25}$$

Equation 5.26 is the result of combining Equations 5.21, 5.23, and 5.26.

$$D_{AB}\lambda\sin\left(\lambda\frac{h}{2}\right)Exp^{\left(-\lambda^2 Dt\right)} = k_{Surf}[B]_{Surf}\frac{V}{A_S}\left([B]_0\cos\left(\lambda\frac{h}{2}\right)\right)Exp^{\left(-\lambda^2 D_{AB}t\right)} \tag{5.26}$$

Canceling like terms and rearranging Equation 5.26 yields Equation 5.27, which can not be solved directly for λ.

$$\tan\left(\lambda\frac{h}{2}\right) = \frac{k_{Surf}}{D_{AB}}\frac{V}{A_S}\frac{1}{\lambda} \tag{5.27}$$

The solution of Equation 5.27 for λ is typically approximated by one of two extremes depending on the relative rates of diffusion and surface reaction (40). The value of λ is approximated by assuming that the tangent term is small and can be represented by its argument (tanα=α), or that the solution occurs near the pole of the tangent function (the argument of the tangent function is equal to π/2). To choice of the appropriate approximation depends on the value of the Damkoler number. The Damkoler number, D_K, is the ratio of the rate of the surface reaction to the rate of diffusion, as shown in Equations 5.28 and 5.29 (40).

$$D_K = \frac{\text{Surface Reaction Rate}}{\text{Diffusion Rate}} \tag{5.28}$$

$$D_K = \frac{k_{Surf}}{D_{AB}} \frac{V}{A_S} h \tag{5.29}$$

If the Damkoler number is much less unity, then the diffusion rate is larger than the surface reaction rate and the tangent term in Equation 5.27 can be approximated by its argument. If the Damkoler number is much greater than one, then the surface reaction rate is much larger than the diffusion rate and the tangent term in Equation 5.27 can be approximated by setting its argument equal to the pole of the tangent function (40). The value of the Damkoler number, based on the diffusion coefficient and surface reaction rate constant k_{Surf}, both averaged over the length of the annular substrate was found to be approximately 0.2. Therefore, the tangent function was replaced by its argument as shown in Equation 5.30, which results in the solution for λ as shown in Equation 5.31.

$$\lambda \frac{h}{2} = \frac{k_{Surf}}{D_{AB}} \frac{V}{A_S} \frac{1}{\lambda} \tag{5.30}$$

$$\lambda = \left(\frac{k_{Surf}}{D_{AB}} \frac{V}{A_S} \frac{2}{h} \right)^{\frac{1}{2}} \tag{5.31}$$

Substituting the value of λ into Equation 5.21 results in the expression for the concentration as a function of y and time presented in Equation 5.32.

$$[B](y,t) = \left([B]_0 \cos\left(\left(\frac{k_{Surf}}{D_{AB}} \frac{V}{A_S} \frac{2}{h} \right)^{\frac{1}{2}} y \right) \right) Exp^{\left(-k_{Surf} \frac{V}{A_S} \frac{2}{h} t \right)} \tag{5.32}$$

Using the notation $[B]_{Surf}(t)$ in place of [B](h/2,t), the concentration of species B at the surface is given by Equation 5.33.

$$[B]_{Surf}(t) = \left([B]_0 \cos\left(\left(\frac{k_{Surf}}{D_{AB}} \frac{V}{A_S} \frac{2}{h} \right)^{\frac{1}{2}} \frac{h}{2} \right) \right) Exp^{\left(-k_{Surf} \frac{V}{A_S} \frac{2}{h} t \right)} \quad (5.33)$$

The surface concentration of embryos calculated using Equation 5.33 is used in conjunction with Equations 5.11, 5.12, and 5.18 to determine the surface adsorption of embryos.

5.6 Gas-phase Reaction Premise

Bimolecular combinations of the type shown in Reaction 5.34 are assumed to be the result thermally activated collisions between molecules.

$$B + C \rightarrow BC \quad (5.34)$$

From kinetic theory the number of B-C collisions per time, per volume is given by Equation 5.35 (37).

$$Z_{BC} = \sigma \left(\frac{8\kappa T}{\pi \mu} \right)^{1/2} A_V{}^2 [B][C] \quad (5.35)$$

Where σ is the collision cross section, μ is the reduced mass, A_V is Avogadro's number, and [B] and [C] are the molar concentrations of species B and C respectively. The collision cross section is a function of the collision diameters of the colliding species d_B and d_C, and is shown in Equation 5.36 (37).

$$\sigma = \pi \left(\frac{d_B + d_C}{2} \right)^2 \quad (5.36)$$

For the purposes of the calculations done in this work, the collision diameter was assumed to be equal to the molecular diameter (37). The collision diameter of methylsilane and methylsylene were assumed to be equal to the sum of the diameters of silicon, carbon, and hydrogen as shown in Equation 5.37 (37).

$$d_{CH_3SiH_3} = d_{CH_3SiH} = d_{Si} + d_C + d_H = 0.63nm \quad (5.37)$$

The collision diameter for embryos was assumed to be equal to the average number size of embryos (S_{EM}) times the collision diameter of methylsilane (Equation 5.38). The average number size of embryos is defined as the average number of silicon atoms present in each embryo. The calculation of embryo size is described later in this report.

$$d_{Embryo} = S_{EM} d_{CH_3SiH_3} \quad (5.38)$$

The reduced mass term of Equation 5.35 is defined as shown in Equation 5.39 (37), where m_B and m_C are the molecular masses of species B and C respectively.

$$\mu = \frac{m_B m_C}{m_B + m_C} \tag{5.39}$$

Assuming Reaction 5.34 is thermally activated the number of collisions that result in a BC pair per time, per volume is given by Equation 5.40.

$$n_C = Z_{BC} Exp^{\left(-E_A/RT\right)} = \sigma\left(\frac{8\kappa T}{\pi\mu}\right)^{1/2} A_V{}^2 Exp^{\left(-E_A/RT\right)}[B][C] \tag{5.40}$$

Converting n_C to a molar basis by dividing by Avogadro's number yields the rate of change of concentration of B, C, and BC.

$$\frac{d[B]}{dt} = \frac{d[C]}{dt} = \frac{-d[BC]}{dt} = \frac{n_C}{A_V} \tag{5.41}$$

$$\frac{d[B]}{dt} = \sigma\left(\frac{8\kappa T}{\pi\mu}\right)^{1/2} A_V Exp^{\left(-E_A/RT\right)}[B][C] \tag{5.42}$$

Notice that Equation 5.42 is of the Arrhenius form with:

$$A = \sigma\left(\frac{8\kappa T}{\pi\mu}\right)^{1/2} A_V \tag{5.43}$$

All of the bimolecular gas-phase reactions considered by the model result in the formation of an embryo. The reacting molecules that result in embryos are methylsilane /methylsilylene (Reaction 5.4), methylsilylene/embryo (Reaction 5.5), methylsilane/radical (Reaction 5.9), and radical/embryo (Reaction 5.10). The rates of each of these reactions are calculated in each segment of the model using Equations 5.11, 5.12 and 5.43.

The rates of the unimolecular reactions 5.1 and 5.7, the formation of mehtylsilylene from methylsilane and the formation of a radical from an embryo, are calculated for each segment in the model using Equations 5.11 and 5.12. The values of the pre-exponential factors for these reactions were taken from the literature (25-28).

5.7 Thermal Model

Each segment of the model is assumed to be a concentric annulus with both the inner and outer surface temperatures equal and constant over the length of the segment. The temperature of the gas is calculated at the outlet of each segment using heat transfer

relations developed for the constant surface temperature concentric annulus geometry with the mass flow rate of the gas and the surface temperature of the annulus as inputs. For the heat transfer calculation, the gas is assumed to be 100% argon as the reactants are highly dilute, with the flow rate equal to the total gas flow rate used in the experiments.

The local heat flux (heat transfer rate per surface area) and the total heat transfer rate between the surface and the gas in the concentric annulus geometry used here are given by Equations 5.44 and 5.45 (38).

$$q''_S = h\left(T_S - T_M\right) \tag{5.44}$$

Where h is the local heat transfer coefficient, T_S is the surface temperature, and T_M is the mean gas temperature.

$$q_{Convection} = \dot{m}Cp\left(T_{M,O} - T_{M,i}\right) \tag{5.45}$$

Where $\dot{m}$ is the mass flow rate, Cp is the specific heat of the gas, and $T_{M,O}$ and $T_{M,i}$ are the mean outlet and inlet temperatures of the gas.

Noting that the total heat transfer is equal to the surface heat flux integrated over the surface area results in Equation 5.46 (P is the wetted perimeter).

$$dq_{Convection} = q''_S P dx \tag{5.46}$$

Substituting from Equations 5.44 and 5.45, assuming constant surface temperature, and using the average in place of the local heat transfer coefficient (denoted by the over bar) leads to Equation 5.47

$$\frac{dT_M}{dx} = \frac{P}{\dot{m}Cp}\bar{h}\left(T_S - T_M\right) \tag{5.47}$$

Integrating 5.47 from the inlet to the outlet of the annulus leads to Equation 5.48 (38).

$$\frac{T_S - T_{M,O}}{T_S - T_{M,i}} = Exp\left(\frac{Px}{\dot{m}Cp}\bar{h}\right) \tag{5.48}$$

Rearrangement of Equation 5.48 leads to the equation used to calculate the gas temperature within each model segment (Equation 5.49).

$$T_{M,O} = T_S - \left(T_S - T_{M,i}\right)Exp\left(\frac{Px}{\dot{m}Cp}\bar{h}\right) \tag{5.49}$$

The average convection heat transfer coefficient in Equation 5.48 is calculated from the Nusselt number as defined in Equation 5.50 (38).

$$Nu_{D_h} \equiv \frac{hD_h}{k_T} \tag{5.50}$$

Where D_h is the hydraulic diameter of the concentric annulus and k_T is the thermal conductivity of the gas. The hydraulic diameter is shown in Equation 5.51 (38).

$$D_h \equiv \frac{4A_C}{P} = D_O - D_i \tag{5.51}$$

The circumferentially averaged Nusselt number for the concentric annulus with constant and equal inner and outer surface temperatures for laminar, fully developed flow (thermal and velocity) is given by Equation 5.52 (36). Note that the Reynolds's number was found to range between approximately fifteen at the inlet to approximately thirty five at the down stream end of the concentric annulus. Also note that the velocity entrance length was found to be approximately one centimeter, and the thermal entrance length was found to be approximately 0.75 cm. Both the thermal and velocity entrance regions were small compared to the fifteen centimeter long concentric annulus, therefore the entire length of the concentric annulus was assumed to be in the fully developed regime.

$$Nu_T = \frac{Nu_O + r^* Nu_i}{1 + r^*} \tag{5.52}$$

Nu_O and Nu_i in Equation 5.52 are the Nusselt numbers for the heat transfer from the outer and inner surfaces of the annulus, respectively. The values for these inner and outer surface Nusselt numbers are tabularized in Rohsenow (36) as a function of inner to outer radius ratio, r* (Equation 5.53). The diameter ratio of the geometry under consideration here is 0.75 which results in a Nu_T of 7.5.

$$r^* = \frac{D_i}{D_O} \tag{5.53}$$

Rearrangement of Equation 5.50 and the use the over bar notation rather than the subscript "T" for the circumferentially averaged heat transfer coefficient yields Equation 5.54, which is used for determining average gas temperature.

$$\bar{h} = h_T = \frac{Nu_T k_T}{D_h} \tag{5.54}$$

5.8 Surface Temperature Determination

In order to model the gas temperature, the surface temperature is needed. The surface temperatures were determined by temperature measurements made using thermocouples that were inserted into the concentric annulus. Six different temperature readings were taken at several locations along the axial length of the substrate. The

various thermocouple positions are shown in Figure 5.2. Thermocouples were inserted into the annular space between the coating chamber and the substrate from the top of the furnace (termed "outside top") and from the bottom of the furnace (termed "outside bottom"). A thermocouple was also inserted from the top of the furnace into a blind hole on the center line along the length of the substrate (termed "inside top"). Temperature readings were taken both with and without 1,000cm^3/min of argon gas flow (1,000cm^3/min was the total gas flow for the majority of the coating experiments). The thermal profiles of the system were determined in this way for nominal or average temperatures of 550°C, 600°C, and 650°C. The resulting thermal profiles for the 600°C nominal temperature case are shown in Figure 5.3.

From these measurements, the surface temperature profile used in the gas temperature calculation was assumed to be equal to the measured profile for the "outside top with argon gas flowing" case. Given that the coating chamber is heated by radiation from the furnace element and it in turn transfers heat to the substrate by radiation, the outside top with argon flowing measurement case seemed the best choice for the average surface temperature of both the inner and outer surfaces of the chamber.

The surface temperature profiles (outside top with argon gas flowing profile) for nominal temperatures of 550°C, 600°C, and 650°C are shown in Figure 5.4. In order to facilitate the incorporation of the surface temperature profile into the model, the measurements were curve fit to a second order polynomial. The curve fits, the associated equations and determination coefficients (R^2) values are shown in Figure 5.4.

In order to model temperatures other than 550°C, 600°C, and 650°C, the coefficients of the polynomial equations relating surface temperature to axial position for 550°C, 600°C, and 650°C, were plotted against the nominal temperature and curve fit to linear equations. The plot of the polynomial coefficients verses the nominal temperature is shown if Figure 5.5. The linear curve fits and the associated equations are also shown in Figure 5.5. This curve fitting strategy allowed easy interpolation and calculation of surface temperature profiles at any nominal temperature in the range of interest here.

Utilizing the surface temperature profile described above, the calculated gas temperatures as a function of axial position for nominal temperatures of 550°C, 600°C, and 650°C are shown in Figure 5.6. All three cases show that the gas, which enters the furnace at room temperature, reaches the surface temperature within approximately one centimeter of the inlet.

5.9 Model Specifics

As mentioned above, the annular geometry is divided into axial segments as shown in Figure 5.7. The model tracks a fixed amount (N_T moles of gas in each segment), or "slug" of gas as it flows through the length of the annular gas space. A block flow diagram of the model is shown in Figure 5.7. All of the model calculations for each segment are based on the inlet conditions for that segment. The model then calculates the outlet conditions of the current segment based on reaction rates, surface temperature, and residence time in the segment. These calculated segment outlet results then become the inlet conditions for the next segment, and the process repeats itself until the gas has traversed the length of the substrate.

5.9.1 Calculate Segment Initial Conditions

The first calculation carried out by the model is the calculation of the volume of the segment (ΔV_j). The volume of the segment varies with temperature (and position). The reason that the volume of the model segments varies is because the model assumes a fixed quantity of gas in each element. The volume of the segment is the volume occupied by the slug of gas under ideal gas assumptions at the segment inlet temperature and pressure (constant atmospheric pressure throughout). The segment volume is calculated using Equation 5.55.

$$\Delta V_j = \frac{N_T R T_{M,i,j}}{p} \tag{5.55}$$

Where N_T, which is constant through out the model calculation, is the number of moles present in the model element, R is the gas constant, $T_{M,i,j}$ is the segment inlet (hence the subscript "i") gas temperature, and p is the pressure. Note that N_T and pressure are constant throughout the model. The value of N_T is 5e-7 moles. This value was chosen because it is near the maximum value that will not result in the model predicting the consumption of more of a species than is initially present in any segment. For the first segment, the inlet gas temperature is ambient.

The total volume up to the jth segment is the sum of the prior segment volumes, Equation 5.56.

$$V_j = \sum_{0}^{j-1} \Delta V_j \tag{5.56}$$

The concentration of the various species present in the segment is equal to the number of species moles $N_{B,j}$ divided by the segment volume, Equation 5.57.

$$[B]_j = \frac{N_{B,j}}{\Delta V_j} \tag{5.57}$$

The "B" is meant to represent each of the species listed in Reactions 5.1-5.10 in a general form.

The length of the segment (Δx_j) is the segment volume divided by cross section of the annular gas space, and the axial position of the segment (x_j) is the sum of the prior segment lengths (Equations 5.58 and 5.59)

$$\Delta x_j = \frac{\Delta V_j}{\pi/4\left(D_O^2 - D_i^2\right)} \tag{5.58}$$

$$x_j = \sum_{0}^{j-1} \Delta x_j \tag{5.59}$$

The residence time in the segment (Δt_j) is segment volume divided by the volumetric flow rate ($\dot{V}$), and the time to reach the segment from the inlet (t_j) is the sum of the residence times for the previous segments (Equations 5.60-5.61).

$$\Delta t_j = \frac{\Delta V_j}{\dot{V}} \tag{5.60}$$

$$t_j = \sum_{0}^{j-1} \Delta t_j \tag{5.61}$$

The diffusion coefficient of embryos in the argon diluent ($D_{EM,j}$) is determined in each segment by the application of Equation 5.22 as shown in Equation 5.62.

$$D_{EM,j} = \frac{2}{3}\sqrt{\frac{\kappa T_{M,j}}{\pi}} \frac{\sqrt{\frac{1}{2}\left(\frac{1}{m_{Ar}} + \frac{1}{S_{EM,j} m_{CH_3SiH_3}}\right)}}{\pi\left(\frac{1}{2}\left(d_{Ar} + S_{EM,j} d_{CH_3SiH_3}\right)\right)^2} \frac{\Delta V_j}{N_T A_V} \tag{5.62}$$

Note that the calculation of the average size of embryos (S_{EM}) is discussed below.

5.9.2 Reaction Rates

The reaction rates in each segment are calculated through the specific application of Equations 5.11, 5.12, 5.18, and 5.43 (Equations 5.63-5.90). The values of the activation energies of the various reactions are given in Table 5.1.

Reaction 5.1 ($CH_3SiH_3 \rightarrow$ Surface)

$$r_{5.1,j} = k_{5.1,j}\left[CH_3SiH_3\right]_j \tag{5.63}$$

$$k_{5.1,j} = \left(\frac{\kappa T_{M,j}}{2\pi m_{CH_3SiH_3}}\right)^{1/2} \frac{A_{S,j}}{\Delta V_j} Exp^{\left(-E_{A,5.1}/RT_{M,j}\right)} \tag{5.64}$$

Reaction 5.2 ($CH_3SiH_3 \rightarrow CH_3SiH+H_2$)

$$r_{5.2,j} = k_{5.2,j}\left[CH_3SiH_3\right]_j \tag{5.65}$$

$$k_{5.2,j} = A_{5.2} Exp^{\left(-E_{A,5.2}/RT_{M,j}\right)} \tag{5.66}$$

Note that the value of $A_{5.2}$ is given in Table 5.1.

Reaction 5.3 ($CH_3SiH \rightarrow$ Surface)

$$r_{5.3,j} = k_{5.3,j}\left[CH_3SiH\right]_j \tag{5.67}$$

$$k_{5.3,j} = \left(\frac{\kappa T_{M,j}}{2\pi m_{CH_3SiH}}\right)^{1/2} \frac{A_{S,j}}{\Delta V_j} Exp^{\left(-E_{A,5.3}/RT_{M,j}\right)} \tag{5.68}$$

Reaction 5.4 ($CH_3SiH + CH_3SiH_3 \rightarrow$ Embryo)

$$r_{5.4,j} = k_{5.4,j}\left[CH_3SiH_3\right]_j\left[CH_3SiH\right]_j \tag{5.69}$$

$$k_{5.4,j} = \sigma_{5.4,j}\left(\frac{8\kappa T}{\pi\mu_{5.4,j}}\right)^{1/2} A_V Exp^{\left(-E_{A,5.4,j}/RT_{M,j}\right)} \tag{5.70}$$

$$\sigma_{5.4,j} = \pi d^2_{CH_3SiH_3} \tag{5.71}$$

$$\mu_{5.4,j} = \frac{m_{CH_3SiH_3} m_{CH_3SiH}}{m_{CH_3SiH_3} + m_{CH_3SiH}} \tag{5.72}$$

Reaction 5.5 ($CH_3SiH +$ Embryo $\rightarrow$ Embryo)

$$r_{5.5,j} = k_{5.5,j}\left[CH_3SiH\right]_j\left[EM\right]_j \tag{5.73}$$

$$k_{5.5,j} = \sigma_{5.5,j}\left(\frac{8\kappa T}{\pi\mu_{5.5,j}}\right)^{1/2} A_V Exp^{\left(-E_{A,5.5,j}/RT_{M,j}\right)} \tag{5.74}$$

$$\sigma_{5.5,j} = \pi\left(\frac{d_{CH_3SiH_3} + S_{EM} d_{CH_3SiH_3}}{2}\right)^2 \tag{5.75}$$

$$\mu_{5.5,j} = \frac{m_{CH_3SiH_3} S_{EM} m_{CH_3SiH_3}}{m_{CH_3SiH_3} + S_{EM} m_{CH_3SiH_3}} \tag{5.76}$$

Reaction 5.6 (Embryo $\rightarrow$ Surface)

$$r_{5.6,j} = k_{5.6,j}\left[Embryo\right]_{Surf,j} \tag{5.77}$$

$$k_{5.6,j} = \left(\frac{\kappa T_{M,j}}{2\pi S_{EM,j} m_{CH_3SiH_3}} \right)^{1/2} \frac{A_{S,j}}{\Delta V_j} Exp^{\left(-E_{A,5.6} / RT_{M,j} \right)} \tag{5.78}$$

Reaction 5.7 (Embryo→Radical+H_X)

$$r_{5.7,j} = k_{5.7,j} \left[EM \right]_j \tag{5.79}$$

$$k_{5.7,j} = A_{5.7} Exp^{\left(-E_{A,5.7} / RT_{M,j} \right)} \tag{5.80}$$

Reaction 5.8 (Radical→Surface)

$$r_{5.8,j} = k_{5.8,j} \left[Radical \right]_j \tag{5.81}$$

$$k_{5.8,j} = \left(\frac{\kappa T_{M,j}}{2\pi S_{EM,j} m_{CH_3SiH_3}} \right)^{1/2} \frac{A_{S,j}}{\Delta V_j} Exp^{\left(-E_{A,5.8} / RT_{M,j} \right)} \tag{5.82}$$

Reaction 5.9 (Radical+CH_3SiH_3→ Embryo)

$$r_{M5.,j} = k_{5.9,j} \left[Radical \right]_j \left[CH_3SiH_3 \right]_j \tag{5.83}$$

$$k_{5.9,j} = \sigma_{5.9,j} \left(\frac{8\kappa T}{\pi \mu_{5.9,j}} \right)^{1/2} A_V Exp^{\left(-E_{A,5.9,j} / RT_{M,j} \right)} \tag{5.84}$$

$$\sigma_{5.9,j} = \pi \left(\frac{S_{EM} d_{CH_3SiH_3} + d_{CH_3SiH_3}}{2} \right)^2 \tag{5.85}$$

$$\mu_{5.9,j} = \frac{m_{CH_3SiH_3} S_{EM} m_{CH_3SiH_3}}{m_{CH_3SiH_3} + S_{EM} m_{CH_3SiH_3}} \tag{5.86}$$

Reaction 5.10 (Radical+Embryo→ Embryo)

$$r_{5.10,j} = k_{5.10,j} \left[Radical \right]_j \left[EM \right]_j \tag{5.87}$$

$$k_{5.10,j} = \sigma_{5.10,j}\left(\frac{8\kappa T}{\pi\mu_{5.10,j}}\right)^{1/2} A_V Exp^{\left(-E_{A,5.10,j}/RT_{M,j}\right)} \tag{5.88}$$

$$\sigma_{5.10,j} = \pi\left(S_{EM} d_{CH_3SiH_3}\right)^2 \tag{5.89}$$

$$\mu_{5.10,j} = \frac{S_{EM} m_{CH_3SiH_3}}{2} \tag{5.90}$$

5.9.3 Calculations of Effective Reaction Rates

As the model was developed it was determined that the rates of Reactions 5.4, 5.5, 5.9 and 5.10 were very high relative to the other reactions. In all cases it was found the rate of consumption of methylsilylene via Reactions 5.4 and 5.5 exceed the rate of its production through Reaction 5.2. Similarly the rates of consumption of radicals by Reactions 5.9 and 5.10 exceeded the rate of radical production through Reaction 5.7. This trend is demonstrated in Figures 5.8 and 5.9.

This observation leads to the conclusion that methylsylene production by Reaction 5.2 is the rate controlling reaction of the scheme envisioned by the model. As a result, effective reaction rates were defined for Reactions 5.3, 5.4, and 5.5. The basis for the effective reaction rates is the assumption that all of the methylsilylene produced in a particular segment is also consumed in that segment. Therefore, effective reaction rates were defined such that the sum of the effective rates of the three consumption reactions ($r_{Eff,5.3,j}$, $r_{Eff,5.4,j}$, and $r_{Eff,5.5,j}$) equaled the rate of methylsilylene production ($r_{5.2,j}$). This scheme ensures that all of the methylsilylene produced in a model segment is also consumed in that segment. The effective rates of Reactions 5.3, 5.4, and 5.5 are shown in Equations 5.91-5.93.

$$r_{Eff,5.3,j} = \frac{r_{5.3,j}}{r_{5.3,j} + r_{5.4,j} + r_{5.5,j}} r_{5.2,j} \tag{5.91}$$

$$r_{Eff,5.4,j} = \frac{r_{5.4,j}}{r_{5.3,j} + r_{5.4,j} + r_{5.5,j}} r_{5.2,j} \tag{5.92}$$

$$r_{Eff,5.5,j} = \frac{r_{5.5,j}}{r_{5.3,j} + r_{5.4,j} + r_{5.5,j}} r_{5.2,j} \tag{5.93}$$

The situation is the same for the production rate of radicals ($r_{5.7,j}$) compared to consumption rate of radicals ($r_{Eff,5.8,j}$, $r_{Eff,5.9,j}$, and $r_{Eff,5.10,j}$). Equations 5.94-5.96 are the effective reaction rates for Reactions 5.8, 5.9, and 5.10.

$$r_{Eff,5.8,j} = \frac{r_{5.8,j}}{r_{5.8,j} + r_{5.9,j} + r_{5.10,j}} r_{5.7,j} \tag{5.94}$$

$$r_{Eff,5.9,j} = \frac{r_{5.9,j}}{r_{5.8,j} + r_{5.9,j} + r_{5.10,j}} r_{5.7,j} \tag{5.95}$$

$$r_{Eff,5.10,j} = \frac{r_{5.10,j}}{r_{5.8,j} + r_{5.9,j} + r_{5.10,j}} r_{5.7,j} \tag{5.96}$$

5.9.4 Changes In Species Concentration And Amounts

The calculation of the rate of change of concentration of the species under consideration in the model is shown in Equations 5.97-5.101. Note that the concentrations (species names within brackets) shown in the following equations are bulk average values within each segment.

Methylsilane is consumed by Reactions 5.1, 5.2, 5.4, and 5.9.

$$\left.\frac{d[CH_3SiH_3]}{dt}\right|_j = -r_{5.1,j} - r_{5.2,j} - r_{Eff,5.4,j} - r_{Eff,5.9,j} \tag{5.97}$$

Methylsilylene is produced by Reaction 5.2 and consumed by Reactions 5.3-5.5.

$$\left.\frac{d[CH_3SiH]}{dt}\right|_j = r_{5.2,j} - r_{Eff,5.3,j} - r_{Eff,5.4,j} - r_{Eff,5.5,j} \tag{5.98}$$

Embryos are produced via Reaction 5.4 and 5.9 and consumed by Reactions 5.6 and 5.7.

$$\left.\frac{d[EM]}{dt}\right|_j = r_{Eff,5.4,j} - r_{5.6,j} - r_{5.7,j} + r_{Eff,5.9,j} \tag{5.99}$$

Radicals are produced through Reaction 5.7 and consumed in Reaction 5.9.

$$\left.\frac{d[Radical]}{dt}\right|_j = r_{5.7,j} - r_{Eff,5.9,j} \tag{5.100}$$

Solid SiC is deposited by Reactions 5.1, 5.3, 5.6, and 5.8. It is assumed that all the molecules that become surface adsorbed become solid SiC on the surface. Since the surface adsorbed SiC is no longer in the gas stream, its concentration is zero in the gas and unity in the coating. It is useful for comparison though to define an effective SiC concentration as the number of moles of surface adsorbed SiC divided by the segment volume ($[SiC]_{Solid}$). The rate of change of this effective concentration of SiC solid is given in Equation 5.101.

$$\left.\frac{d[SiC]_{Solid}}{dt}\right|_j = r_{5.1,j} + r_{Eff,5.3,j} + S_{EM} r_{5.6,j} + S_{EM} r_{Eff,5.8,j} \tag{5.101}$$

The model assumes that the reaction rates are constant within each segment so that the change in species concentration is equal to the rate of change of concentration multiplied by the residence time, as shown in general form with B representing the various species in Equation 5.102.

$$\left.\frac{d[B]}{dt}\right|_j \Delta t_j \approx \Delta[B]_j \tag{5.102}$$

Since the SiC solid is no longer in the gas stream it does not travel along with the gas into the next segment. Therefore, for comparison with other species concentrations the effective SiC concentration as a function of position is equal to the sum of the effective concentrations of the surface adsorbed SiC for each prior segment, as shown in Equation 5.103.

$$[SiC_{Solid}]_j = \sum_0^{j-1} \Delta[SiC_{Solid}]_j \tag{5.103}$$

Recall that model is based on a fixed amount of gas that travels through the annular gas path. Therefore, the absolute amount of each species present at the outlet of each segment is needed as input for calculations in the next segment. The molar amount of each species, after the reactions have occurred in each segment, is equal to the original concentration plus the change in concentration, multiplied by the segment volume, as shown in general for all species in Equation 5.104.

$$N_{B,j+1} = ([B]_j + \Delta[B])\Delta V_j \tag{5.104}$$

It is useful for comparison with experimental results to calculate the model predicted thickness of SiC (δ_{SiC}). Equation 5.105 calculates the SiC thickness for each segment from the amount of surface adsorbed SiC in each segment, the molecular weight (MW_{SiC}) and density of SiC (ρ_{SiC}), the surface area of the segment ($A_{S,j}$), the segment residence time, and the total experimental run time (t_{Tot}), Equation 5.105.

$$\delta_{SiC,j} = \left(\Delta[SiC_{Solid}]_j \Delta V_j\right)\frac{MW_{SiC}}{\rho_{SiC}}\frac{1}{A_{S,j}}\frac{t_{Tot}}{\Delta t_j} \tag{5.105}$$

5.9.5 Calculation of Embryo Concentration at the Surface

The concentration of embryos at the surface in each model segment ($[EM]_{Surf,j}$) is determined by the application of Equation 5.53 as shown in Equation 5.106 with λ as shown in Equation 5.107.

$$[EM]_{Surf,j} = [EM]_j \cos\left(\lambda \frac{h}{2}\right) Exp^{\left(-\lambda^2 D_{EM} \Delta t_j\right)} \tag{5.106}$$

$$\lambda = \left(\frac{k_{5.6,j}}{D_{EM,j}} \frac{V}{A_S} \frac{2}{h}\right)^{\frac{1}{2}} \tag{5.107}$$

The time rate of change of the surface concentration of embryos due to adsorption and diffusion is determined by taking the partial derivative with respect to time of Equation 5.106, the result of which is presented in Equation 5.108.

$$\frac{\partial [EM]_{Surf,j}}{\partial t} = \left(-\lambda^2 D_{EM} [EM]_j \cos\left(\lambda \frac{h}{2}\right)\right) Exp^{\left(-\lambda^2 D_{EM} \Delta t_j\right)} \tag{5.108}$$

For the model calculation, the change in surface concentration due to adsorption and diffusion is approximated as shown in Equations 5.109 and 5.110.

$$\Delta [EM]_{Surf,j} \approx \frac{\partial [EM]_{Surf,j}}{\partial t} \Delta t_j \tag{5.109}$$

$$\Delta [EM]_{Surf,j} = \left(\left(-\lambda^2 D_{EM} [EM]_j \cos\left(\lambda \frac{h}{2}\right)\right) Exp^{\left(-\lambda^2 D_{EM} \Delta t_j\right)}\right) \Delta t_j \tag{5.110}$$

Note that the concentration of embryos, both in the bulk gas and at the surface, is effected by chemical reactions, surface adsorption, and diffusion towards the surface. Therefore, the calculation of the surface concentration at the outlet of each segment needs to include the contribution from each of these sources of change. Equation 5.111 is an expression for the surface concentration of embryos at the end, or outlet, of each segment ($[EM]_{Surf,j,outlet}$). The outlet embryo surface concentration is equal to the inlet concentration ($[EM]_{Surf,j,inlet}$) plus the change due to adsorption and diffusion calculated using Equation 5.110 ($[EM]_{Surf,j}$), plus the change due to chemical reaction ($\Delta[EM]_j$) calculated with Equations 5.99 and 5.102.

$$[EM]_{Surf,j,outlet} = [EM]_{Surf,j,inlet} + \Delta [EM]_{Surf,j} + \Delta [EM]_j \tag{5.111}$$

Recall that the model is based on the premise of a fixed amount of gas in each model segment, and that the concentration of species in each segment is calculated based on the number of moles of each species present at the end of the previous segment (Equation 5.101). When this premise applied to the surface concentration of embryos, the result is Equation 5.112.

$$N_{Surf,EM,j+1} = [EM]_{Surf,j,outlet} \Delta V_j \quad (5.112)$$

Equation 5.112 is an expression for an effective number of moles of embryos at the surface at the end of the current segment and the beginning of the next model segment ($N_{Surf,EM,j+1}$). This procedure of using the effective number of moles of embryos at the surface is needed to account for the fact that each segment in the model is not the necessarily the same volume due to the assumption of a constant overall number of moles of gas for each segment and the variation of temperature from one segment to another.

5.9.6 Calculation of Embryo Size

The size of embryos is defined as the number of silicon atoms in each embryo. In order to calculate the average size of embryos, the number of moles of and the size of the various kinds of embryos is needed. There are five kinds of embryos: Embryos nucleated by Reaction 5.4, Embryos growing by each of Reactions 5.5, 5.9, or 5.10, and Embryos becoming surface adsorbed. The molar amount of each type of embryo is the associated rate of reaction multiplied by the segment residence time and by the segment volume. Equation 5.113 gives the number of moles of embryos nucleated in each segment, $N_{EM,5.4,j}$.

$$N_{EM,5.4,j} = r_{5.4,j} \Delta t_j \Delta V_j \quad (5.113)$$

Equation 5.114 gives the number of moles of embryos growing by Reaction 5.5 in each segment, $N_{EM,5.5,j}$.

$$N_{EM,5.5,j} = r_{5.5,j} \Delta t_j \Delta V_j \quad (5.114)$$

Equation 5.115 gives the number of moles of embryos growing by Reaction 5.9 in each segment, $N_{EM,5.9,j}$.

$$N_{EM,5.9,j} = r_{5.9,j} \Delta t_j \Delta V_j \quad (5.115)$$

Equation 5.116 gives the number of moles of embryos growing by Reaction 5.10 in each segment, $N_{EM,5.10,j}$.

$$N_{EM,5.10,j} = r_{5.10,j} \Delta t_j \Delta V_j \quad (5.116)$$

Equation 5.117 gives the number of moles of embryos being surface adsorbed by Reactions 5.6 and 5.8 in each segment, $N_{EM,Surf,j}$.

$$N_{EM,Surf,j} = r_{5.6,j} \Delta t_j \Delta V_j + r_{5.8,j} \Delta t_j \Delta V_j \quad (5.117)$$

Equation 5.118 gives the total number of moles of embryos in the gas stream in each segment, $N_{EM,Tot,j}$. The total number of moles of embryos in each segment is equal to the number in the previous segment, plus the number nucleated, minus the number surface adsorbed.

$$N_{EM,Tot,j} = N_{EM,Tot,j-1} + N_{EM,5.4,j} - N_{EM,Surf,j} \tag{5.118}$$

In order to calculate the average size of embryos it has to be noted that initially there are no embryos, and that all nucleated embryos start with a size of two (two Si atoms in an embryo formed by Reaction 5.4). Also note that all embryos growing by Reactions 5.5 and 5.9 are growing by one silicon atom, and all embryos that are growing by Reaction 5.10 are doubling in size. (The size of an embryo is assumed equal to the size of a radical.)

Equation 5.119 is the equation used to calculate the average size of embryos at the end of the current model segment, $S_{EM,j}$. The first term in the equation is the fraction of embryos that do not change size in the current segment multiplied by the average size of embryos in the previous segment, $S_{EM,j-1}$. The second term is the fraction of embryos nucleated in the current segment multiplied by their size, which is two. The third term is the fraction of embryos growing by Reaction 5.5 multiplied by their size, which is $S_{EM,j-1}$ + 1. The fourth term in Equation 5.119 is the fraction of embryos growing by Reaction 5.9 multiplied by their size, which is also $S_{EM,j-1}$ +1. The fifth term is the fraction of embryos growing by Reaction 5.10 multiplied their size, which is $2*S_{EM,j-1}$. This approach of finding the average is similar to calculating an average by the rule of mixtures.

$$\begin{aligned} S_{EM,j} = {} & \frac{\left(N_{EM,Tot,j-1} - N_{EM,5.5,j} - N_{EM,5.9,j} - N_{EM,5.10,j}\right)}{N_{EM,Tot,j}} S_{EM,j-1} + \\ & + \frac{N_{EM,5.4,j}}{N_{EM,Tot,j}} * 2 + \frac{N_{EM,5.5,j}}{N_{EM,Tot,j}} \left(S_{EM,j-1} + 1\right) + \\ & + \frac{N_{EM,5.9,j}}{N_{EM,Tot,j}} \left(S_{EM,j-1} + 1\right) + \frac{N_{EM,5.10,j}}{N_{EM,Tot,j}} \left(2 * S_{EM,j-1}\right) \end{aligned} \tag{5.119}$$

5.9.7 Calculation of the Temperature

The outlet temperature of each segment is determined through the application of Equations 5.49 and 5.54. The form of Equations 5.49 and 5.54 used in each segment are shown in Equations 5.120 and 5.121. Recall that the value of the circumferentially average Nusselt number Nu_T, was found to be 7.5 (36). The Hydraulic diameter of the annulus is a constant, so the only variable in the calculation of the average convection heat transfer coefficient is temperature dependence of the thermal conductivity. For the purposes of the thermal calculation, the gas is assumed be 100% argon. The value of the thermal conductivity for argon that used in Equation 5.120 is from Rohsenow (36).

$$\bar{h}_j = \left.\frac{Nu_T k_T}{D_h}\right|_{@T_{M,j}} \tag{5.120}$$

The outlet temperature of the current segment is equal to the inlet temperature of the next segment; therefore the temperature for the next segment is given by Equation 5.121.

$$T_{M,j+1} = T_{S,j} - \left(T_{S,j} - T_{M,j}\right) Exp\left(\frac{P\Delta x_j}{\dot{m}Cp}\bar{h}_j\right) \tag{5.121}$$

After the segment outlet conditions are determined, the model indexes to the next segment and begins the calculation process again.

5.10 Embryo Surface Reaction Activation Energy

The activation energy for the surface adsorption of embryos, Reaction 5.6, was determined from the experimental results of coating thickness as a function of axial position. Experimental coating thickness was measured at several places along the length of specimens AFCI-SiC-10, 11, 12, 14, and 15. (A discussion of the specifics of these measurements is included in the experimental results section of this report.) The model predicted and experimental coating thicknesses were compared, and an iterative procedure was used to arrive at a value of the activation energy that minimized the difference between the model predicted and experimental coating thicknesses.

The error between the model predicted and experimental coating thickness for each specimen was defined as the sum of the squares of the differences between each experimental thickness measurement ($\alpha_{S,Exp,i}$) and the corresponding model prediction ($\alpha_{S,Mod,i}$) (Equations 5.122).

$$Error_S = \sum_1^i \left(\alpha_{S,Exp,i} - \alpha_{S,Mod,i}\right)^2 \tag{5.122}$$

Where $Error_S$ is the error for each of the specimens AFCI-SiC-10, 11, 12, 14, and 15, and the subscript "i" represents each of the individual thickness measurements.

The total error was defined as the sum of the errors for each of the specimens (Equation 5.123).

$$Error_{Tot} = \sum_S Error_S \tag{5.123}$$

The value of the activation energy for Reaction 5.6 was input into the model and the resulting total error was noted. Then the value of the activation energy was changed to produce a new value of the total error. The value of the activation energy that minimized the total error, 89 kJ/mol, was used in all subsequent model calculations. The

model predicted and experimental coating thicknesses plotted against axial position for each of the specimens AFCI-SiC-10, 11, 12, 14, and 15 are shown in Figures 5.10-5.14.

6 Modeling Results

The model predicts the species concentrations, species amounts, individual reaction rates, species production/consumption rates, and the average size of embryos for each volume segment. In the following sections these results will be discussed and compared to experimental observations and results.

6.1 Predicted Species Concentration Profiles

Figures 6.1-6.8 are model-predicted concentration and thermal profiles for run numbers AFCI-SiC-8, 11, 14, 12, 10, 15, 1, and 4 (in order of increasing coating temperature and methylsilane flow rate). The predicted gas temperature and the concentrations of methylsilane, embryos, and SiC solid are plotted as functions of axial position. For samples 11, 14, 10, 12 and 15, an effective experimental concentration of surface deposited SiC, which was calculated from the experimental thickness measurements, is included for comparison. Also included in each figure is a photograph of the associated coated specimen. The specimen photograph is scaled to match the x-axis of each plot to facilitate comparison of local conditions with the observed coating.

Figures 6.1-6.8 show that the extent of methylsilane consumption increases with increasing nominal coating temperature, but this observation is obscured by the concentration change due to the temperature variation along the length of the specimen. The sharp drop in concentration within the first couple of centimeters of the inlet is due to the sharp increase in gas temperature in that area, and since the temperature does not reach a constant value, the concentrations vary over the length of the sample due to temperature as well as chemical reaction. In order to better present the effects of chemical reactions alone, plots of model-predicted molar quantities of methylsilane, embryos, and surface deposited SiC are presented in Figures 6.9-6.16 for samples AFCI-SIC-8, 11, 14, 12, 10, 15, 1, and 4 respectively. Note that the molar quantity is the number of moles of a species present in each model segment. Also included in each figure is the thermal profile for the sample in question and a photograph of the corresponding specimen scaled to match the x-axis of the plot for comparison.

6.2 Predicted Molar Amount Profiles

6.2.1 575°C Case

Figure 6.9 shows the model-predicted molar amounts of the various species for run number AFCI-SiC-8, which had a nominal coating temperature of 575°C and a methylsilane flow rate of 89 cm^3/min. The figure demonstrates that little reaction occurs at this temperature. Note the magnitude of the distance from the inlet to the point where noticeable amounts of embryos are formed and also note where the coating is visible on the sample. This long entrance length, where little reaction is predicted and little coating is produced, indicates that gas-phase reactions occur prior to deposition. If the deposition of coatings was due to methylsilane surface reactions, one would expect that the coating would begin to form within a couple of centimeters of the inlet, when the gas temperature approaches the nominal temperature. Instead, there is the observation that the

appearance of a coating seems to correspond with the increase in the amount of embryos in the gas stream, indicating that the SiC deposition is the result of surface reactions of embryos rather than methylsilane.

6.2.2 600°C Case

Figures 6.10 and 6.11 are the species molar amount plots for AFCI-SiC-11 and 14, which were run at the same nominal temperature of 600°C, but with different methylsilane flow rates (89 cm^3/min for number 11 and 126 cm^3/min for number 14). The figures show that a greater extent of gas-phase reactions occur at 600°C compared to 575°C, and that there is evidence of some gas-phase nucleation of particles on the down stream end of the sample (the light colored deposit in the photograph). The distance from the inlet to the first observation of coating (uncoated inlet length) again corresponds with predicted increase in embryo amount, but this distance is shorter compared to the 575°C case. The observation of coating and embryo formation closer to the inlet of the specimen makes sense, as the gas-phase reaction rates are higher at higher temperature.

Based on the similar shapes of the molar amount profiles of Figures 6.10 and 6.11, the difference in methylsilane flow rate does not appear to affect the reaction mode. The curves are just shifted to higher values for the higher methylsilane flow rate case. This observation indicates that the reaction mode is function of temperature and not concentration.

It should be noted that there is a characteristic of sample AFCI-SiC-14 that is puzzling. The distance from the inlet to the first observation of coating (uncoated inlet length) is longer for sample 14 that for 11. Based on this observation, one might assume that sample 14 could have been coated at a lower temperature than run number 11, but the appearance of homogeneously nucleated particles on the down stream end of the sample would tend to indicate otherwise. The reason for these observations is unknown, but it is theorized that a malfunction of the furnace cooling system may have cause a decrease in substrate temperature on the up-stream end (left end in the picture) of the sample while the temperature on the down stream end was at the expected value.

6.2.3 625°C Case

Figures 6.12, 6.13, and 14 are the species molar amount profiles for samples AFCI-SiC-12, 10, and 15 respectively. All three of these samples were coated at a nominal temperature of 625°C, with methylsilane flow rates of 65, 89, and 142 cm^3/min respectively. The molar amount profiles for these 625°C runs show significantly greater extent of gas-phase reactions compared to the lower temperature cases, and again the difference in methylsilane flow rates does not seem to affect the reaction modes, only the amounts. Also note that the distance from the inlet to the first observation of coating and to the production of embryos is shorter than the lower temperature cases, and the trend of SiC deposition tracking with increased embryo amount is evident in the 625°C case as well. In addition, the zone where the coating morphology is dominated by homogeneously nucleated particles is significantly larger for the 625°C case than the lower temperature cases.

The 625°C case is the first to show a noticeable difference between the concentration of embryos at the surface and in the gas stream, and this deviation of

surface amount from that in the gas stream appears to correspond with the homogeneous nucleation zone.

6.2.4 650°C Case

Figure 6.15 is the molar profile plot for sample AFCI-SiC-1, which was coated at a nominal temperature of 650°C with a methylsilane flow rate of 21 cm^3/min. The molar amount profiles for the 650°C case show a significant increase in the extent of gas-phase reactions compared to the 625°C. In fact, the prediction shows that methylsilane is roughly 90% depleted by the time it reaches the outlet end of the sample. The familiar trend of increased SiC deposition following the increase in embryo amount is again demonstrated in this 650°C case. Also as expected, the axial position of the transition from molecular deposition to homogeneous nucleation is closer to the inlet. The deviation between surface and free stream embryo amount is more pronounced in the 650°C compared to the 625°C case, and it again appears to correspond with the homogeneous nucleation zone.

6.2.5 700°C Case

The predicted molar amount profiles for the 700°C case, run number AFCI-SiC-4, are presented in Figure 6.16. The plot shows complete depletion of methylsilane by the time the gas reaches the eight centimeter position, and depletion of embryos prior to the gas reaching the down stream end of the sample. The deposition of SiC again tracks with the embryo amount, and the deviation of embryo surface amount from the free stream amount again corresponds with the homogeneous nucleation zone.

6.3 Predicted Reaction Rate Profiles

The rates of the reactions considered in the model are plotted as a function of axial position for run numbers AFCI-SIC-8, 11, 14, 12, 10, 15, 1, and 4 in Figures 6.17-6.24 respectively. Recall that the reaction rates are calculated in every segment by the model using Equations 5.63-5.96. Note also that the rates of Reactions 5.1, 5.3, and 5.8 are not shown on the figures. Those rates were insignificant and were therefore omitted.

6.3.1 575°C Case

The reaction rate profiles for AFCI-SiC-8, which was run at a nominal temperature of 575°C, are shown in Figure 6.17. As the figure shows, there are two dominant reactions, first the decomposition of methylsilane to form methylsilylene and hydrogen (Reaction 5.2), followed by the formation of embryos (Reaction 5.4). The other reaction rates are small in comparison to these dominant reactions, but the profile of the rate of embryo surface adsorption does fit well with the location of observed coating.

6.3.2 600°C Case

Figure 6.18 and 6.19 are the predicted reaction rate profiles for coating runs made at 600°C (AFCI-SiC-11 and 14). These figures show that Reactions 5.2 and 5.4 are still dominant, but the other reactions are becoming more significant. Similar to the 575°C

case, the profile of the surface adsorption rate of embryos corresponds well with the observed coating on the substrate.

Also shown on these figures is an effective experimental SiC deposition rate. The effective deposition rate is calculated from the experimental thickness measurements and the geometry of the annular substrate. The experimental deposition reaction rate is shown by the plots to be larger than the predicted rate of surface adsorption of embryos, but recall that each embryo contains more than one Si-C pair.

Note that embryo growth by methylsilylene/embryo combination (Reaction 5.5) has the third highest reaction rate, after the two dominant reactions, and recall that the difference between runs 11 and 14 is the methylsilane flow rate, 89 cm^3/min for number 11 verses 126 cm^3/min for number 14. Unlike the concentration and molar amount profiles, the reaction rate profiles show a difference, other than overall magnitude, caused by the difference methylsilane flow rate. The higher methlysilane flow rate of run number 14 caused a higher relative contribution of Reaction 5.5 compared to the same for run 11 with the lower flow rate.

6.3.3 625°C Case

The predicted reaction rate profiles along with the experimental deposition reaction rates for the 625°C case are shown in Figures 6.20, 6.21, and 6.22. Although these coating runs were done at the same nominal temperature, they each had different methylsilane flow rates. AFCI-SiC-12, 10, and 15 employed methylsilane flow rates of 65, 89, and 142 cm^3/min respectively. The dominant predicted reaction rates for these coating runs are again Reactions 5.2 and 5.4, but the other reactions are becoming more significant, and the trend of increased contribution of the Reaction 5.5 with increased methylsilane flow rate is demonstrated in 625°C case like it was in the 600°C case.

6.3.4 650°C Case

In the 650°C case, Figure 6.23, the rates of gas-phase reactions involving radicals (5.7 and 5.9) exceed the rates of Reactions 5.2 and 5.4 beyond axial position of approximately nine to ten centimeters. Below that position, the former reactions are still dominant. Also note that the rate of Reaction 5.5 is among the lowest. This contrasts with the lower temperature cases, but notice that the methylsilane flow rate for this case is only 21 cm^3/min. This indicates that the cause for the low relative contribution of Reaction 5.5 is due to lower methylsilane concentration rather than a temperature effect.

6.3.5 700°C Case

Figure 6.24 shows the model-predicted reaction rate profiles for run number AFCI-SiC-4, which was run at 700°C with a methylsilane flow rate of 65 cm^3/min. At this temperature, the rates of reactions 5.2 and 5.4 are initially greater than the others, but by the four centimeter axial position, the rates of Reactions 5.7 and 5.9 are the largest. This indicates that embryo formation slows significantly and embryo growth is the dominant process.

6.4 Predicted Species Production Rates

The model is based on tracking the progress of ten reactions, but those ten reactions ultimately result in the production (or consumption) of three species, methylsilane, embryos, and surface deposited SiC. Equations 5.97-5.102 show the relationships between the individual reactions and the production/consumption of the chemical species. Figures 6.25-6.32 show the species production/consumption rates as a function of axial position that result from the individual reactions.

6.4.1 575°C Case

Figure 6.25 shows the model-predicted production rate profiles of methylsilane, embryos, and surface adsorbed SiC for AFCI-SiC-8. The figure demonstrates that at 575°C, little SiC is produced, and that methylsilane is consumed at roughly twice the rate of embryo production. This two to one ratio of methylsilane consumption to embryo production is indicative of embryo formation via 5.4, where methylsilane and methylsilylene combine to form an embryo.

6.4.2 600°C Case

Figures 6.26 and 6.27 are species production rate profiles for AFCI-SiC-11 and 14 respectively. Also included in these plots is the experimental SiC deposition reaction rate.

There are two things to note from the species production rate profiles of the 600°C case. First, the methylsilane consumption rate to embryo production rate ratio for the lower methylsilane flow rate of run number 11 appears slightly lower than that of run number 14 (the higher methylsilane flow rate case). This is indicative of more embryo growth under the conditions of run number 14 compared to run 11. This observation fits the earlier observation that embryo growth by reaction 5.5 increases with increasing methylsilane flow rate.

The second thing to note from the species production rate profiles is the relatively good agreement between the experimental and model-predicted SiC growth rates. Recall that the experimental SiC growth rate exceeded the rate of surface adsorption of embryos, and the apparent disagreement was due to the fact that embryos contain more than one Si-C pair. The model-predicted production rates take the stoichiometry of the reaction into account (See Equations 5.97-5.102).

Also note that the experimental SiC deposition rates exceed the model prediction at higher axial positions. This may be due, at least in part, to the assumption of constant density in the calculation of molar deposition rate from the thickness measurement data. The density of the coating as a function of position has not been measured, but since the coating mechanism transitions from molecular deposition to the adherence of homogeneously nucleated particles in the region where the experimental rate exceeds the predicted deposition rate, it is reasonable to assume that the density of the coating would be less in this area. If the density is less, then the actual experimental molar deposition rate would actually be less than the values shown in the figures.

6.4.3 625°C Case

The predicted production rate profiles for AFCI-SiC-12, 10, and 15 are presented in Figures 6.28, 6.29, and 6.30. Recall that the difference in these coating runs is the methylsilane flow rate (65, 89, and 142 cm^3/min respectively). These figures show the same trends that were observed at the lower temperatures. Namely, the experimental deposition rates are in good agreement with the model-predicted SiC production rates, and the ratio of methylsilane consumption to embryo production appears to increase due to both increased temperature and increased methylsilane flow rate.

6.4.4 650°C Case

The embryo production rate profile for the 650°C case, shown in Figure 6.31, is significantly different than that of the lower temperature cases. At the higher temperature, the model predicts that the embryo production rate goes negative near the end of the substrate, indicating that the surface adsorption rate exceeds the embryo formation rates. This trend was also seen in the individual reaction rate profiles of Figure 6.23.

6.4.5 700°C Case

The species production rate profile for AFCI-SiC-4, which was coated at 700°C, is presented in Figure 6.32. Similar to the 650°C case but more pronounced at 700°C, the embryo production rate goes significantly negative near five centimeters axial displacement. Then it increases to zero as embryo growth by agglomeration goes on after the methylsilane is completely depleted.

6.5 Embryo Growth Mode

The model assumes that embryos are nucleated by the combination of methylsilane and methylsilylene via Reaction 5.4. The model also accounts for embryo growth by what can be thought of as two mechanisms, either molecular growth or agglomeration. Molecular growth is characterized by a combination of an embryo with either methlysilane or methylsilylene via Reactions 5.5 or 5.9. Agglomeration occurs by Reaction 5.10 and is characterized by combination of a radical and an embryo. The relative contribution to overall embryo production and growth by each of these three mechanisms, nucleation, molecular growth, and agglomeration, is demonstrated in Figures 6.33-6.40.

6.5.1 575°C and 600°C Cases

Figures 6.33-6.35 are embryo nucleation and growth reaction profiles for run numbers 8, 11, and 14, which represent both the 575°C and 600°C nominal temperature cases. The figures show that nucleation is dominant over the entire length of the specimens, and that the only embryo growth mode taking place is molecular growth. This trend fits well with the relative lack of a homogeneous nucleation zone on the specimens (also pictured in the figures).

6.5.2 625ºC Case

The embryo growth mode profiles for runs conducted at 625°C (AFCI-SiC-12, 10, and 14) are shown in Figures 6.36-6.38. These embryo production and growth profiles illustrate that agglomeration is active, but small compared to nucleation and molecular growth. The region where agglomeration is active (approximately six to twelve centimeters of axial displacement) roughly corresponds with the homogeneous nucleation zone on the substrate. The figures also demonstrate that molecular growth is increased with increased methylsilane flow rate.

6.5.3 650°C Case

The embryo growth mode profile for the 650°C case shown in Figure 6.39 (AFCI-SiC-1) demonstrates that nucleation is dominant, but that embryo growth by agglomeration is approximately equal to molecular embryo growth. Also, on the extreme downstream end of the substrate the agglomeration growth rate exceeds both the nucleation rate and the molecular growth rate.

6.5.4 700°C Case

The profile of embryo growth rate for AFCI-SiC-4, which was coated at 700°C is presented in Figure 6.40. The figure illustrates that at 700°C that nucleation, molecular growth, and agglomeration are all three active in roughly equal magnitude, and that above an axial displacement of approximately six centimeters, agglomeration is the dominant mode. Also as was the case with the lower temperature cases, the region where agglomeration is active corresponds well with the homogeneous nucleation region on the coated substrate.

6.6 Embryo Size Prediction

The average size of embryos, defined as the number of silicon atoms present in each embryo, is calculated in each segment of the model using Equation 5.119. The resulting model-predicted embryo size profiles for specimens AFCI-SIC-8, 11, 14, 12, 10, 15, 1, and 4 are shown in Figures 6.40-6.48 respectively.

Since the size of all nucleated embryos is two, each of the embryo size profiles starts at two. At temperatures between 575°C and 600°C (Figures 6.41-6.43), the embryo size increases almost linearly with axial displacement to values between 2.3 and 2.6. When the nominal coating temperature is 625°C, the maximum embryo size is in the range of three to 3.2, and the homogeneous nucleation zone corresponds with average embryo sizes of approximately 2.5 and greater (Figures 6.44-6.46). At temperatures of 625°C and above, the model-predicted embryo size profile becomes less linear and approaches plateau near the down stream end of the specimen. At 650°C coating temperature (Figure 6.47), the plateau value of average embryo size is approximately 4, and the observation of the homogeneous zone at average embryo sizes above 2.5 still holds. At 700°C (Figure 6.48) where growth by agglomeration becomes the prevailing mode, the model-predicted embryo size rises quickly to a plateau value near fifty five.

It should be noted here that no attempt was made in the model to determine the embryo size distribution, only the average size was calculated. Also, it is presumed that when the average predicted embryo size becomes significantly larger than two that the

maximum embryo size is likely to be so large as to behave as a particle rather than a molecule, and at this point this model is no longer valid. Even with this stipulation, it is instructive to consider the average embryo size and how it compares with experimental observations.

7 Discussion

The results of the particle coating experiments indicated that the difference in the observed coating morphology as a function of coating temperature was due to a competition between surface and gas-phase reactions. The theory was that the high density coating (deposited at relatively low temperature) was the result of molecular surface adsorption, and the low density coating (deposited at relatively high temperature) resulted from homogeneous nucleation. The concentric annulus experiments and modeling results seemed to agree with this theory and indicated the dominant surface and gas-phase reactions. Following is a discussion of the predicted reaction mechanisms and how they correspond to the experimental observations and with information in the literature.

7.1 Surface Deposition Zone

The literature review indicated that methylsilane surface adsorption could be responsible for the seal coatings (high density-low temperature coatings) produced in the particle coating experiments and the coatings present in the surface deposition zone of the concentric annulus experiments (31-32). Figure 6.9 shows clearly that SiC formation tracks with embryo concentration and not methylsilane concentration. The model predicted surface adsorption rate for methylsilane is insignificant. Also, if the high density coating was due to methylsilane adsorption, then the appearance of coating on the substrate of AFCI-SiC-8 would have started approximately two centimeters from the inlet, where the gas temperature approaches the coating temperature, rather than the eight centimeter position seen in Figure 6.9.

The literature also suggested that methylsilylene surface adsorption might also be a contributor to deposition of the high density coatings, but the model predicts that methylsilylene surface adsorption is not taking place. The model predicts that the consumption rate of methylsilylene by Reactions 5.4 and 5.5 is significantly higher than its surface adsorption rate by Reaction 5.3. Reactions 5.4 and 5.5 are predicted to take place at very high rates because the activation energy of those reactions is effectively zero (25). In simple terms, zero activation energy for these reactions means that every collision between methylsilylene and methylsilane or an embryo results in a successful reaction. By contrast, the activation energy for methylsilylene surface adsorption is reported as180 kJ/mol (32). Also, the predicted intermolecular collision frequencies involving methylsilylene are significantly higher than the predicted collision frequency of methylsilylene with the surface of the substrate. In addition, during the model development calculations were conducted assuming that embryo formation did not occur. This assumption allowed the concentration of methylsilylene to build up along the length of the substrate, and even under these assumptions the surface adsorption rate of methylsilylene was insignificant.

Rather than methylsilane or methylsilylene, the results indicate that the coating in the surface deposition zone (relatively dense and continuous coating) is due to the surface adsorption of small embryos (embryos with only two Si-C pairs). This scenario fits with the observation of a long uncoated inlet length in the low temperature case. The uncoated entrance length indicates that time is required for the concentration of embryos to reach a

level sufficient for detectable SiC deposition. In addition, the fact that the model predicts embryo growth rate increasing with coating temperature also fits with the observation of decreasing surface deposition zone length with increasing coating temperature.

7.2 Transition Zone

In the transition zone, the theory is that particles form in the gas-phase and that when particles become surface bound, they are covered by surface deposits from molecular species. Note that the term particle is used to indicate an embryo that has grown to the point where, due to its size, it no longer behaves like a molecular species. This particle adherence and over-coating by surface deposition gives rise to the nodular appearance in the transition zone. As one traverses through the transition zone, the number of surface bound particles increases, and the amount of surface deposition covering the particles decreases.

The model does not include a prediction of particle formation from embryos, nor does it predict any characteristics of the size distribution of embryos. The model assumes that all embryos are of average size, with the average size calculated as described in the modeling section of this document. The model does include a prediction of embryo nucleation and growth rates, as well as a prediction of average embryo size. Figures 7.1-7.3 are comparisons of model predictions and experimental observations for samples AFCI-SiC-10, 1, and 4. Recall that samples 10, 1, and 4 are from coating runs conducted at 625°C, 650°C, and 700°C, respectively. Each figure shows plots of model-predicted embryo nucleation rate, embryo molecular growth rate, embryo agglomeration growth rate, and average embryo size. Recall that molecular growth is defined in the model as embryos growing by the addition of a species containing one Si atom, and agglomeration growth is defined as embryo growth by combination with another embryo. Each figure also includes a photograph of the coated specimen scaled to match the x-axis of the plot. Additionally, each figure includes SEM micrographs of the coating surface taken at two magnifications at the approximate beginning, middle, and end of the transition zone of each specimen.

Comparing the Figures 7.1-7.3, it is interesting to note the location of the transition zone relative to the features in the plots. In all three cases the transition zone corresponds approximately with the region where embryo growth by agglomeration becomes significant. This observation is significant because it qualitatively points to the region where particle formation is likely to occur, because embryos growing by agglomeration should quickly reach a size where they behave as particles rather than molecular species.

7.3 Homogeneous Nucleation Zone

The assumptions about embryo growth in the model, i.e., that all embryos are of the same size, limit its utility in predicting anything about homogeneous nucleation other than the onset of particle formation. A model that predicts a distribution of embryo/particle sizes by taking into account the rates of molecular growth and agglomeration as a function of the sizes of the reacting species is necessary to fully describe the homogeneous nucleation zone. Development of a model of that type was not attempted in this work, but Onischuk conducted just such an effort related to

homogeneous particle formation by thermal decomposition of silane (42-43). The results of the experimental and numerical treatment of homogeneous nucleation and growth in the silane system are quite similar to the observations made here on the methylsilane system, and the gas-borne particle growth modeling provides insight that is relevant to this work.

Onischuk conducted particle nucleation and growth experiments in a cylindrical hot wall reactor with a cross section within a factor of two to the concentric annulus geometry used here, and the experimental flow rates used provided a similar residence time in the reactor compared to that of the methylsilane experiments conducted here. Moreover, the silane concentration and reaction zone temperature was comparable that used in this work with methylsilane.

Onischuk found that irregularly shaped aggregates consisting of nearly spherical particles formed as a result of silane decomposition at 580°C with a residence time of 0.87s (the residence time in the concentric annulus with 1,000 cm^3/min total gas flow is 0.71s). The appearance of these aggregates is very similar to that observed in the homogeneous nucleation zone in the SiC coatings from methylsilane (Figures 7.1-7.3). A schematic drawing of an example aggregate is provided in Figure 7.4. The aggregates consist of homogeneously nucleated particles that become bound together in random orientations through particle agglomeration. This random assembly of particles to form the aggregates is the explanation for the observation of dendrite-like branched structures discussed in Chapter 4.

Onischuk found that the average size of the silane derived aggregates ranged between 0.1μm and 0.2μm, and the approximate size of the spherical constituent particles that make up these aggregates is estimated at 0.05 to 0.08μm. Looking at the SEM micrographs of the coating surface in the transition zone in this work (Figures 7.1-7.3), the apparent aggregate size is approximately 1μm with a constituent particle size estimate of 0.15 to 0.3 μm. The similarity in the experimental observations between the silane and methylsilane systems indicates that similar mechanisms are may be at work.

Onischuk carried out a numerical simulation of nucleation and growth of the aggregate formation process in the silane system. The model employed considered nineteen silane thermal decomposition reactions and took into account the collision interaction kinetics of particles ranging in size from two silicon atoms to more than 10^7 silicon atoms (approximately 0.1μm under spherical assumptions).

The numerical simulation agreed well with the experimental results. The model showed that aggregate growth at a temperature of 580°C with residence times greater than 0.3s was primarily due to agglomeration with particles greater than 0.03μm in diameter, and above 0.5s residence time that growth was due to agglomeration of particles that were greater than 0.11μm in diameter. These results agree with the prediction by the methylsilane model of this work that growth by agglomeration becomes significant at residence times greater than 0.38s, 0.34s, and 0.37s respectively for coating temperatures of 625°C, 650°C, and 700°C, as depicted in Figures 7.5-7.7.

The silane modeling results provide additional insight into the transition zone and homogeneous nucleation zone. At 580°C, the silane system model predicted an increase in constituent particle size as residence time increased to approximately 0.7s. At longer residence times, the model predicted that aggregates would continue to grow by

agglomeration with additional particles, but that the constituent particle size would not significantly increase. This result fits with the observation that aggregate and constituent particle size increase through the transition zone (Figures 7.1-7.3). It also fits with the observation that constituent particle size does not change significantly beyond the transition zone along the length the homogeneous nucleation zone. The homogeneous nucleation zone of samples AFCI-SiC-10, 1, and 4 is illustrated in Figures 7.8-7.10.

8 Conclusions

In support of the Generation IV Gas-Cooled Fast Reactor fuel development program, CVD techniques for the deposition of SiC from the decomposition of methylsilane were investigated. The research was conducted in two phases. In the first phase, the feasibility of producing both porous SiC buffer coatings and dense SiC seal coatings on surrogate fuel particles by FBCVD using gas mixtures of methylsilane and argon was demonstrated. In the second phase, a combined experimental and modeling effort was carried out to elucidate the deposition mechanisms that result in either porous or dense SiC coatings, depending on the coating conditions.

During the particle coating phase, the properties of the SiC coatings were found to be controlled by the deposition temperature. At relatively low deposition temperatures (900°C to 1,000°C), relatively high density (90% of theoretical) SiC seal coatings were produced. At higher coating temperature (1,200°C), low density (<50% of theoretical) SiC buffer coatings were produced. X-ray powder diffraction analysis of the coatings revealed that the coatings were partially crystalline SiC, and that the degree of crystallinity increased with increasing coating or annealing temperature. SEM examination of the coatings demonstrated that the low density buffer coatings consisted of SiC particles that nucleated in the gas-phase and then adhered to the surface of the particles, while the high density seal coatings appeared to be due to surface deposition of molecular species.

For the single-substrate experiments, a cylindrical graphite substrate held within a tubular coating chamber was used in place of the fluidized bed of particles. The single substrate experiments revealed a temperature effect on the coating properties similar to the particle coating experiments. The coating experiments demonstrated that at low coating temperatures (600°C and below), the coating was the smooth continuous type over most of the length of the specimen. Then at higher temperatures (625°C and above), there were three coating regions, or zones, along the length of the substrate. In the zone near the reactant gas inlet, the coating was smooth and continuous (termed the surface deposition zone). Immediately down stream of the surface deposition zone was a region where the coating became more nodular as axial position increased until the coating had completely transitioned to one that consisted of an agglomeration of particles that were randomly bound together (termed the homogeneous nucleation zone). As coating temperature increased, the length of the surface deposition zone decreased and the length of the homogeneous nucleation zone increased.

In parallel with the experimental coating program, the axial distributions of the gas temperature, gas concentration, and the magnitude of several gas-phase and surface reactions were modeled under the conditions employed in the single-substrate experiments. The model assumed that methylsilane decomposed and reacted to form species called embryos. Embryos are species containing from two to many silicon (and carbon) atoms that result from the reaction of methylsilane and its decomposition products. Embryos were assumed to be the initial stage of gas-phase particle nucleation. The model calculation was based on first order reaction kinetics assumptions using rate constant data from the literature and from the experiments conducted in this study.

Based on the experimental and modeling results presented here, the deposition of SiC from methylsilane is controlled by the extent of gas-phase reaction, and is therefore highly sensitive to temperature. The results show that all SiC coatings, regardless of type (surface deposition or homogeneous nucleation), are due to the surface adsorption of species that result from gas-phase reactions. The model terms these gas-borne species embryos, and while the model does not include a prediction of coating morphology, a comparison of the model and experimental results indicates that the morphology of the coatings is controlled by the nucleation and growth of the embryos. The coating that results from small embryos (embryos with only two Si-C pairs) appears relatively dense and continuous (surface deposition zone), while the coating that results from larger embryos becomes less continuous and more nodular as embryo size increases (transition zone). At some point in the growth of embryos they cease to behave as molecular species and instead behave as particles that grow by either agglomeration or by incorporation of molecular species on their surface. As these particles adhere to the substrate surface and become fixed in place by surface deposition in the interstices between adjacent particles, a low density coating consisting of these particles results (homogeneous nucleation zone).

9 Recommendations

The research described in this report lays the ground work for further research into the feasibility of this GFR coated particle fuel concept. Both the buffer and seal coatings merit further investigation. Studies of the reaction kinetics of the decomposition of methylsilane are needed to identify the dominant reactions and reaction rates under the conditions encountered in particle coating. Measurements of sticking coefficients of predominant species formed during gas-phase reactions are also needed and augment the understanding of deposition mechanisms present in range of conditions that result in either surface deposition or homogeneous nucleation.

In addition to the reaction kinetics and deposition studies, research into the homogeneous nucleation and growth of particles and aggregates is needed in order to more fully understand the deposition of low density SiC buffer coatings derived from methylsilane. An approach that accounts for the size distribution of particles and its effect on the particle and aggregate growth rates is needed. With the results of such an investigation, the porosity and mechanical compliance of the buffer coating could be optimized for the in-service environment.

The seal coating properties such as the microstructure, density, permeability, composition, degree of crystallinity, and mechanical behavior should be should be systematically investigated over a range of coating conditions and annealing treatments. There is evidence in the literature that coating density near 100% of theoretical is possible with the addition of hydrogen to the coating gas (16, 17). Unfortunately, the addition of hydrogen to the coating gas resulted in the appearance of free silicon in the coating. In order to achieve the desired density and permeability, without the presence of free silicon, methylsilane gas mixtures that included both hydrogen and selected hydrocarbons were considered, but not thoroughly explored (16, 17).

In addition to the coating gas composition investigation, the effect of annealing treatments should also be studied. The particle coating experiments conducted here included limited comparison of annealed and unannealed seal coatings. Only one annealing treatment was attempted. The annealing conditions were chosen to mimic the coating conditions of TRISO-type MTS derived SiC (1,500°C in a hydrogen atmosphere). This choice was made because these are conditions that the particles would experience if they were over-coated with the familiar TRISO-type SiC, but other conditions may prove to be beneficial.

As an element of the gas composition and annealing investigation, the mechanical properties of the seal coating should be evaluated. The seal coating's primary role is the containment of the nuclear material during and after irradiation. Therefore, the mechanical properties of the seal coating are of significant importance, but no effort has been made thus far to evaluate the strength of the seal coating or to tailor the processing conditions for optimum mechanical behavior. A systematic investigation of the properties of the seal coating is one of the key areas that needs attention in the effort to determining the feasibility of this GFR fuel concept.

In addition, the lessons learned in this work and the recommended follow-on buffer and seal coating research should be applied to the particle coating system. The

most advantageous way to apply these results is to leverage the modeling resources that are currently being used for FBCVD of TRISO fuel particles (21-23).

The ultimate step in determining the feasibility of this fuel concept will be the inclusion of fuel particles coated with methylsilane derived SiC in irradiation experiments and then subjecting them to post irradiation examination (PIE).

References

1. Beatty, R. L., "Pyrolytic Carbon Deposited From Propane In A Fluidized Bed," ORNL-TM-1649, January 1967.
2. Pelissier, J., Yust, C. S., Kaae, J. L., "Transmission Electron Microscopy of Pyrocarbon Coatings," Nuclear Technology, Vol. 35, No. 2, pp. 301-309, 1977.
3. Krautwasser, P., Nickel, H., "Influence of Porosity on the Irradiation Performance of Pyrocarbon Coatings," Nuclear Technology, Vol. 35, No. 2, pp. 310-319, 1977.
4. Harmon, D. P., Scott, C. B., "Properties Influencing High-Temperature Gas-Cooled Reactor Coated Fuel Particle Performance," Nuclear Technology, Vol. 35, No. 2, pp. 343-352, 1977.
5. Kaae, J. L., Bullock, R. E., Scott, C, B., Harmon, D. P., "The Mechanical Behavior of Biso-Coated Fuel Particles During Irradiation. Part II: Prediction of Biso Particle Behavior During Irradiation with a Stress-Analysis Model," Nuclear Technology, Vol. 35, No. 2, pp. 368-678, 1977.
6. Wagner-Loffler, M., "Amoeba Behavior of UO_2 Coated Fuel," Nuclear Technology, Vol. 35, No. 2, pp. 392-401, 1977.
7. Grubmeier, H. Naoumidis, A., Thiele, B. A., "Silicon Carbide Corrosion in High-Temperature Gas-Cooled Reactor Fuel Particles," Nuclear Technology, Vol. 35, No. 2, pp. 413-427, 1977.
8. Kaae, J. L., "The Mechanism of the Deposition of Pyrolitic Carbons," Carbon, Vol. 23, No. 6, pp. 665-673, 1985.
9. Kaae, J. L., "Microstructures of Isotropic Pyrolitic Carbons," Carbon, Vol. 13, pp. 55-62, 1975.
10. Kaae, J. L., "Implications Of The Structure Of Pyrolitic Carbons On The Deposition Mechanism," GA-A14673, 1978.
11. Petti, D. A., Maki, J. T., Buongiorno, J., Hobbins, R. R., Miller, G. K., "Key Differences In The Fabrication, Irradiation And Safety Testing Of U.S. And German TRISO-Coated Particle Fuel And Their Implications On Fuel Performance," INEEL/EXT-02-00300, 2002.
12. Petti, D. A., Maki, J. T., Buongiorno, J., Hobbins, R. R., Miller, G. K., "Key Differences In The Fabrication, Irradiation And Safety Testing Of U.S. And German TRISO-Coated Particle Fuel And Their Implications On Fuel Performance," Nuclear Engineering and Design, Vol. 222, pp. 281-297, 2003.
13. Stansfield, O. M., "Evolution of HTGR Particle Fuel Design," Energy, Vol. 16, No. 1/2, pp. 33-45, 1991.
14. Federer, J. I., "Deposition of Silicon Carbide Coatings on Particles in a Fluidized Bed Using Silane and Tetramethylsilane-A Feasibility Study," ORNL/TM-6185, 1978.
15. "A Technology Roadmap for Generation IV Nuclear Energy Systems," Issued by the U.S. DOE Nuclear Energy Research Advisory Committee and the Generation IV International Forum, GIF-002-00, 2002.
16. Angelini, P., "Chemical Vapor Deposition Of Silicon Carbide From Methylsilane And Coating of Nuclear Waste Ceramics," Dissertation, University of Tennessee, Knoxville, June 1985.

17. Angelini, P, DeVore, C. E., Lackey, W. J., Blanco, R. E., Stinton, D. P., "Method of Deposition of Silicon Carbide Layers on Substrates and Product," United States Patent No. 4,459,338, July 10, 1984.
18. Narita, Y., Inubushi, T., Yasui, K., Akahane, T., "Si c(4X4) Structure Appeared in the Initial Stage of 3C-SiC Epitaxial Growth on Si(001) Using Monomethylsilane and Dimethylsilane," Applied Surface Science, Vol. 212-213, pp. 730-734, 2003.
19. Narita, Y., Inubushi, T., Harashima, M., Yasui, K., Akahane, T., "Initial Stage of 3C-SiC Growth on Si(001)-2 X 1 Surface using Monomethylsilane," Applied Surface Science, Vol. 216, pp. 575-579, 2003.
20. Krotz, G., Legner, W., Muller, G., Grueninger, H. W., Smith, L., Leese, B., Jones, A., Rushworth, S., "Structural and Electronic Characterization of β-SiC Films on Si Grom from Mono-Methylsilane Precursors," Materials Science and Engineering B, Vol. 29, pp. 154-159, 1995.
21. Sanchez, E. C., Siberer, S. J., "Low-Temperature Growth of Epitaxial β-SiC on Si(001) Using Supersonic Molecular Beams of Methylsilane," Journal of Physical Chemistry B, Vol. 106, pp. 8019-8028, 2002.
22. Golecki, I., Reidinger, F., Marti, J., "Single-Crystalline, Epitaxial Cubic SiC Films Grown on (100) Si at 750C by Chemical Vapor Deposition," Applied Physics Letters, Vol. 60, No. 14, pp. 1703-1705, 1992.
23. Shinohara, M., Maehama, T., Niwano, M., "Adsorption and Decomposition of Methylsilanes on Si(100)," Applied Surface Science, Vol. 162-163, pp. 161-167, 2000.
24. Lee, M., Bent, S. F., "Bonding and Thermal Reactivity in Thin a-SiC:H Films by Methylsilane CVD," Journal of Physical Chemistry B, Vol. 101, pp. 9195-9205, 1997.
25. Neudorfl, P. S., Lown, E. M., Safarik, I., Jodhan, A., Strausz, O. P., "Mechanism of the Gas-Phase Thermolysis of Monomethylsilane," Journal of the American Ceramic Society, Vol. 109, pp. 5780-5789, 1987.
26. Sawery, B. A., O'Neal, H. E., Ring, M. A., Coffey, D., "The Gas-Phase Decompisition of Methylsilane. Part I. Mechanism of Decomposition Under Shock-Tube Conditions," International Journal of Chemical Kinetics, Vol. 16, pp. 7-21, 1984.
27. Sawery, B. A., O'Neal, H. E., Ring, "The Gas-Phase Decompisition of Methylsilane. Part II. Mechanisms of Decomposition Under Static Systems Conditions," International Journal of Chemical Kinetics, Vol. 16, pp. 23-30, 1984.
28. Sawery, B. A., O'Neal, H. E., Ring, M. A., Coffey, D., "The Gas-Phase Decompisition of Methylsilane. Part III. Kinetics," International Journal of Chemical Kinetics, Vol. 16, pp. 31-39, 1984.
29. Bakhtiar, R., Holznagel, C. M., Jacobson, D. B., "Unimolecular Dissociation of CH_3SiH_2+ and $CH_3Si(Cl)H$+ in the Gas-phase," Journal of Physical Chemistry, Vol. 97, pp. 12710-12717, 1993.
30. Gordon, M. S., Truong, T. N., "Potential Primary Pyrolysis Processes of Methylsilane," Chemical Physics Letters, Vol. 142, No. 1-2, pp. 110-114, 1987.

31. Johnson, A. D., Perrin, J., Mucha, J. A., Ibbotson, D. E., "Kinetics of SiC CVD: Surface Decomposition of Silacyclobutane and Methylsilane," Journal of Physical Chemistry, Vol. 97, pp. 12937-12948, 1993.
32. Ohshita, Y., "Reactants in SiC Chemical Vapor Deposition Using CH_3SiH_3 as a Source Gas," Journal of Crystal Growth Vol. 147, pp. 111-116, 1995.
33. Pannala, S., Boyalakuntla, D., Finney, C. E. A., Miller, J. H., Lowden R. A., Daw, C. S., "Simulations of Spouted Beds for Coating TRISO Fuel Particles," Presented at the 2005 AIChE Annual Meeting October 30-November 4, 2005
34. Boyalakuntla, D.S., Pannala, S., Finney, C.E.A., and Daw, C.S., "ORNL FY05 Process Modeling Summary Report for the Advanced Gas Reactor Fuel Development and Qualification Program: Hydrodynamics, Heat and Mass Transfer," ORNL/CF-05/13, August 2005.
35. Finney, C. E. A., Pannala, S., Boyalakuntla, D., and Daw, C. S., "ORNL FY05 Process Modeling Summary Report for the Advanced Gas Reactor Fuel Development and Qualification Program Hydrodynamics, Heat and Mass Transfer for NUCO Particles," ORNL/CF-05/14, September 2005.
36. "Handbook of Heat and Mass Transfer, Third Edition," Rosenow, W. M., Hartnett, J. P., and Cho, Y. I., Eds., McGraw Hill 1998.
37. "Physical Chemistry, Fourth Edition," Atkins, P. W., W. H. Freeman and Company, New York, 1990.
38. "Fundamentals of Heat and Mass Transfer, Third Edition," Incropera, F. P., DeWitt, D. P., John Wiley and Sons, New York, 1990.
39. "Transport Phenomena, Second Edition," Bird, R. B., Stewart, W. E., Lightfoot, E. N., John Wiley and Sons, New York, 2002.
40. "Principals of Chemical Vapor Deposition," Dobkin, D. M., Zuraw, M. K., Eds., Kluwer Academic Publishers, 2003.
41. "Diffusion in Solids, Second Edition," Shewmon, P., The Minerals, Metals, and Materials Society, 1989.
42. Onischuk, A. A., Levykin, A. I., Strunin, V. P., Ushakova, M. A., Samoilova, R. I., Sabelfeld, K. K., Panfilov, V. N., "Aerosol Formation Under Heterogeneous/Homogeneous Thermal Decomposition of Silane: Experiment and Numerical Modeling," Journal of Aerosol Science, Vol. 31, No. 8, pp. 879-906, 2000.
43. Onischuk, A. A., Levykin, A. I., Strunin, V. P., Sabelfeld, K. K., Panfilov, V. N., "Aggregate Formation Under Homogeneous Silane Thermal Decomposition," Journal of Aerosol Science, Vol. 31, No. 11, pp. 1263-1281, 2000.
44. Card # 29-1129, PDF file, International Centre for Diffraction Data, Newtown Square, PA, 2006.
45. Card # 79-1767, PDF file, International Centre for Diffraction Data, Newtown Square, PA, 2006.
46. Card # 41-1487, PDF file, International Centre for Diffraction Data, Newtown Square, PA, 2006.
47. ImageJ 1.33u, Wayne Rasband National Institutes of Health, USA, http://rsb.info.nih.gov/ij/

Appendix

Table 2.1. Arrehnius Parameters and Efficiency Of Reactions 2.1-2.3

Reaction	Log A (1/s)	Ea (kJ/mol)	Efficiency	Reaction Number
$CH_3SiH_3 \rightarrow CH_3SiH+H_2$ $CH_3SiH_3 \rightarrow H_2Si=CH_2+H_2$	15.2	271	91%	2.1+2.3
$CH_3SiH_3 \rightarrow CH_4+SiH_2$	14.5	283	9%	2.2
$CH_3SiD_3 \rightarrow CH_3SiD+D_2$	14.99	271	71%	2.1a
$CH_3SiD_3 \rightarrow D_2Si=CH_2+HD$	14.30	271	14%	2.3a
$CH_3SiD_3 \rightarrow CH_4+SiD_2$	14.68	279	15%	2.2a

Table 2.2. Methylsilane Decomposition Scheme Proposed By Nuedorfl (25)

Reaction Step	Log A*	Ea (kJ/mol)	Reaction Number
$CH_3SiH_3 \rightarrow CH_3SiH+H_2$	14.87	264	2.1
$CH_3SiH+ CH_3SiH_3 \rightarrow (CH_3SiH_2)_2$	10	0	2.5
$(CH_3SiH_2)_2 \rightarrow CH_3SiH+ CH_3SiH_3$	14	209	-2.5
$CH_3SiH_3 \rightarrow CH_3SiH_2+H$ (Surface Reaction)	12.7	242	2.6
$H + CH_3SiH_3 \rightarrow CH_3SiH_2+H_2$	10.2	9	2.7
$CH_3SiH_2+ CH_3SiH_3 \rightarrow (CH_3SiH_2)_2+H$	9	71	2.8
$2CH_3SiH_2 \rightarrow (CH_3SiH_2)_2$	9.5	0	2.9
$CH_3SiH_2 \rightarrow$Polymer (Surface Reaction)	NR**	NR**	2.10
$CH_3SiH_2 \rightarrow (CH_3)_2SiH_2$ (Surface Reaction)	NR**	NR**	2.11

* Units for A factors are 1/s for unimolecular reactions and 1/(mol-s) for bimolecular reactions.

** NR = not reported

Table 3.1. Summary List of Particle Coating Experiments

Run Number	Total Gas Flow (cm^3/min)	MS/SA**	Coating Time (min)	Coating Temp. (°C)	% Theoretical Density (g/cm^3)	Comments
30	4000	0.08	60	900	91%	Single
37	5000	0.08	180	1000	91%	layer
39	5000	0.10	180	1100	86%	coatings for
41	5000	0.11	180	1100	84%	density
32	4500	0.09	120	1200	45%	measureme
38	5000	0.09	210	1200	33%	nts
35	5000	0.14	180	900	*NM	X-ray specimens
36	5000	0.14	180	1000	*NM	with carbon
40	5000	0.10	180	1100	*NM	buffer coating to
42	5000	0.11	180	1200	*NM	prevent SiC spalling
29	4000	0.11	90, 120	1200, 900	*NM	Dual Layer
34	4500, 5000, 10000	0.12	120, 120, 40	1200, 900, 1500(MTS)	*NM	Tri-Layer

*NM-Not measured

** Methylsilane flow rate divided by substrate surface area with units $cm^3/min/cm^2$ or cm/min.

Table 3.2. Experimental Conditions of the X-Ray Measurements RTXRD.

Parameter	Condition
Equipment	Scintag θ-2θ goniometer
	Spellman DF3 series 4.0 kW generator
	Scintag thermoelectrically-cooled Si(Li) detector
Power	1.8 kW; 45 kV, 40 mA
Radiation	Cu, λ = 1.54059 Å
Incidence slit divergence	0.7°
Receiving slit acceptance	<1.1°
Source to specimen distance	225 mm
Specimen to back slit distance	225 mm
Scans	0.02 °2Θ/step; 2.5°/min.

Table 4.1. Summary of Coating Experiments

Run Number	Nominal Temperature (°C)	Length (cm)	Dia. (cm)	Weight Gain (g)	Total Gas Flow (cm^3/min)	Ar/MS	Run Time (min)
AFCI-SiC-1	650	17.348	1.905	0.316	900	42	45
AFCI-SiC-2	630	13.805	1.946	0.372	900	42	45
AFCI-SiC-3	600	15.265	1.910	0.303	500	*	45
AFCI-SiC-4	700	15.545	1.908	1.418	1000	14	45
AFCI-SiC-5	575	15.451	1.908	0.041	1000	29	60
AFCI-SiC-6	600	15.608	1.915	0.094	1000	29	60
AFCI-SiC-7	625	15.458	1.908	0.151	1000	29	60
AFCI-SiC-8	575	15.433	1.908	0.042	1000	11	60
AFCI-SiC-9	600	15.466	1.918	0.032	1000	14	60
AFCI-SiC-10	625	15.596	1.915	0.461	1000	10	60
AFCI-SiC-11	600	15.291	1.913	0.438	1000	13	180
AFCI-SiC-12	625	15.461	1.910	1.692	1000	14	180
AFCI-SiC-13	650	15.497	1.915	**	1000	12	180
AFCI-SiC-14	600	15.552	1.905	0.629	1000	6	120
AFCI-SiC-15	625	15.296	1.905	2.069	1000	6	120

* Flow meter malfunction
** The coating completely filled the annulus between specimen and coating chamber preventing accurate measurements.

Table 5.1. Summary of Kinetic Parameters Used In Model Calculations

Reaction	Number	Log (A (1/s))	E_A (kJ/mol)	Source
CH_3SiH_3→ Surface	5.1	Calculated from collision theory	213	Ohshita (32)
CH_3SiH_3→ CH_3SiH+H_2	5.2	14.87	264	Nuedorfl (25)
CH_3SiH→ Surface	5.3	Calculated from collision theory	180	Ohshita (32)
$CH_3SiH+CH_3SiH_3$→Embryo	5.4	Calculated from collision theory	0	Nuedorfl (25)
CH_3SiH+ Embryo→Embryo	5.5	Calculated from collision theory	0 (analogous to 5.4)*	Nuedorfl (25)
Embryo→Surface	5.6	Calculated from collision theory	89	This study
Embryo→Radical+H_X	5.7	Calculated from collision theory	264 (analogous to 5.2)*	Nuedorfl (25)
Radical→Surface	5.8	Calculated from collision theory	180 (analogous to 5.3)*	Ohshita (32)
Radical+CH_3SiH_3→ Embryo	5.9	Calculated from collision theory	0 (analogous to 5.4)*	Nuedorfl (25)
Radical+Embryo→ Embryo	5.10	Calculated from collision theory	0 (analogous to 5.4)*	Nuedorfl (25)

*See text for explanation.

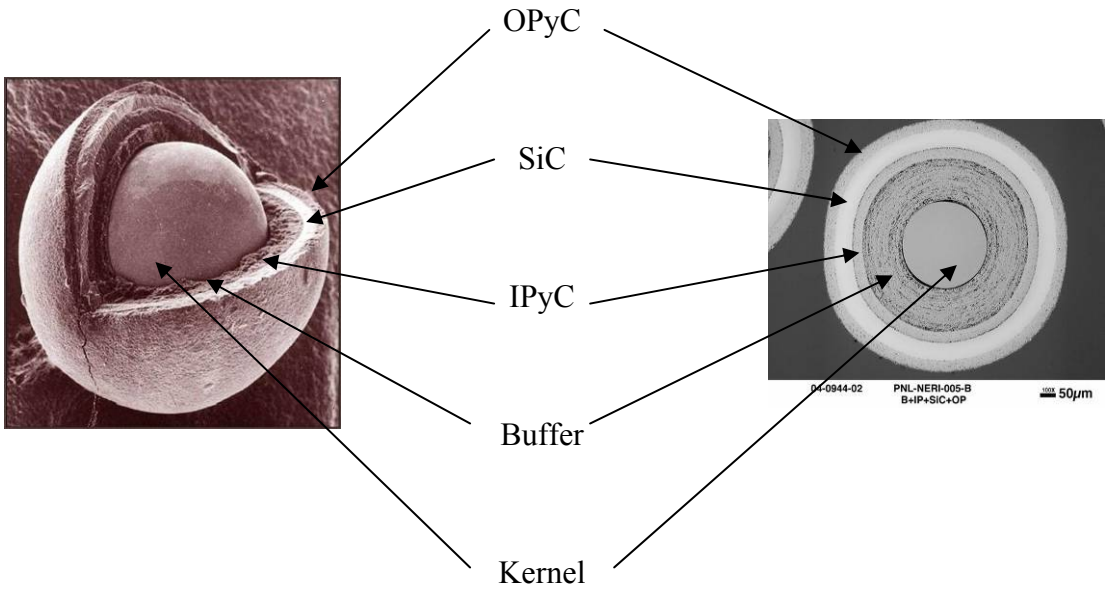

Figure 1.1. The anatomy of a typical TRISO coated particle.

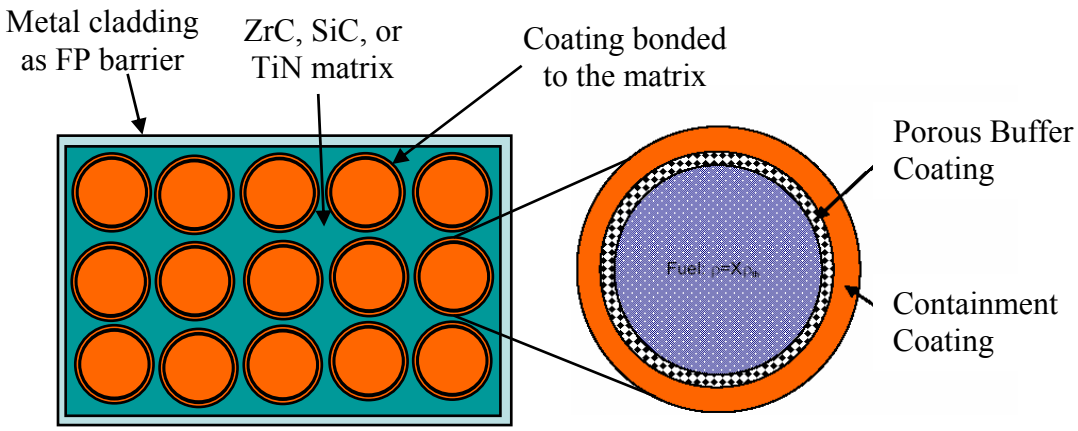

Figure 1.2. Schematic of GFR dispersion fuel concept.

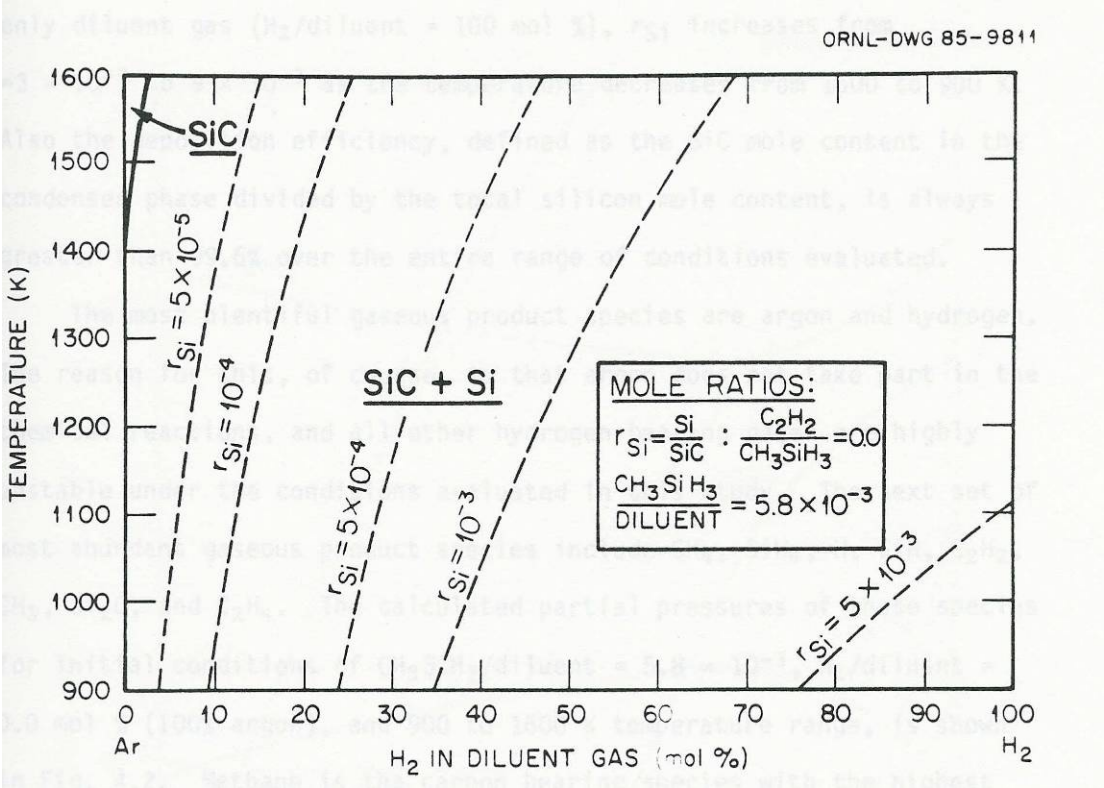

Figure 2.1. Calculated CVD phase diagram for the CH_3SiH_3-(Ar-H_2) system. From Angelini (16-17).

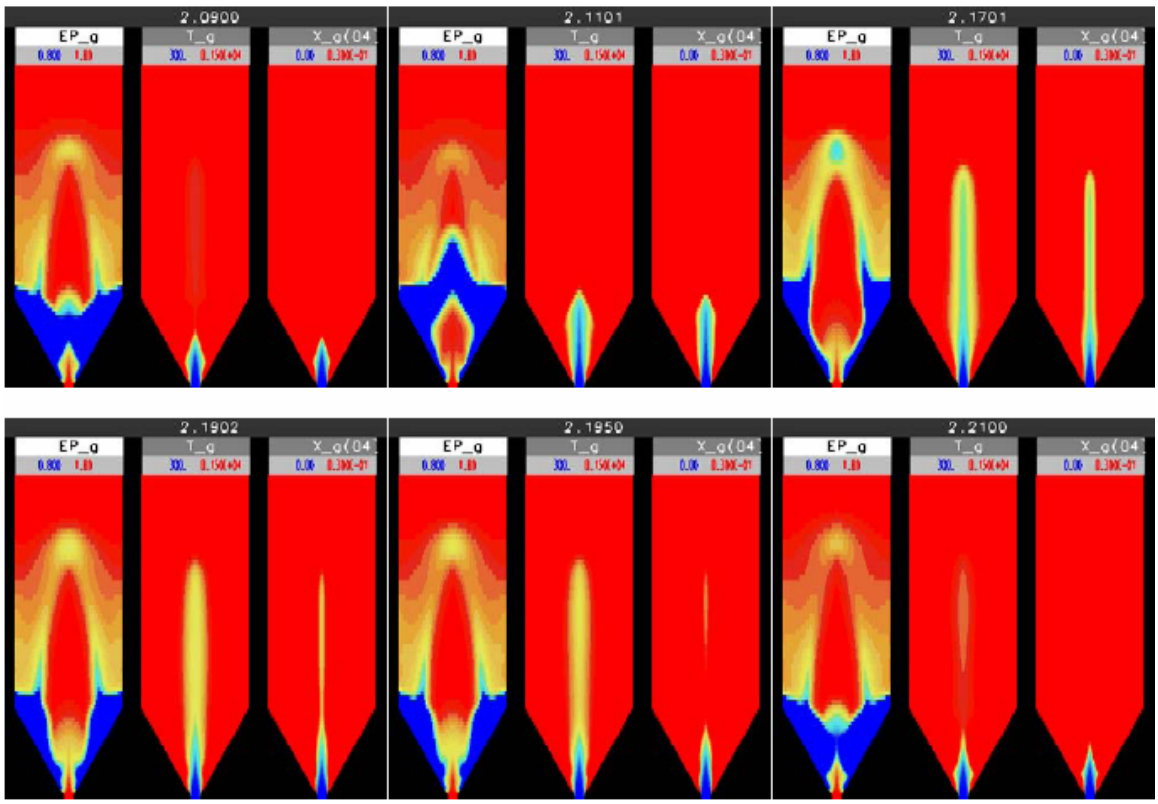

Figure 2.2. FBCVD-Model-predicted temperature, void fraction, and hydrogen fraction. Six frames of three pictures each. Each frame represents a different time step in the FBCVD simulation. The six frames in Figure 2.2 span approximately one tenth of a second. The three pictures within each frame are simulated void fraction, temperature, and H_2 mole fraction respectively. The color scheme for the void fraction is blue = 0.8 and red = 1.0 (blue for solids and red for gas). The color scheme for temperature is blue = 27°C and red = 1227°C. The color scheme for hydrogen mole fraction is blue = 0 and red = .03 (red for high and blue for low). Figure reproduced from reference (35).

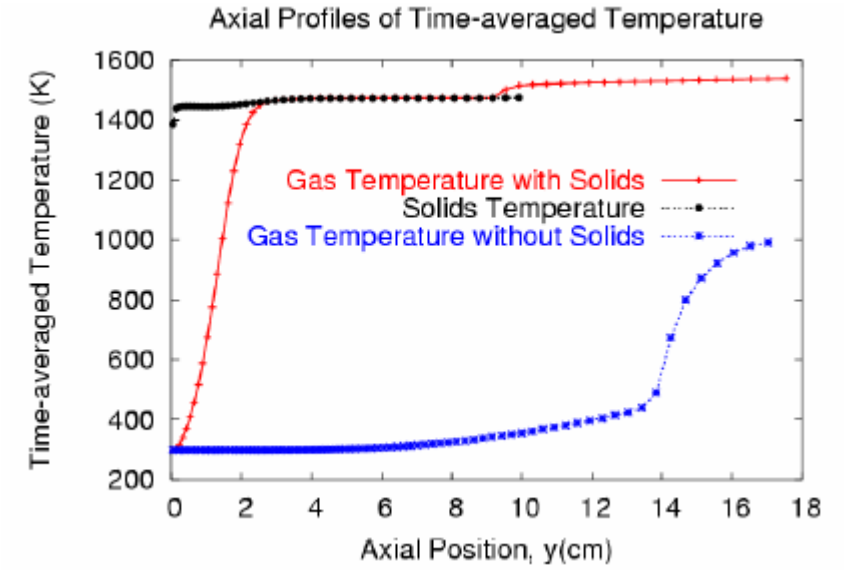

Figure 2.3. Time-averaged centerline temperature profiles of the gas and solids as a function of axial position along the height of the conical coating chamber. Figure is reproduced from reference 34.

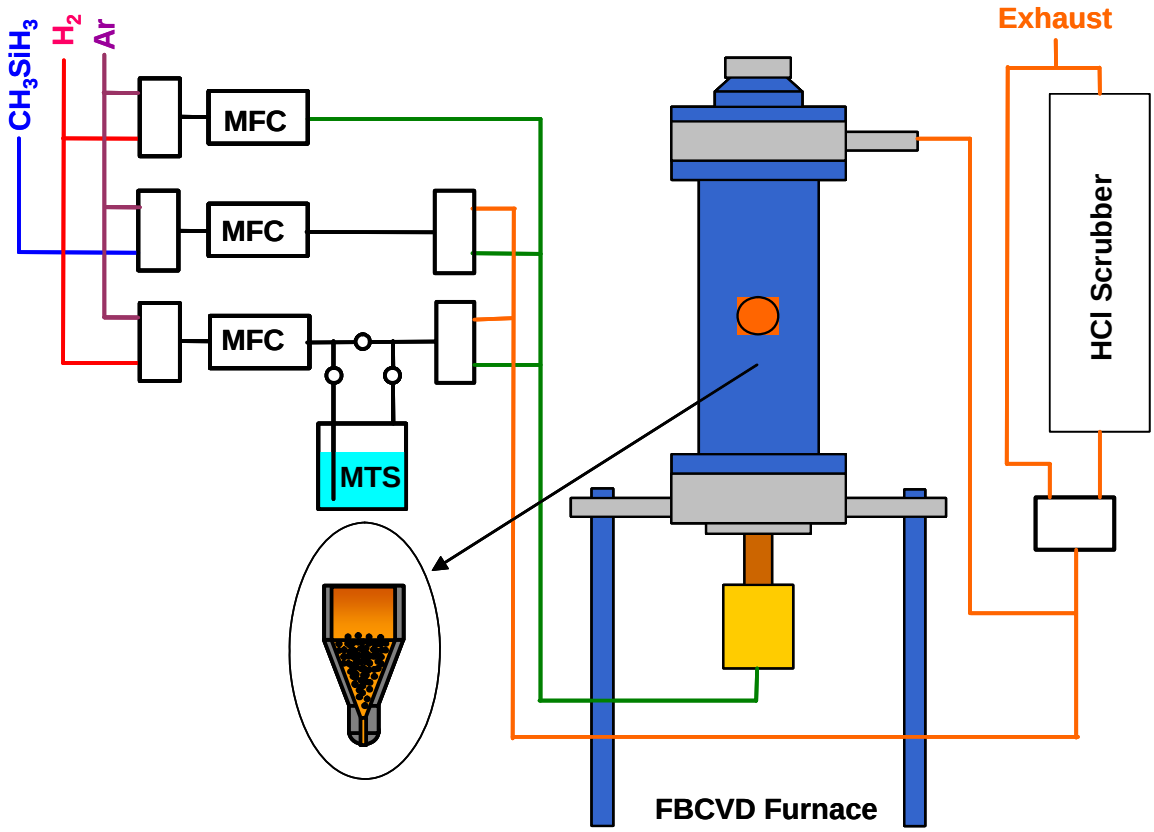

Figure 3.1. Schematic the FBCVD furnace showing the configuration of the reactant and exhaust gas lines.

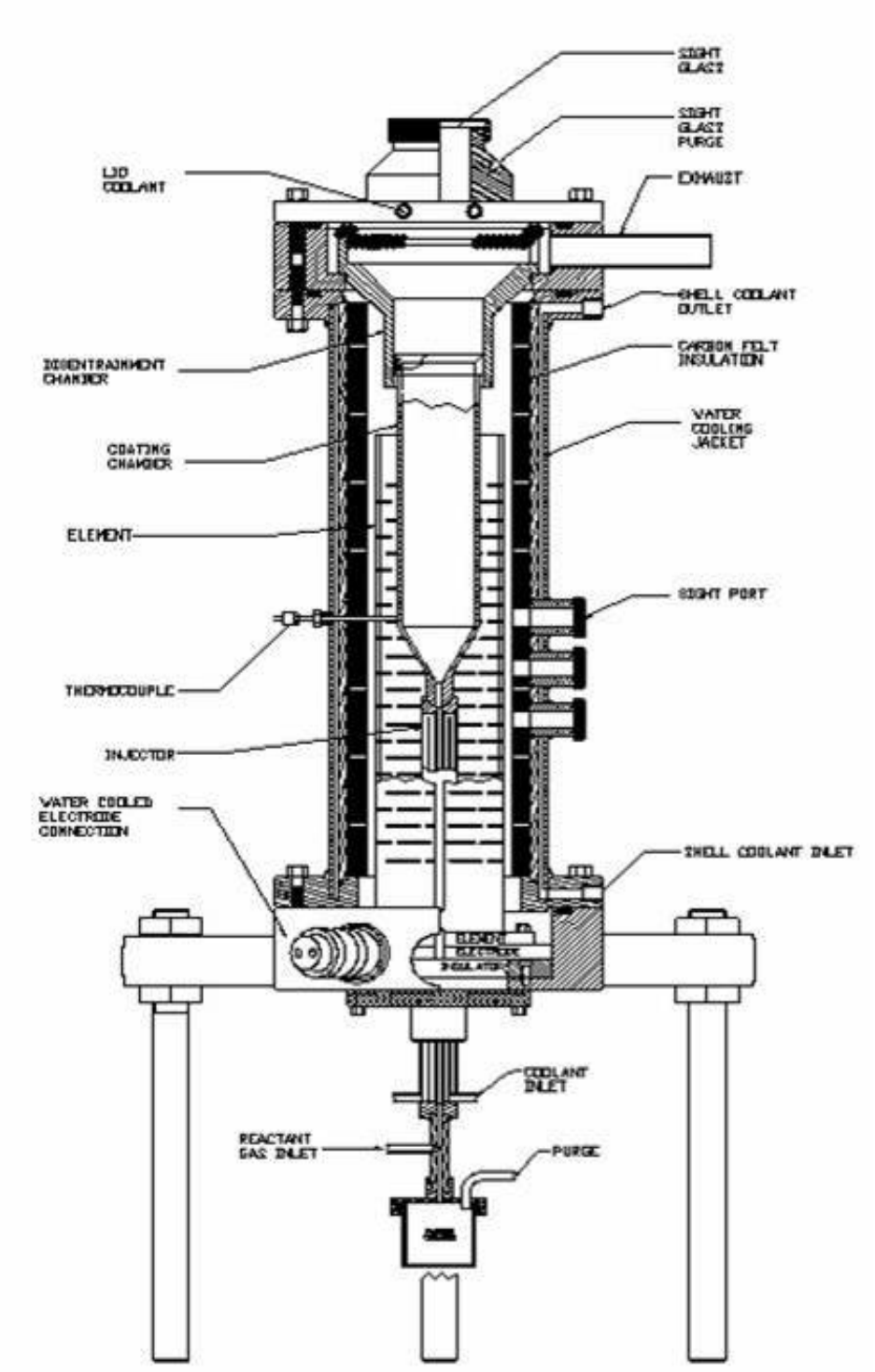

Figure 3.2. Cutaway drawing of FBCVD reactor.

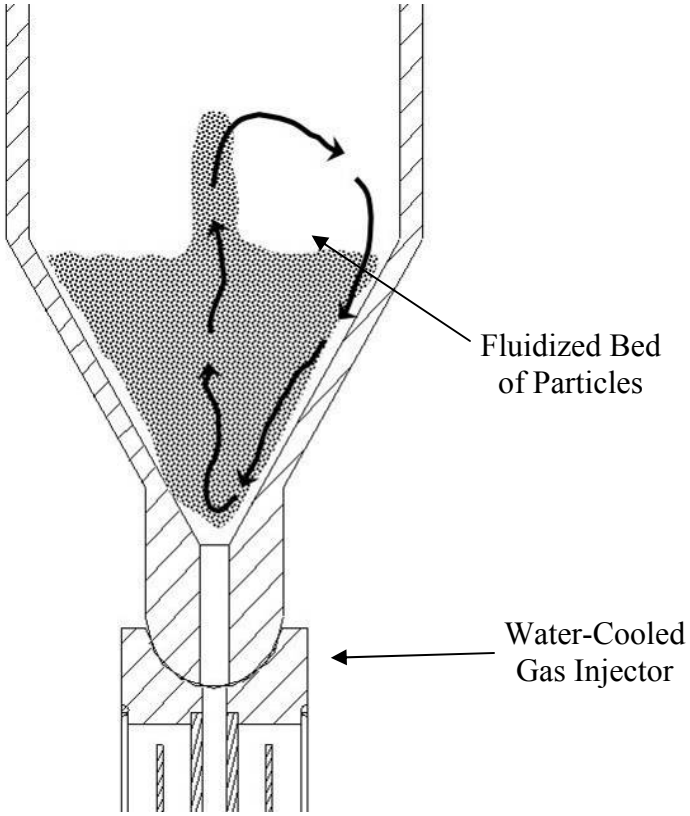

Figure 3.3. Enlarged schematic of spouting bed, graphite cone, and water-cooled injector.

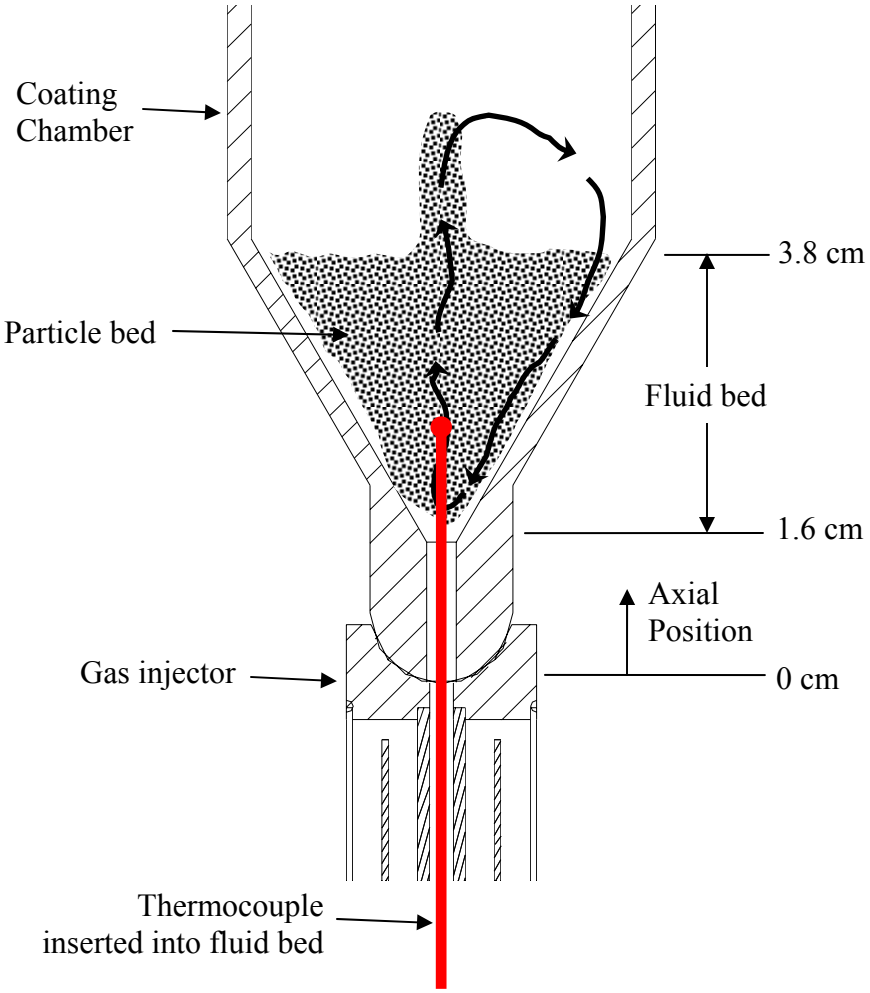

Figure 3.4. Schematic cut away view of the particle bed, coating chamber, and water-cooled gas injector showing the manner in which the fluid bed thermal profile measurements were made.

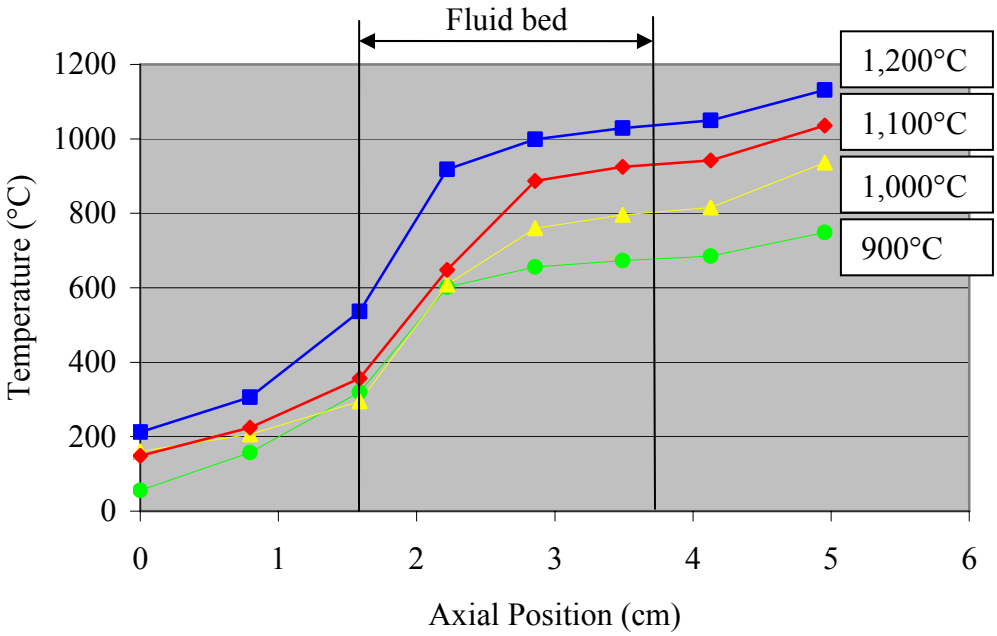

Figure 3.5. Thermocouple readings as a function of axial position inside a fluidized particle bed at four nominal coating temperatures.

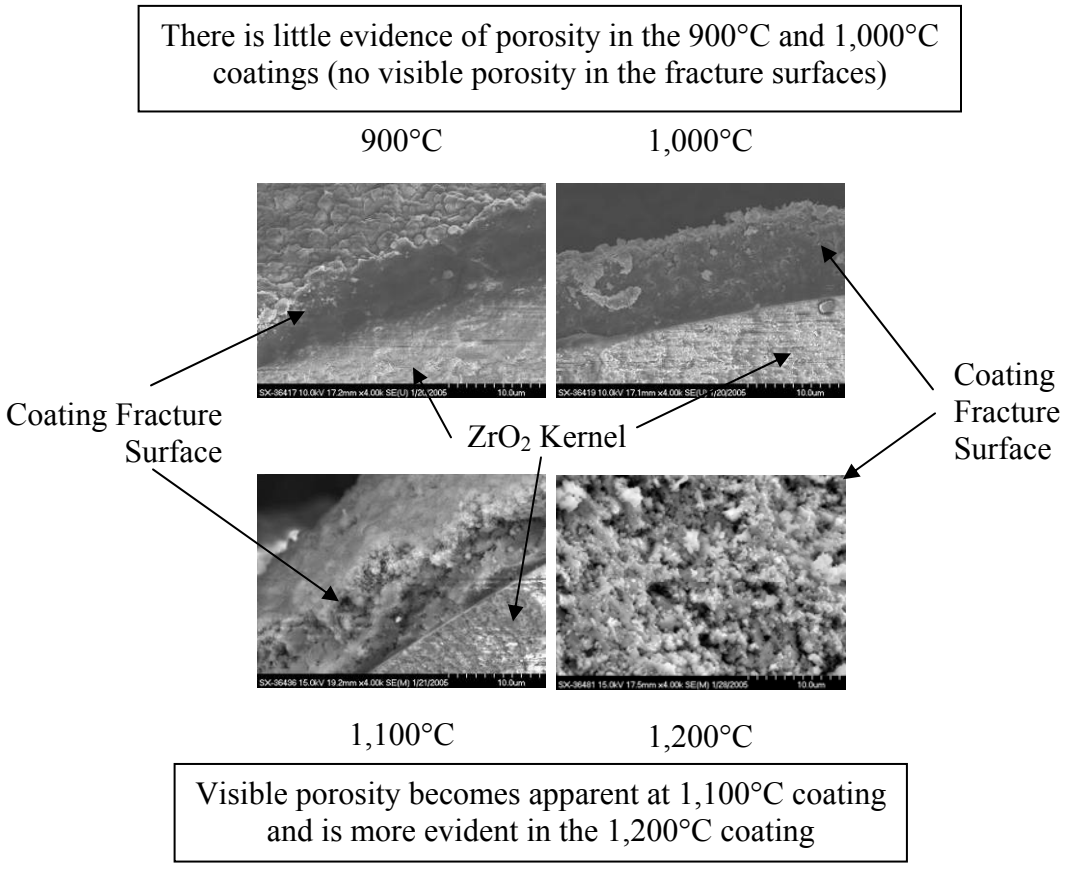

Figure 3.6. SEM micrographs of fracture surfaces of SiC coatings produced over the range of temperatures.

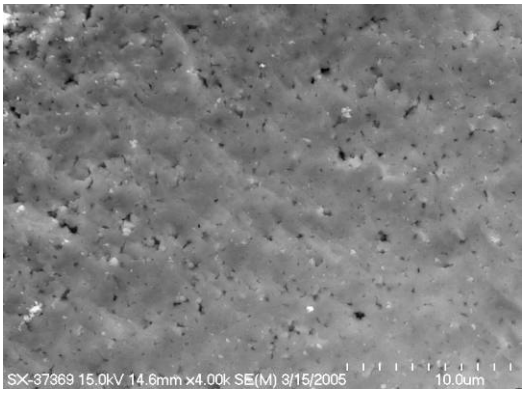

900°C
2.93 ± 0.15 g/cc
91± 5% of Theoretical

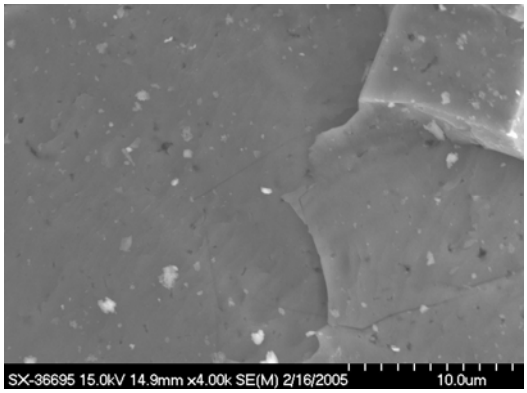

1,000°C
2.92 ± 0.15 g/cc
91± 5% of Theoretical

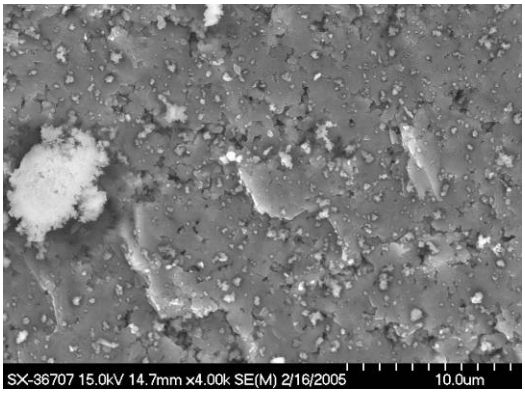

1,100°C
2.75 ± 0.15 g/cc
85± 5% of Theoretical

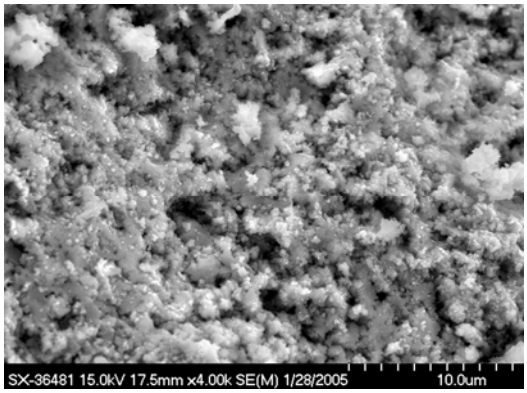

1,200°C
1.05 ± 0.15 g/cc
33± 5% of Theoretical

Figure 3.7. SEM photographs of the fracture surfaces of crushed particles from the second set of coating experiments (900-1,200°C).

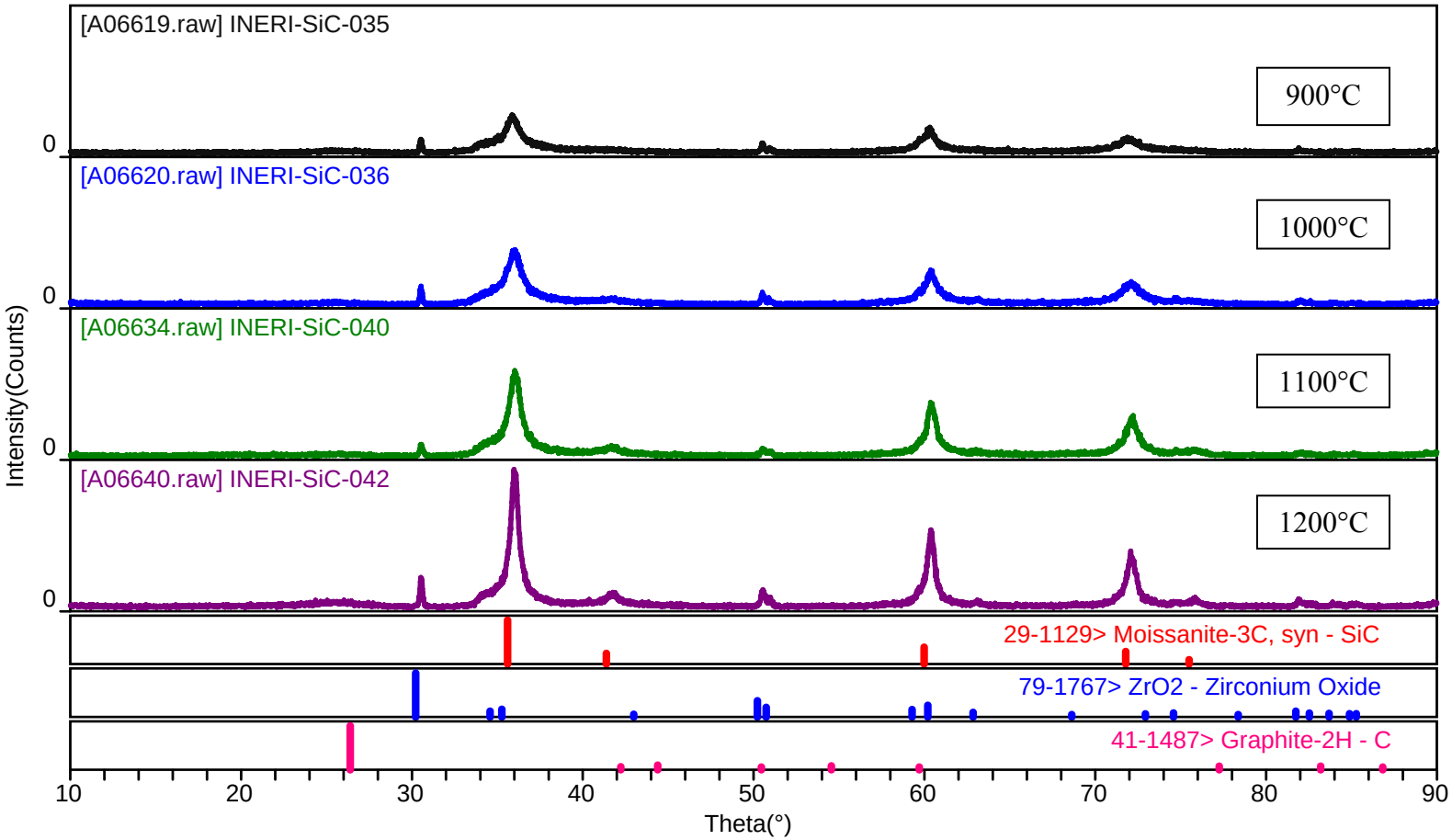

Figure 3.8. Particle XRD patterns for the SiC coatings produced over the range of coating temperature.

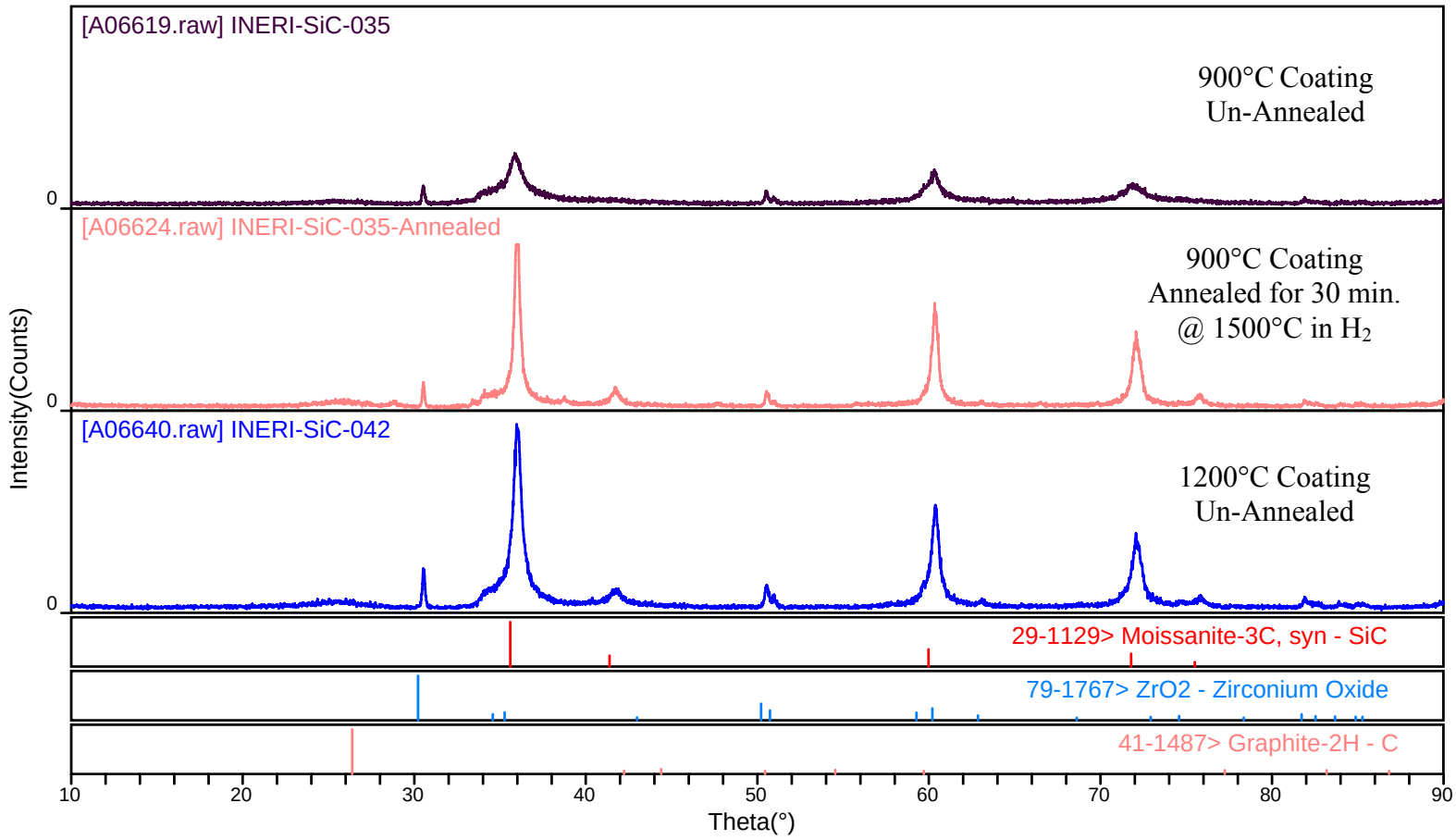

Figure 3.9. Particle XRD patterns of both annealed and un-annealed 900 °C SiC coatings along with the pattern for the 1200°C SiC coating and reference patterns for cubic SiC, ZrO_2, and graphite for comparison.

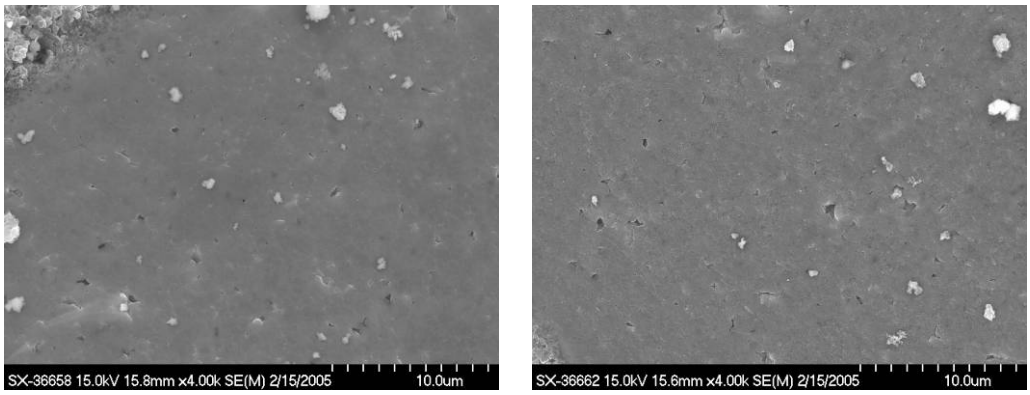

900°C SiC Coating Un-Annealed

900°C SiC Coating Annealed 30 min. at 1500°C in H_2

Figure 3.10. SEM micrographs of fracture surface of un-annealed and annealed 1173 K SiC coatings.

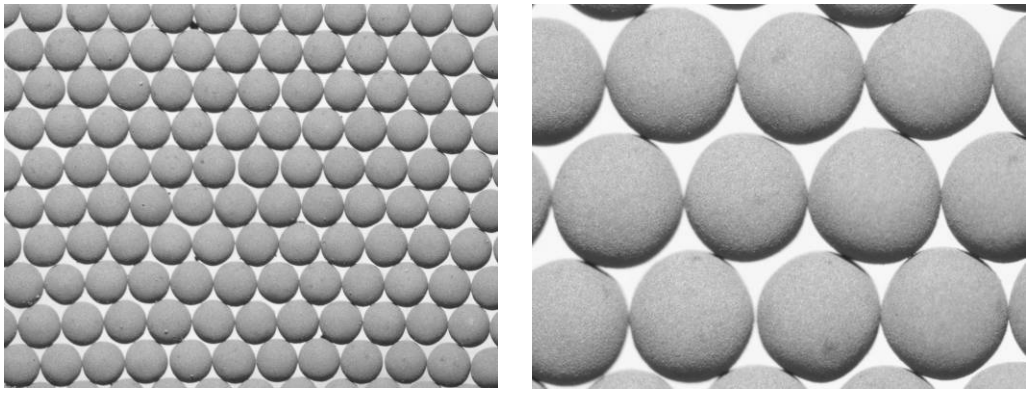

SiC Seal Coated Particles

Figure 3.11. Low magnification optical photographs of SiC seal coated particles.

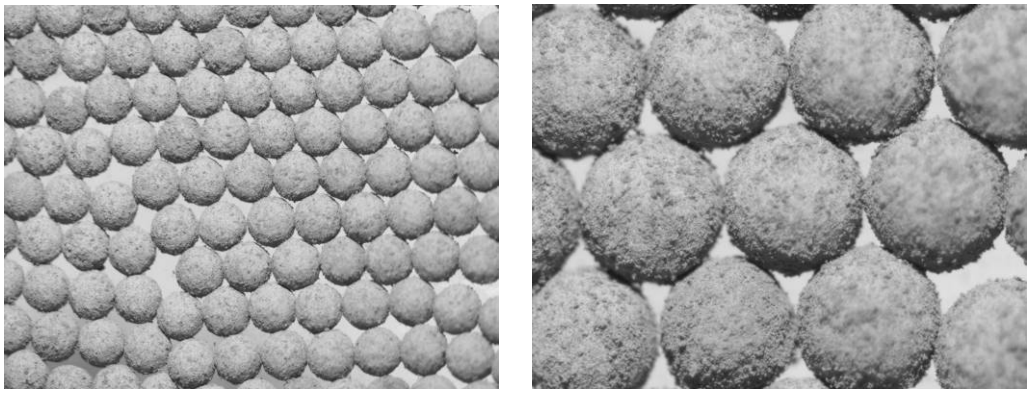

Figure 3.12. Low magnification optical photographs of SiC buffer coated particles.

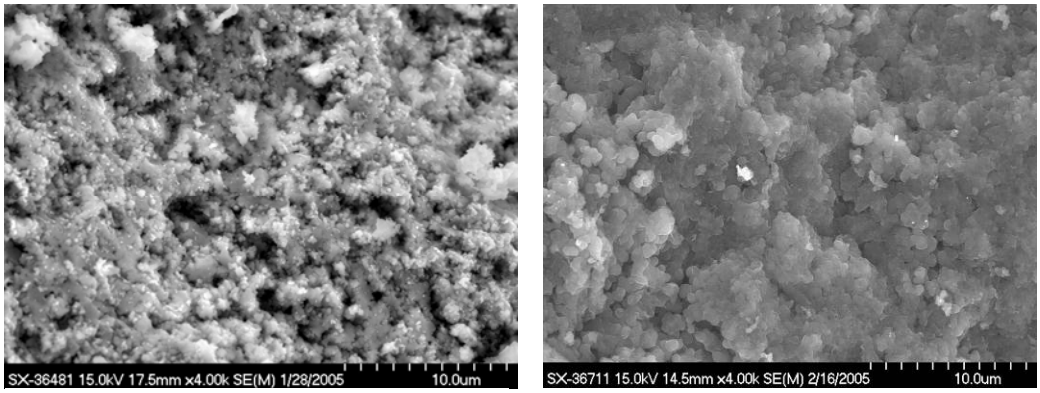

Figure 3.13. SEM micrographs of fracture surface of SiC buffer and TRISO-type carbon buffer coatings.

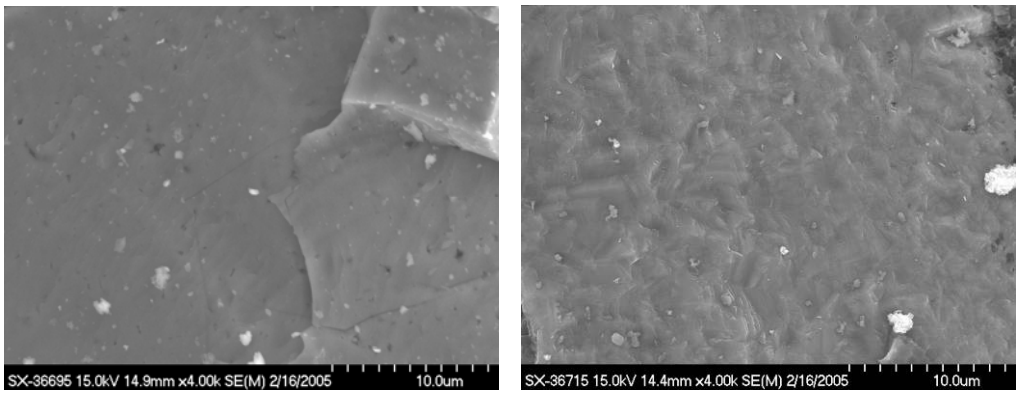

Low Temperature SiC Seal Coating

1500°C MTS-SiC Coating

Figure 3.14. SEM micrographs of fracture surface of SiC seal and TRISO-type MTS derived SiC coatings.

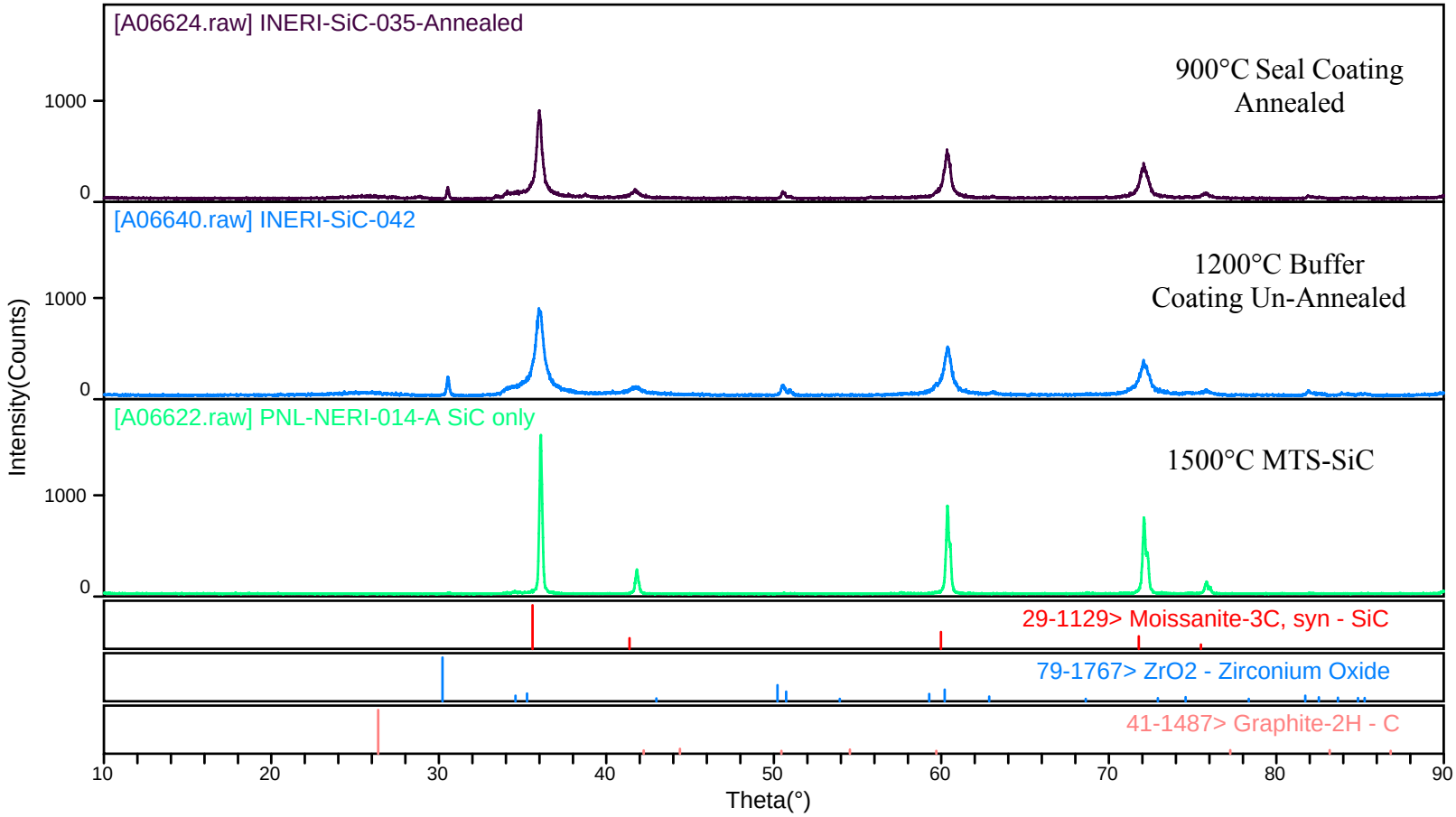

Figure 3.15. Particle XRD patterns of the annealed SiC seal coating, the SiC buffer coating, the TRISO-type MTS-SiC, and the reference patterns for cubic SiC, ZrO_2, and graphite for comparison.

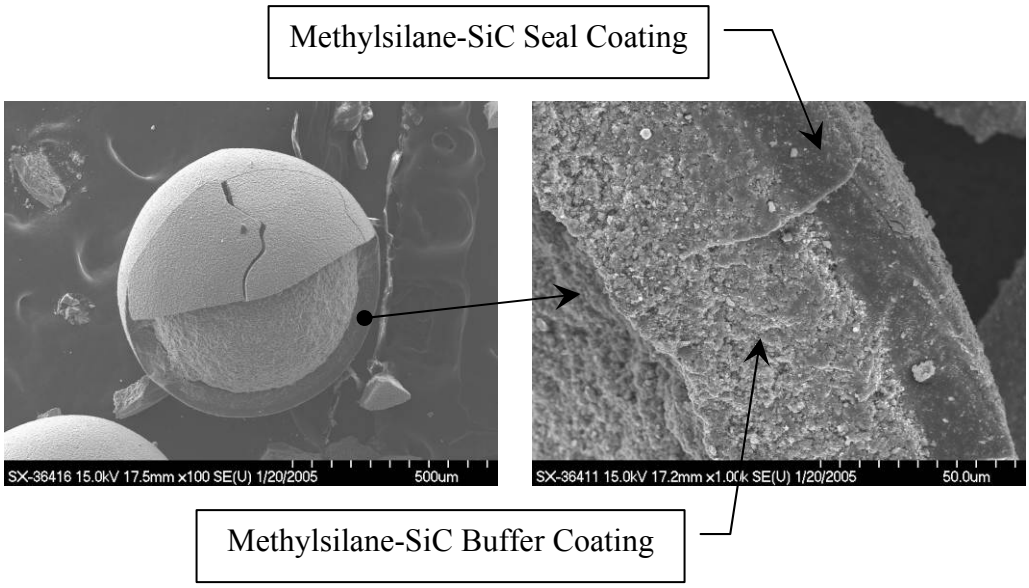

Figure 3.16. SEM photographs of a dual layer SiC coated particle.

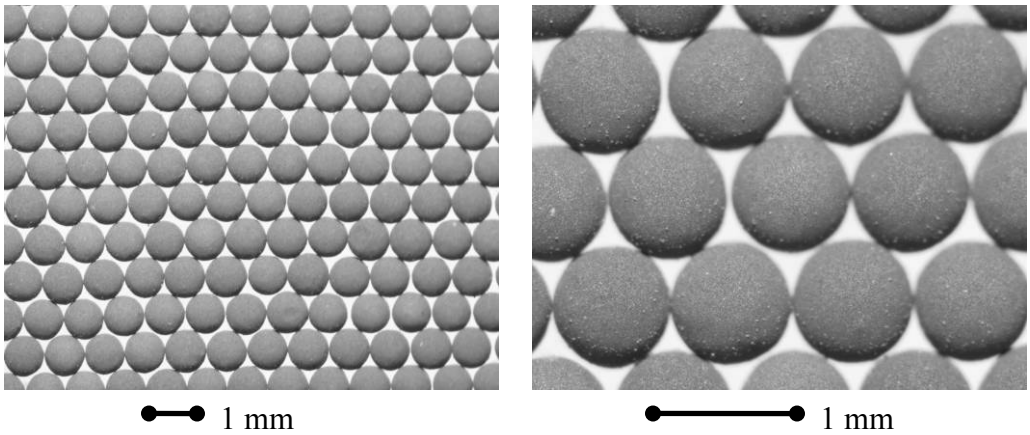

Figure 3.17. Low magnification optical photographs of dual layer SiC coated particles.

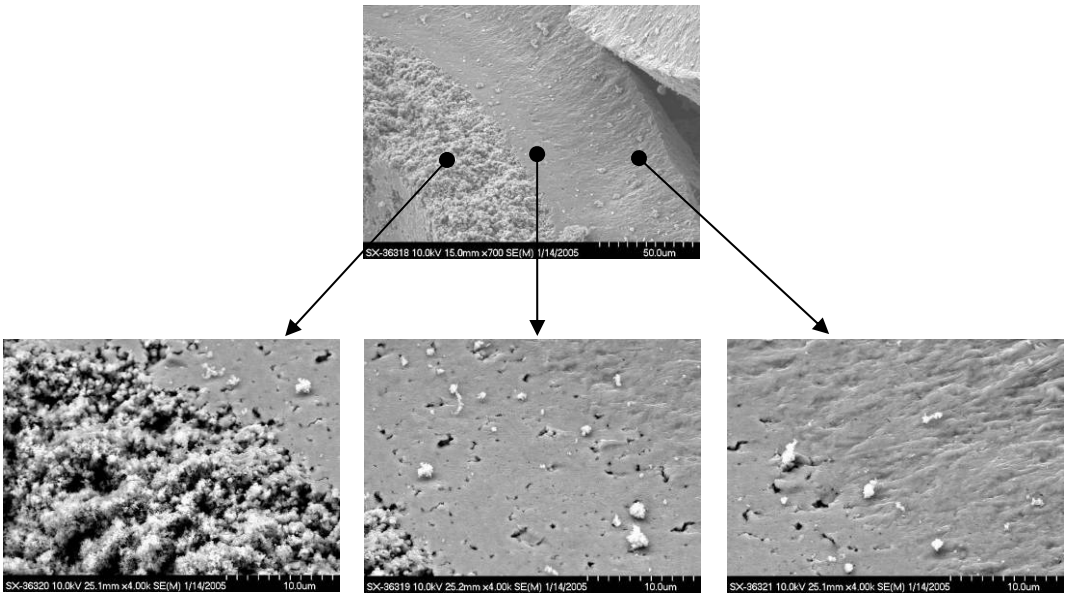

Figure 3.18. SEM photographs of the fracture surface of a three layer SiC coated particle.

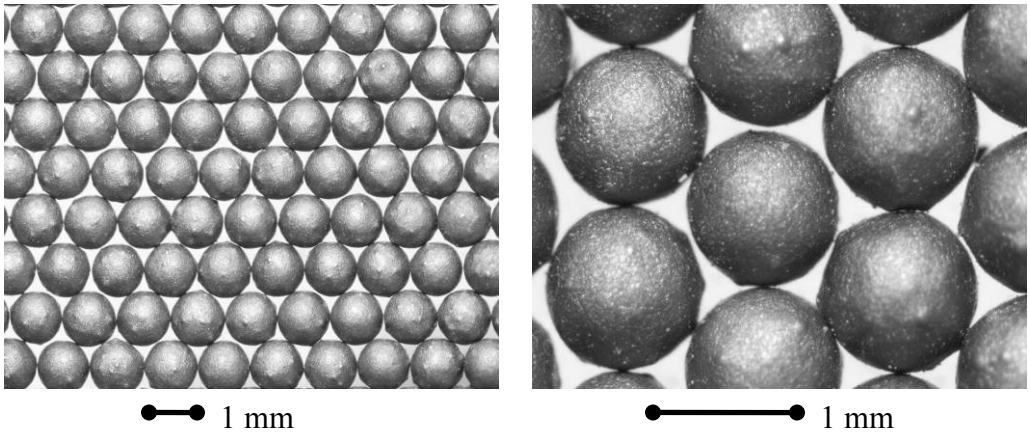

Figure 3.19. Low magnification optical photographs of the three layer SiC coated particles

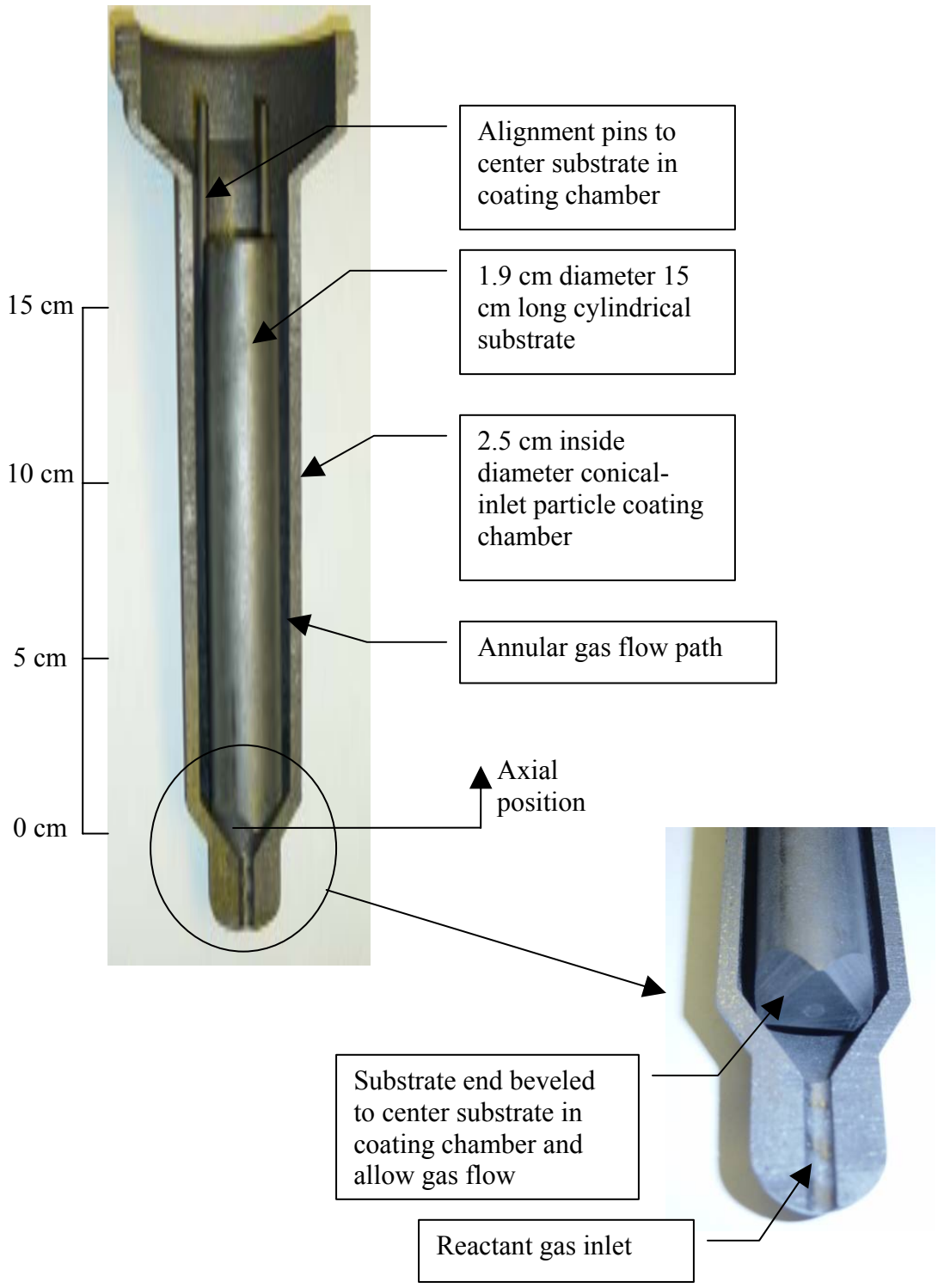

Figure 4.1. Coating chamber and substrate configuration used in coating experiments.

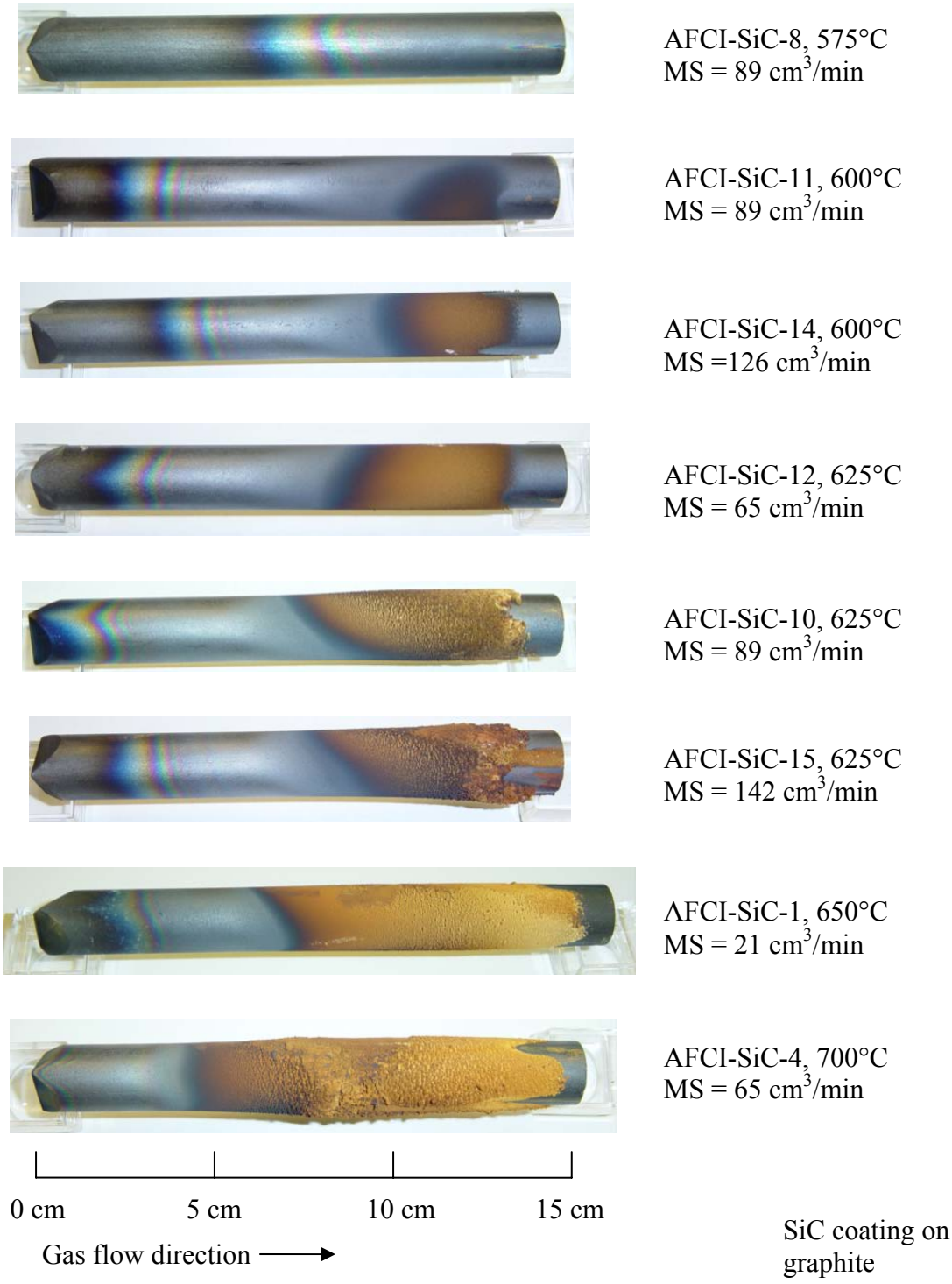

Figure 4.2. Photographs of specimens coated a variety of temperatures and methylsilane flow rates.

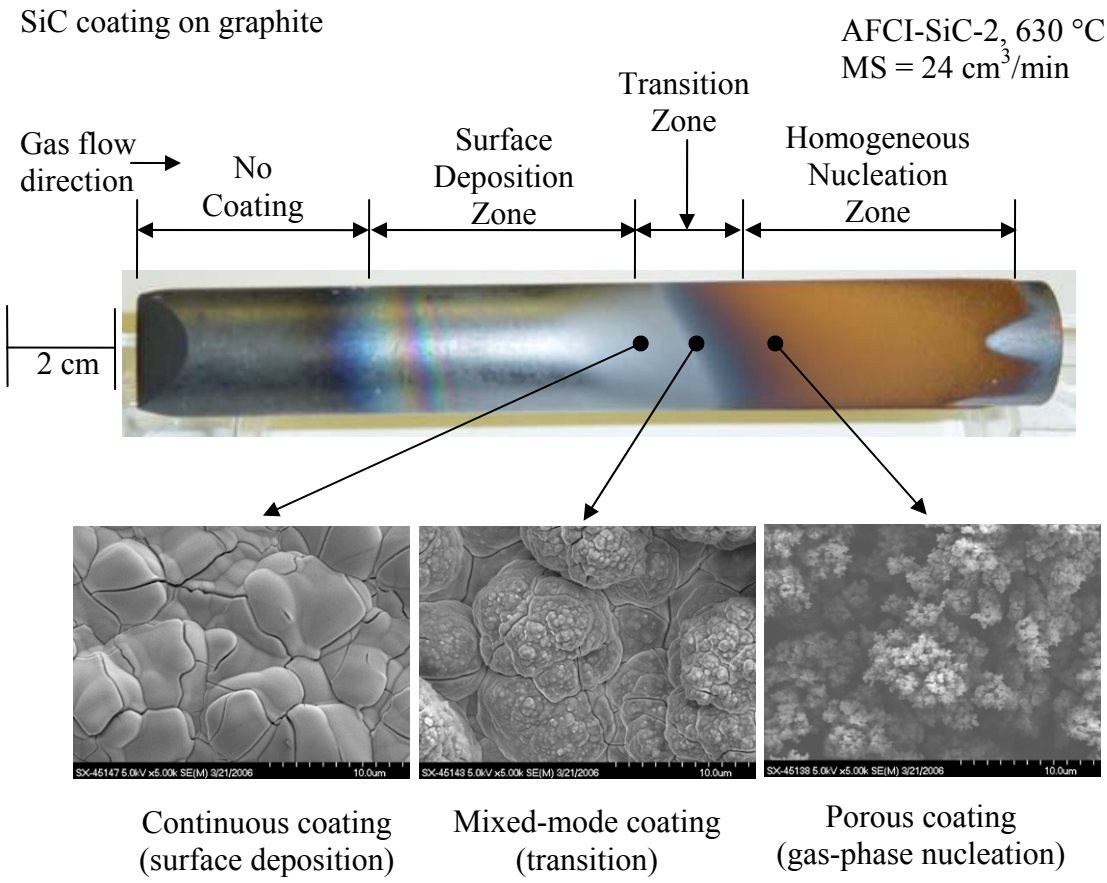

Figure 4.3. A photograph of AFCI-SiC-2 accompanied by SEM photographs showing the coating surface morphology in the three deposition mode zones.

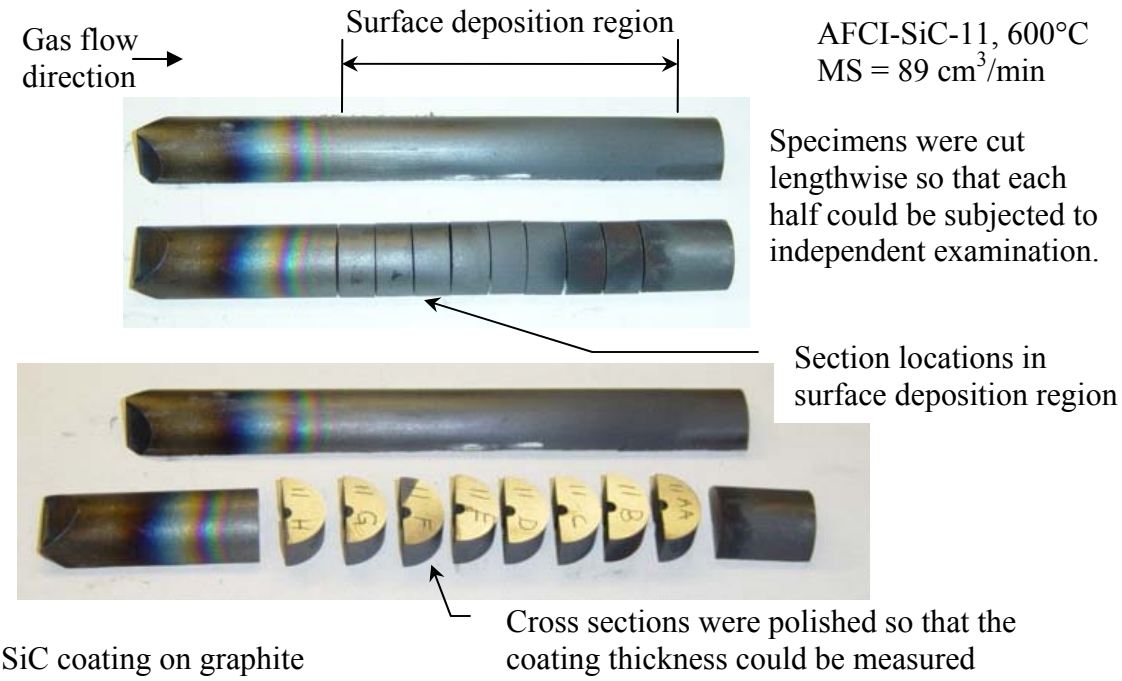

Figure 4.4. Photographs showing the sectioning details of AFCI-SiC-11. MS = methylsilane.

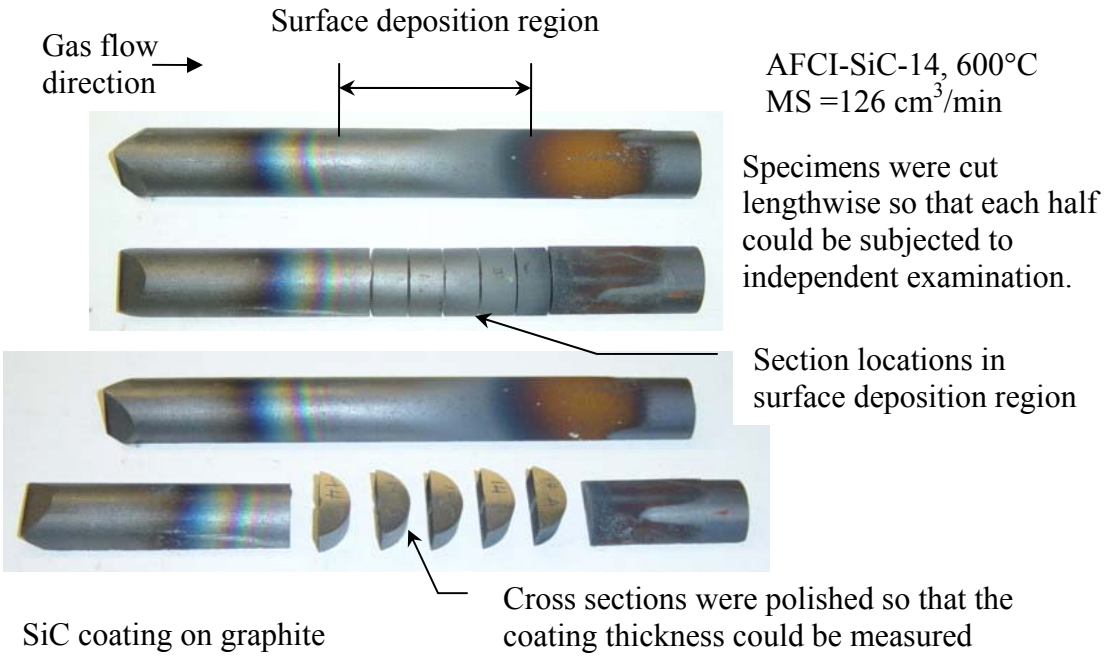

Figure 4.5. Photographs showing the sectioning details of AFCI-SiC-14. MS = methylsilane

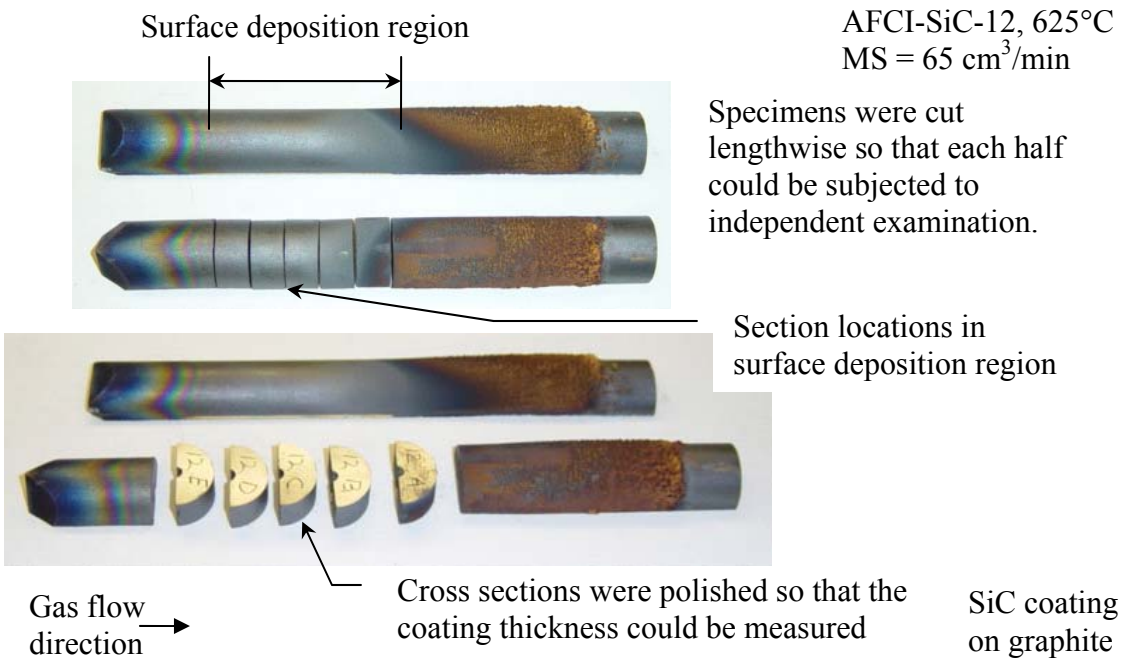

Figure 4.6. Photographs showing the sectioning details of AFCI-SiC-12. MS = methylsilane.

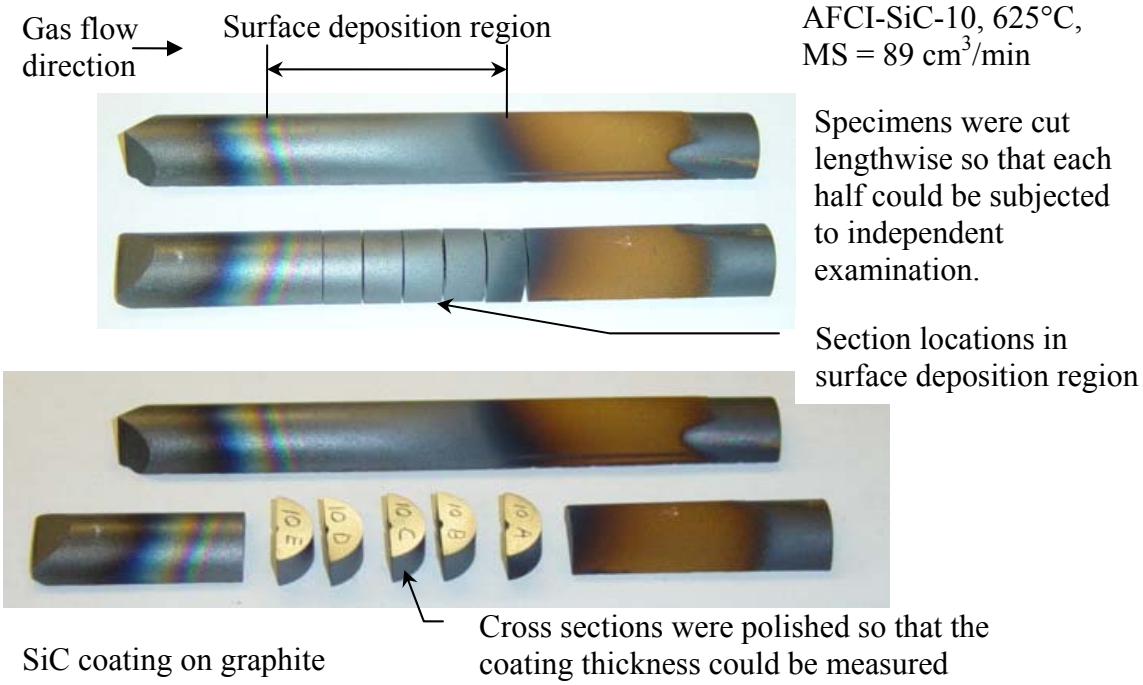

Figure 4.7. Photographs showing the sectioning details of AFCI-SiC-10. MS = methylsilane.

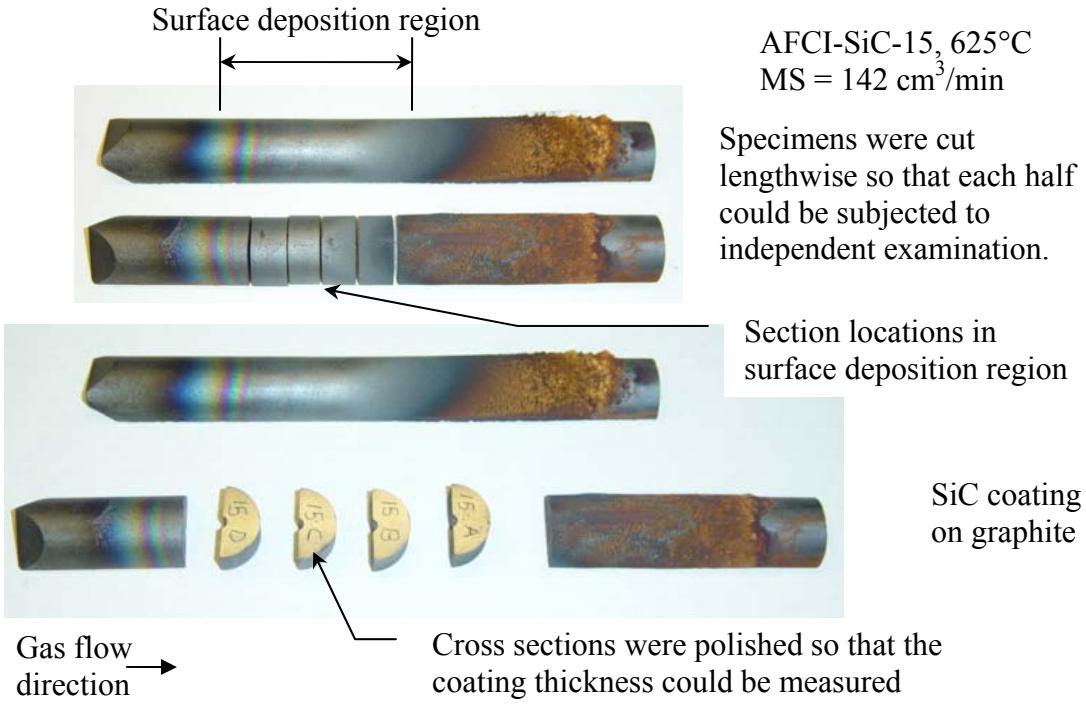

Figure 4.8. Photographs showing the sectioning details of AFCI-SiC-15. MS = methylsilane.

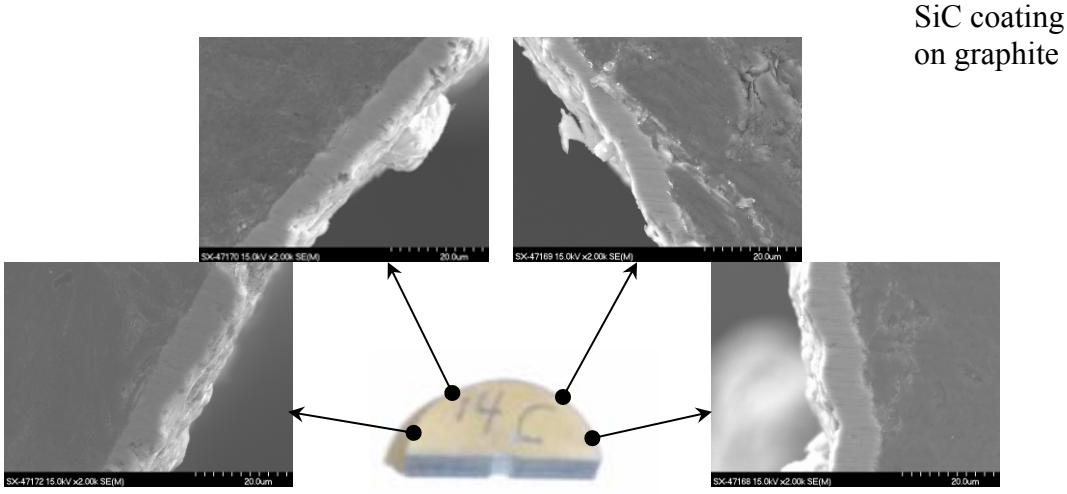

Figure 4.9. Photographs of specimen segment AFCI-SiC-14C showing locations where and SEM micrographs (also shown) were taken from for coating thickness measurements.

SiC coating on graphite AFCI-SiC-14C

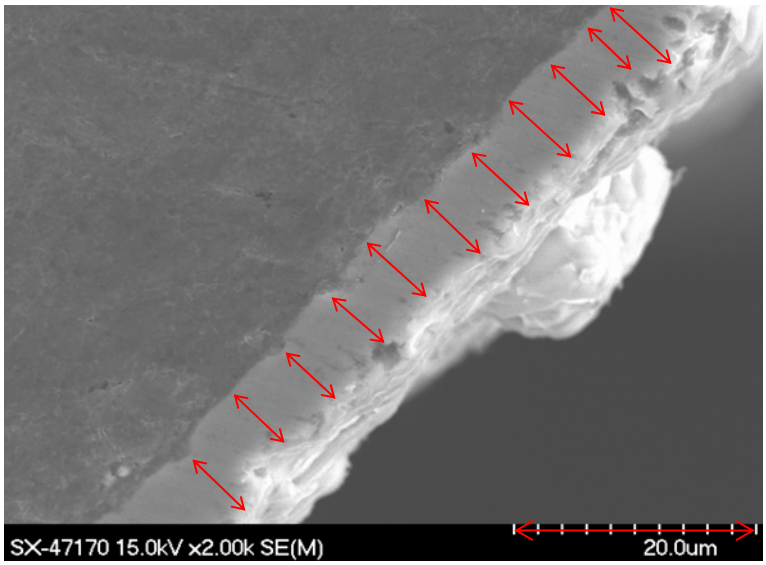

Measured Thickness (μm)
7.260
6.792
6.931
7.608
7.360
7.632
7.704
7.524
8.041
7.541
8.203
20.000 (reference)

Figure 4.10. A typical SEM micrograph from sample AFCI-SiC-14C showing the approximate locations where length measurements were made. Length data obtained from this micrograph are also shown.

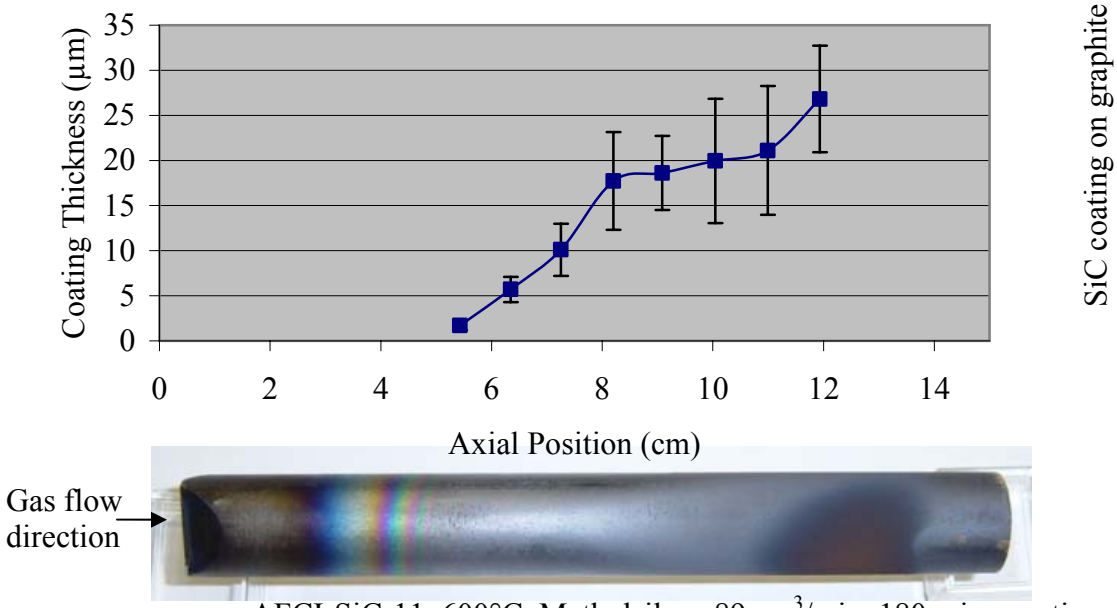

Figure 4.11. Coating thickness as a function of axial position for sample AFCI-SiC-11. The points are the average coating thickness and the error bars are the standard deviations.

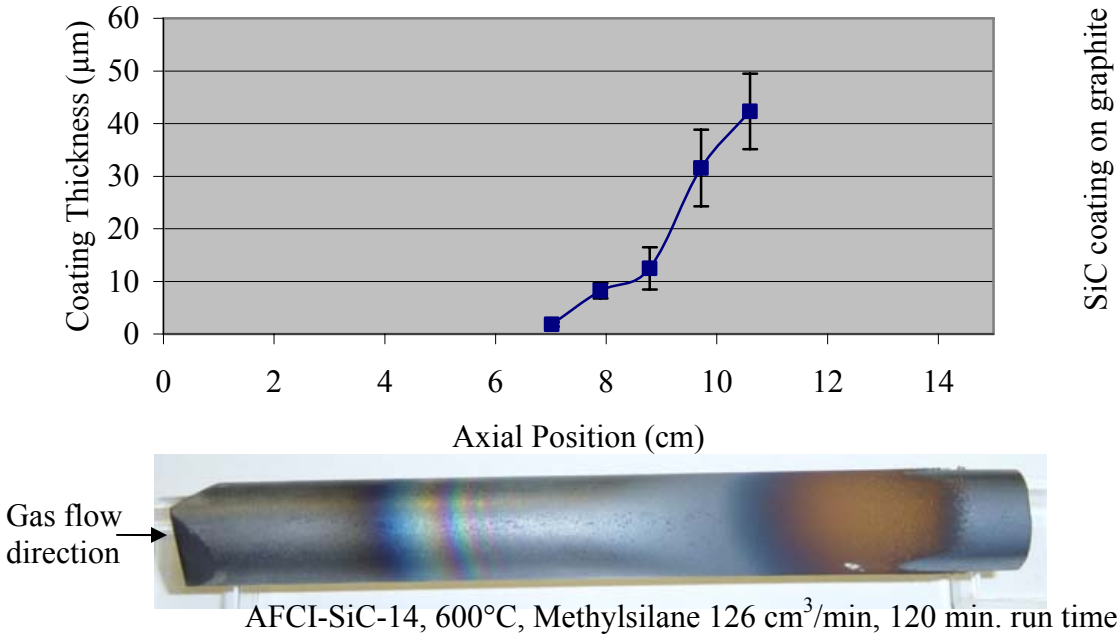

Figure 4.12. Coating thickness as a function of axial position for sample AFCI-SiC-14. The points are the average coating thickness and the error bars are the standard deviations.

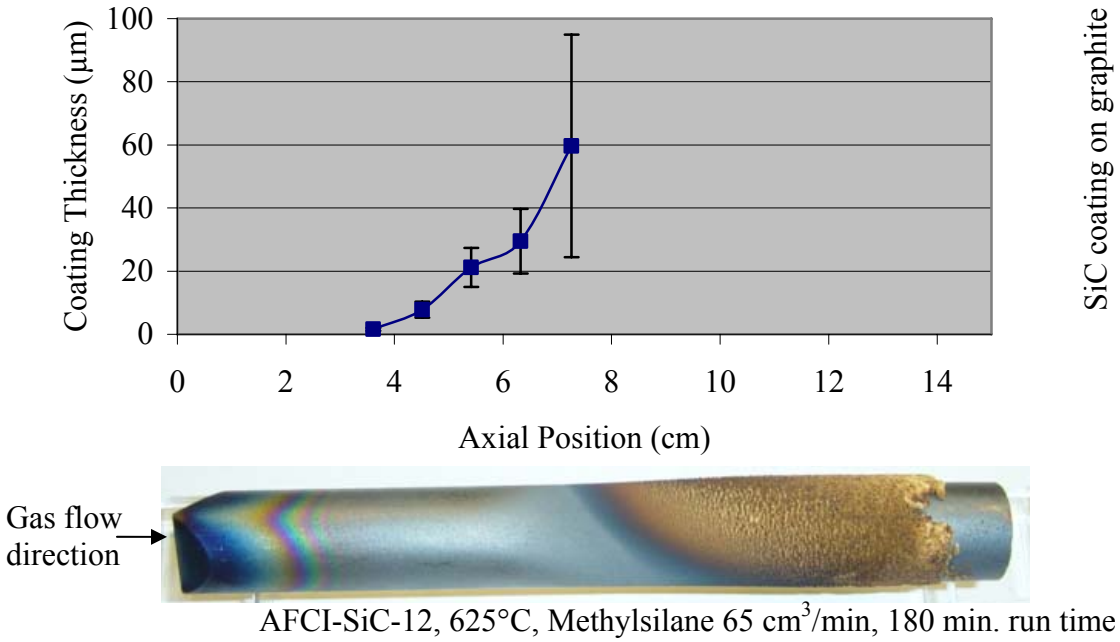

Figure 4.13. Coating thickness as a function of axial position for sample AFCI-SiC-12. The points are the average coating thickness and the error bars are the standard deviations.

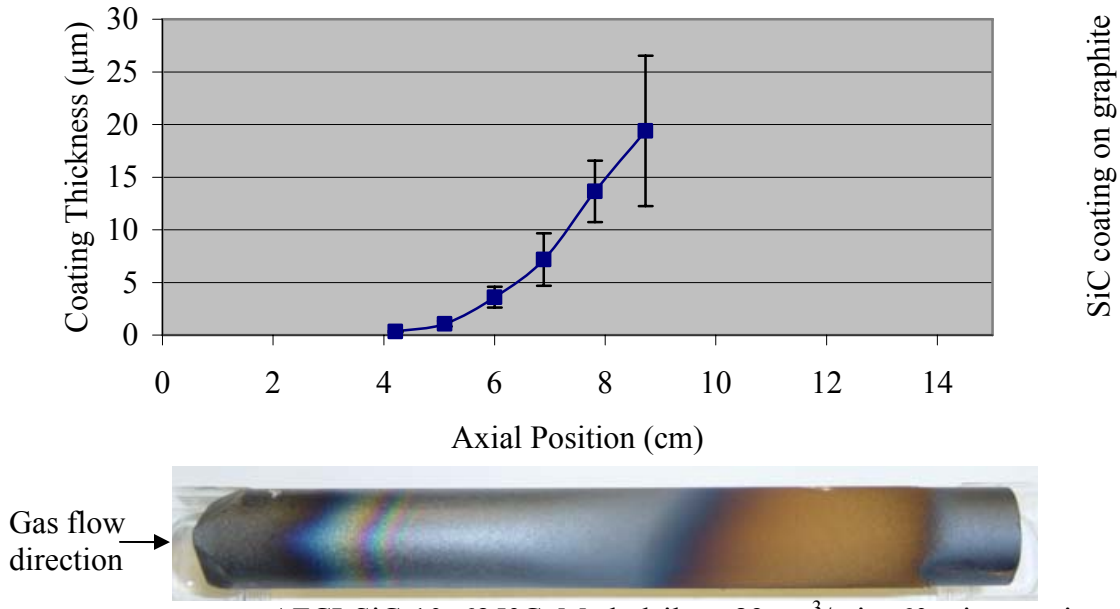

Figure 4.14. Coating thickness as a function of axial position for sample AFCI-SiC-10. The points are the average coating thickness and the error bars are the standard deviations.

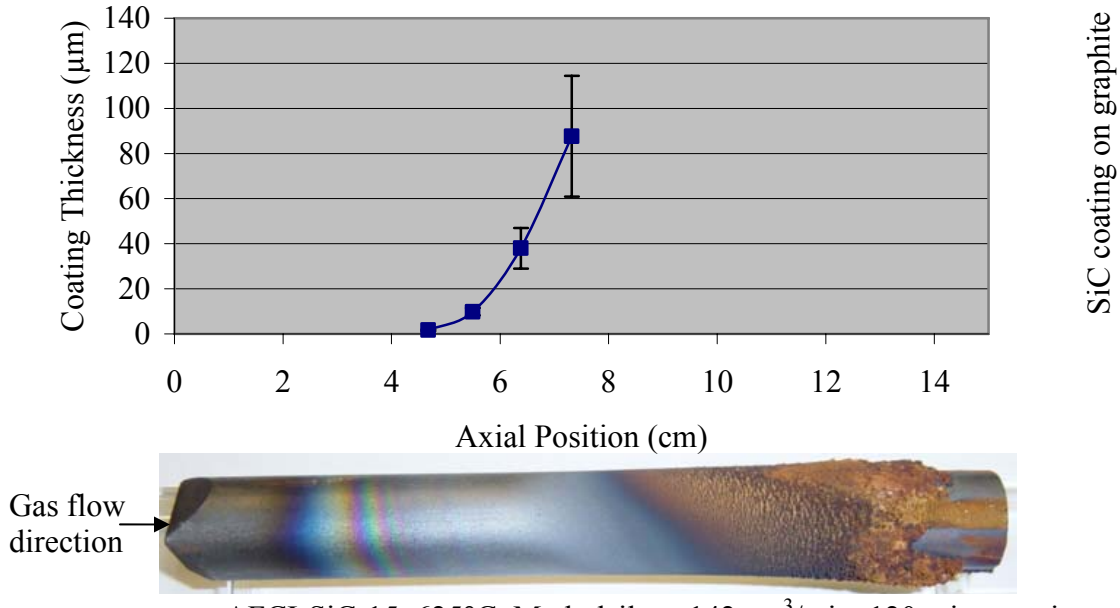

Figure 4.15. Coating thickness as a function of axial position for sample AFCI-SiC-15. The points are the average coating thickness and the error bars are the standard deviations.

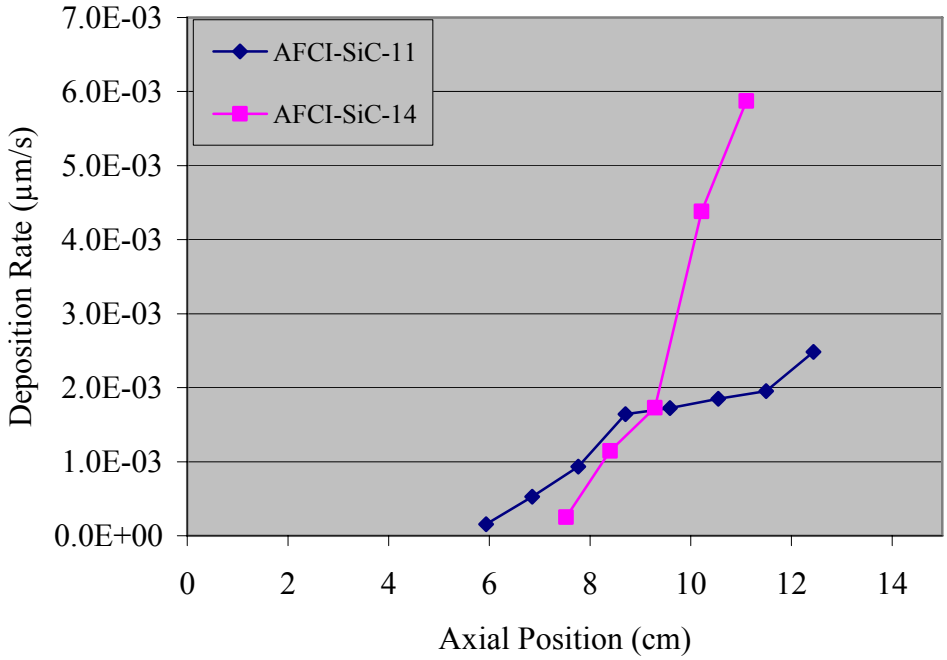

Figure 4.16. Experimental deposition rate verses axial position for specimens coated at 600°C (AFCI-SiC-11 and 14)

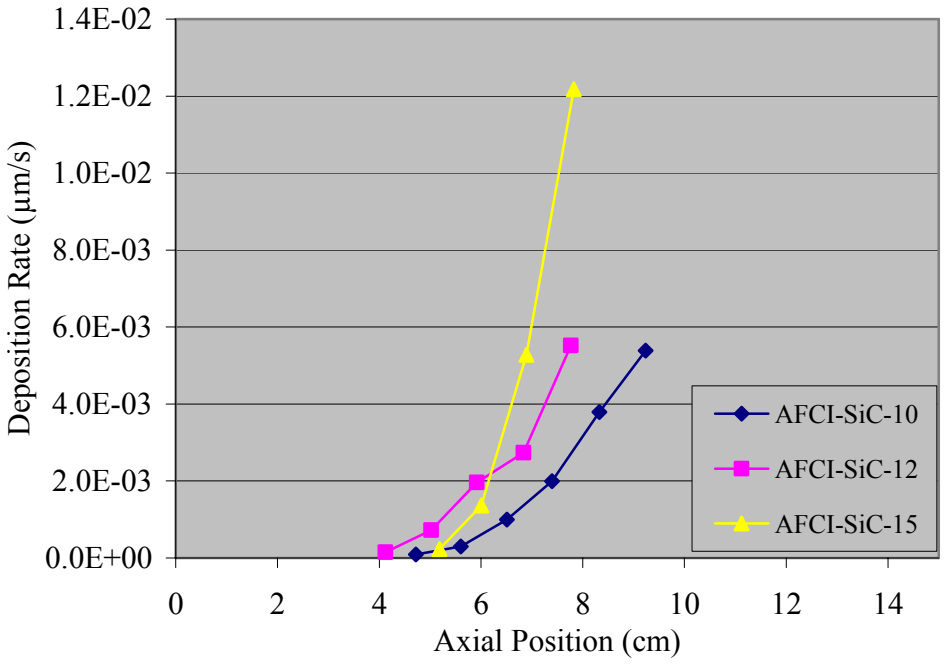

Figure 4.17. Experimental deposition rate verses axial position for specimens coated at 625°C (AFCI-SiC-10, 12, and 15).

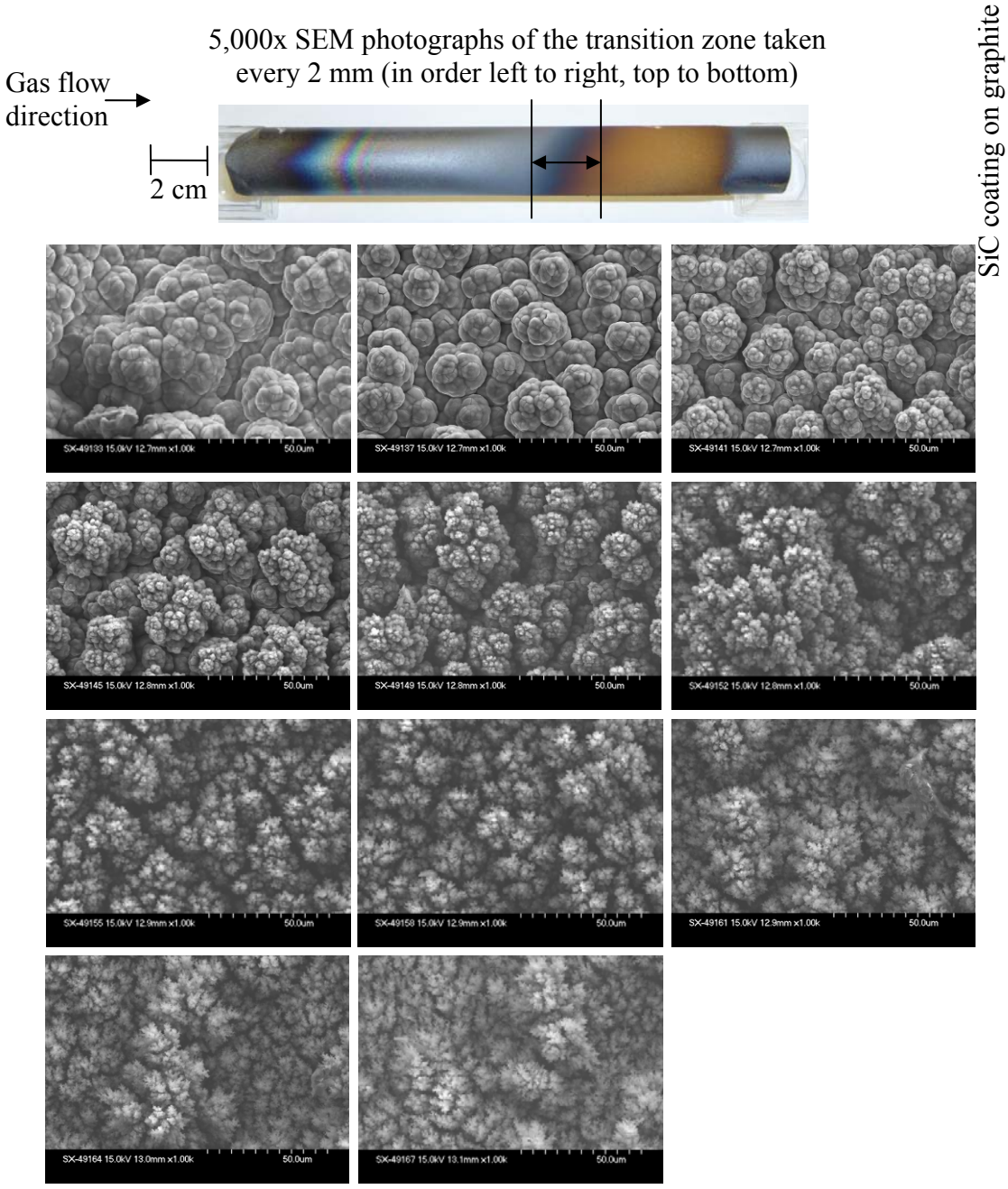

Figure 4.18. SEM micrographs, taken at a magnification of 5,000x, of the coating surface taken every two millimeters (in order left to right, top to bottom) in the transition zone of specimen number AFCI-SiC-10.

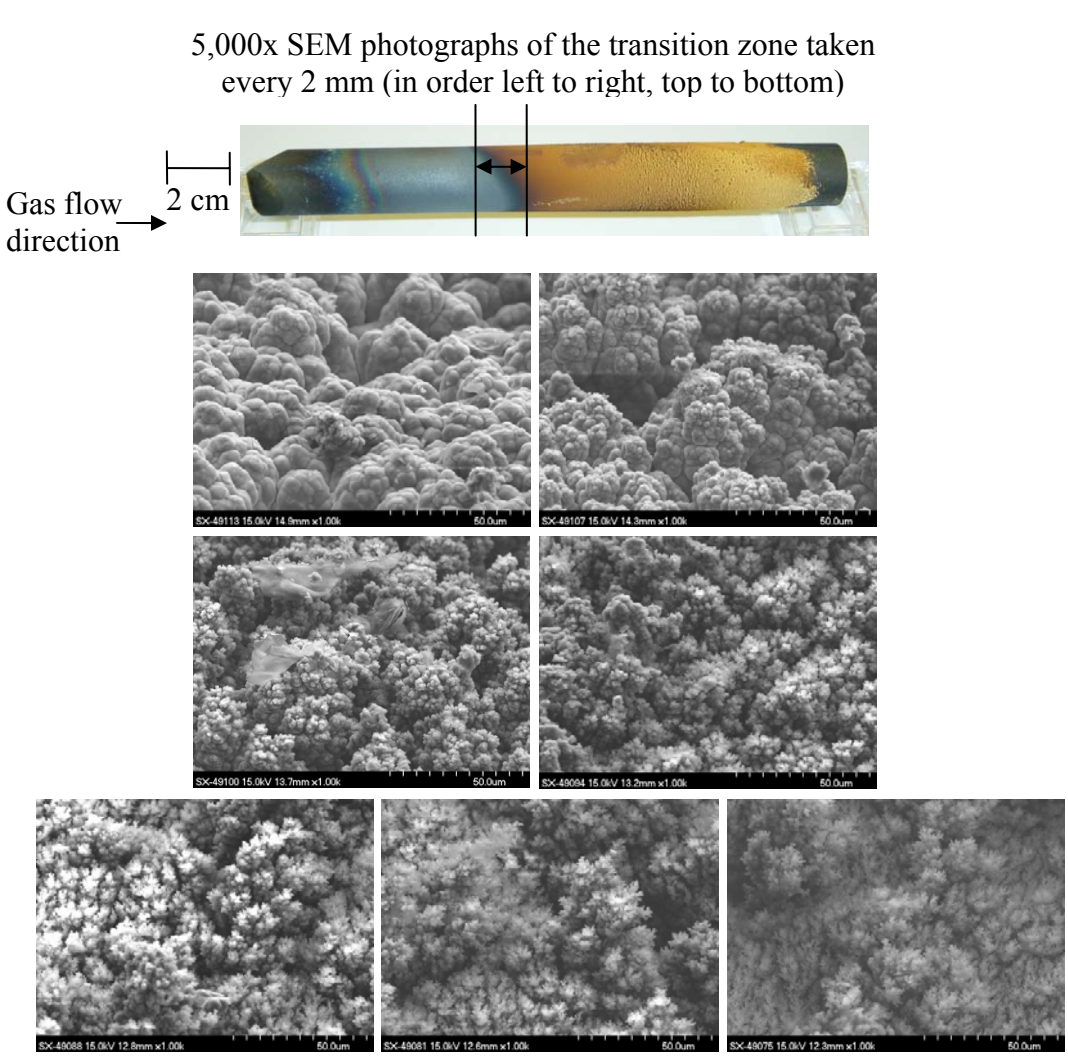

Figure 4.19. SEM micrographs, taken at a magnification of 5,000x, of the coating surface taken every two millimeters (in order left to right, top to bottom) in the transition zone of specimen number AFCI-SiC-1.

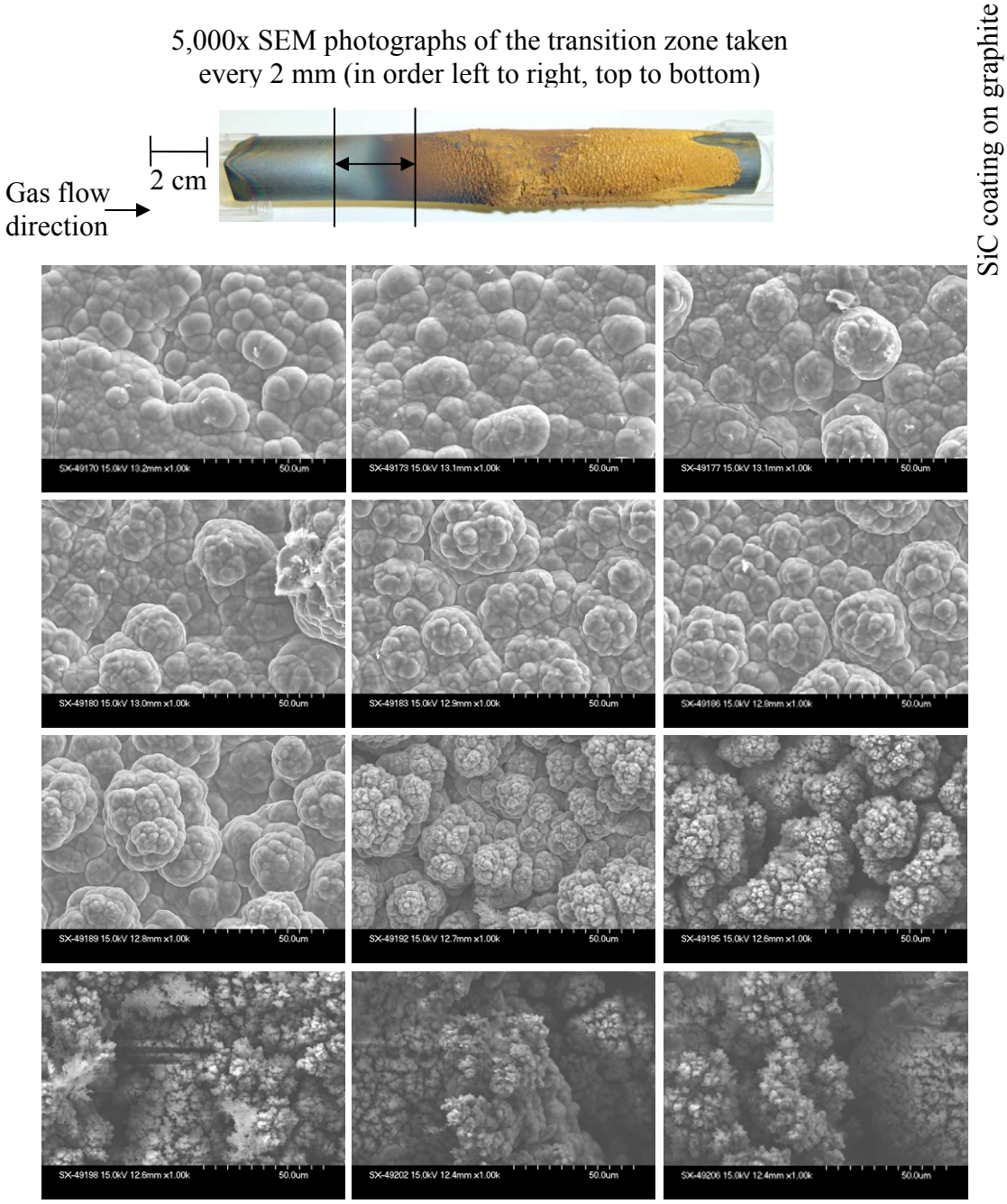

Figure 4.20. SEM micrographs, taken at a magnification of 5,000x, of the coating surface taken every two millimeters (in order left to right, top to bottom) in the transition zone of specimen number AFCI-SiC-4.

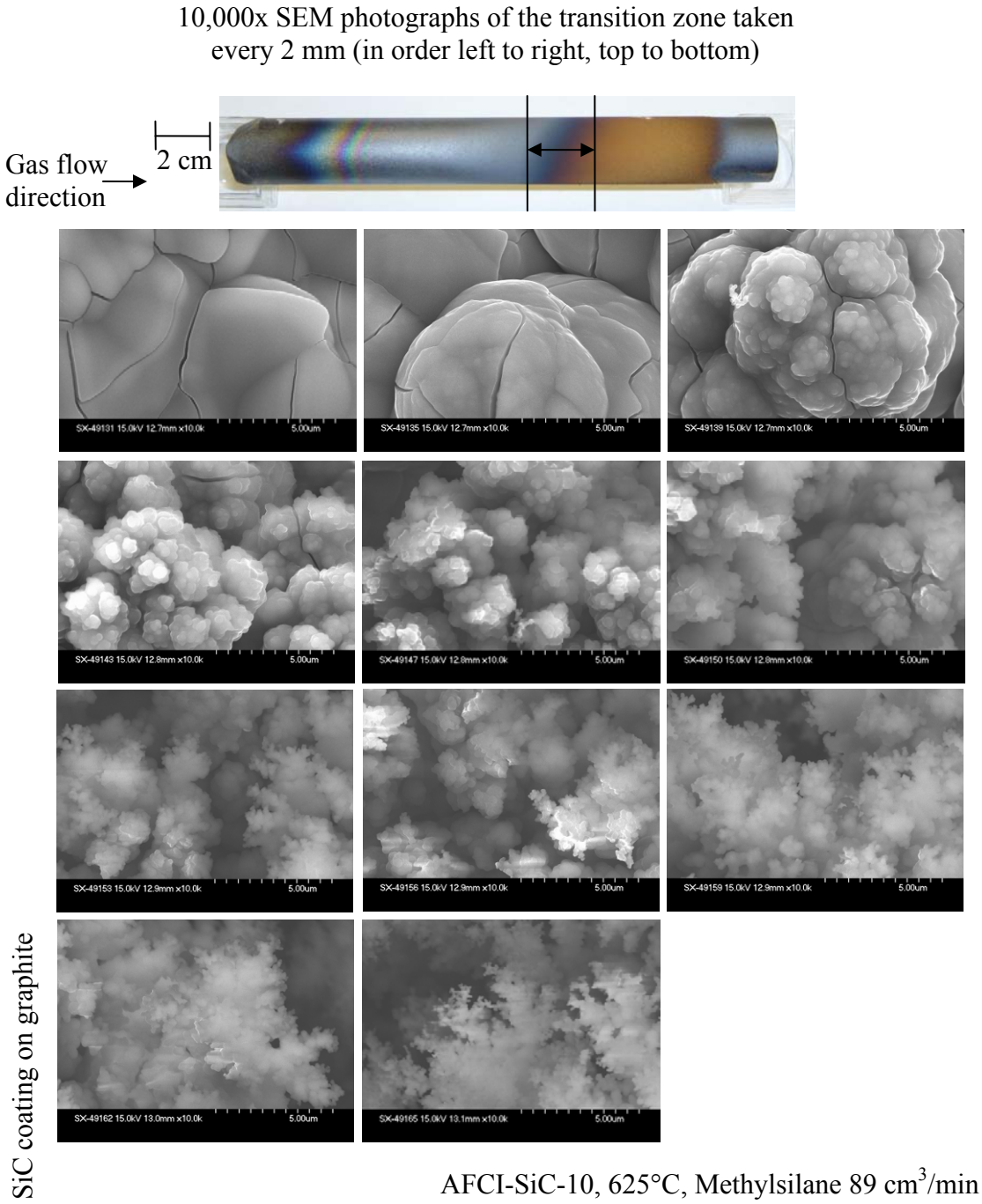

Figure 4.21. SEM micrographs, taken at a magnification of 10,000x, of the coating surface taken every two millimeters (in order left to right, top to bottom) in the transition zone of specimen number AFCI-SiC-10.

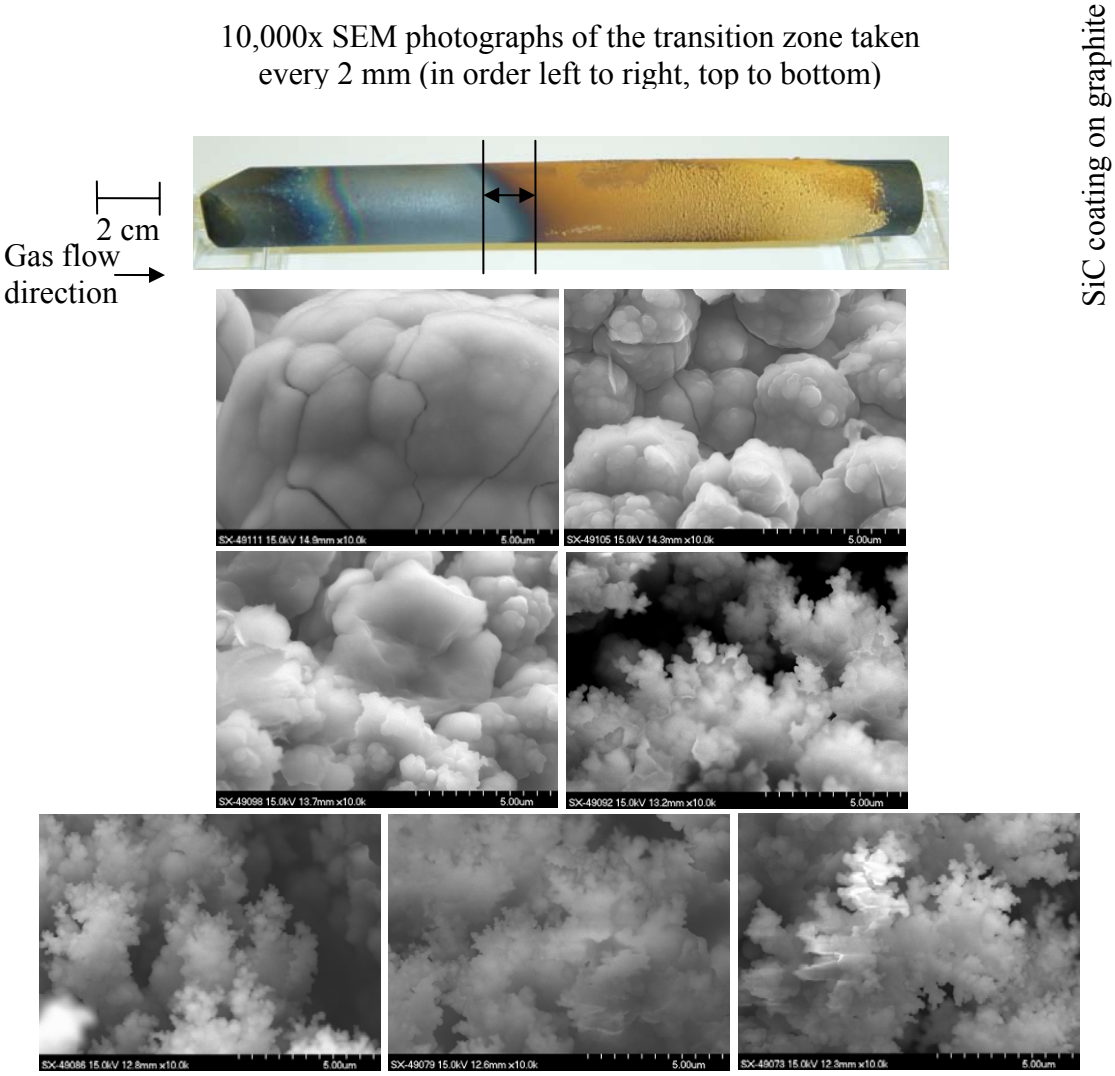

Figure 4.22. SEM micrographs, taken at a magnification of 10,000x, of the coating surface taken every two millimeters (in order left to right, top to bottom) in the transition zone of specimen number AFCI-SiC-1.

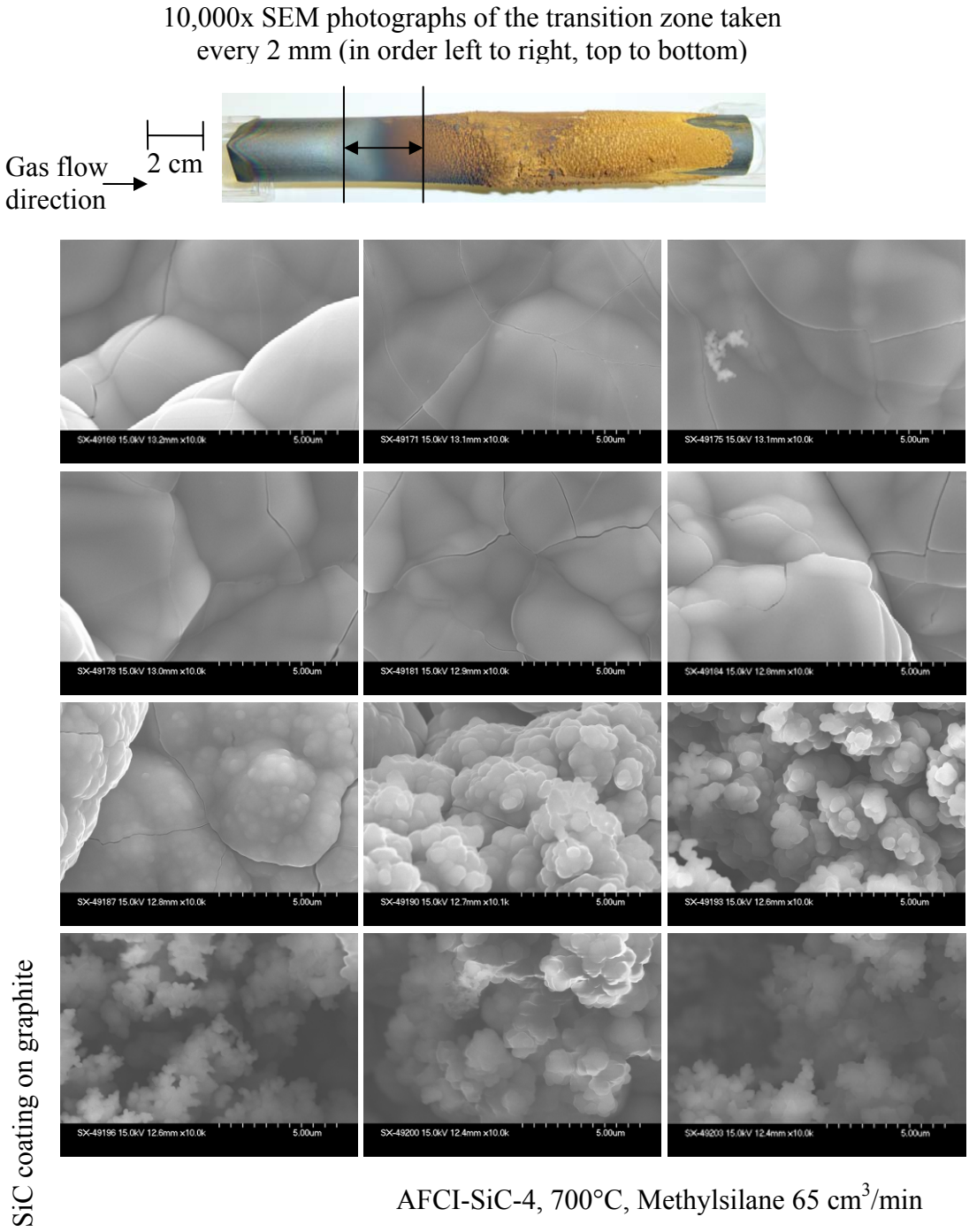

Figure 4.23. SEM micrographs, taken at a magnification of 10,000x, of the coating surface taken every two millimeters (in order left to right, top to bottom) in the transition zone of specimen number AFCI-SiC-4.

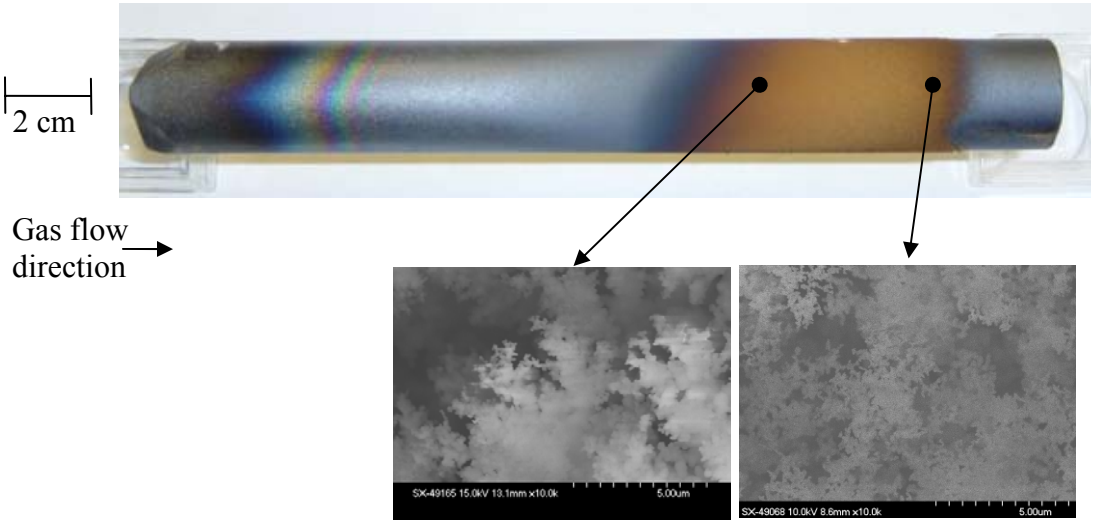

Figure 4.24. A photograph of specimen number AFCI-SiC-10 with SEM micrographs of selected areas in the homogeneous nucleation zone.

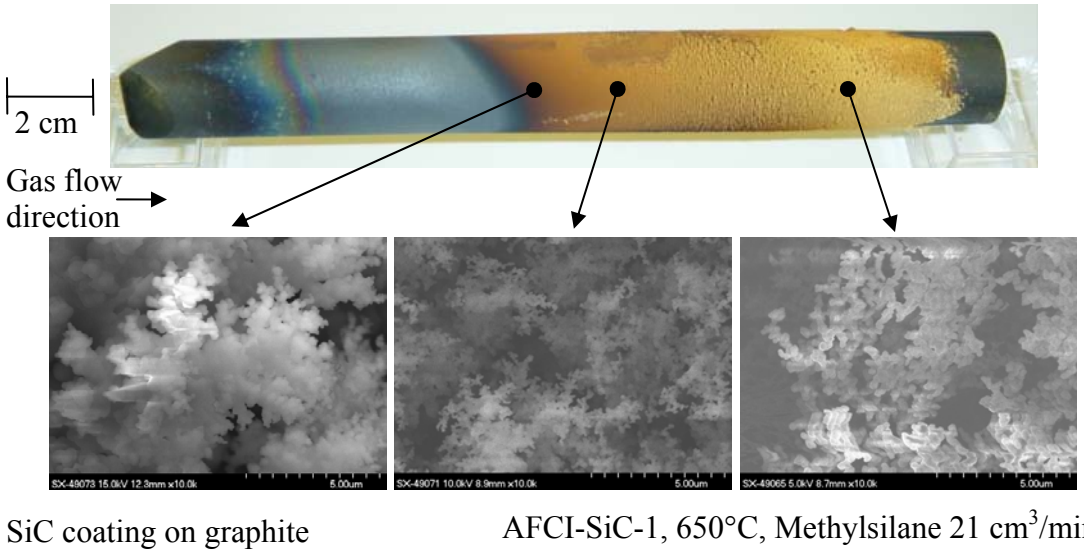

Figure 4.25. A photograph of specimen number AFCI-SiC-1 with SEM micrographs of selected areas in the homogeneous nucleation zone.

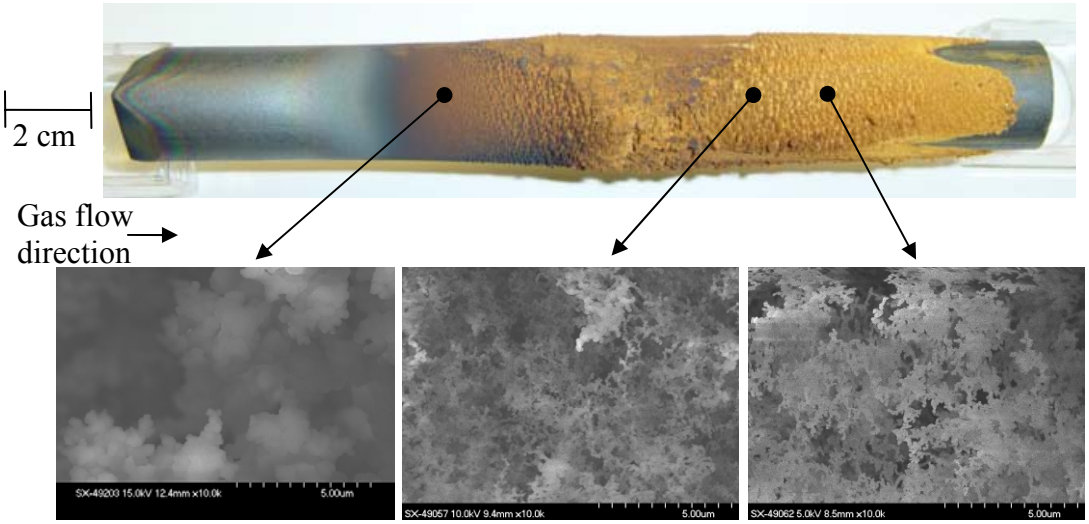

Figure 4.26. A photograph of specimen number AFCI-SiC-4 with SEM micrographs of selected areas in the homogeneous nucleation zone.

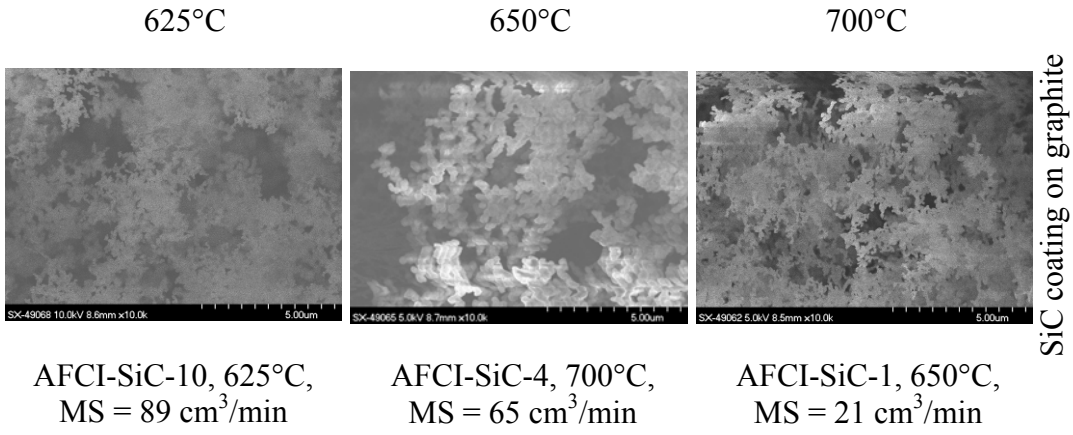

Figure 4.27. SEM micrographs taken near the down stream end of homogeneous nucleation zone of specimens AFCI-SiC-10, 4, and 1 respectively.

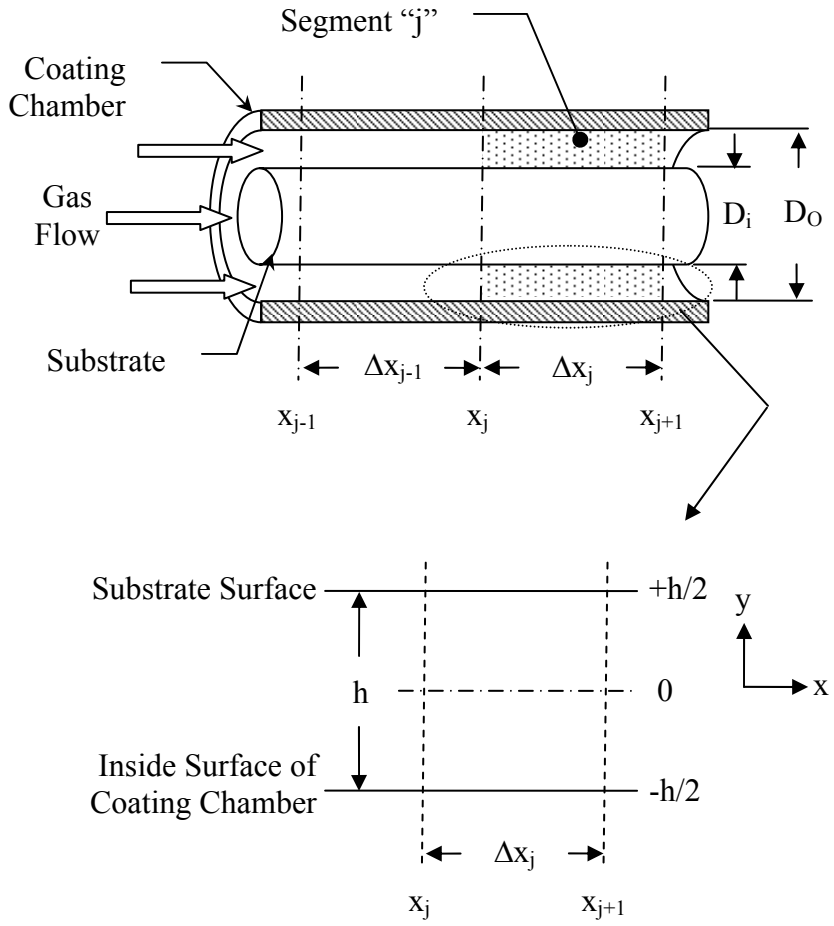

Figure 5.1. Schematic of a portion of the concentric annulus substrate demonstrating how this geometry is treated by the model as individual axial segments.

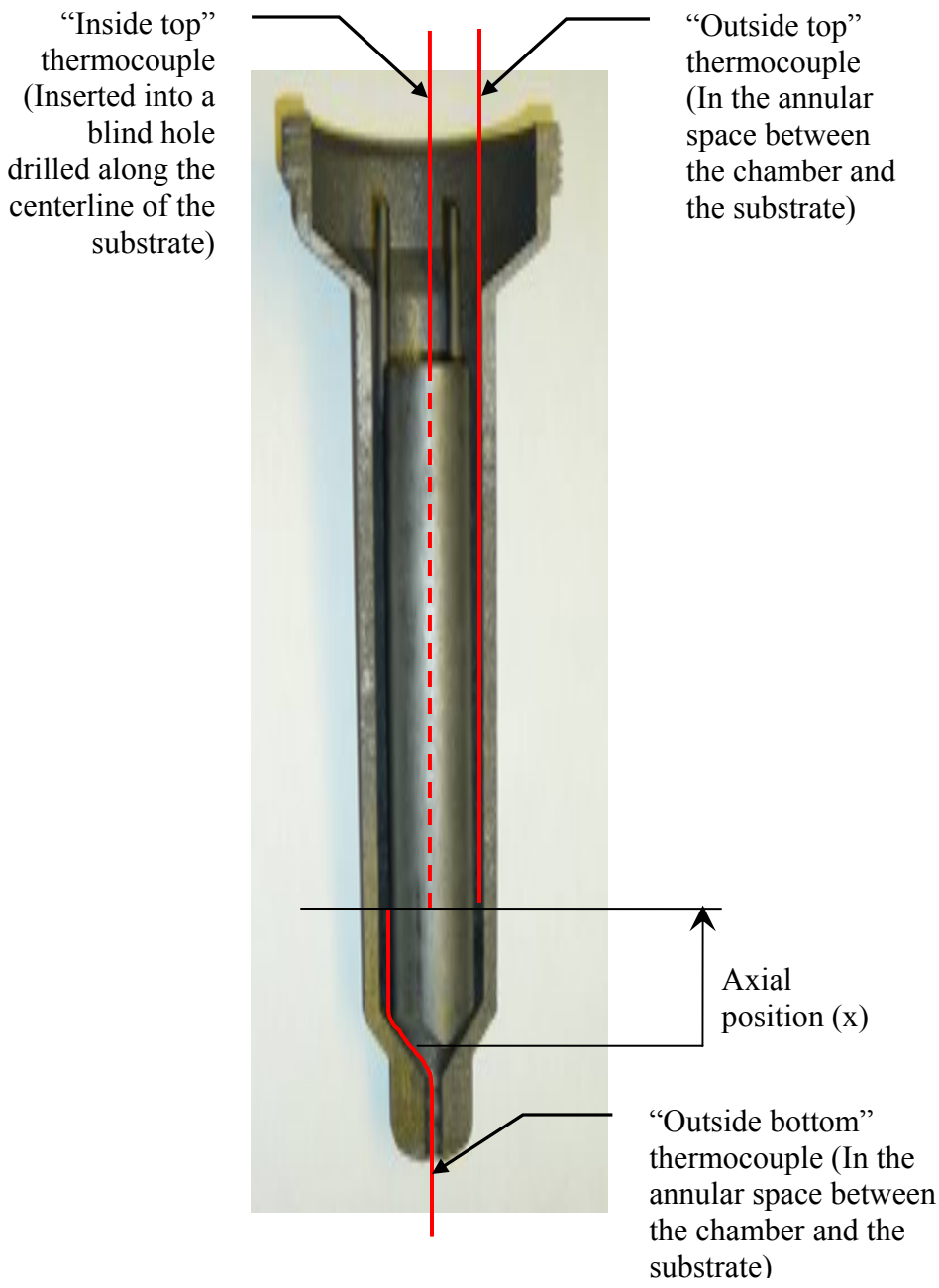

Figure 5.2. Photograph of the concentric annulus substrate with the thermocouple positions shown.

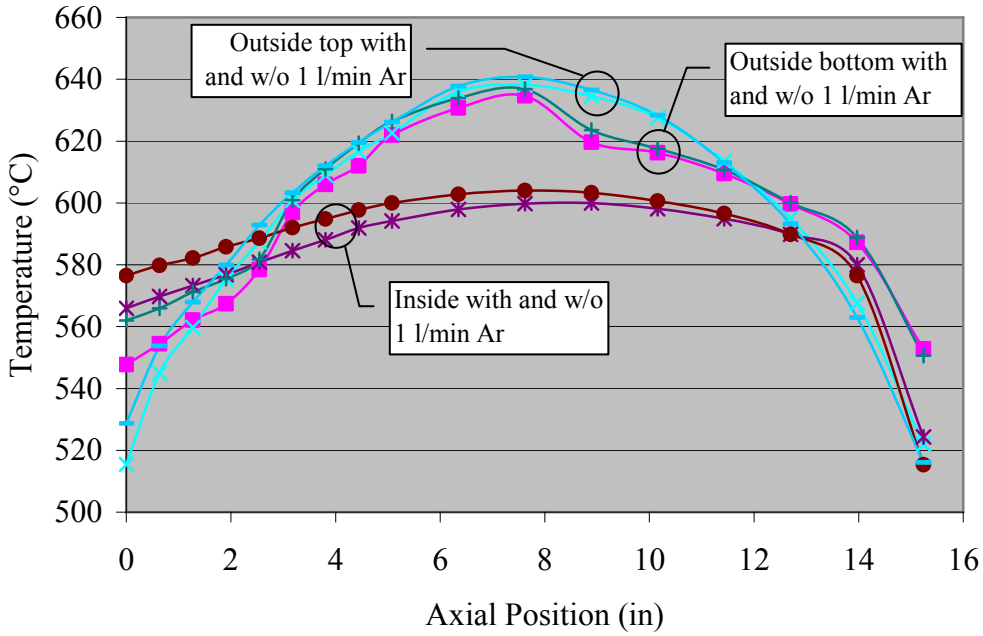

Figure 5.3. Temperature measurements for the 600°C nominal case showing the six types of temperature measurements that were made.

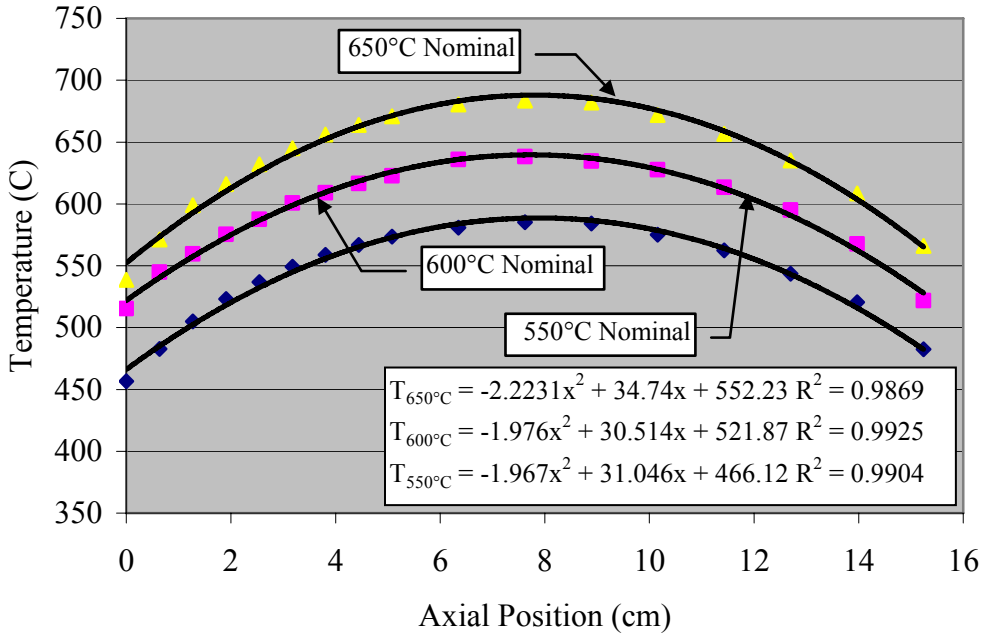

Figure 5.4. Temperature measurements and curve fits that represent the surface temperature as a function of axial position of the concentric annulus.

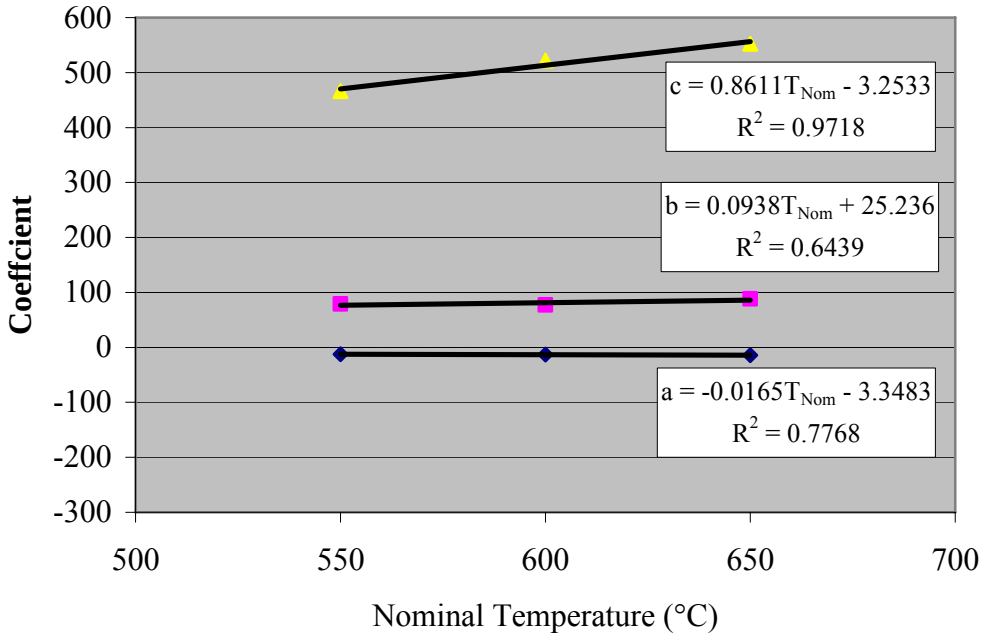

Figure 5.5. Plot of the coefficients of the curve fits of surface temperature as a function of axial position ($T_S=ax^2+bx+c$). The curve fits for the coefficients as a function of nominal temperature are also shown.

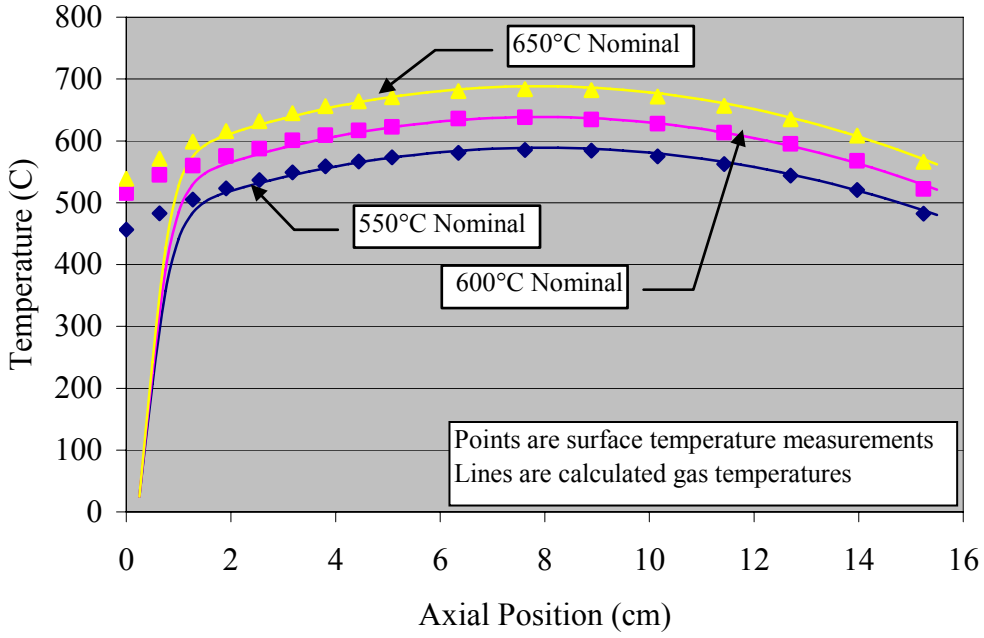

Figure 5.6. Measured surface temperature and calculated gas temperature as a function of axial position.

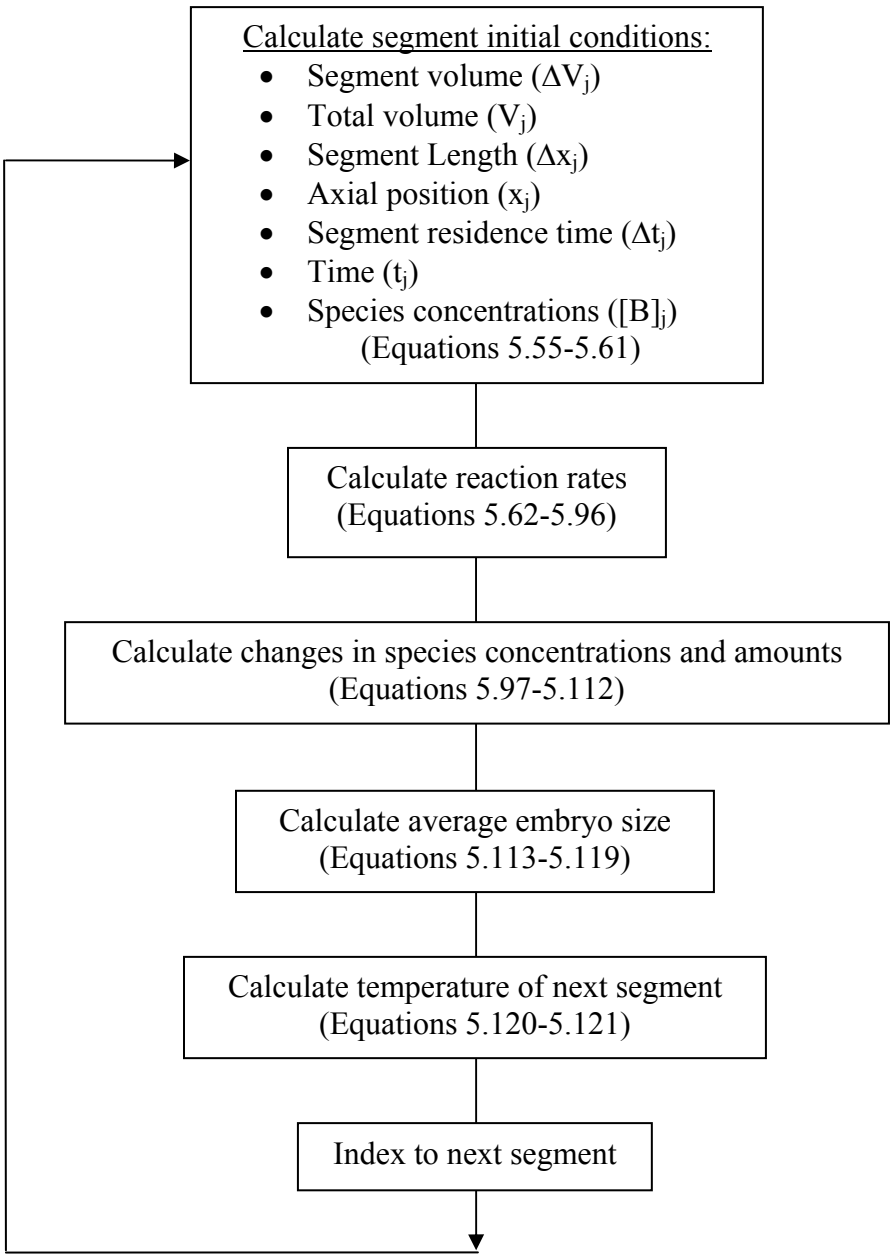

Figure 5.7. Block flow diagram of the model calculation sequence.

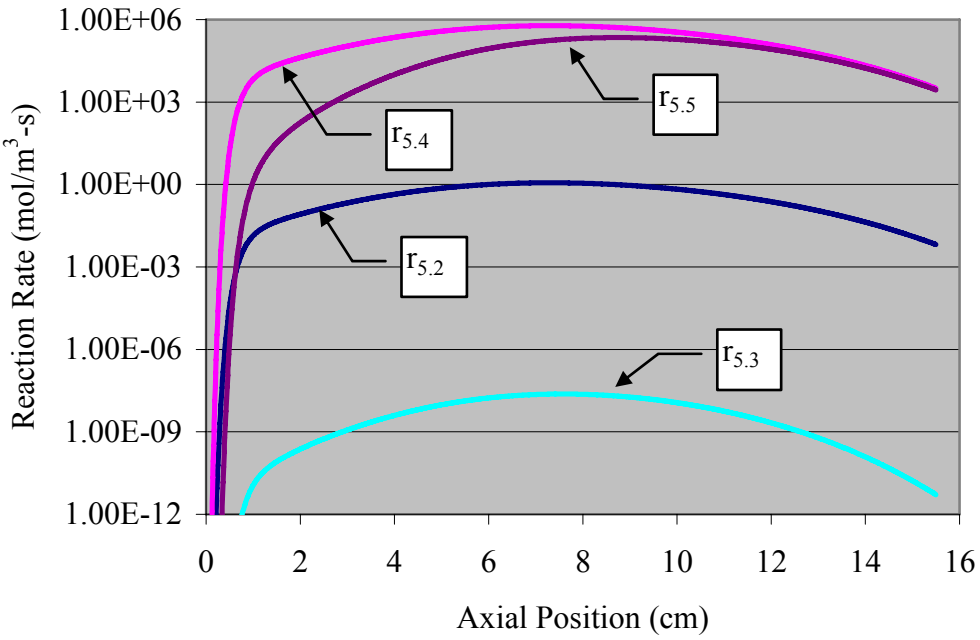

Figure 5.8. Typical rates of Reactions 5.2-5.5 demonstrating methylsilylene production via Reaction 5.2 is the rate limiting step.

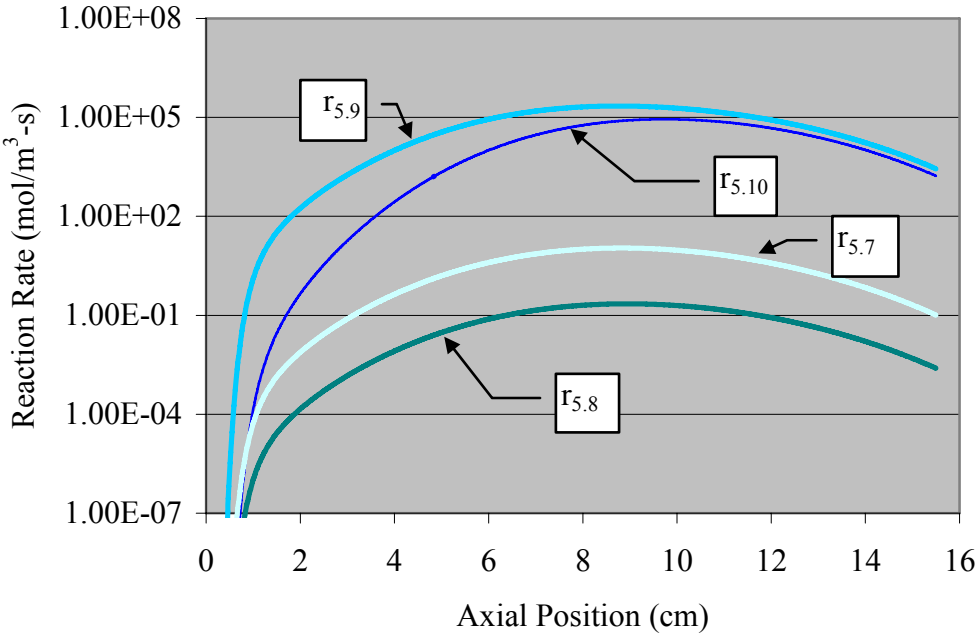

Figure 5.9. Typical rates of Reactions 5.7-5.10 demonstrating radical production via Reaction 5.7 is the rate limiting step.

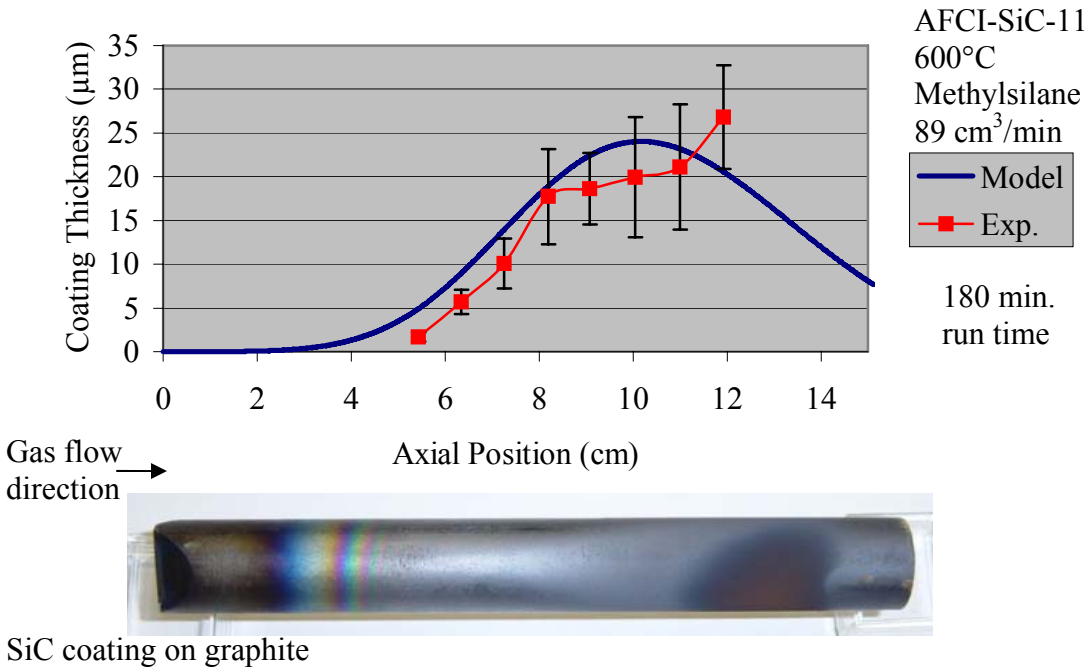

Figure 5.10. Model predicted coating thickness profile for AFCI-SiC-11 with a photograph of the specimen shown at the approximate scale of the x-axis for comparison.

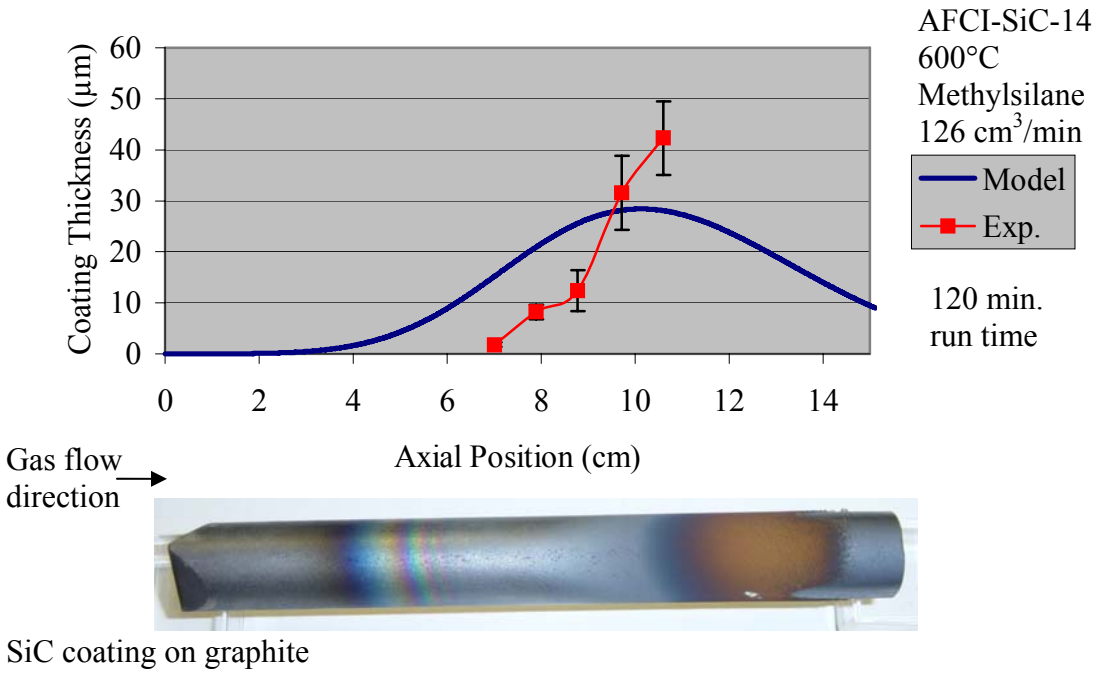

Figure 5.11. Model predicted coating thickness profile for AFCI-SiC-14 with a photograph of the specimen shown at the approximate scale of the x-axis for comparison.

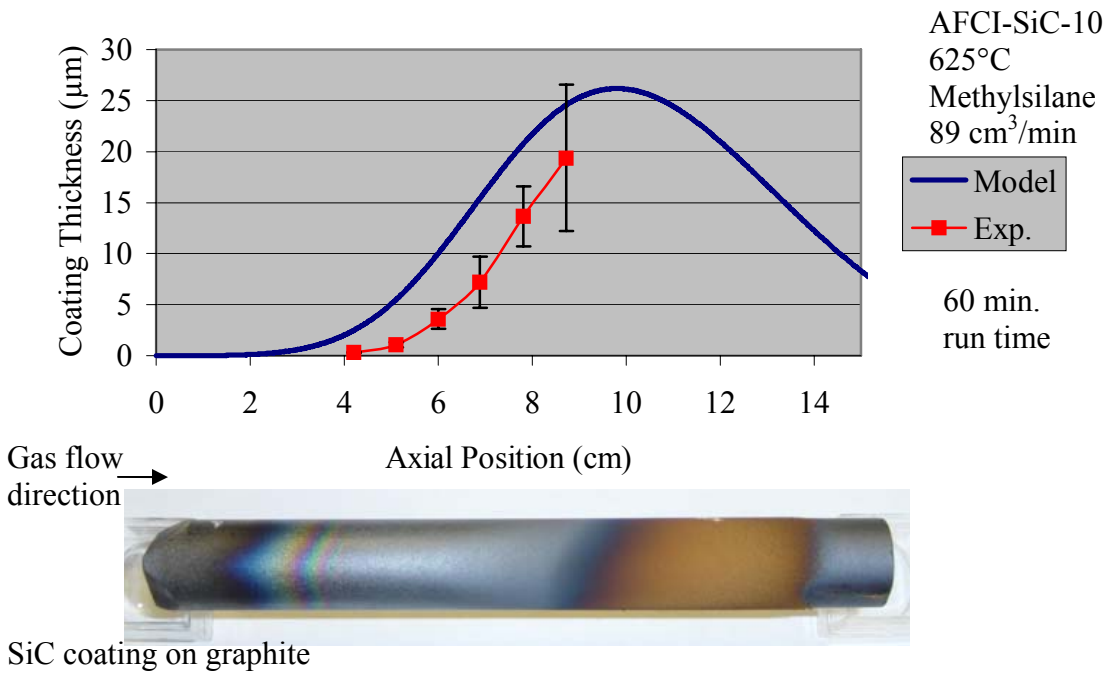

Figure 5.12. Model predicted coating thickness profile for AFCI-SiC-10 with a photograph of the specimen shown at the approximate scale of the x-axis for comparison.

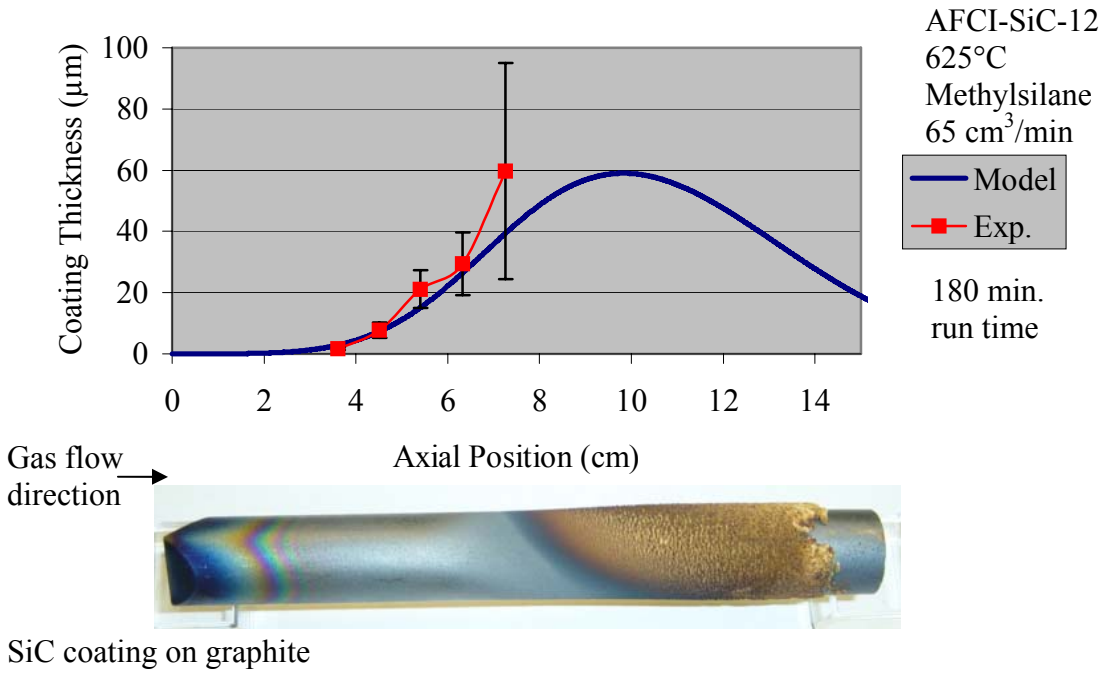

Figure 5.13. Model predicted coating thickness profile for AFCI-SiC-12 with a photograph of the specimen shown at the approximate scale of the x-axis for comparison.

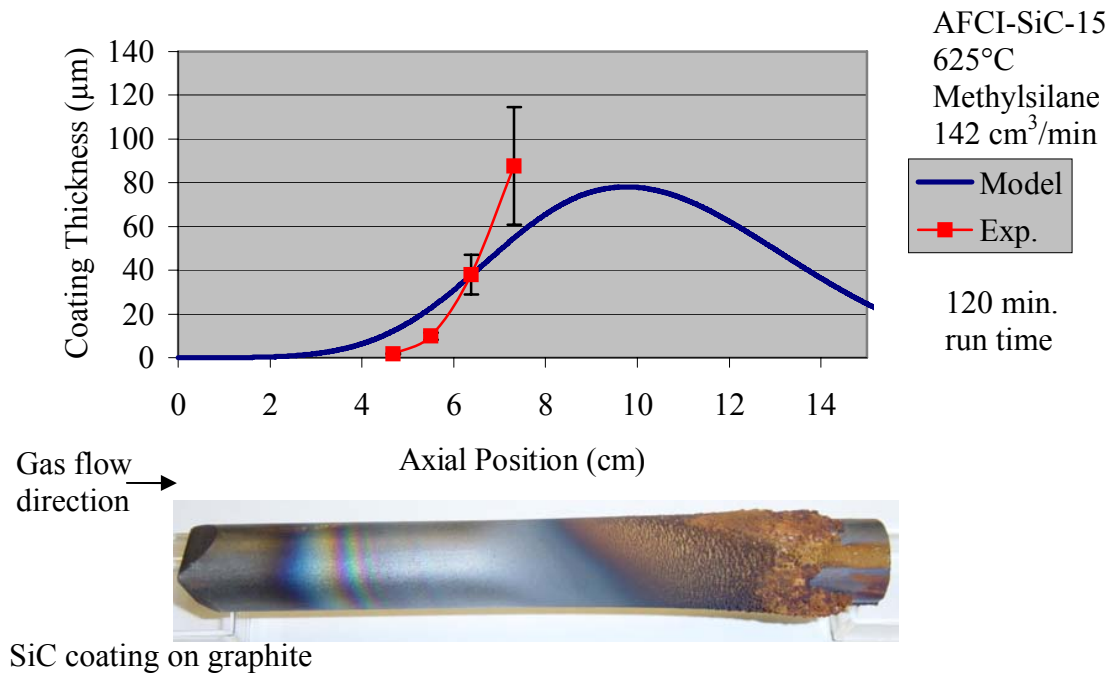

Figure 5.14. Model predicted coating thickness profile for AFCI-SiC-15 with a photograph of the specimen shown at the approximate scale of the x-axis for comparison.

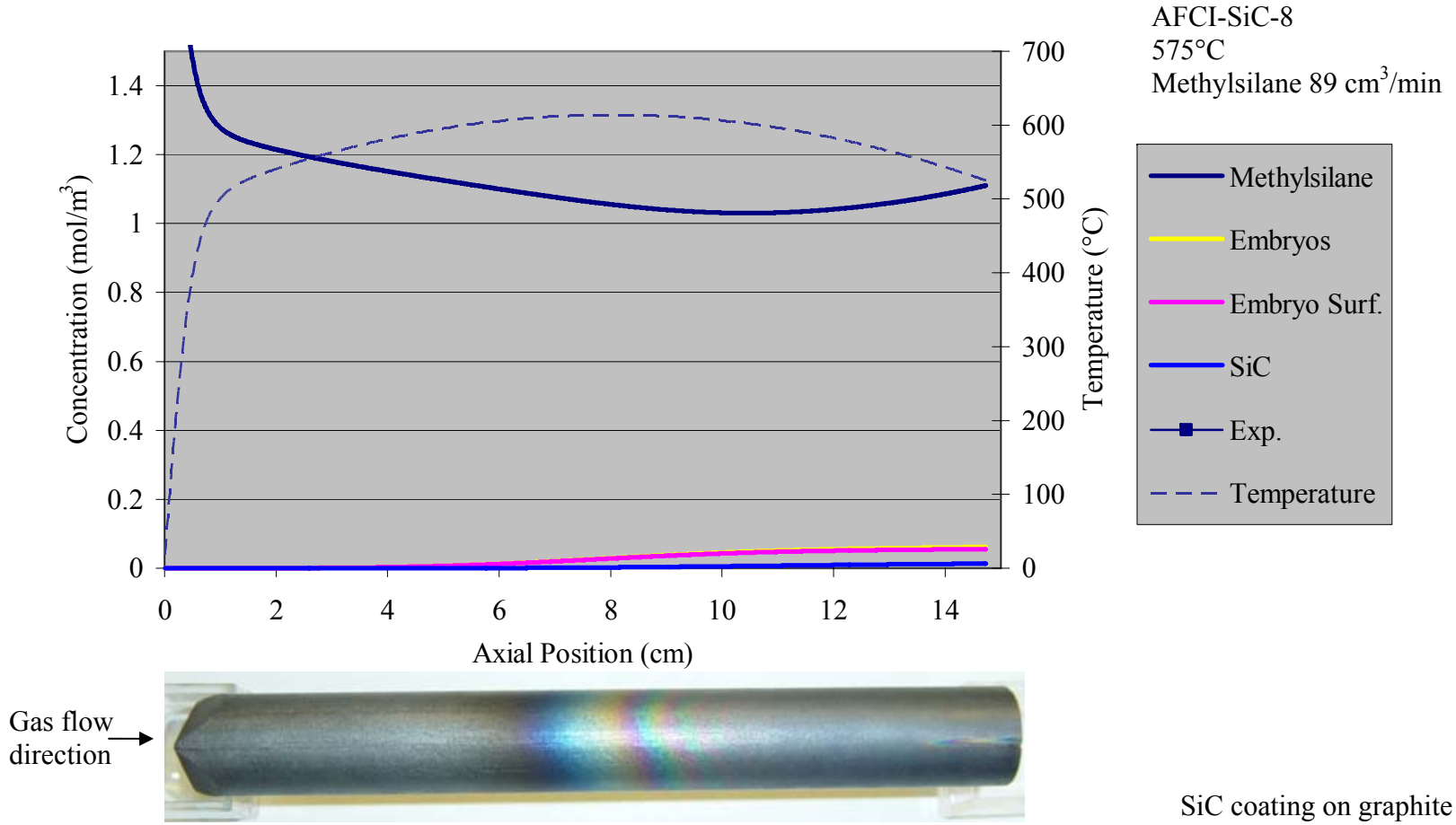

Figure 6.1. Model-predicted concentration profile for AFCI-SiC-8 with a photograph of the specimen shown at the approximate scale of the x-axis for comparison.

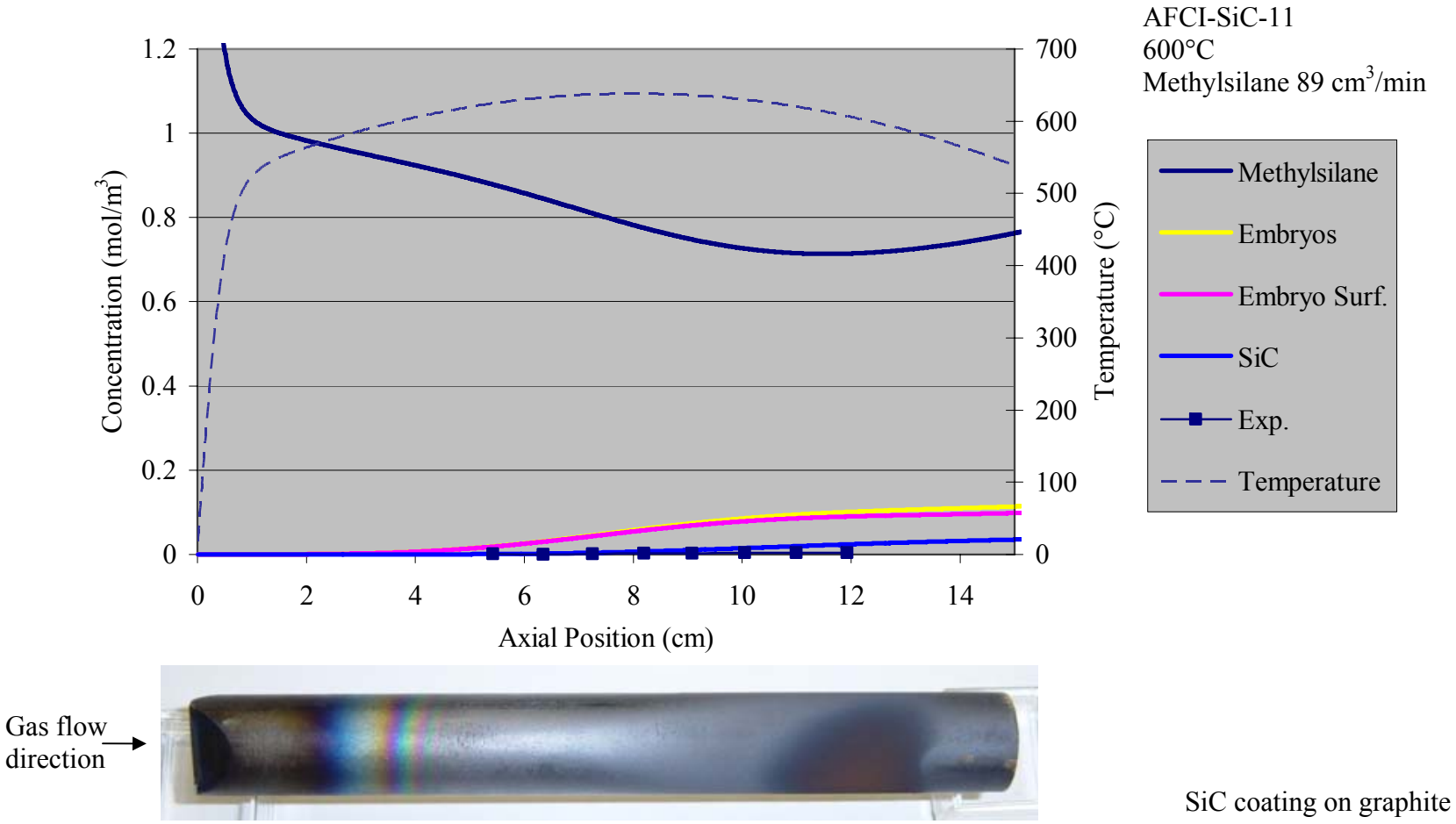

Figure 6.2. Model-predicted concentration profile for AFCI-SiC-11 with a photograph of the specimen shown at the approximate scale of the x-axis for comparison.

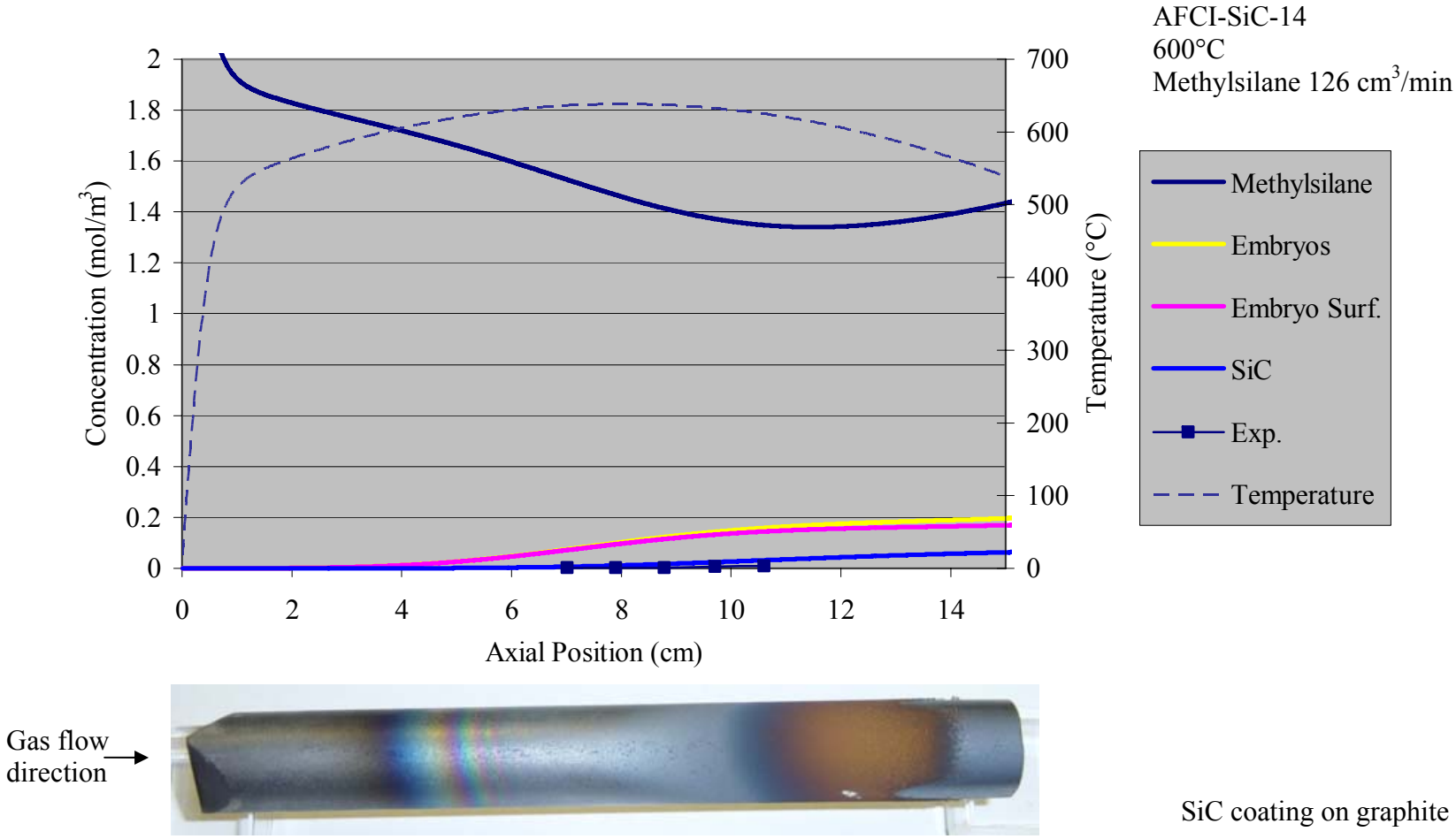

Figure 6.3. Model-predicted concentration profile for AFCI-SiC-14 with a photograph of the specimen shown at the approximate scale of the x-axis for comparison.

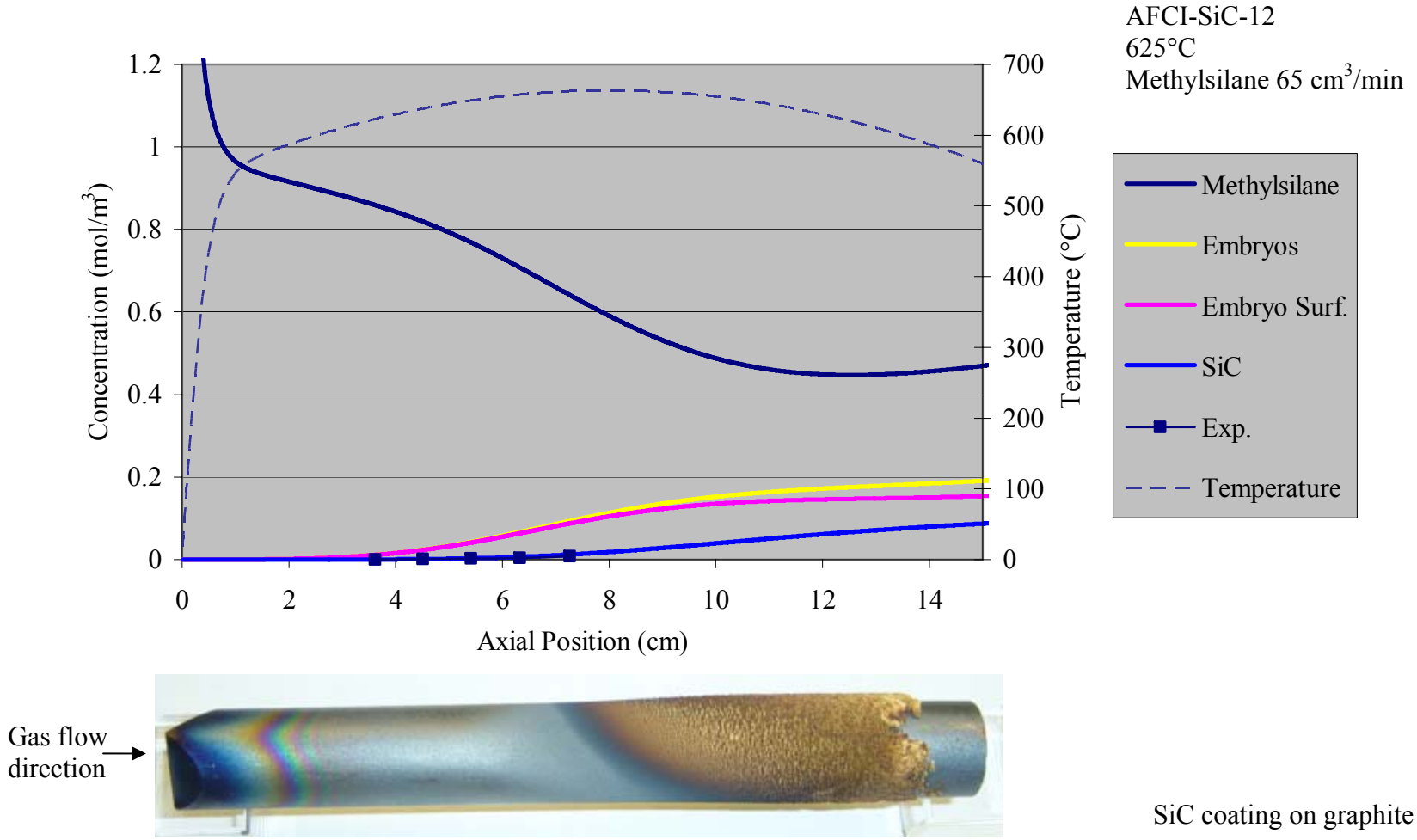

Figure 6.4. Model-predicted concentration profile for AFCI-SiC-12 with a photograph of the specimen shown at the approximate scale of the x-axis for comparison.

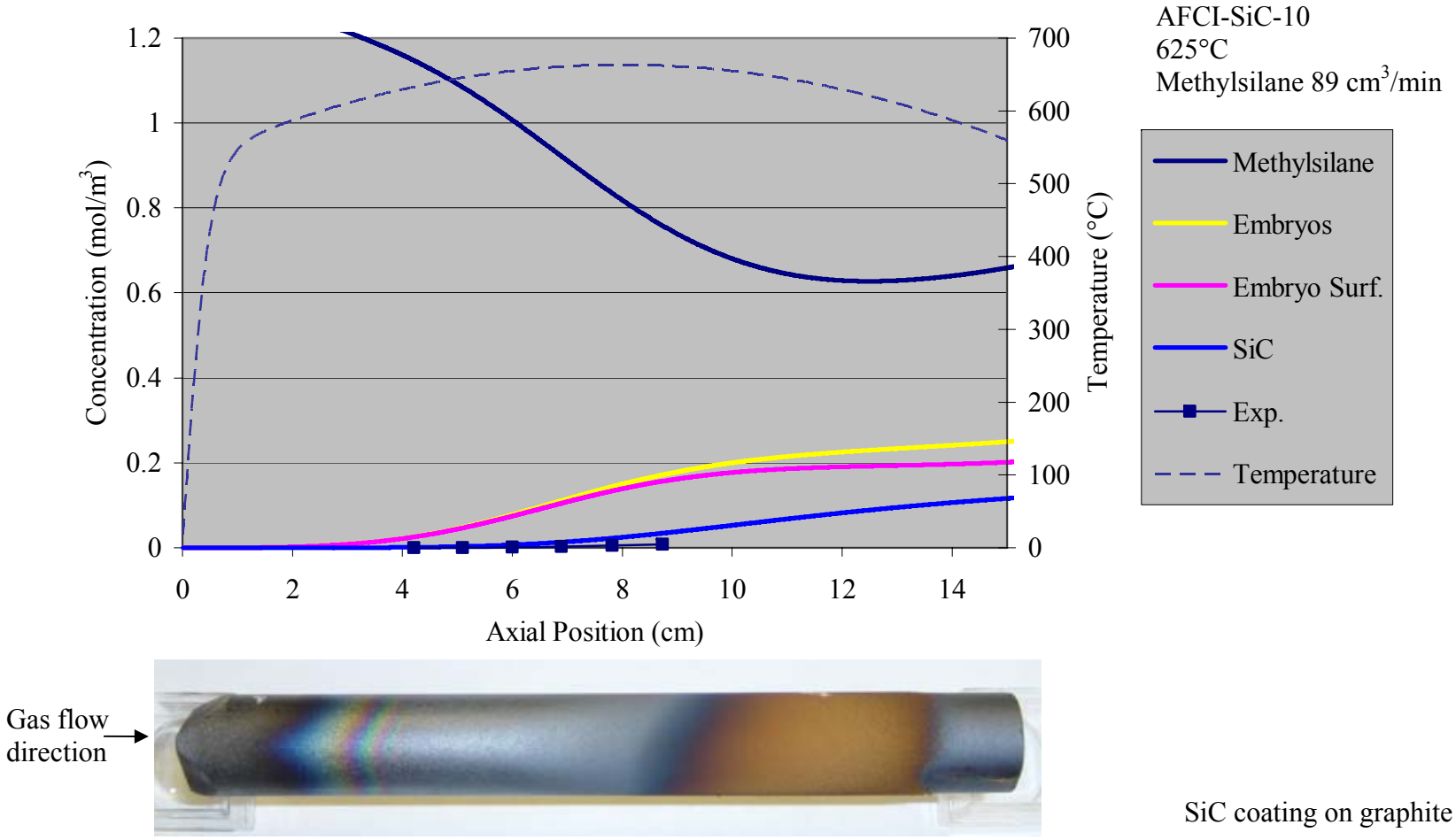

Figure 6.5. Model-predicted concentration profile for AFCI-SiC-10 with a photograph of the specimen shown at the approximate scale of the x-axis for comparison.

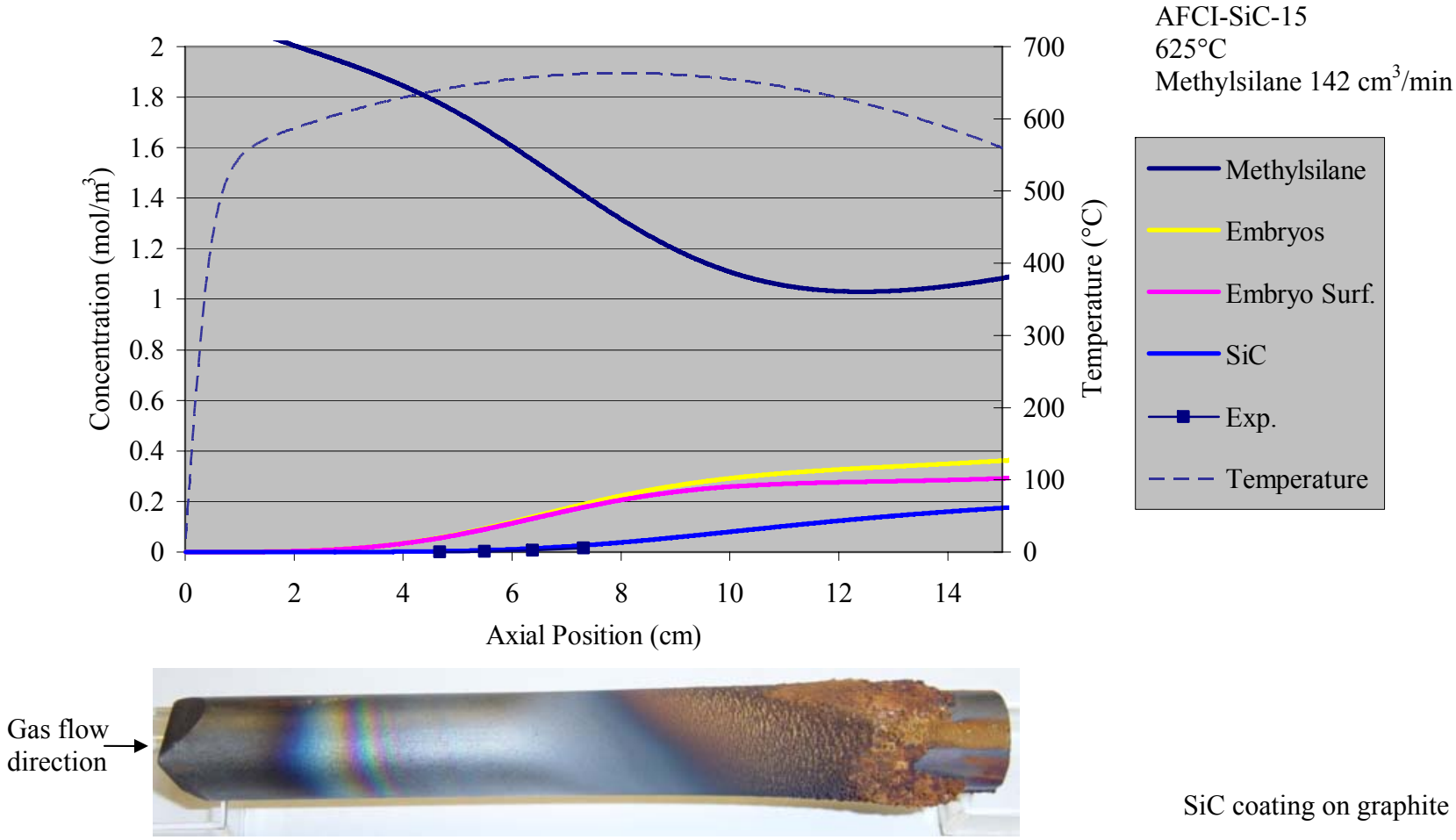

Figure 6.6. Model-predicted concentration profile for AFCI-SiC-15 with a photograph of the specimen shown at the approximate scale of the x-axis for comparison.

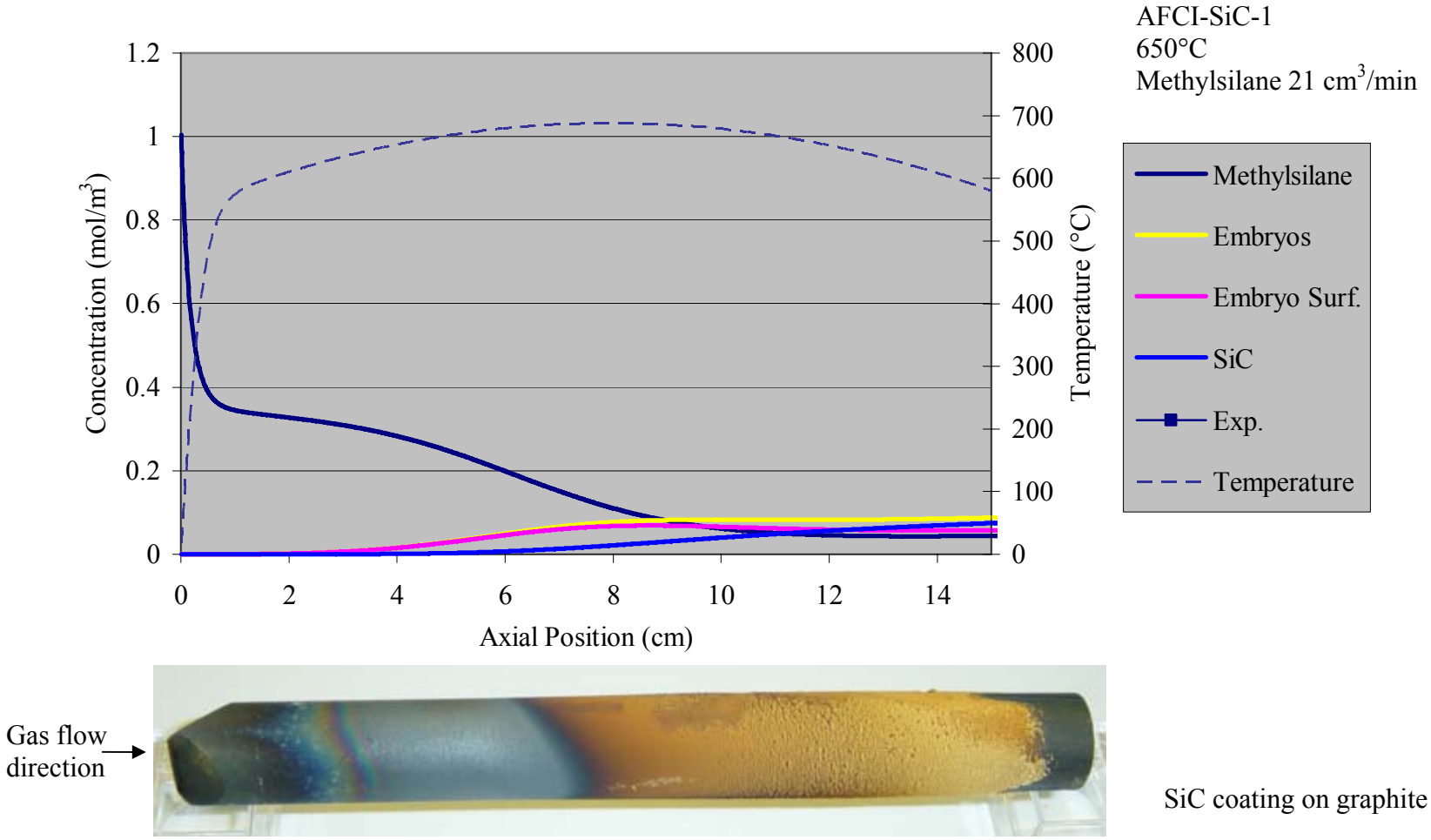

Figure 6.7. Model-predicted concentration profile for AFCI-SiC-1 with a photograph of the specimen shown at the approximate scale of the x-axis for comparison.

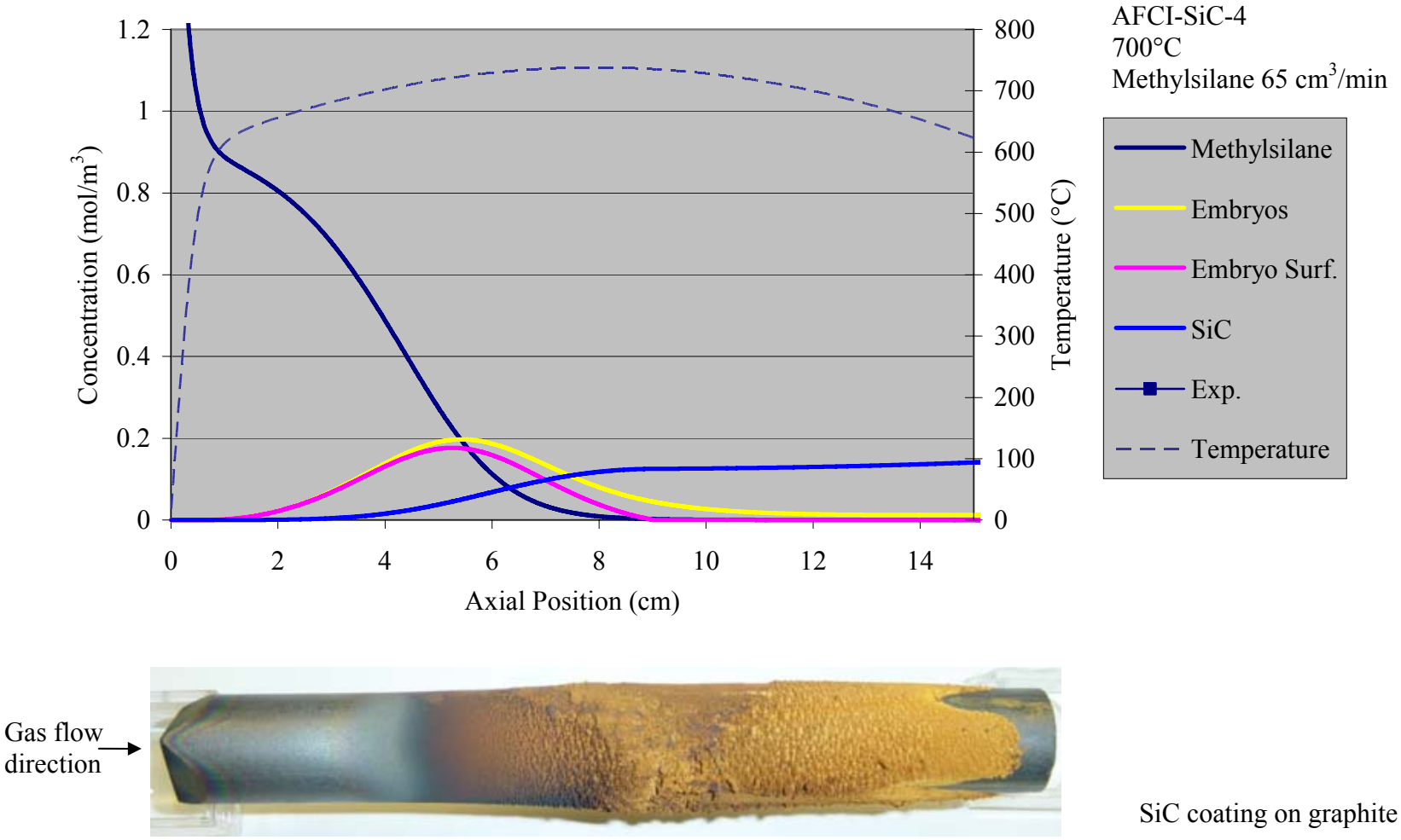

Figure 6.8. Model-predicted concentration profile for AFCI-SiC-4 with a photograph of the specimen shown at the approximate scale of the x-axis for comparison.

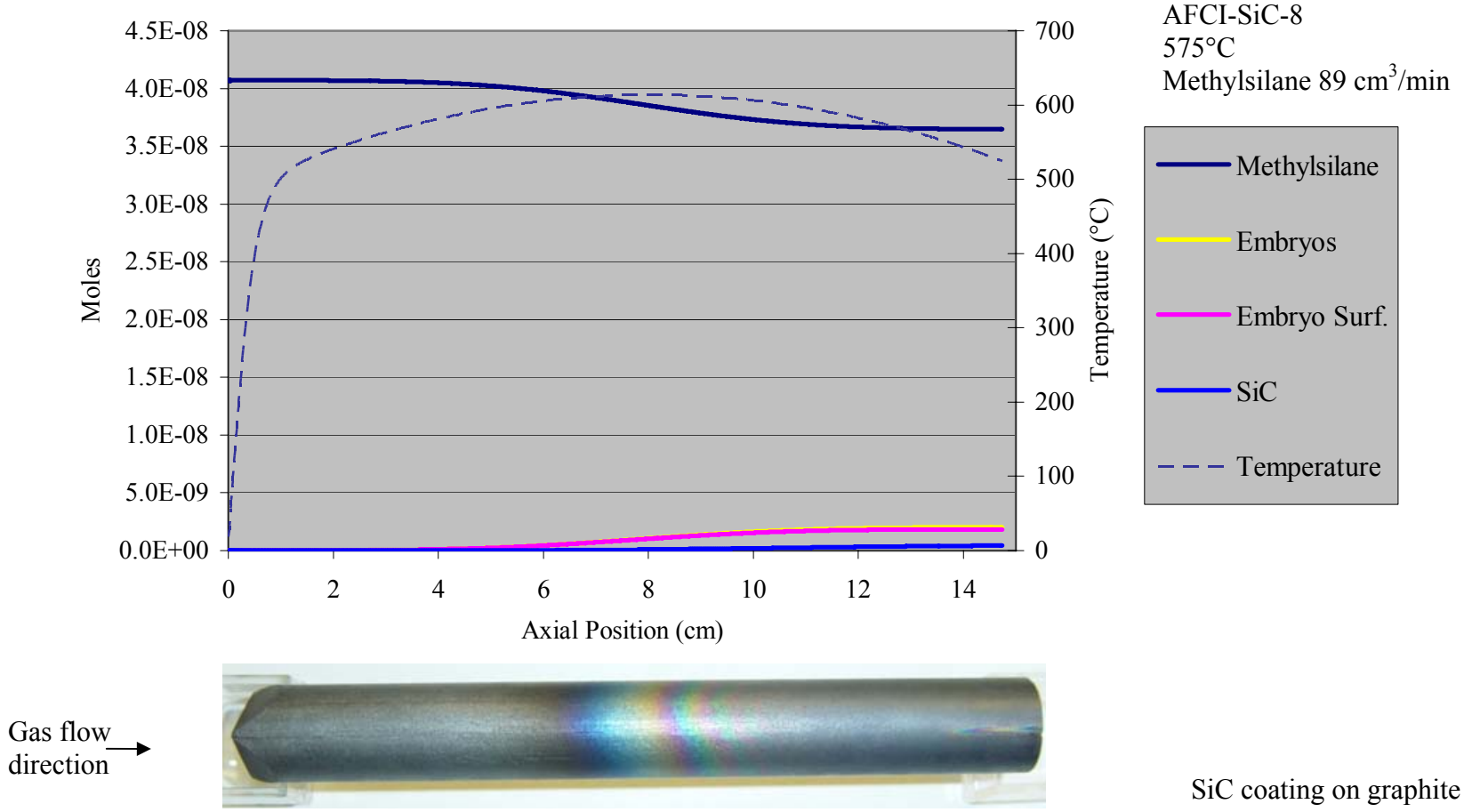

Figure 6.9. Model-predicted profile of the molar amounts of species for AFCI-SiC-8 with a photograph of the specimen shown at the approximate scale of the x-axis for comparison.

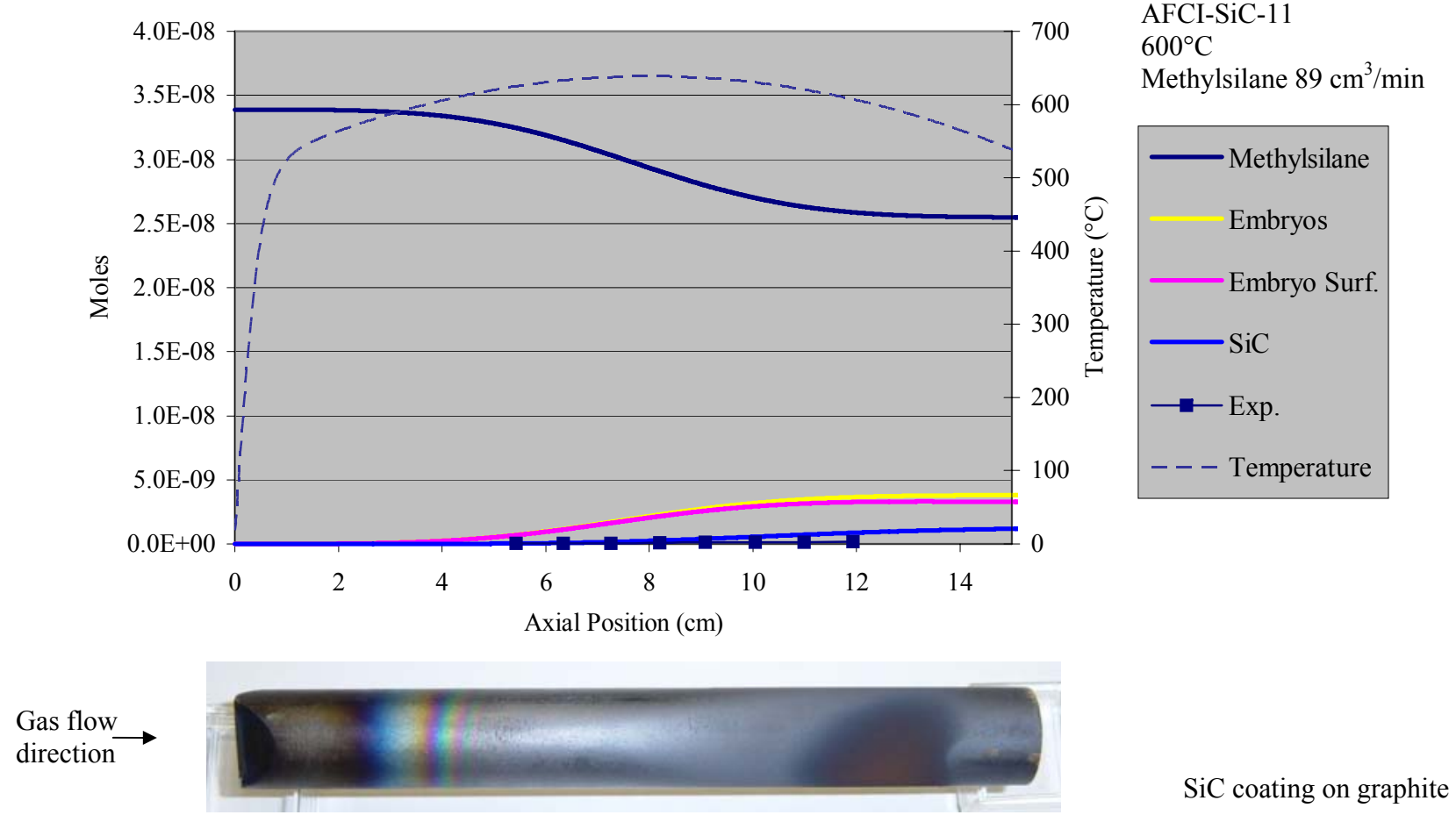

Figure 6.10. Model-predicted profile of the molar amounts of species for AFCI-SiC-11 with a photograph of the specimen shown at the approximate scale of the x-axis for comparison.

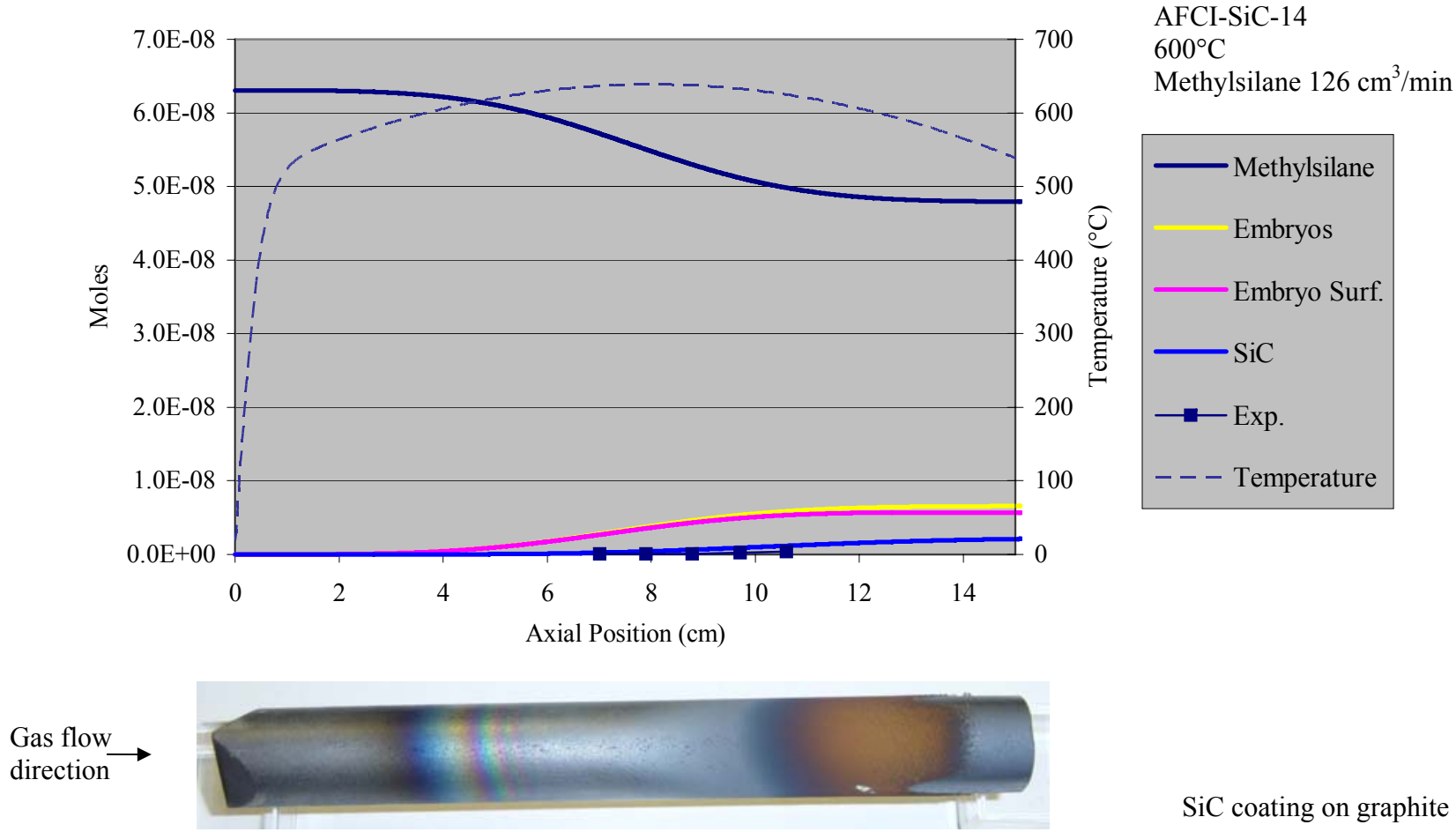

Figure 6.11. Model-predicted profile of the molar amounts of species for AFCI-SiC-14 with a photograph of the specimen shown at the approximate scale of the x-axis for comparison.

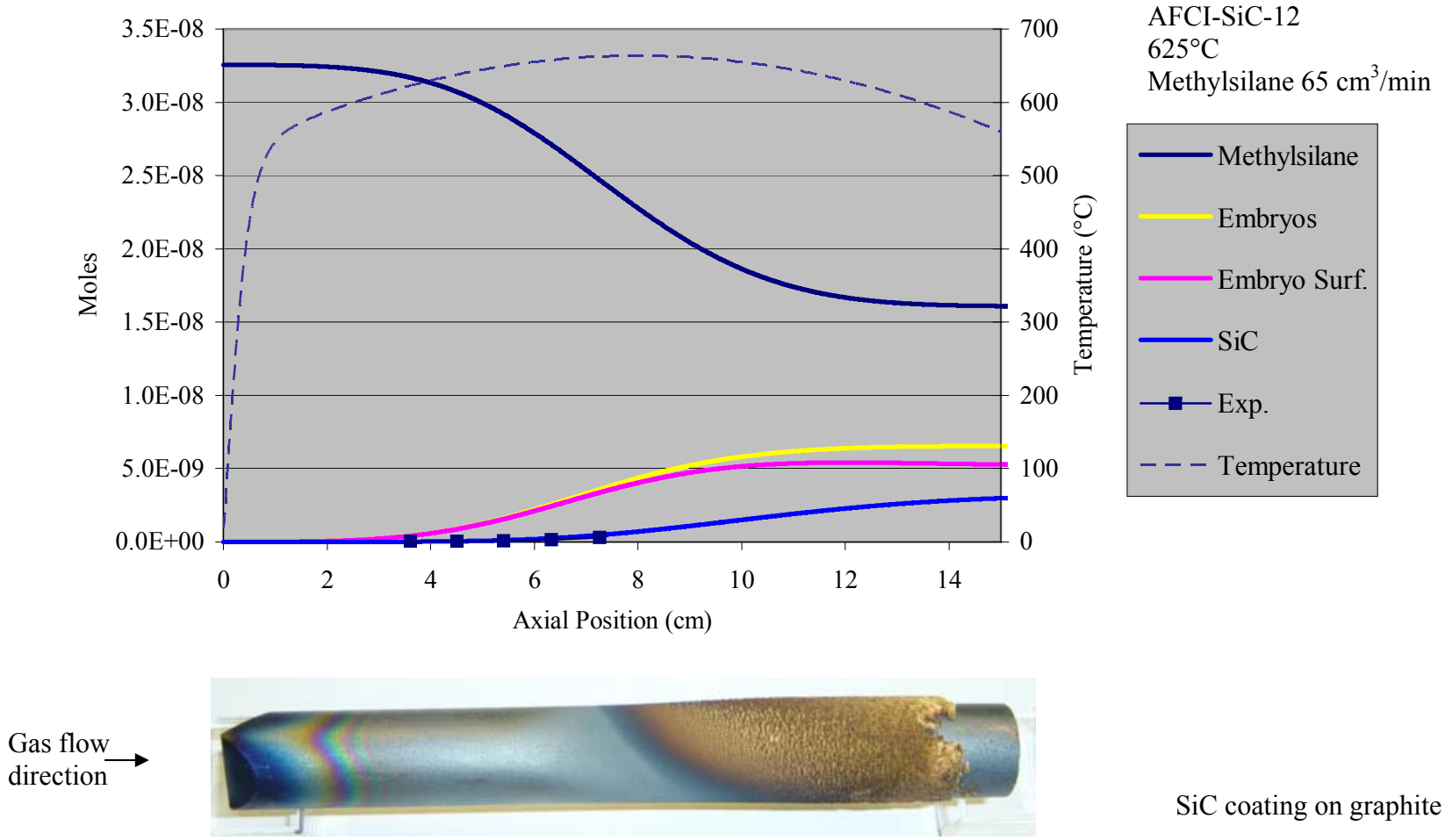

Figure 6.12. Model-predicted profile of the molar amounts of species for AFCI-SiC-12 with a photograph of the specimen shown at the approximate scale of the x-axis for comparison.

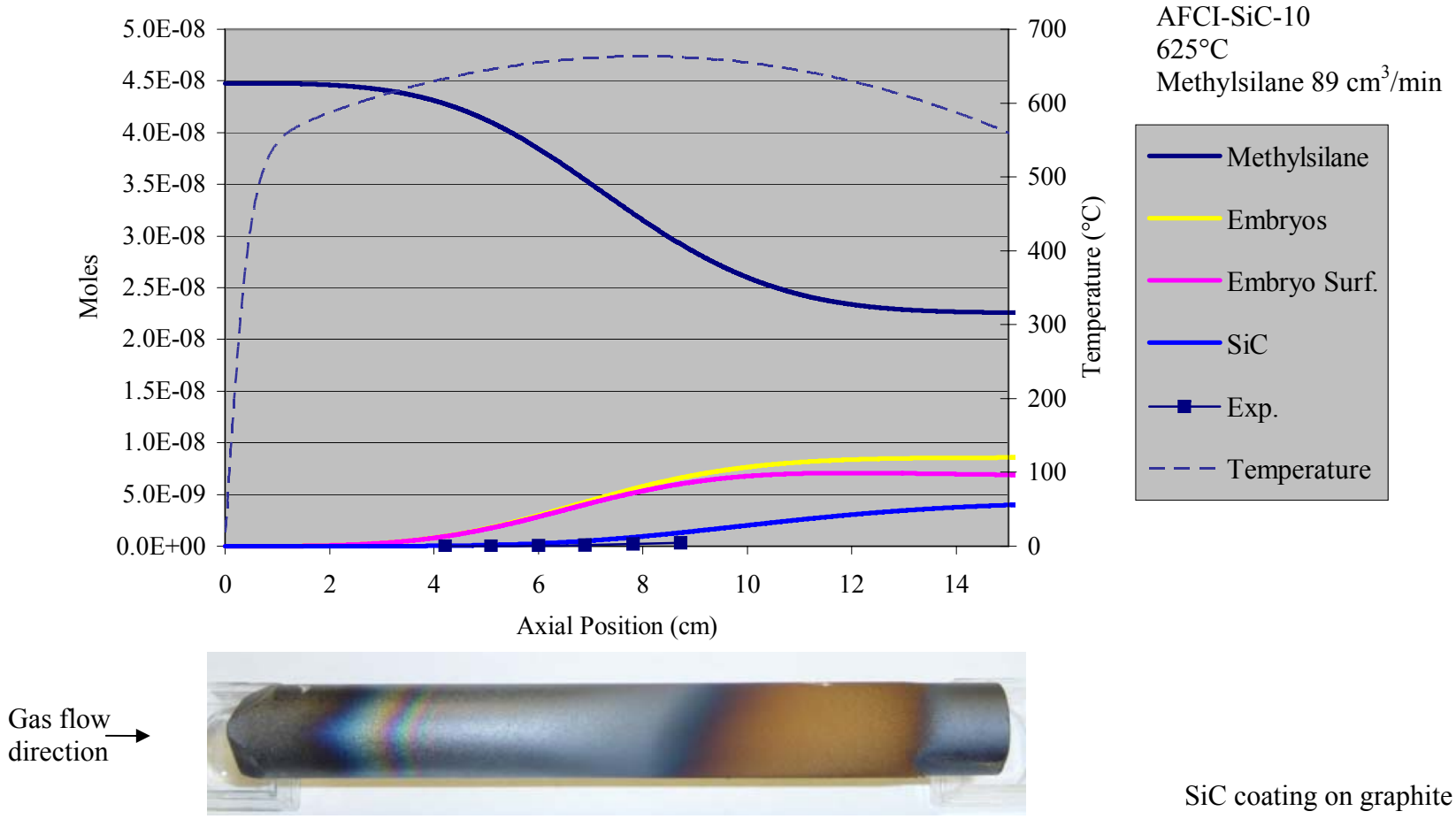

Figure 6.13. Model-predicted profile of the molar amounts of species for AFCI-SiC-10 with a photograph of the specimen shown at the approximate scale of the x-axis for comparison.

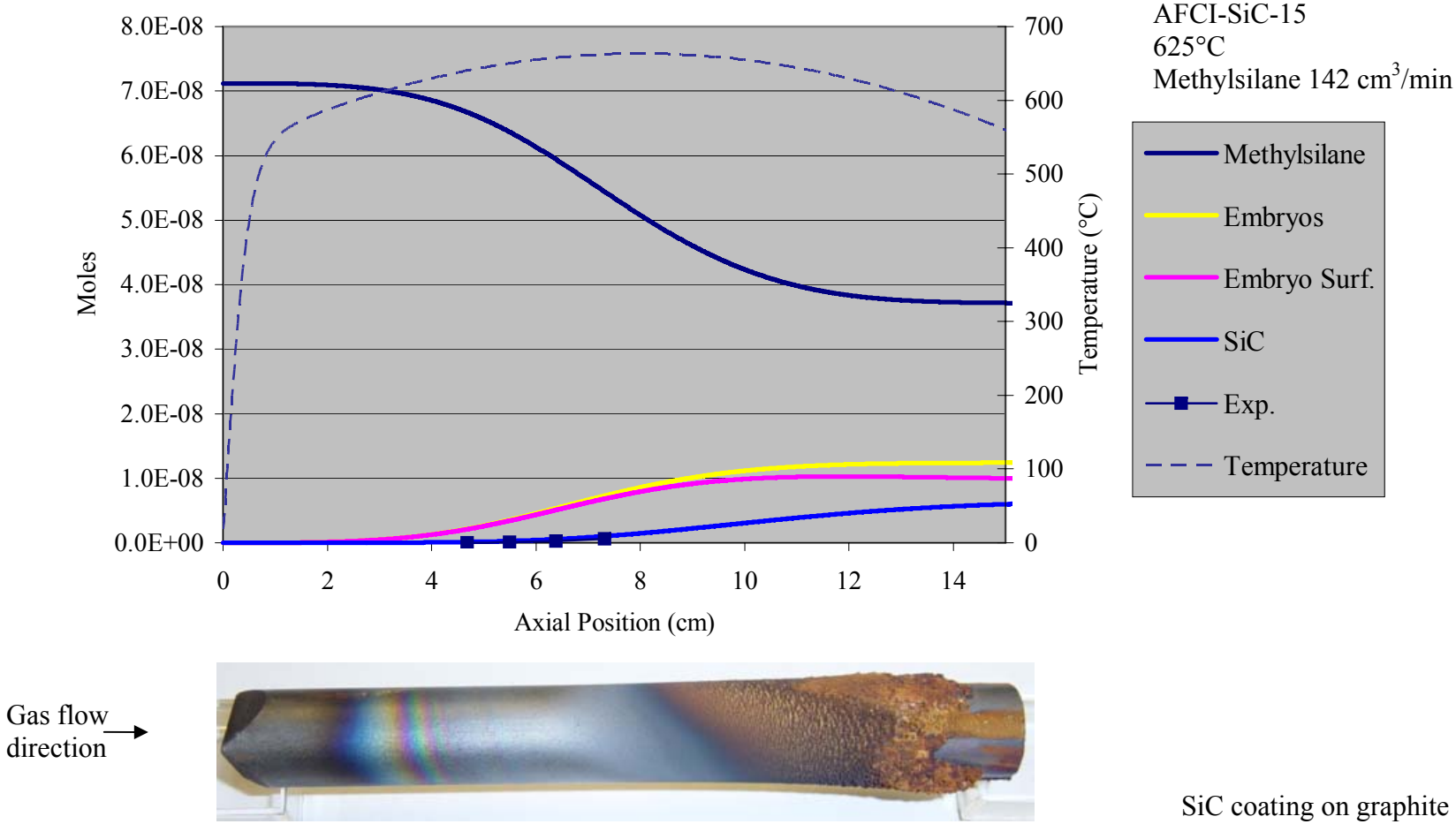

Figure 6.14. Model-predicted profile of the molar amounts of species for AFCI-SiC-15 with a photograph of the specimen shown at the approximate scale of the x-axis for comparison.

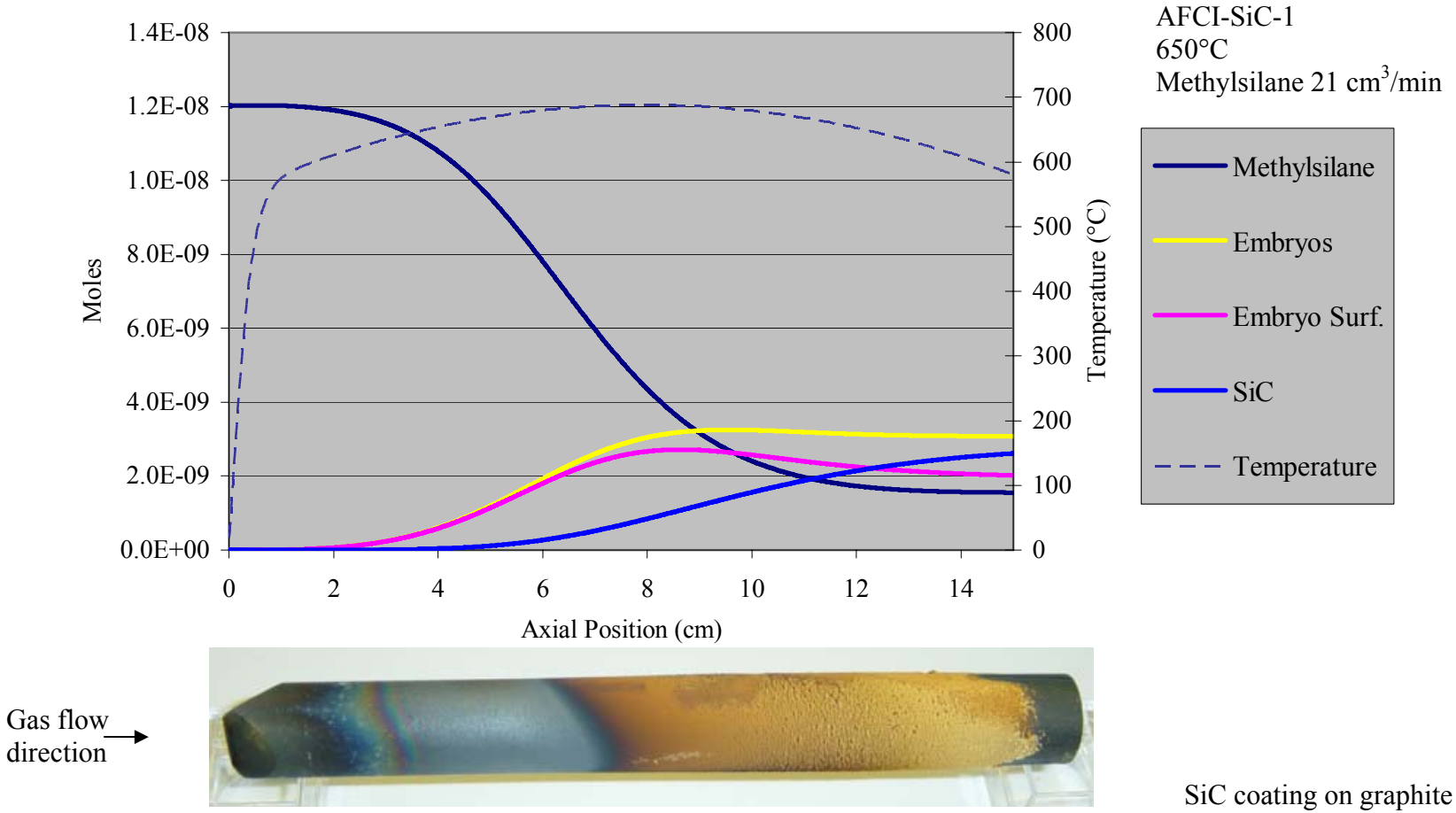

Figure 6.15. Model-predicted profile of the molar amounts of species for AFCI-SiC-1 with a photograph of the specimen shown at the approximate scale of the x-axis for comparison.

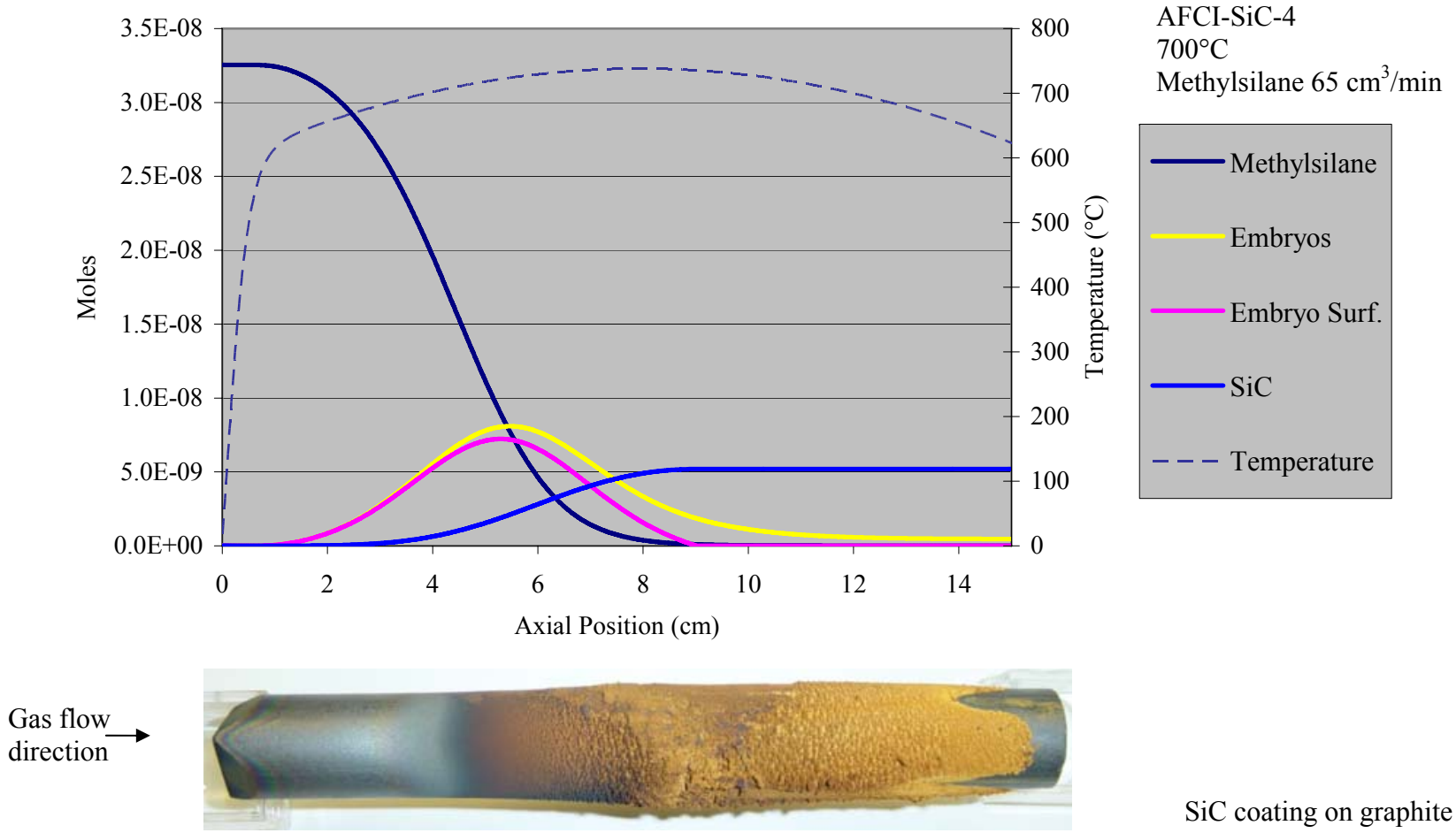

Figure 6.16. Model-predicted profile of the molar amounts of species for AFCI-SiC-4 with a photograph of the specimen shown at the approximate scale of the x-axis for comparison.

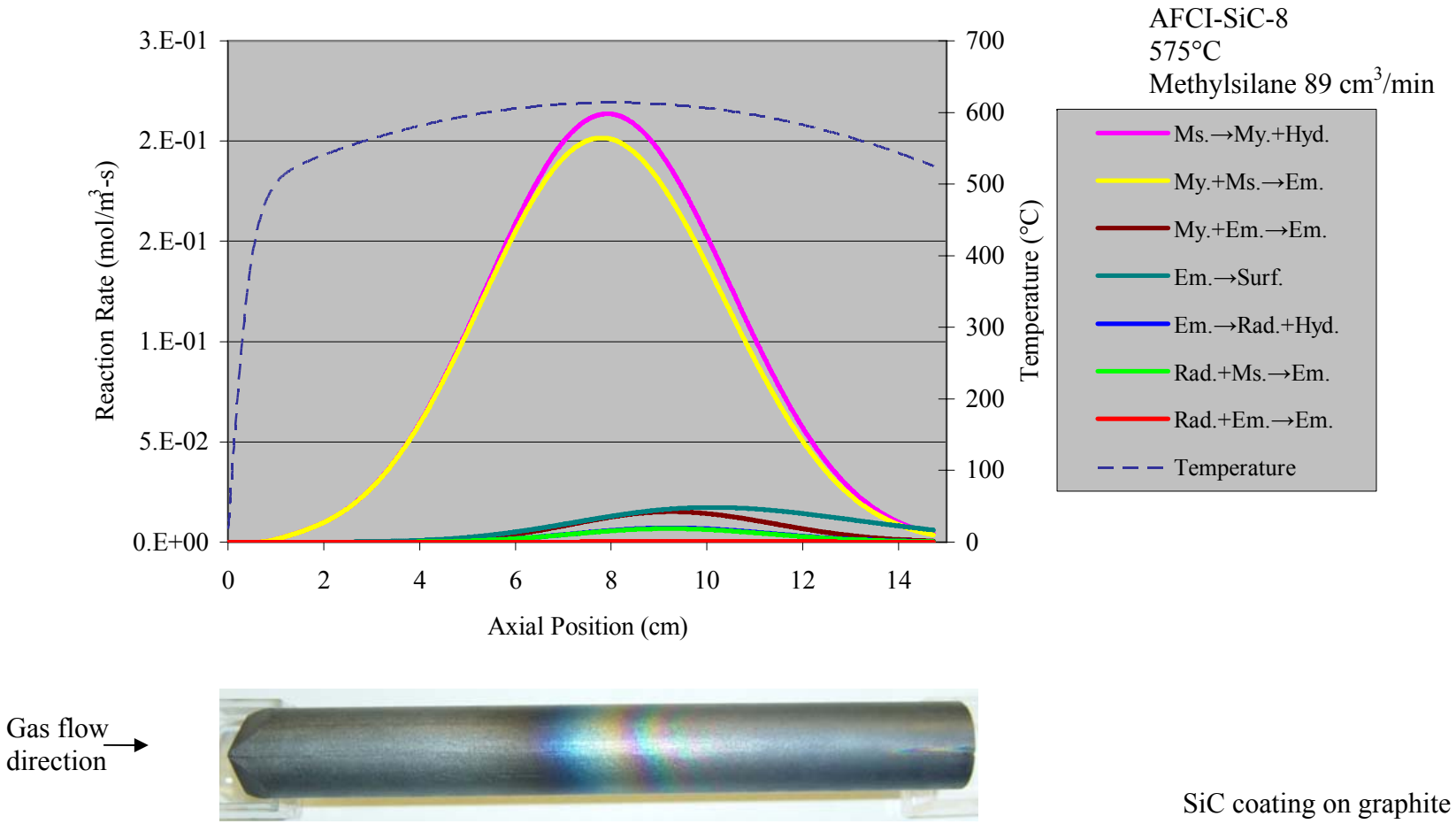

Figure 6.17. Model-predicted reaction rate profile for AFCI-SiC-8 with a photograph of the specimen shown at the approximate scale of the x-axis for comparison. Note that Ms. = Methylsilane, My. = Methylsilylene, Em. = Embryo, Rad. = Radical, and Hyd. = Hydrogen.

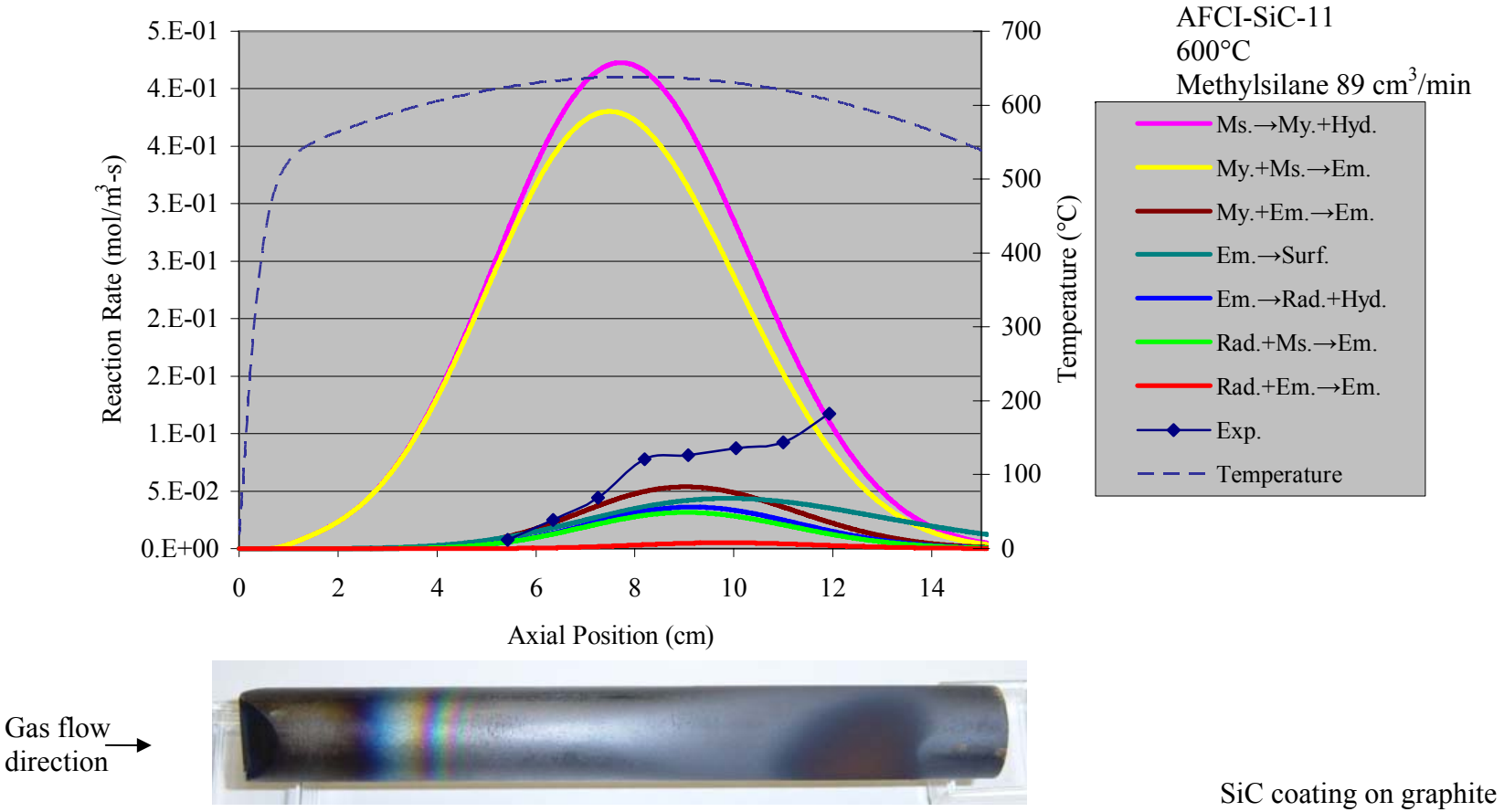

Figure 6.18. Model-predicted reaction rate profile for AFCI-SiC-11 with a photograph of the specimen shown at the approximate scale of the x-axis for comparison. Note that Ms. = Methylsilane, My. = Methylsilylene, Em. = Embryo, Rad. = Radical, and Hyd. = Hydrogen.

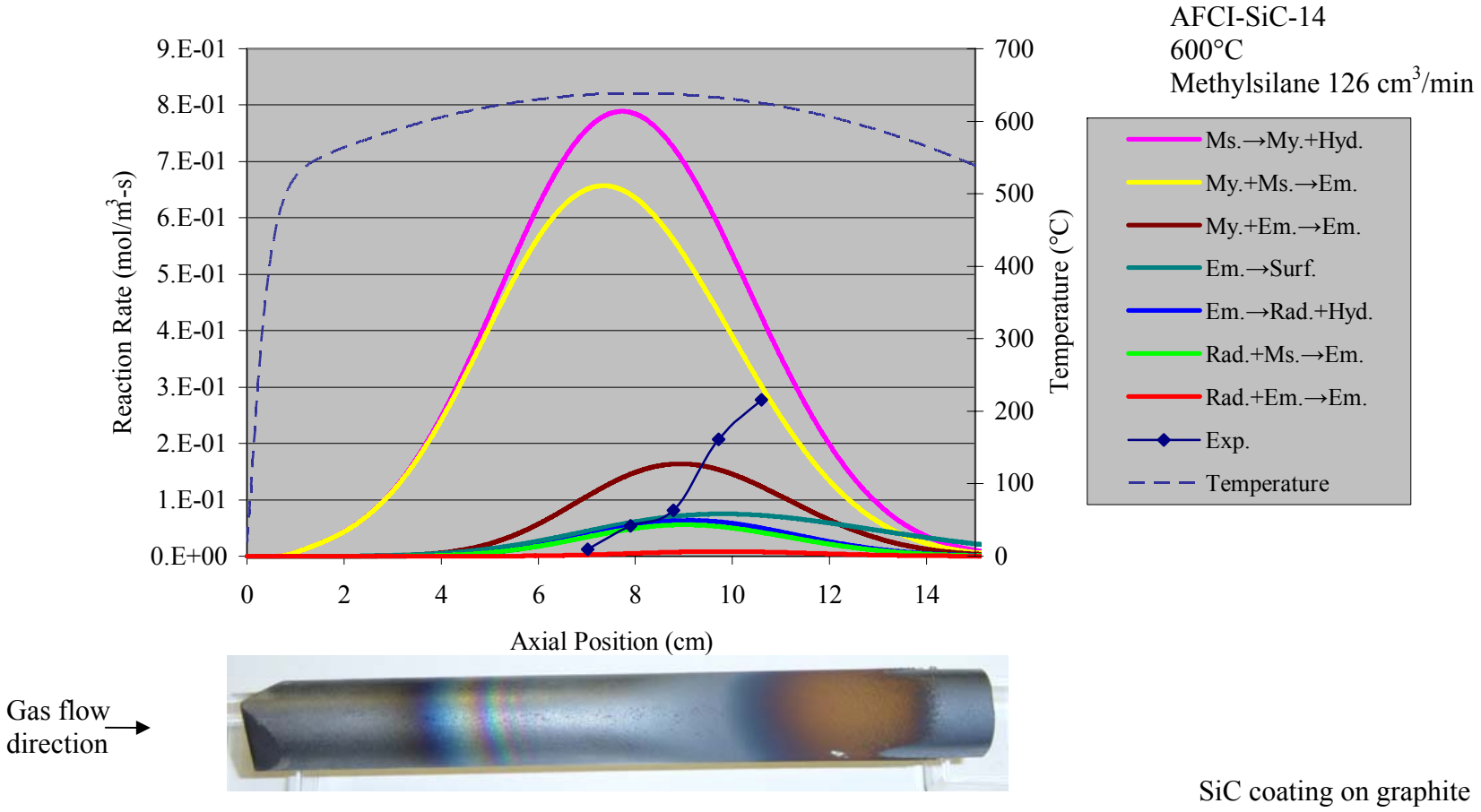

Figure 6.19. Model-predicted reaction rate profile for AFCI-SiC-14 with a photograph of the specimen shown at the approximate scale of the x-axis for comparison. Note that Ms. = Methylsilane, My. = Methylsilylene, Em. = Embryo, Rad. = Radical, and Hyd. = Hydrogen.

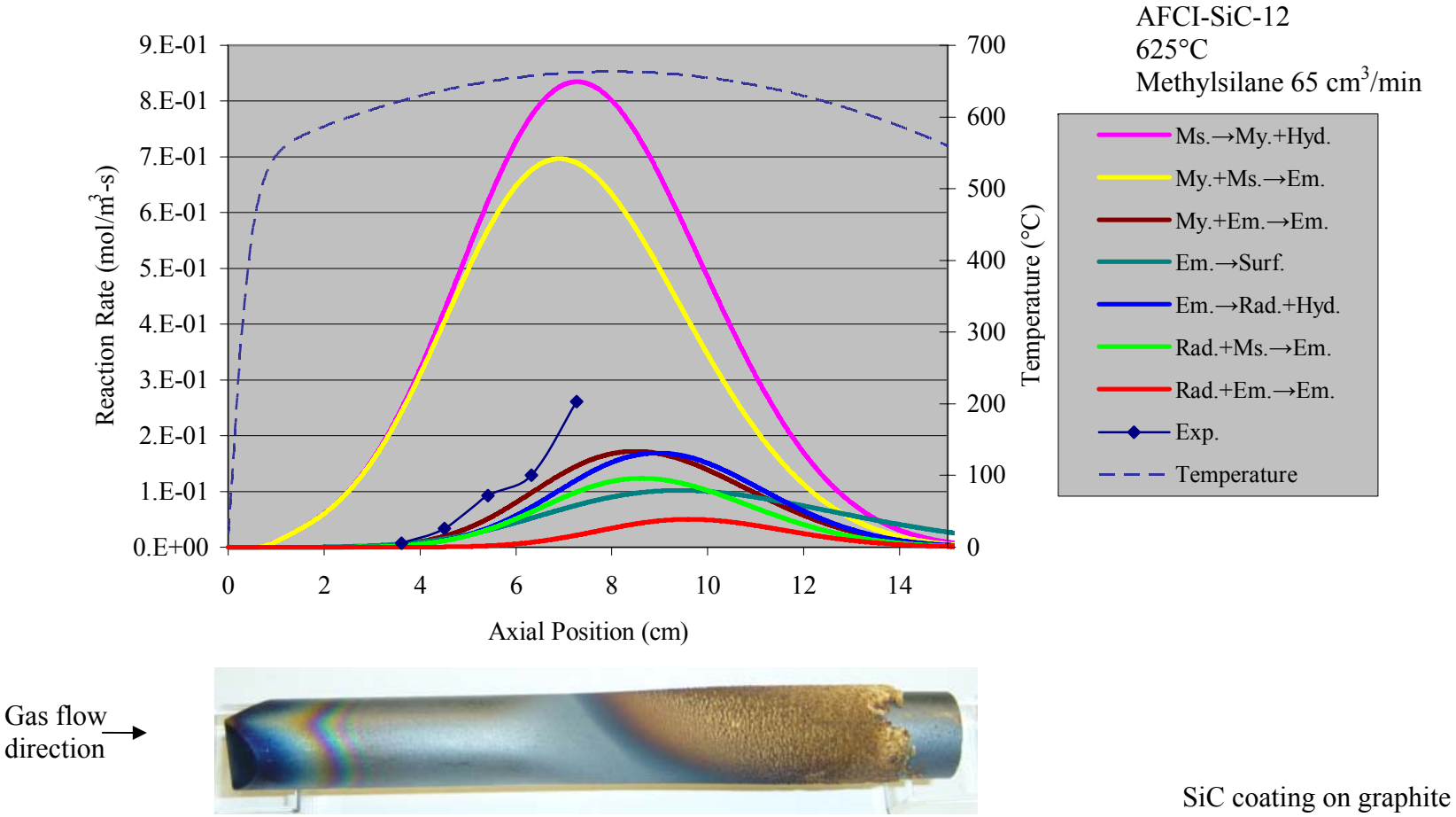

Figure 6.20. Model-predicted reaction rate profile for AFCI-SiC-12 with a photograph of the specimen shown at the approximate scale of the x-axis for comparison. Note that Ms. = Methylsilane, My. = Methylsilylene, Em. = Embryo, Rad. = Radical, and Hyd. = Hydrogen.

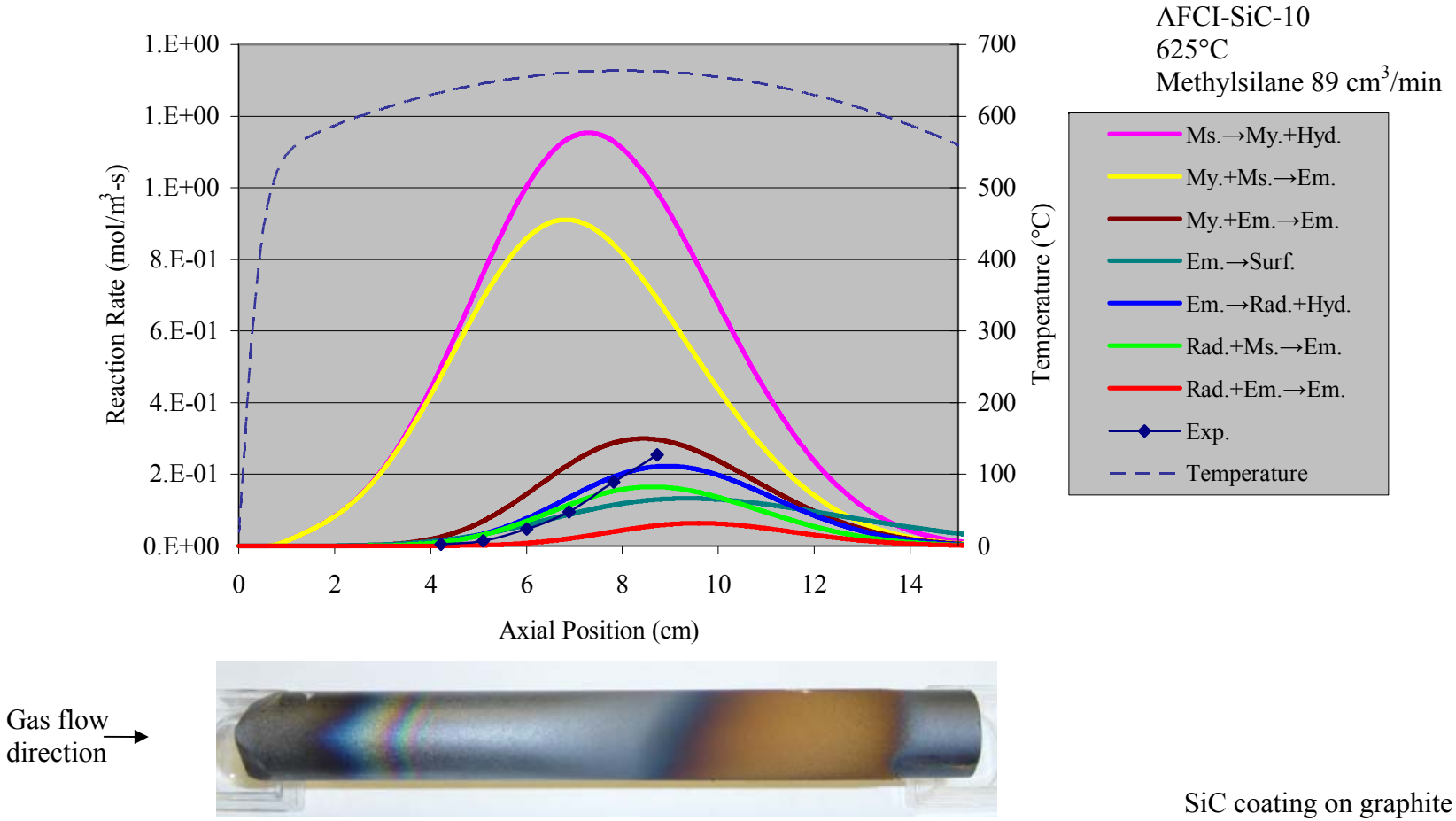

Figure 6.21. Model-predicted reaction rate profile for AFCI-SiC-10 with a photograph of the specimen shown at the approximate scale of the x-axis for comparison. Note that Ms. = Methylsilane, My. = Methylsilylene, Em. = Embryo, Rad. = Radical, and Hyd. = Hydrogen.

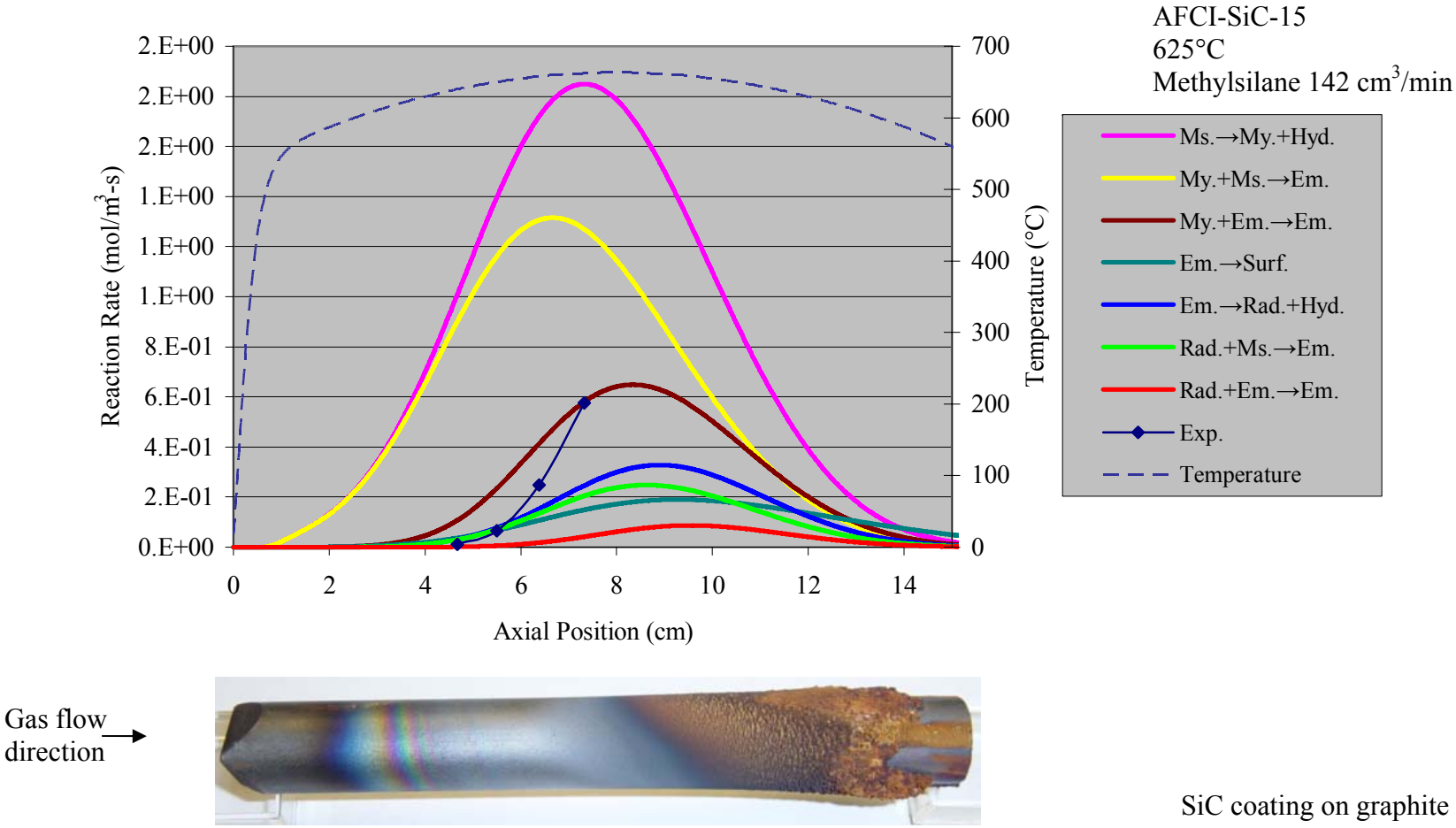

Figure 6.22. Model-predicted reaction rate profile for AFCI-SiC-15 with a photograph of the specimen shown at the approximate scale of the x-axis for comparison. Note that Ms. = Methylsilane, My. = Methylsilylene, Em. = Embryo, Rad. = Radical, and Hyd. = Hydrogen.

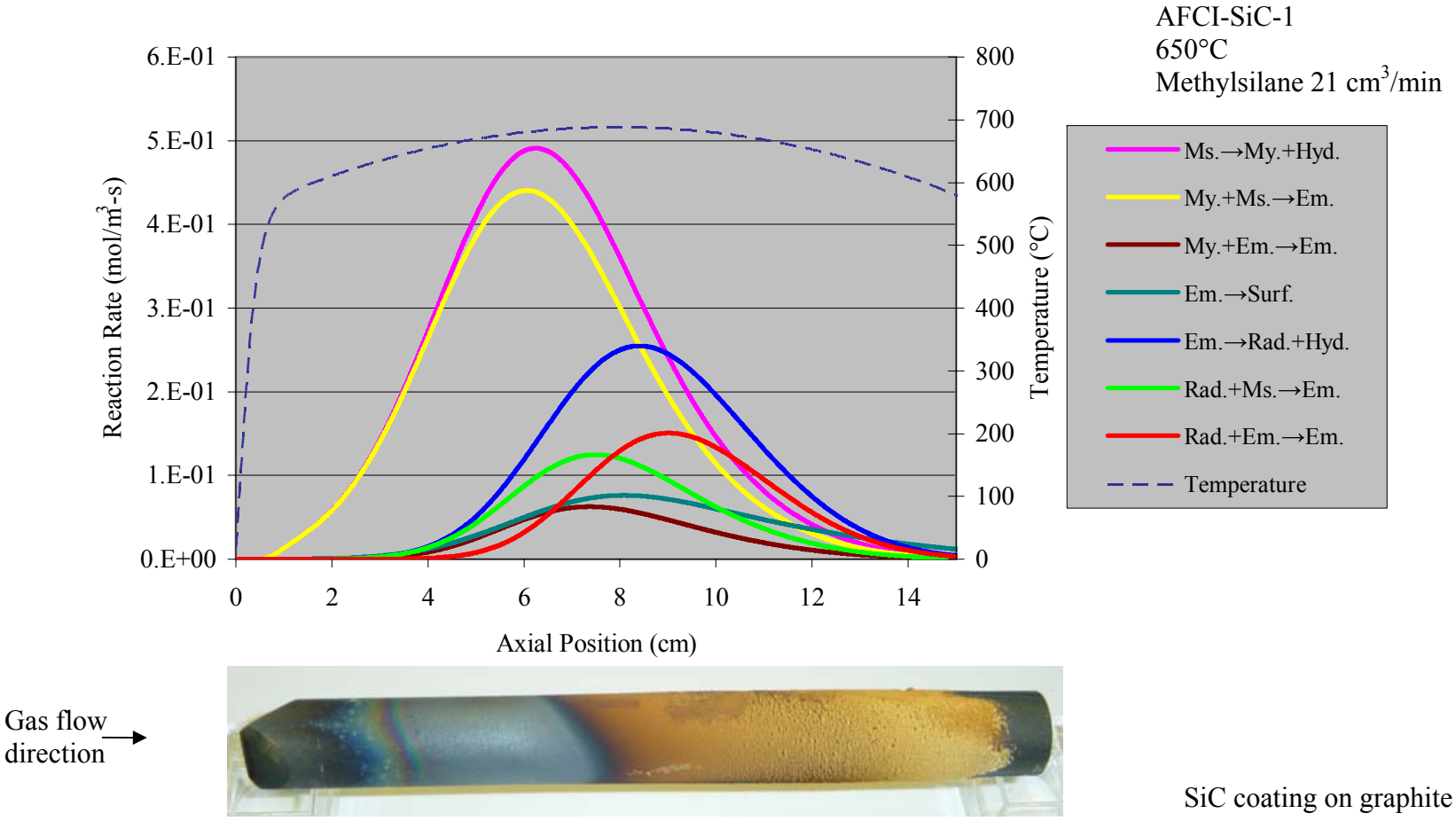

Figure 6.23. Model-predicted reaction rate profile for AFCI-SiC-1 with a photograph of the specimen shown at the approximate scale of the x-axis for comparison. Note that Ms. = Methylsilane, My. = Methylsilylene, Em. = Embryo, Rad. = Radical, and Hyd. = Hydrogen.

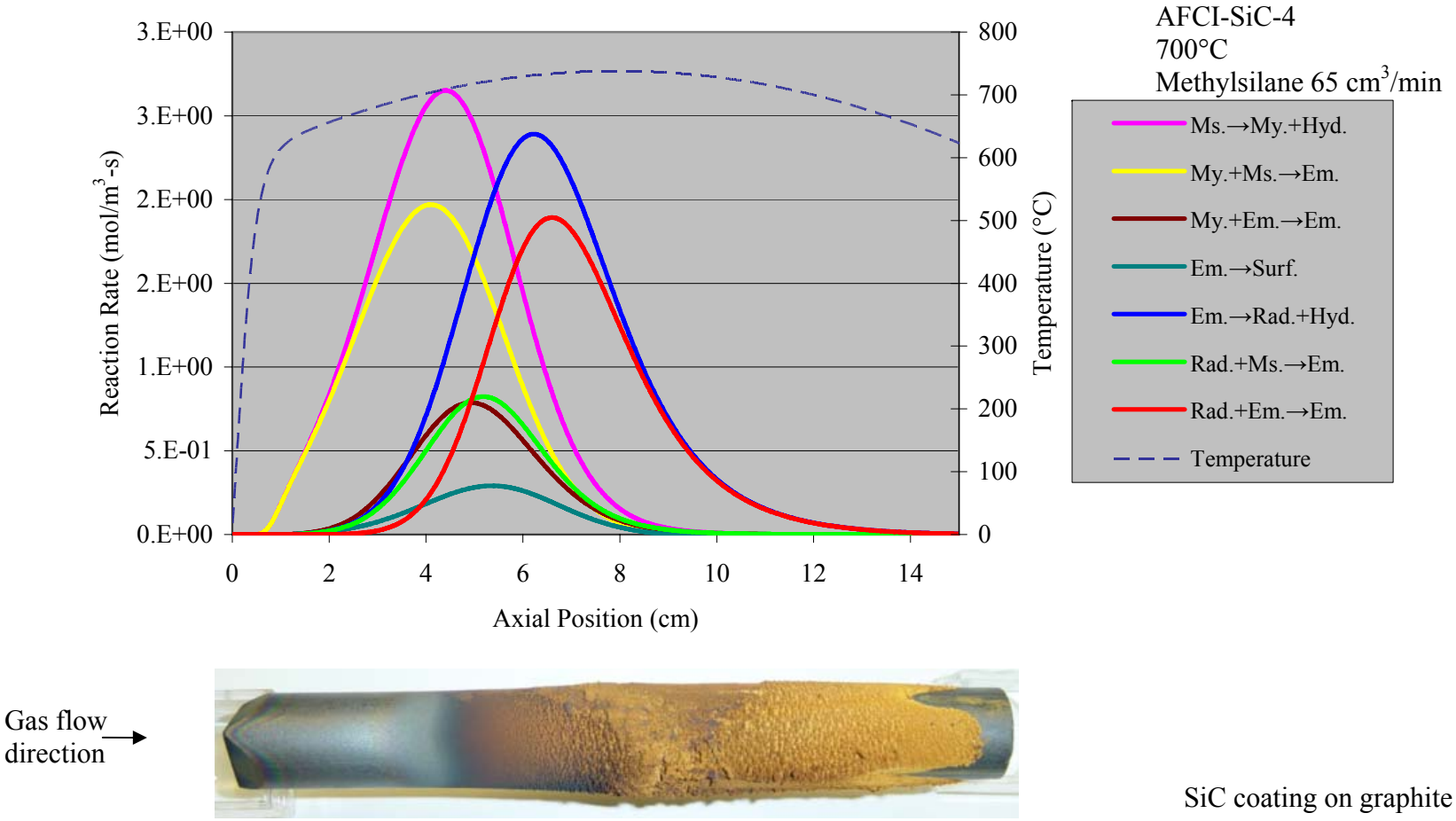

Figure 6.24. Model-predicted reaction rate profile for AFCI-SiC-4 with a photograph of the specimen shown at the approximate scale of the x-axis for comparison. Note that Ms. = Methylsilane, My. = Methylsilylene, Em. = Embryo, Rad. = Radical, and Hyd. = Hydrogen.

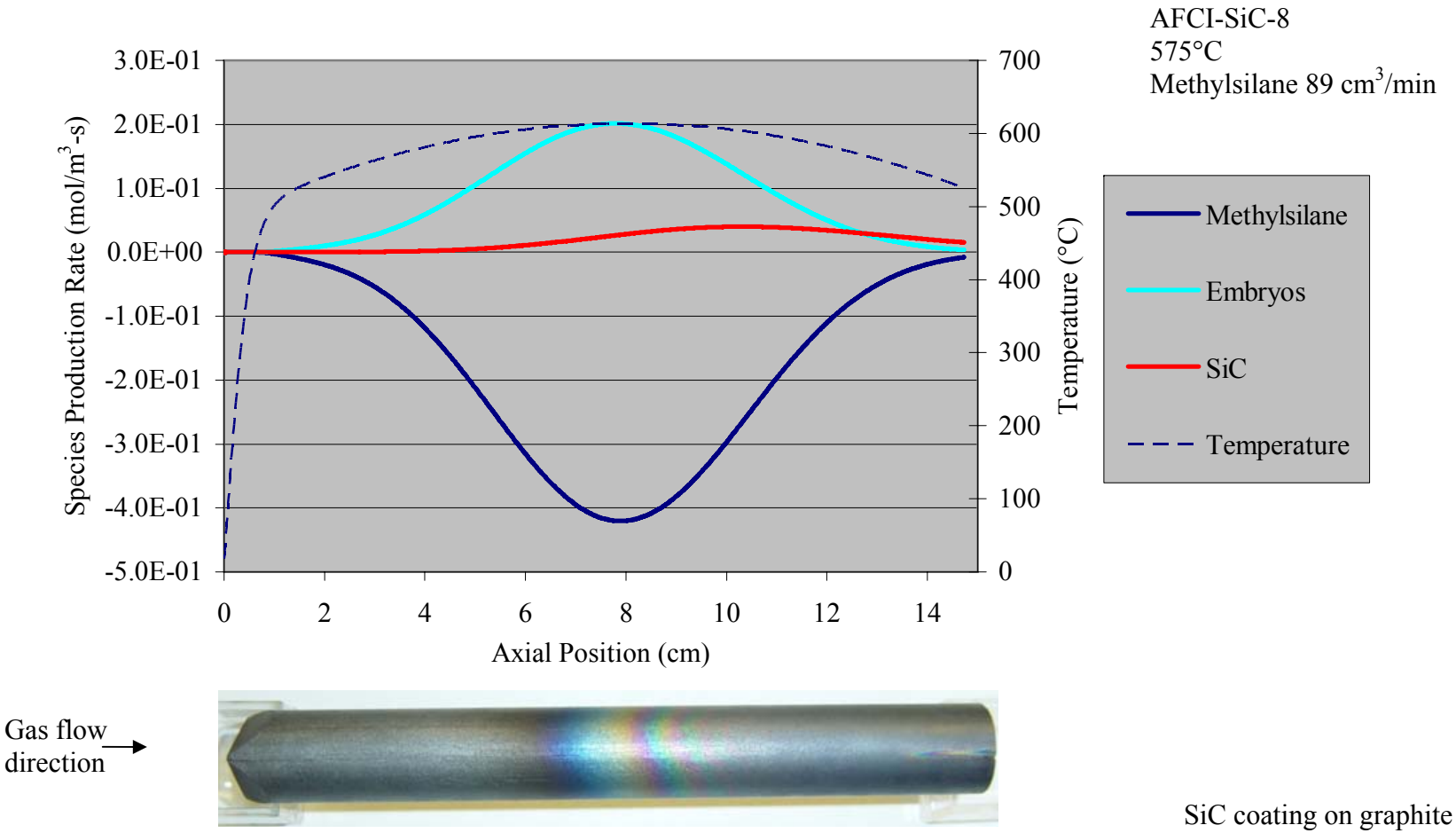

Figure 6.25. Model-predicted species rates of production as a function of axial position for AFCI-SiC-8 with a photograph of the specimen shown at the approximate scale of the x-axis for comparison.

.

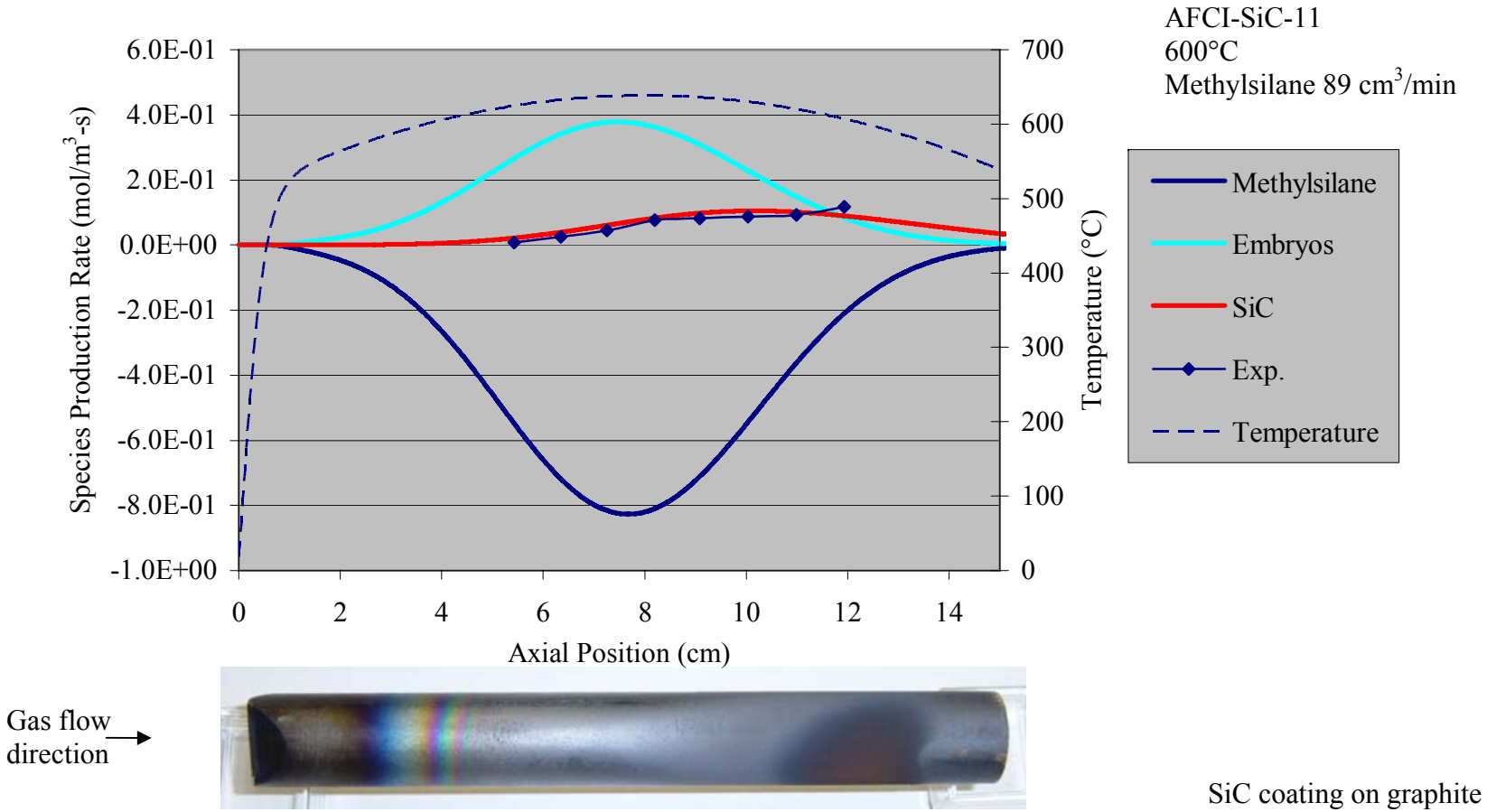

Figure 6.26. Model-predicted species rates of production as a function of axial position for AFCI-SiC-11 with a photograph of the specimen shown at the approximate scale of the x-axis for comparison.

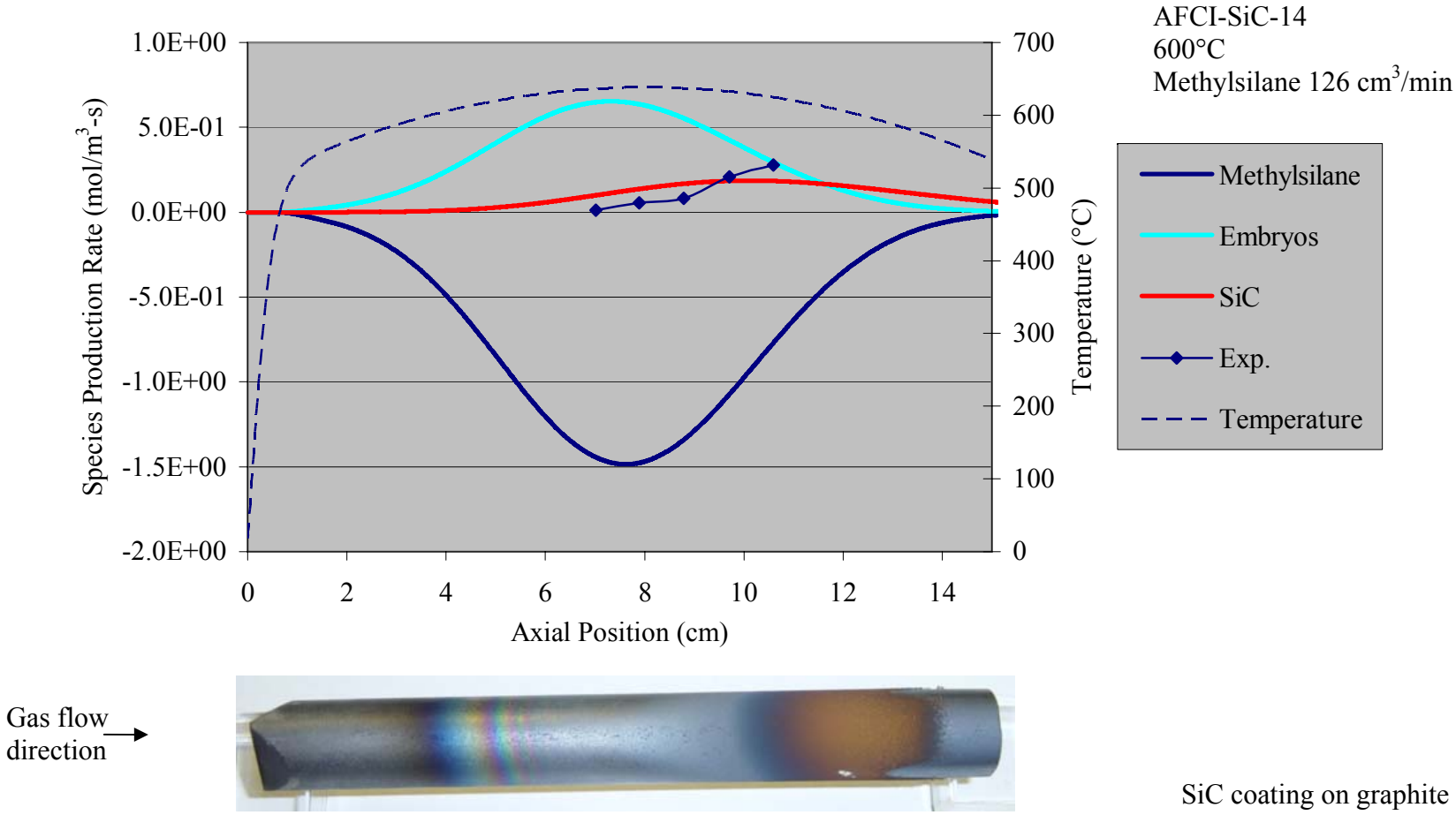

Figure 6.27. Model-predicted species rates of production as a function of axial position for AFCI-SiC-14 with a photograph of the specimen shown at the approximate scale of the x-axis for comparison.

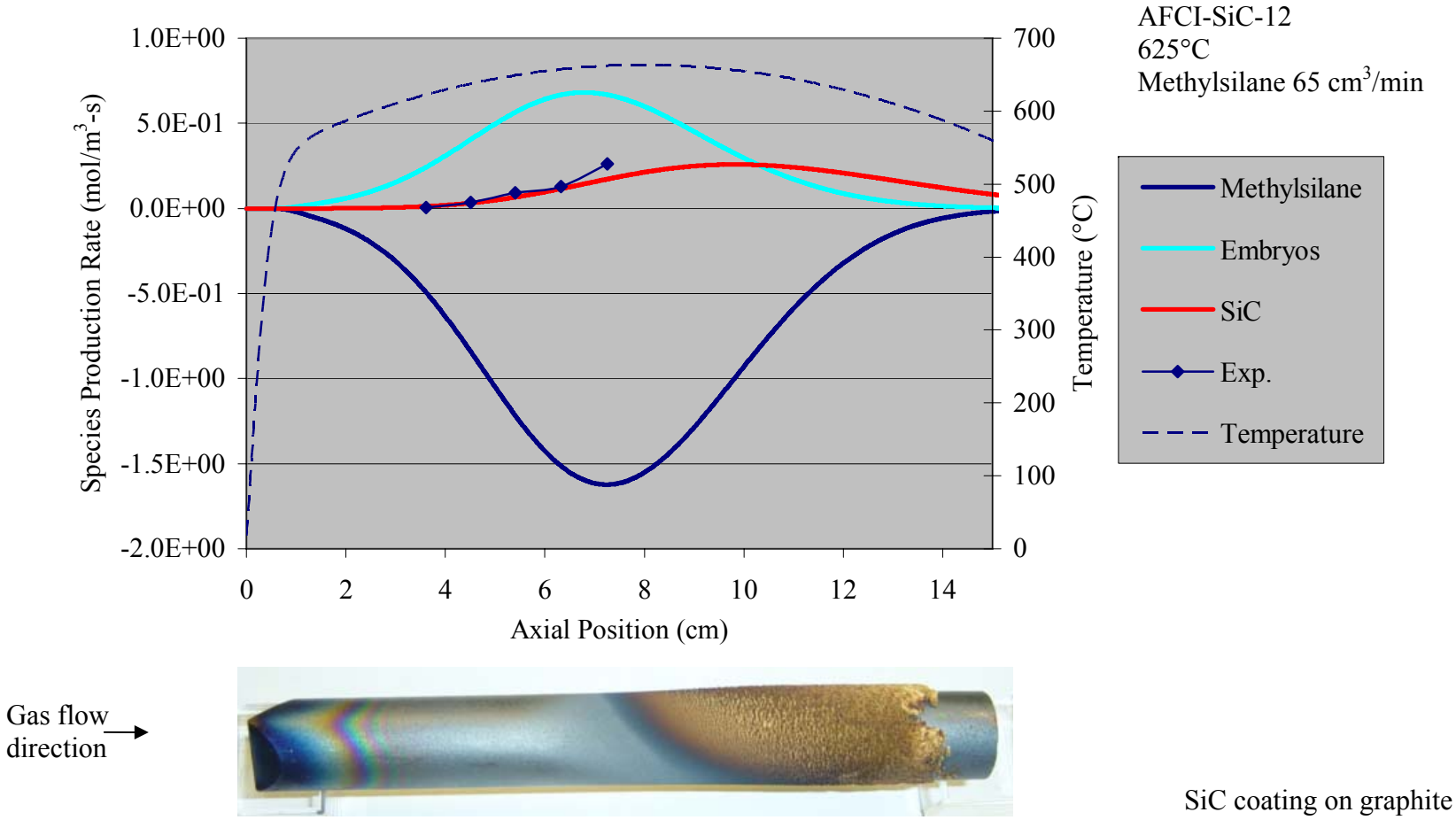

Figure 6.28. Model-predicted species rates of production as a function of axial position for AFCI-SiC-12 with a photograph of the specimen shown at the approximate scale of the x-axis for comparison.

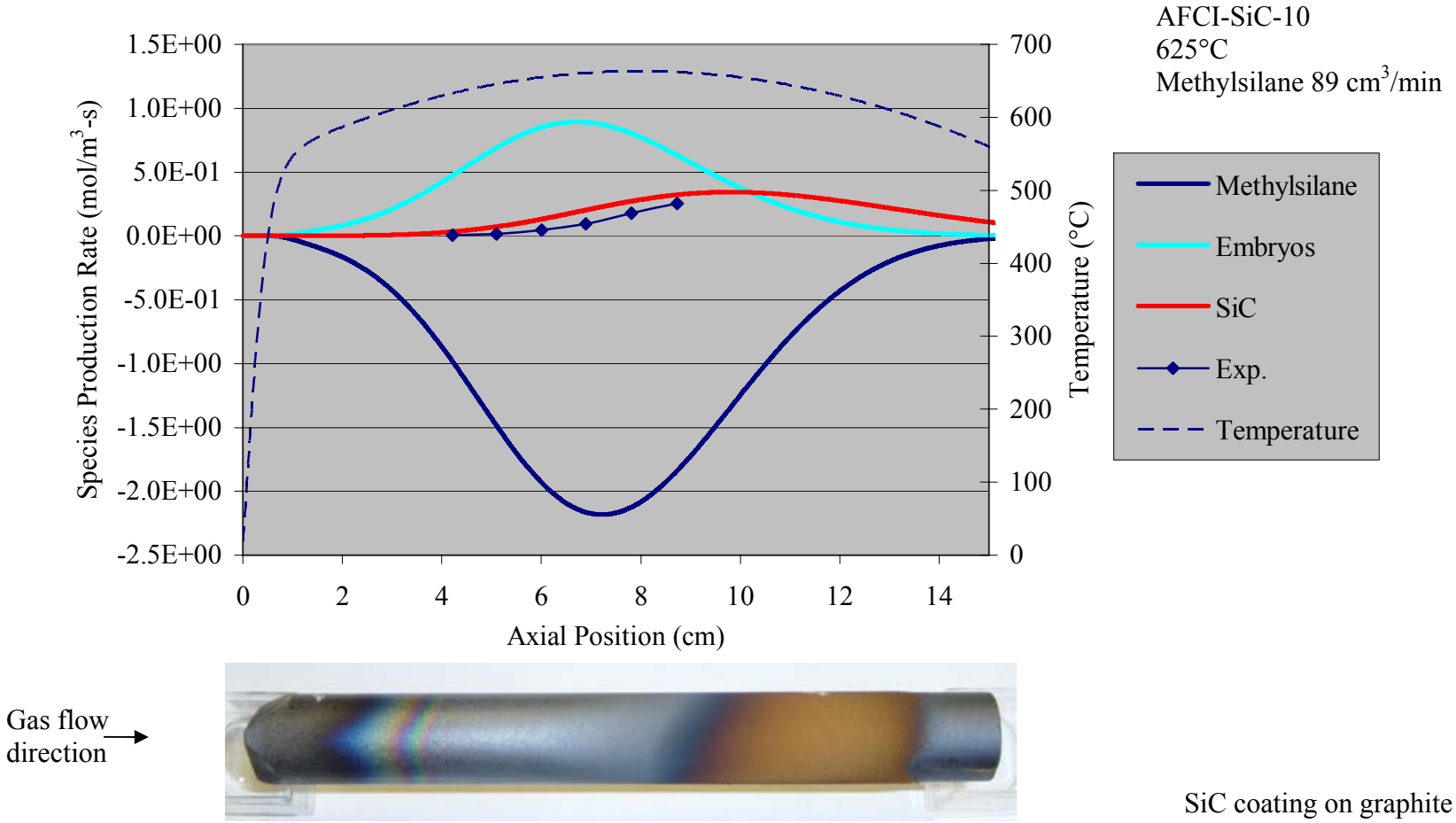

Figure 6.29. Model-predicted species rates of production as a function of axial position for AFCI-SiC-10 with a photograph of the specimen shown at the approximate scale of the x-axis for comparison.

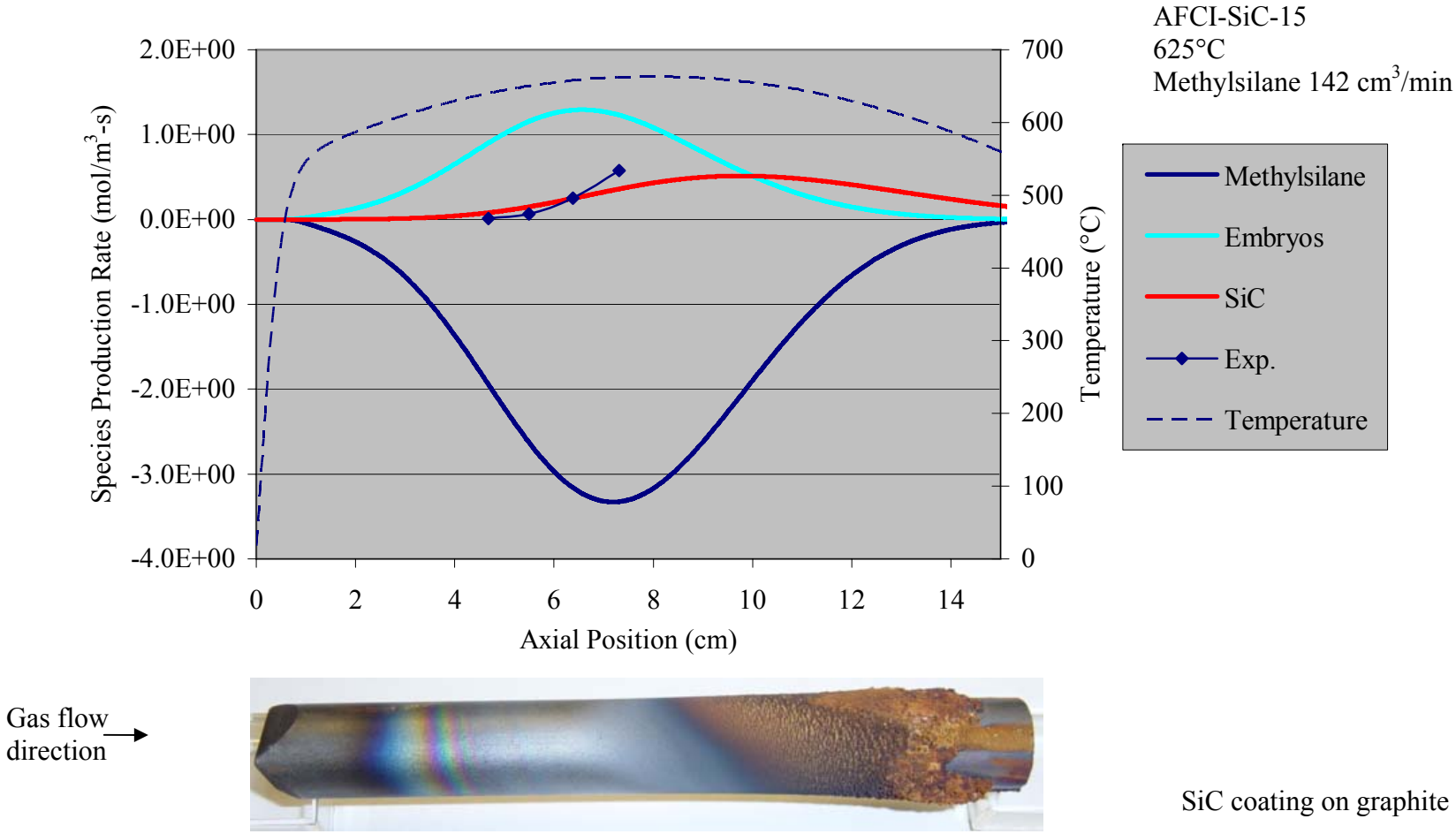

Figure 6.30. Model-predicted species rates of production as a function of axial position for AFCI-SiC-15 with a photograph of the specimen shown at the approximate scale of the x-axis for comparison.

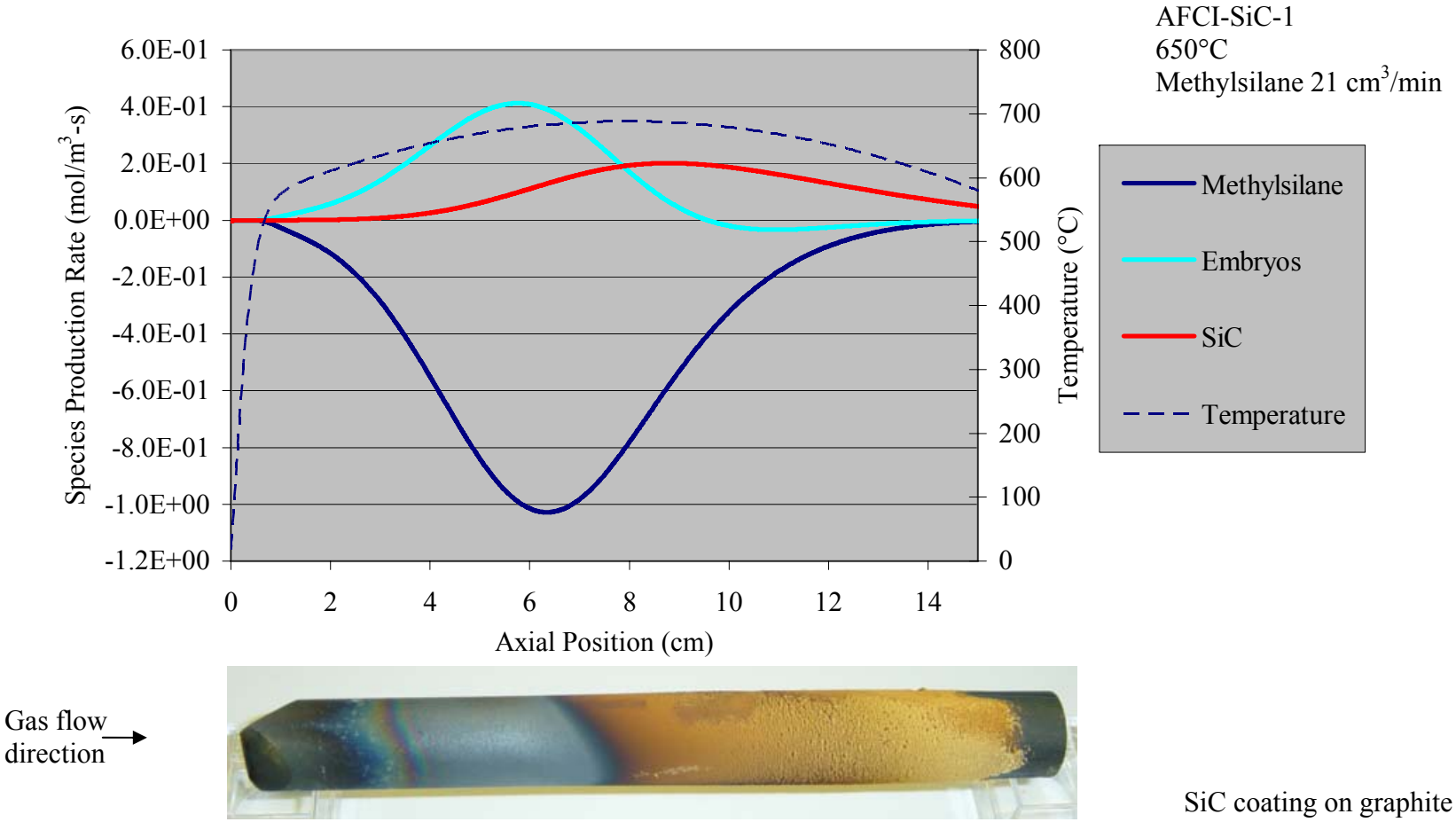

Figure 6.31. Model-predicted species rates of production as a function of axial position for AFCI-SiC-1 with a photograph of the specimen shown at the approximate scale of the x-axis for comparison.

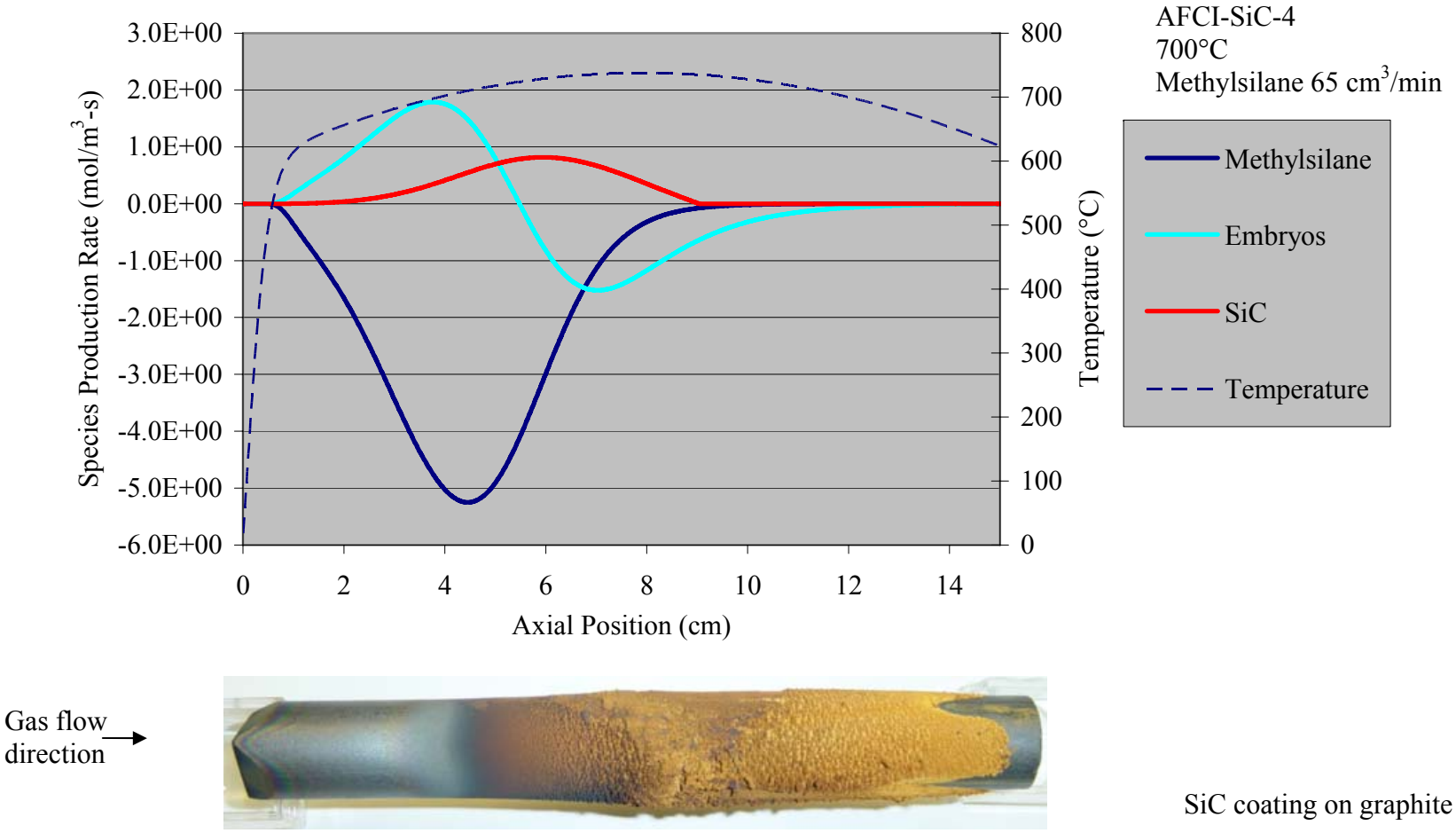

Figure 6.32. Model-predicted species rates of production as a function of axial position for AFCI-SiC-4 with a photograph of the specimen shown at the approximate scale of the x-axis for comparison.

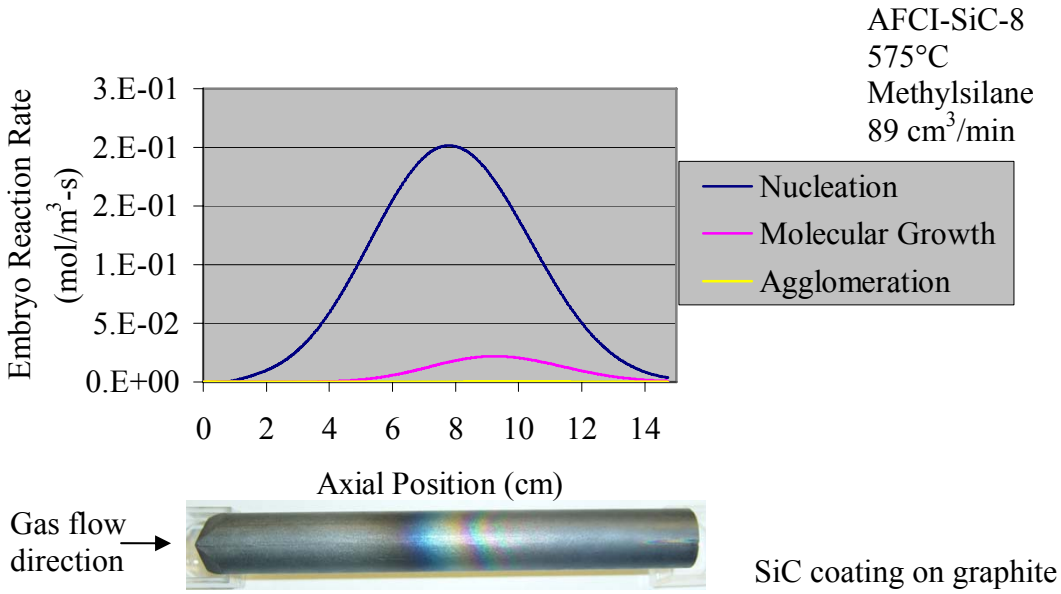

Figure 6.33. Model-predicted embryo reaction rates as a function of axial position for AFCI-SiC-8 with a photograph of the specimen shown at the approximate scale of the x-axis for comparison.

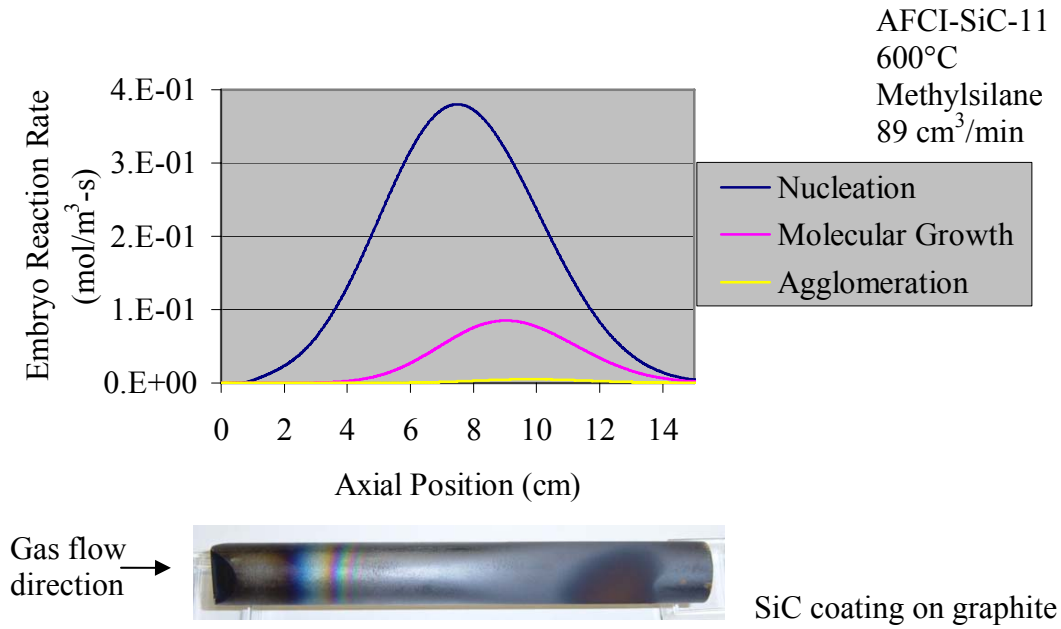

Figure 6.34. Model-predicted embryo reaction rates as a function of axial position for AFCI-SiC-11 with a photograph of the specimen shown at the approximate scale of the x-axis for comparison.

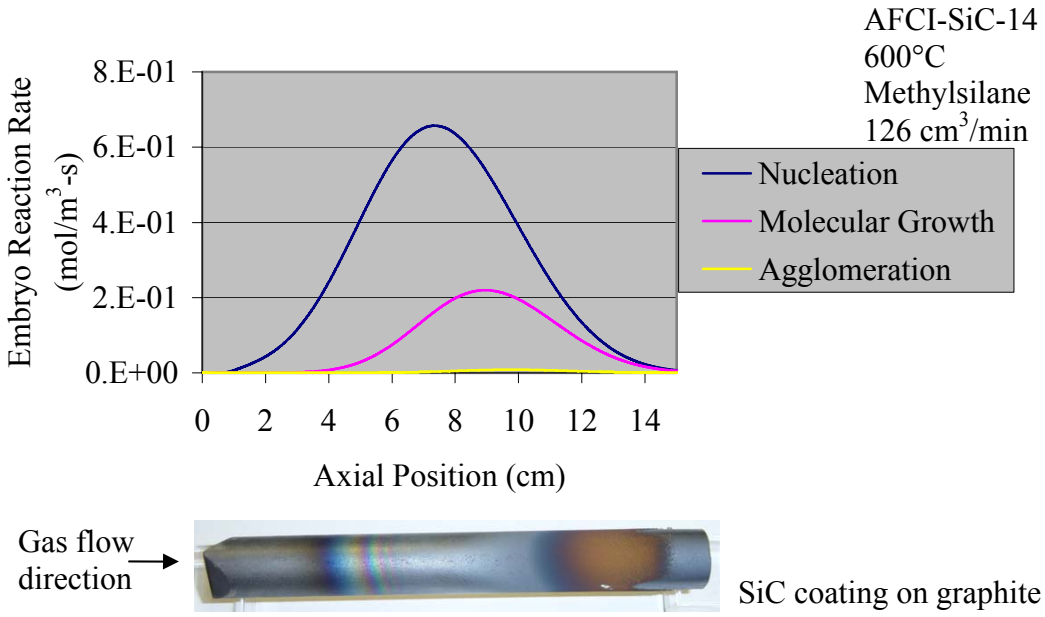

Figure 6.35. Model-predicted embryo reaction rates as a function of axial position for AFCI-SiC-14 with a photograph of the specimen shown at the approximate scale of the x-axis for comparison.

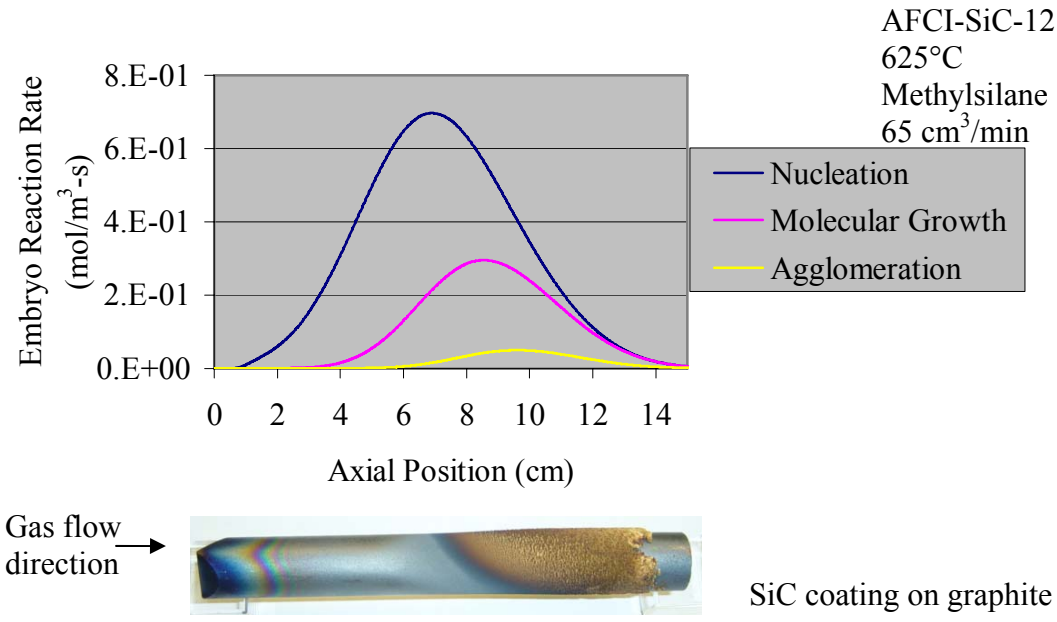

Figure 6.36. Model-predicted embryo reaction rates as a function of axial position for AFCI-SiC-12 with a photograph of the specimen shown at the approximate scale of the x-axis for comparison.

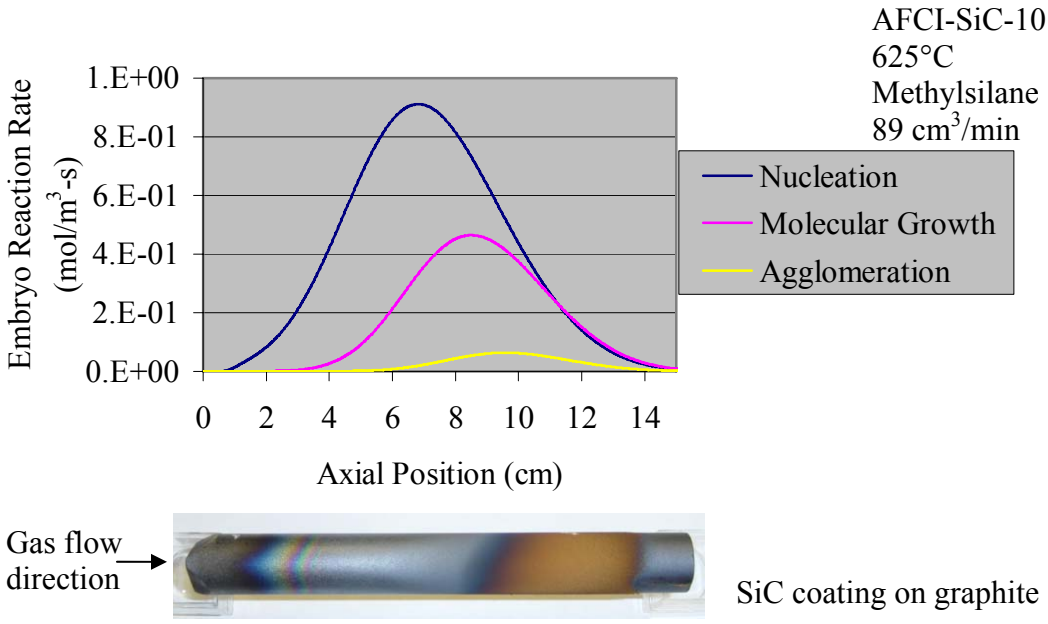

Figure 6.37. Model-predicted embryo reaction rates as a function of axial position for AFCI-SiC-10 with a photograph of the specimen shown at the approximate scale of the x-axis for comparison.

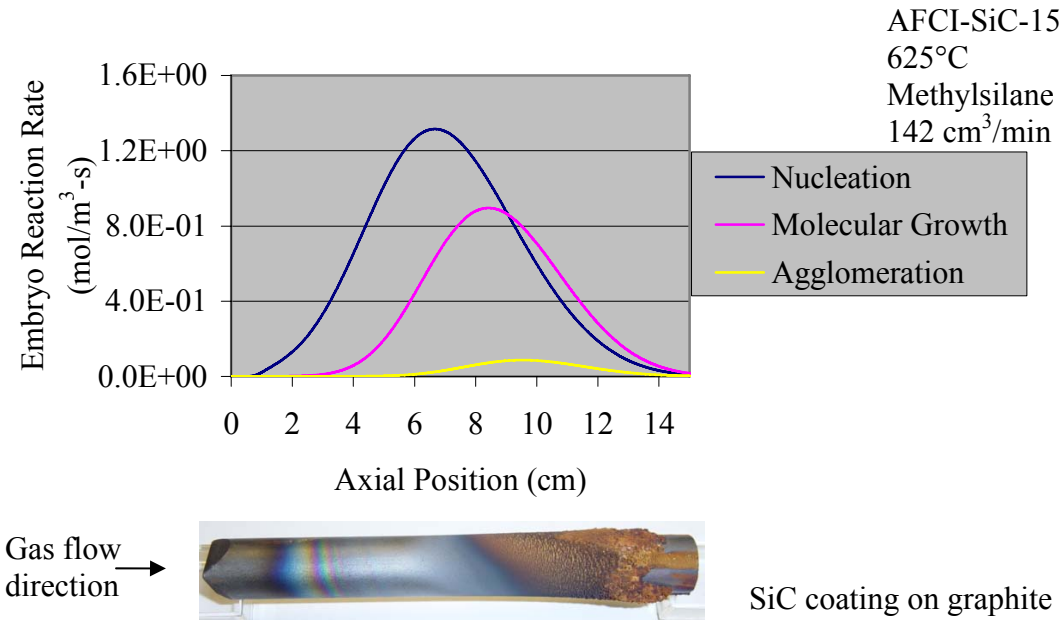

Figure 6.38. Model-predicted embryo reaction rates as a function of axial position for AFCI-SiC-15 with a photograph of the specimen shown at the approximate scale of the x-axis for comparison.

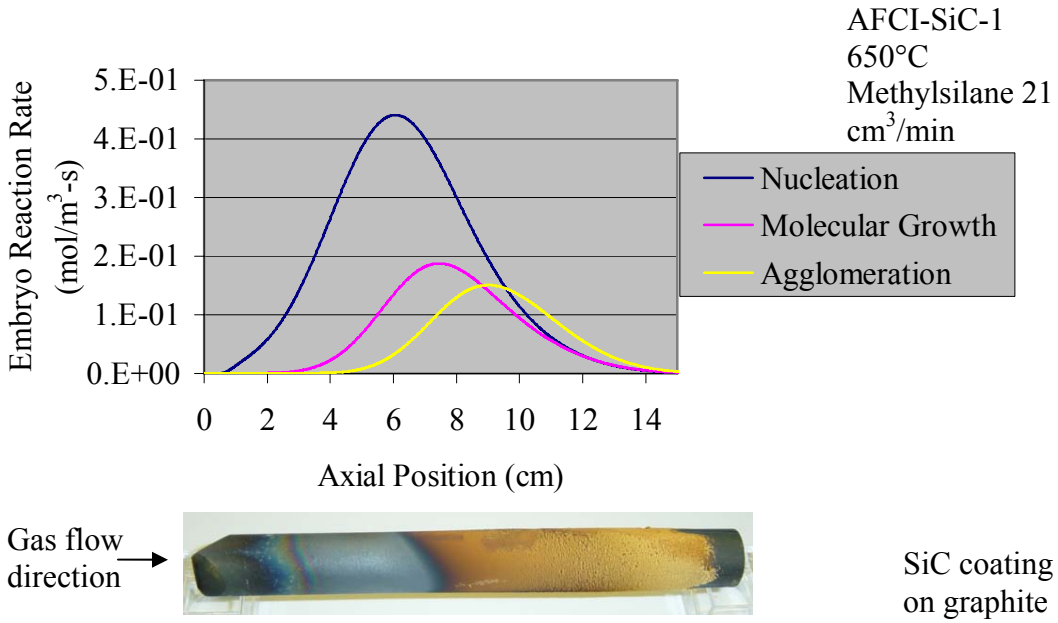

Figure 6.39. Model-predicted embryo reaction rates as a function of axial position for AFCI-SiC-1 with a photograph of the specimen shown at the approximate scale of the x-axis for comparison.

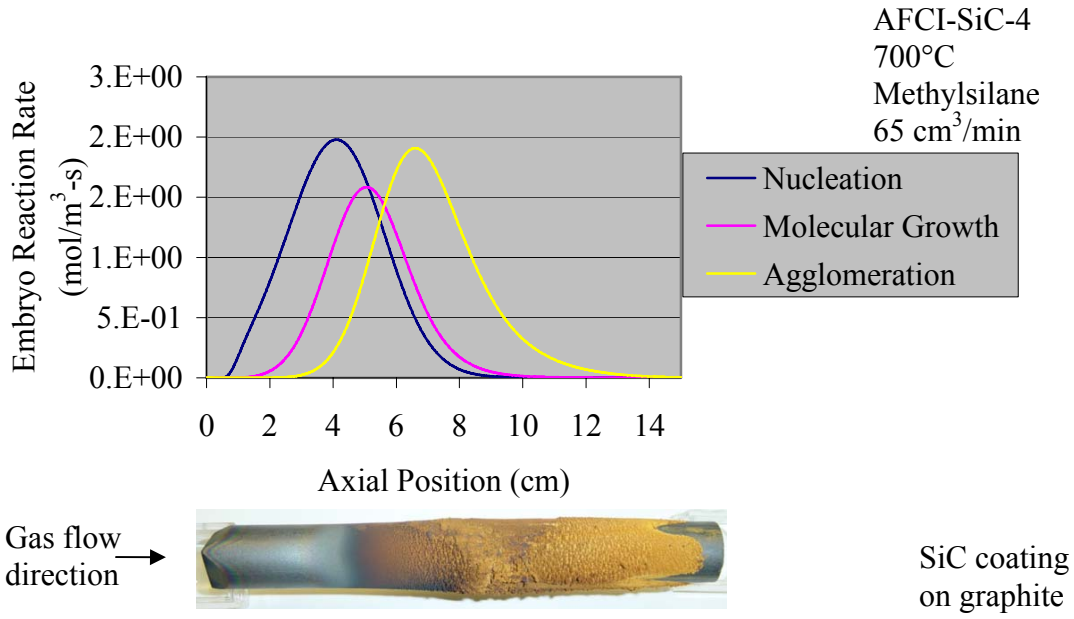

Figure 6.40. Model-predicted embryo reaction rates as a function of axial position for AFCI-SiC-4 with a photograph of the specimen shown at the approximate scale of the x-axis for comparison.

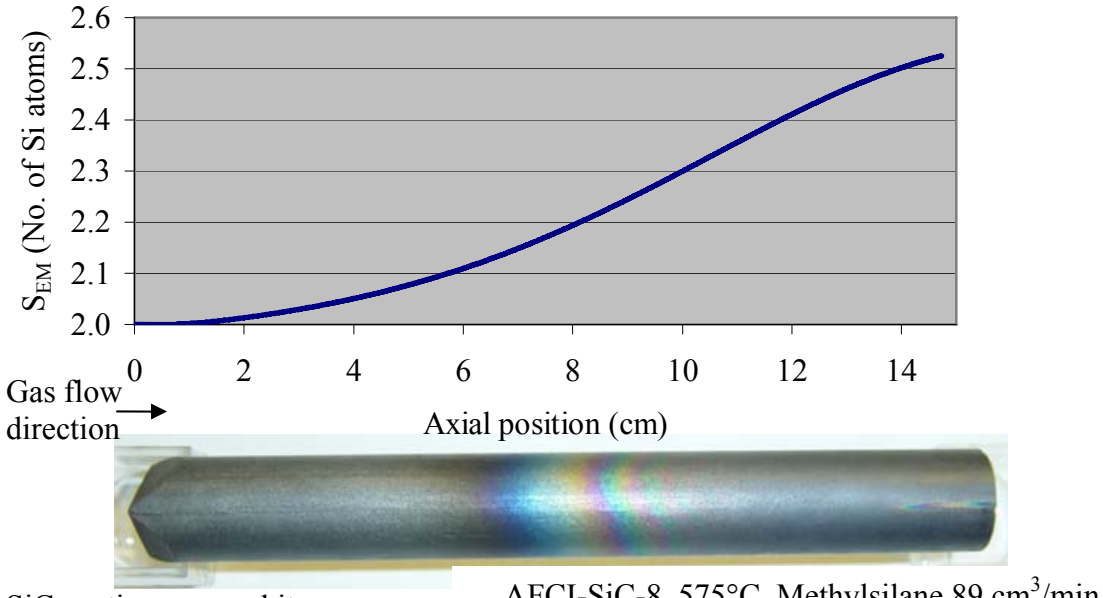

Figure 6.41. Model-predicted profile of the average size of embryos for AFCI-SiC-8 with a photograph of the specimen shown at the approximate scale of the x-axis for comparison.

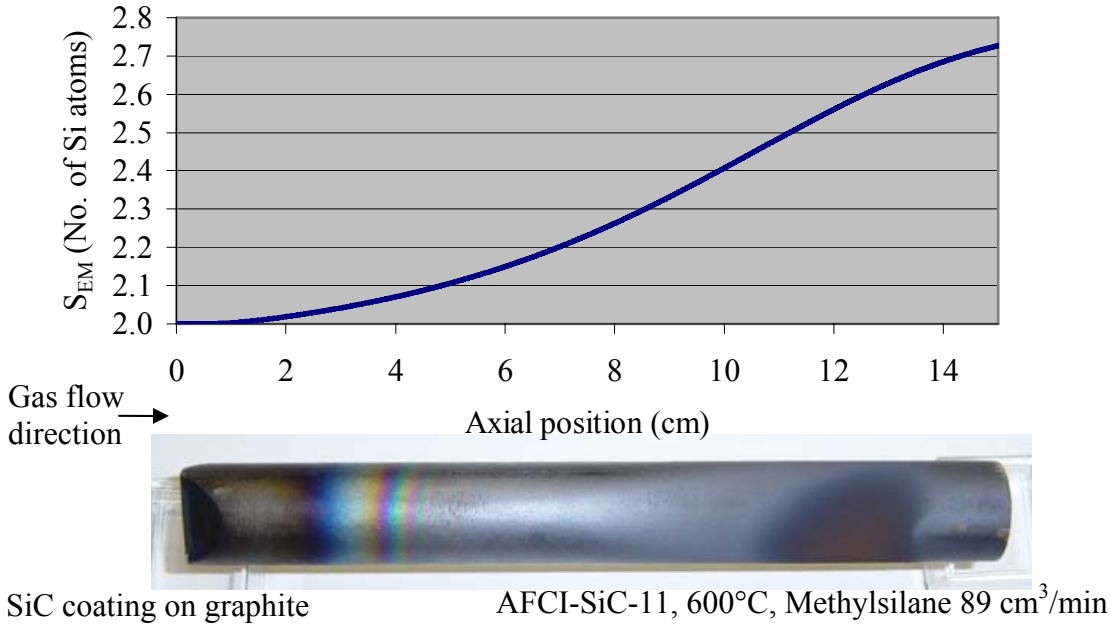

Figure 6.42. Model-predicted profile of the average size of embryos for AFCI-SiC-11 with a photograph of the specimen shown at the approximate scale of the x-axis for comparison.

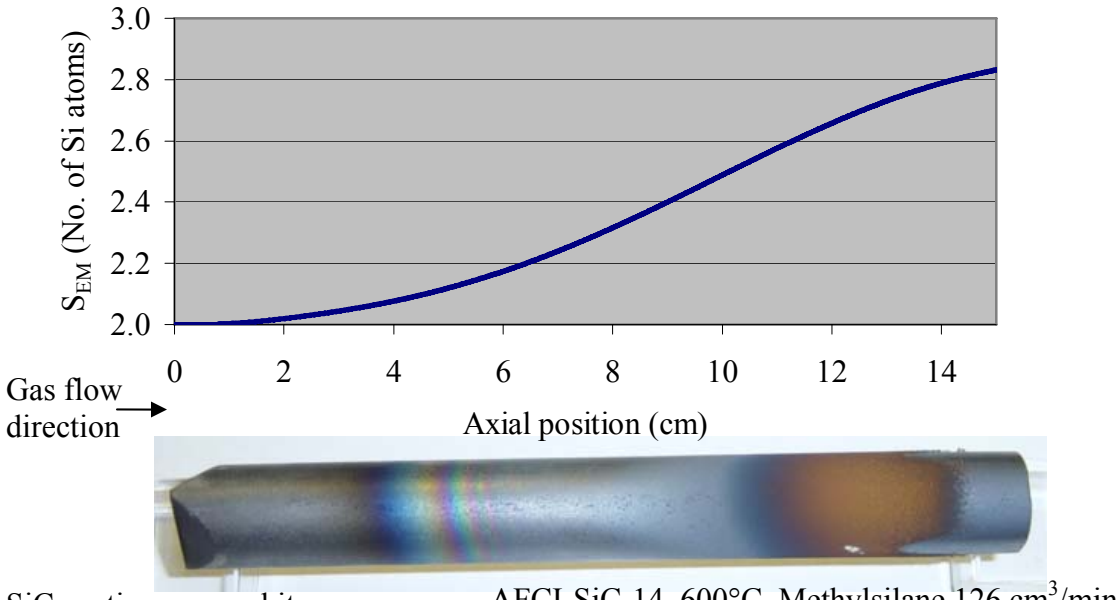

Figure 6.43. Model-predicted profile of the average size of embryos for AFCI-SiC-14 with a photograph of the specimen shown at the approximate scale of the x-axis for comparison.

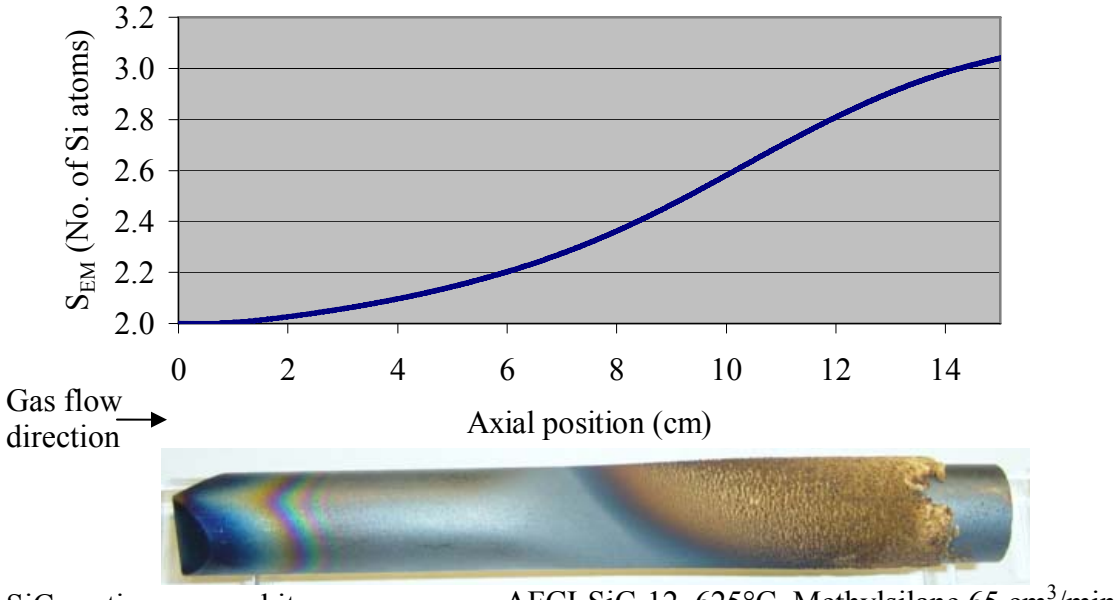

Figure 6.44. Model-predicted profile of the average size of embryos for AFCI-SiC-12 with a photograph of the specimen shown at the approximate scale of the x-axis for comparison.

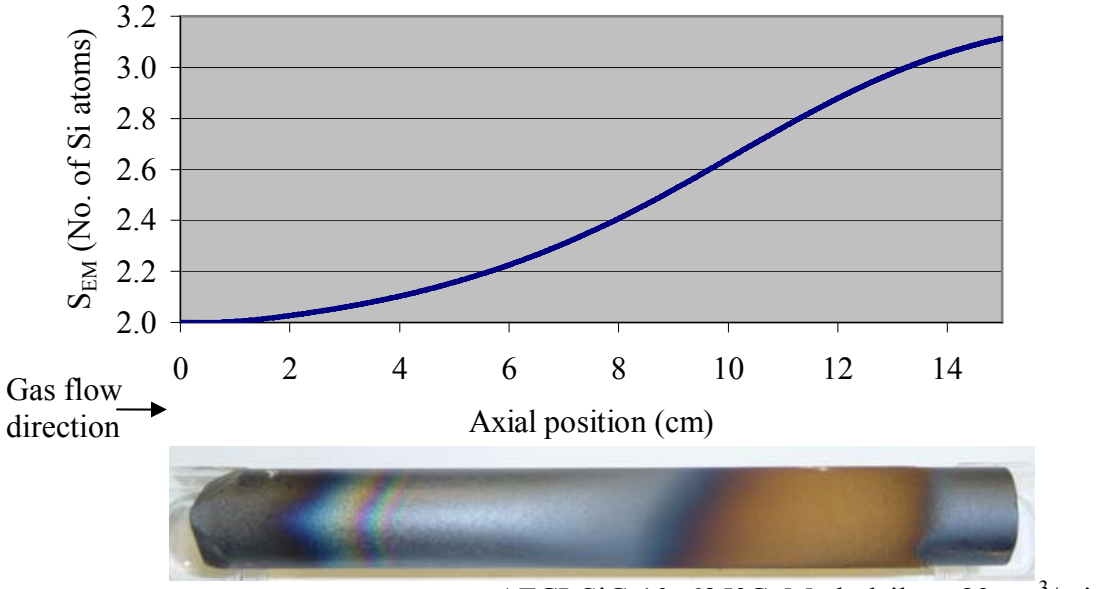

Figure 6.45. Model-predicted profile of the average size of embryos for AFCI-SiC-10 with a photograph of the specimen shown at the approximate scale of the x-axis for comparison.

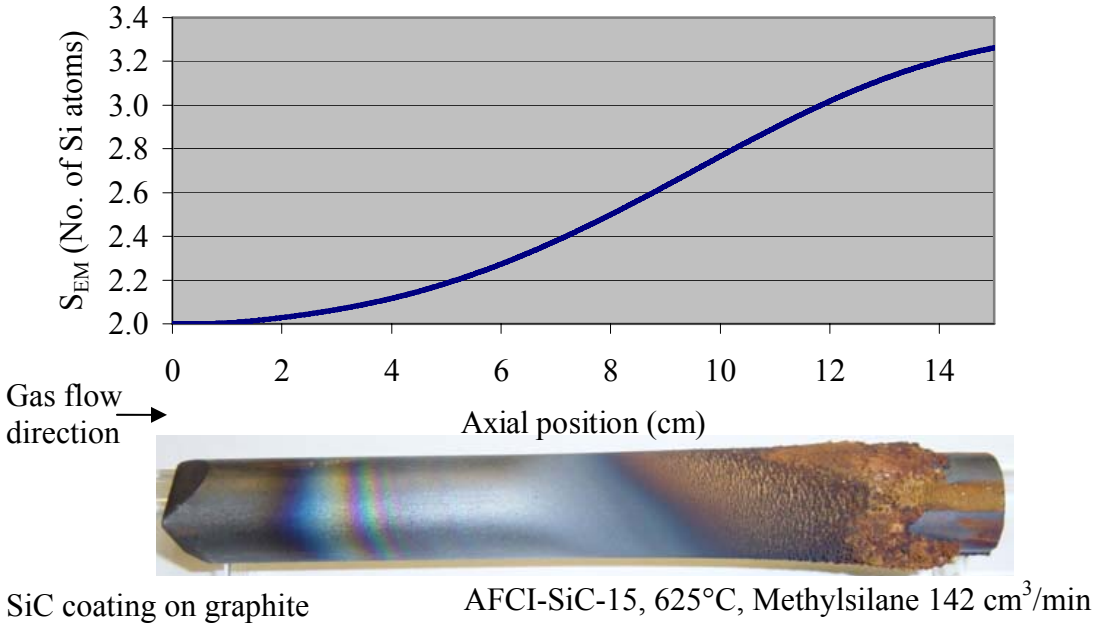

Figure 6.46. Model-predicted profile of the average size of embryos for AFCI-SiC-15 with a photograph of the specimen shown at the approximate scale of the x-axis for comparison.

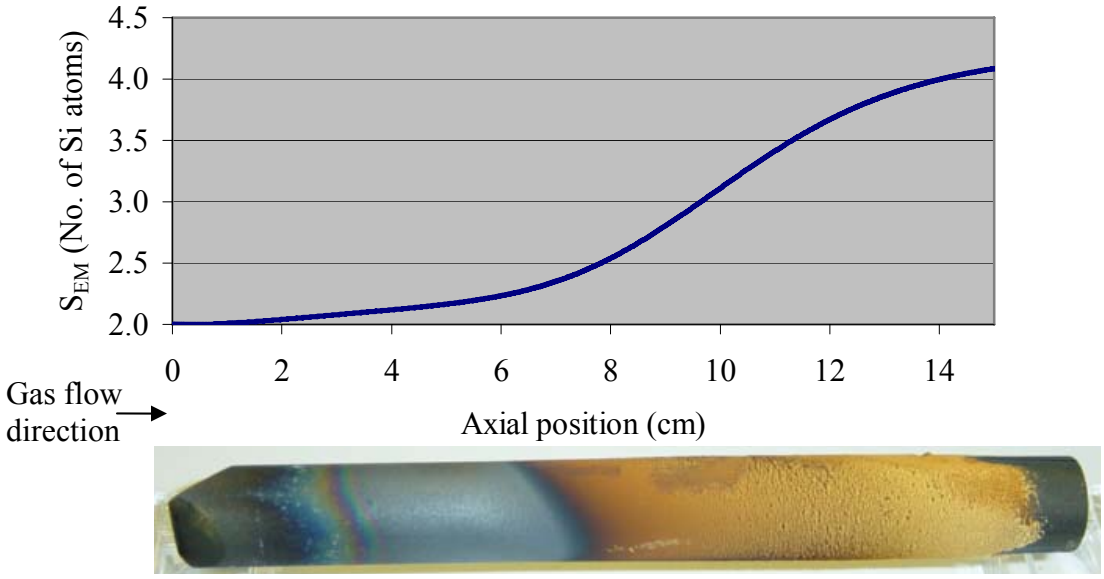

Figure 6.47. Model-predicted profile of the average size of embryos for AFCI-SiC-1 with a photograph of the specimen shown at the approximate scale of the x-axis for comparison.

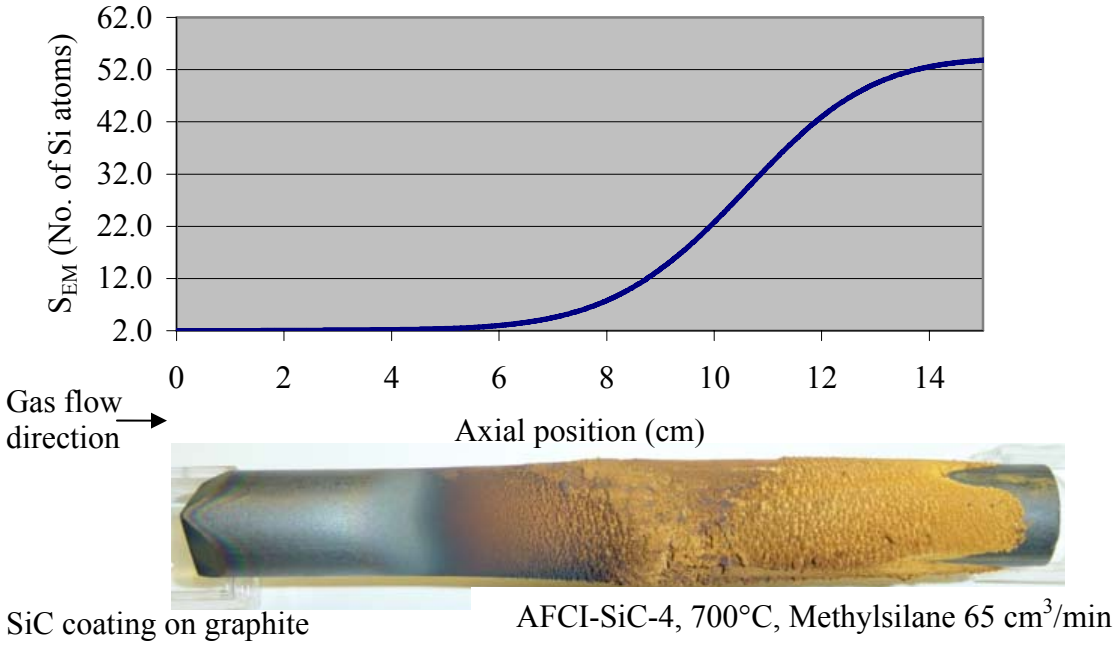

Figure 6.48. Model-predicted profile of the average size of embryos for AFCI-SiC-4 with a photograph of the specimen shown at the approximate scale of the x-axis for comparison.

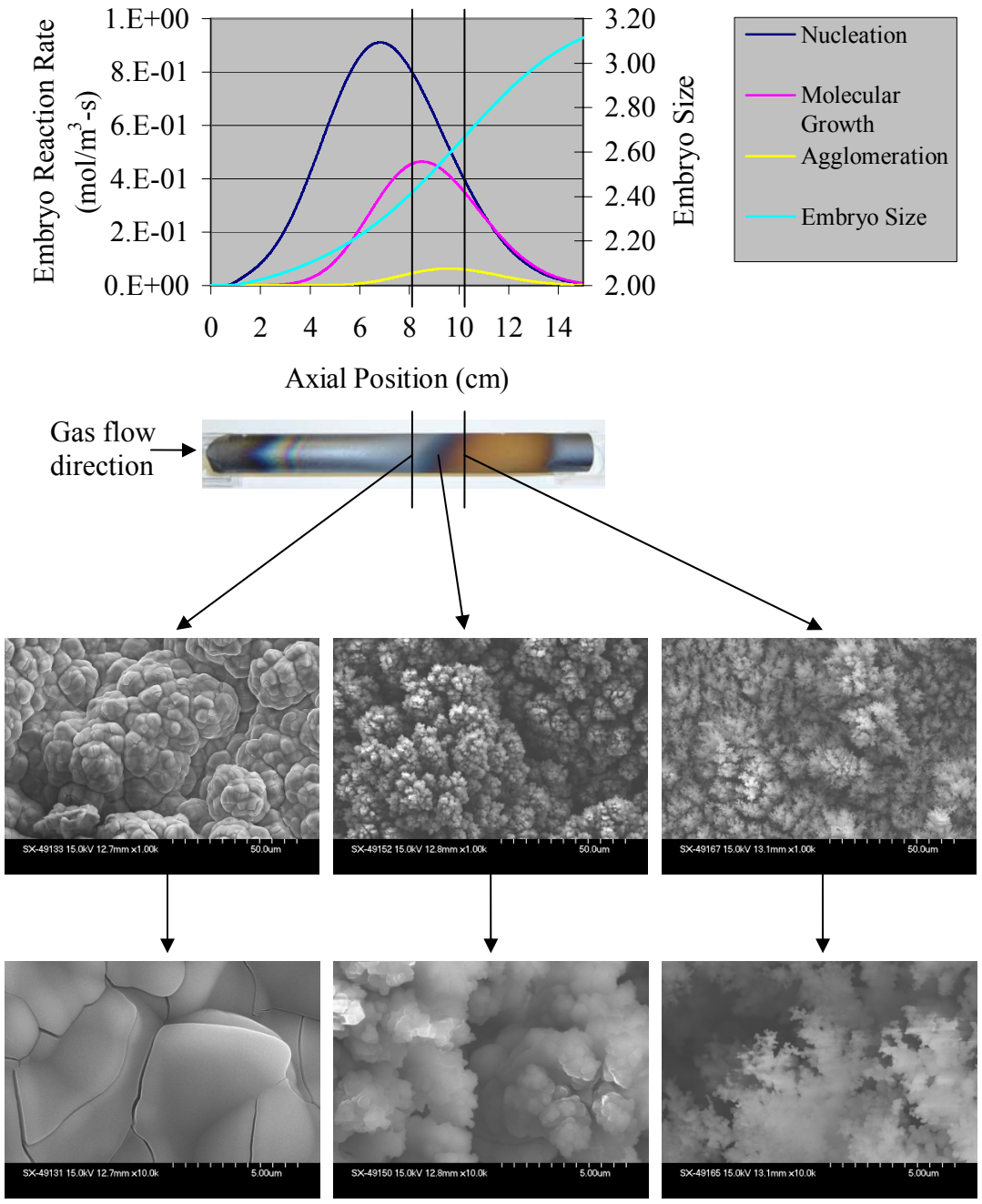

Figure 7.1. Predicted embryo growth mode rates and average size plot with SEM micrographs of selected areas shown for comparison for specimen AFCI-SiC-10.

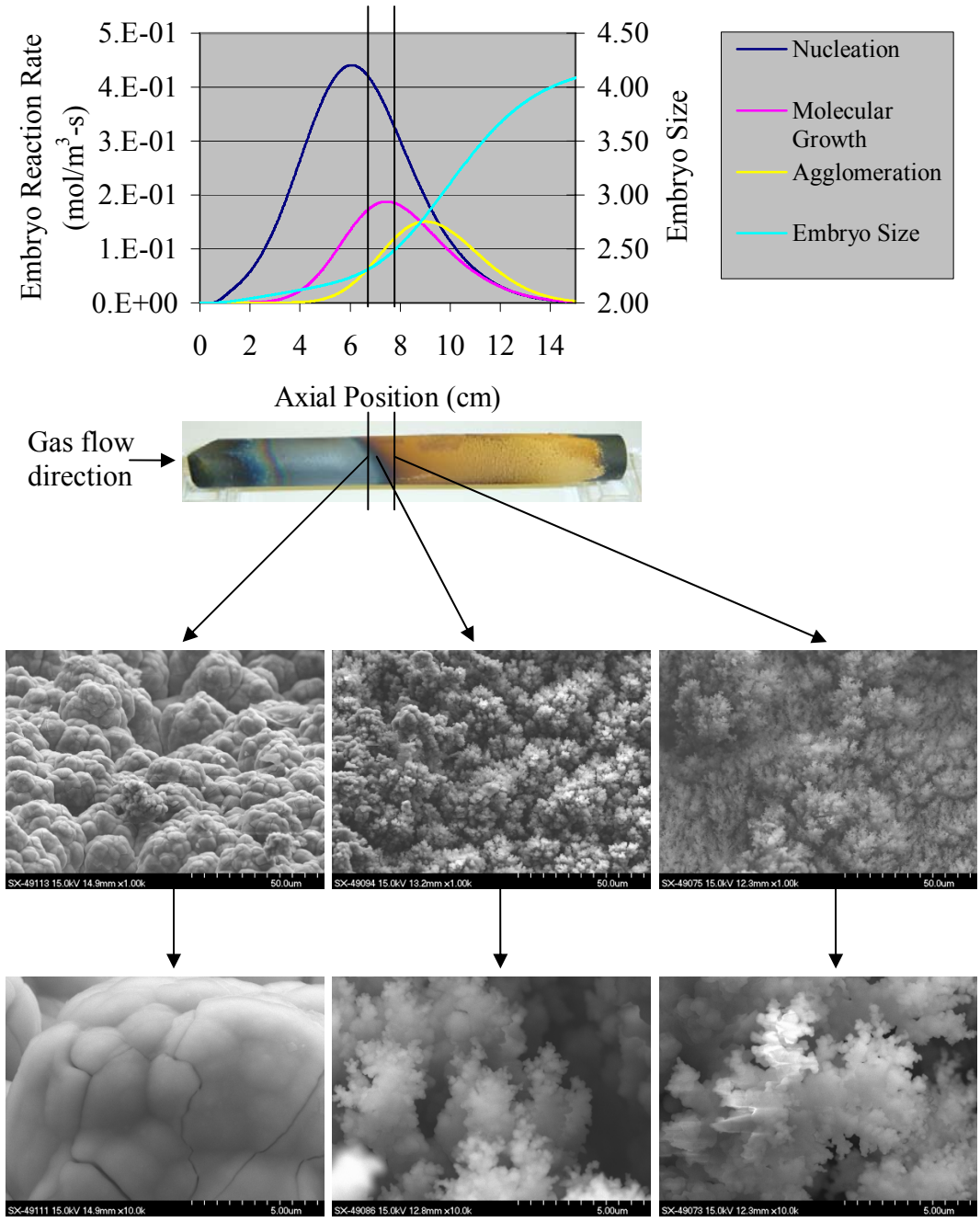

Figure 7.2. Predicted embryo growth mode rates and average size plot with SEM micrographs of selected areas shown for comparison for specimen AFCI-SiC-1.

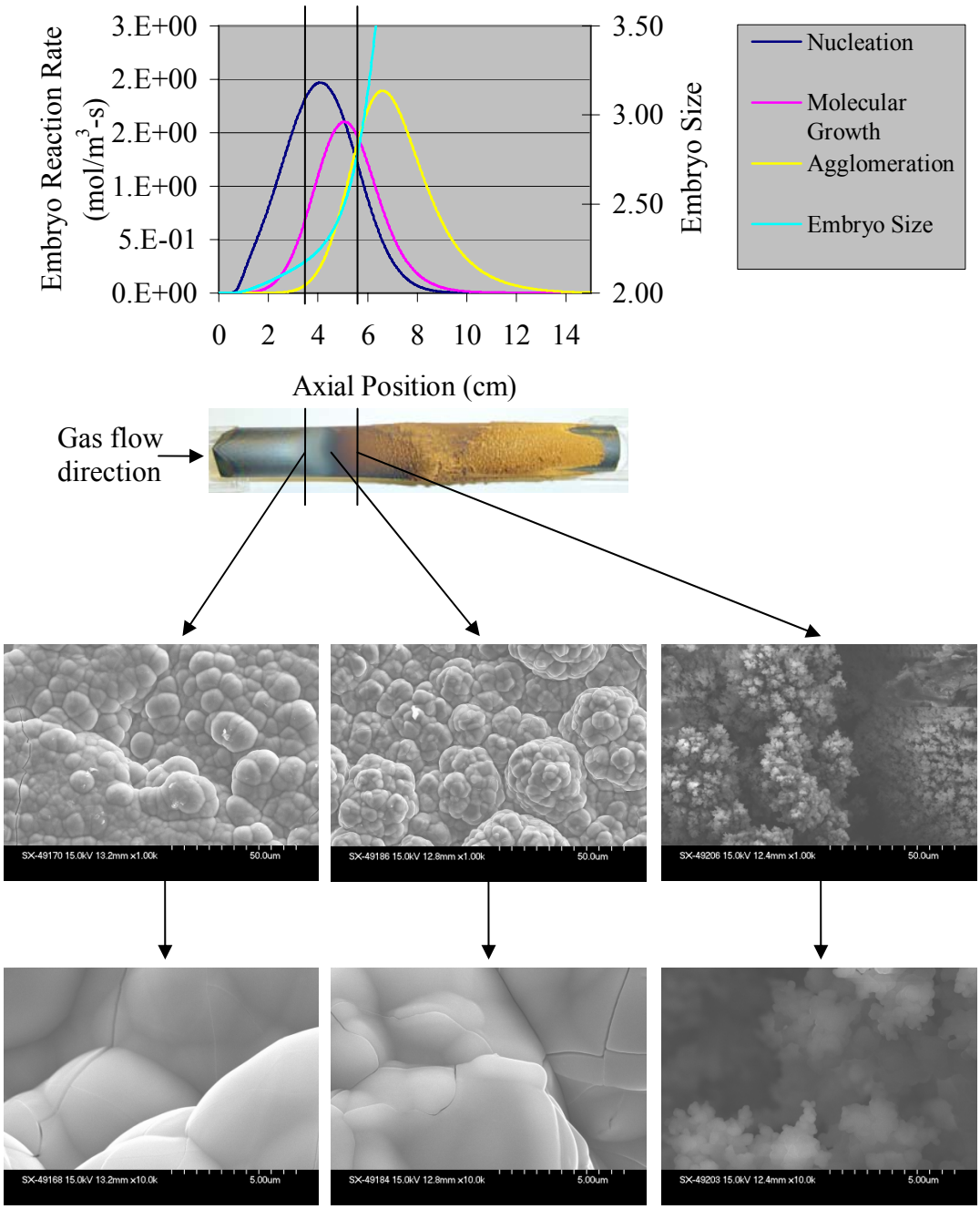

AFCI-SiC-4, 700°C, Methylsilane 65 cm^3/min

SiC coating on graphite

Figure 7.3. Predicted embryo growth mode rates and average size plot with SEM micrographs of selected areas shown for comparison for specimen AFCI-SiC-4.

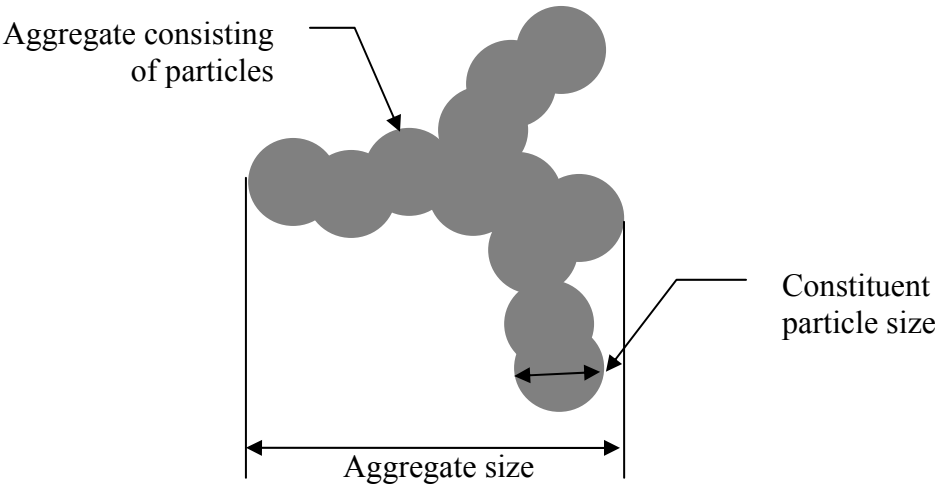

Figure 7.4. Schematic drawing of a typical gas-borne aggregate.

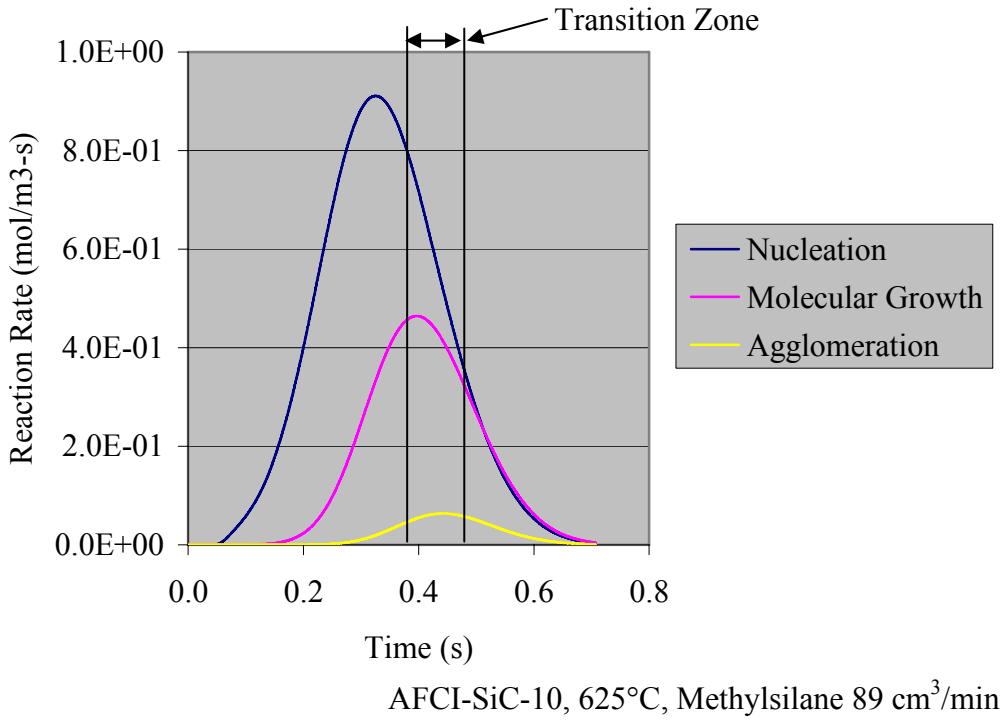

Figure 7.5. Predicted embryo growth mode rates as a function of time of flight in the reactor for specimen AFCI-SiC-10.

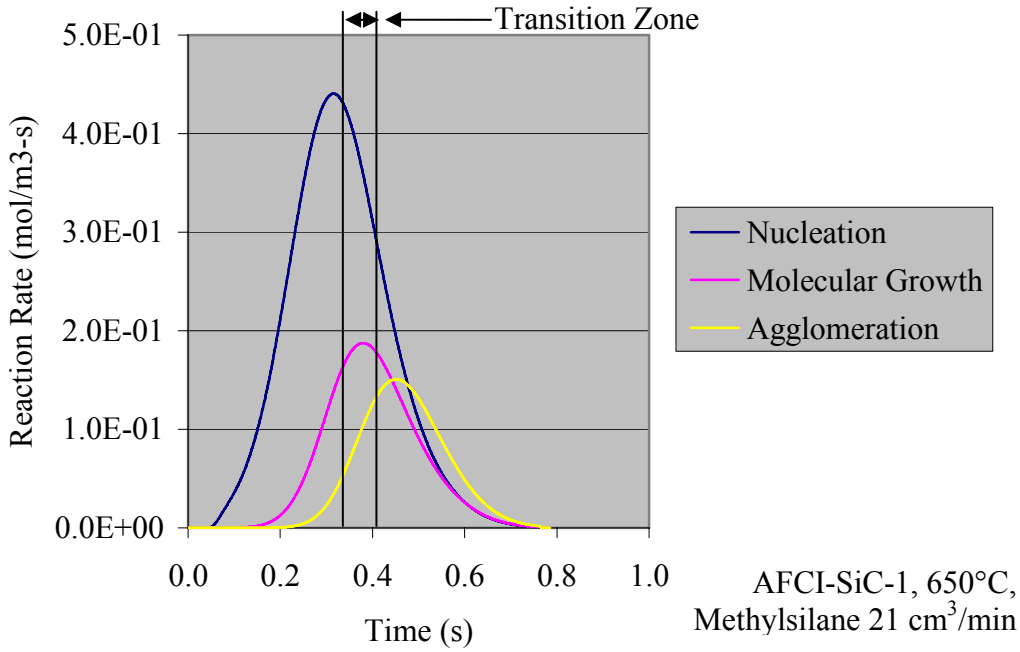

Figure 7.6. Predicted embryo growth mode rates as a function of time of flight in the reactor for specimen AFCI-SiC-1.

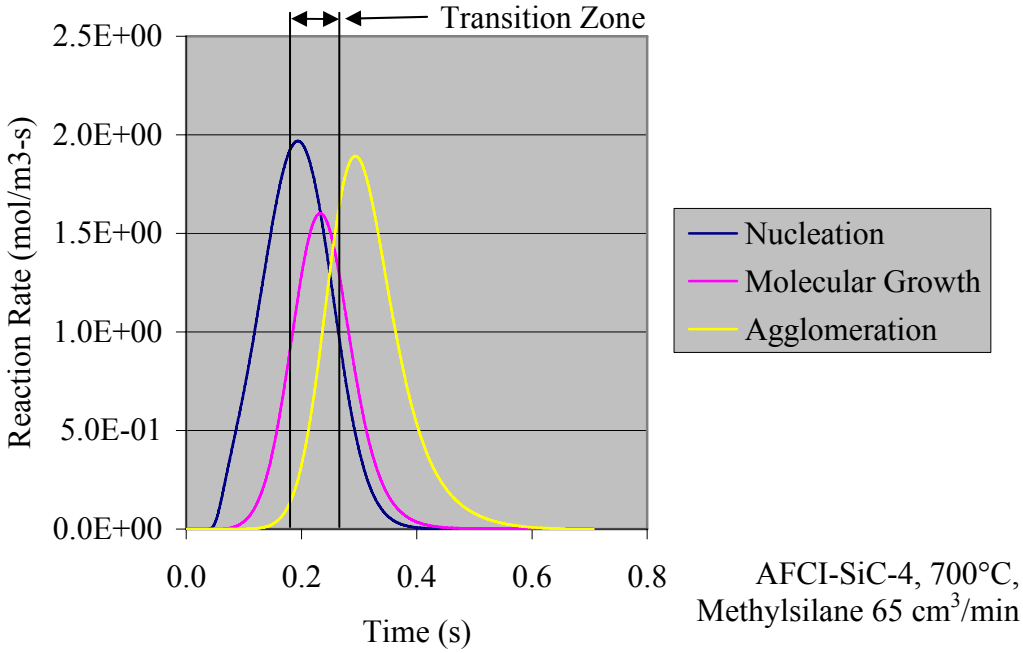

Figure 7.7. Predicted embryo growth mode rates as a function of time of flight in the reactor for specimen AFCI-SiC-4.

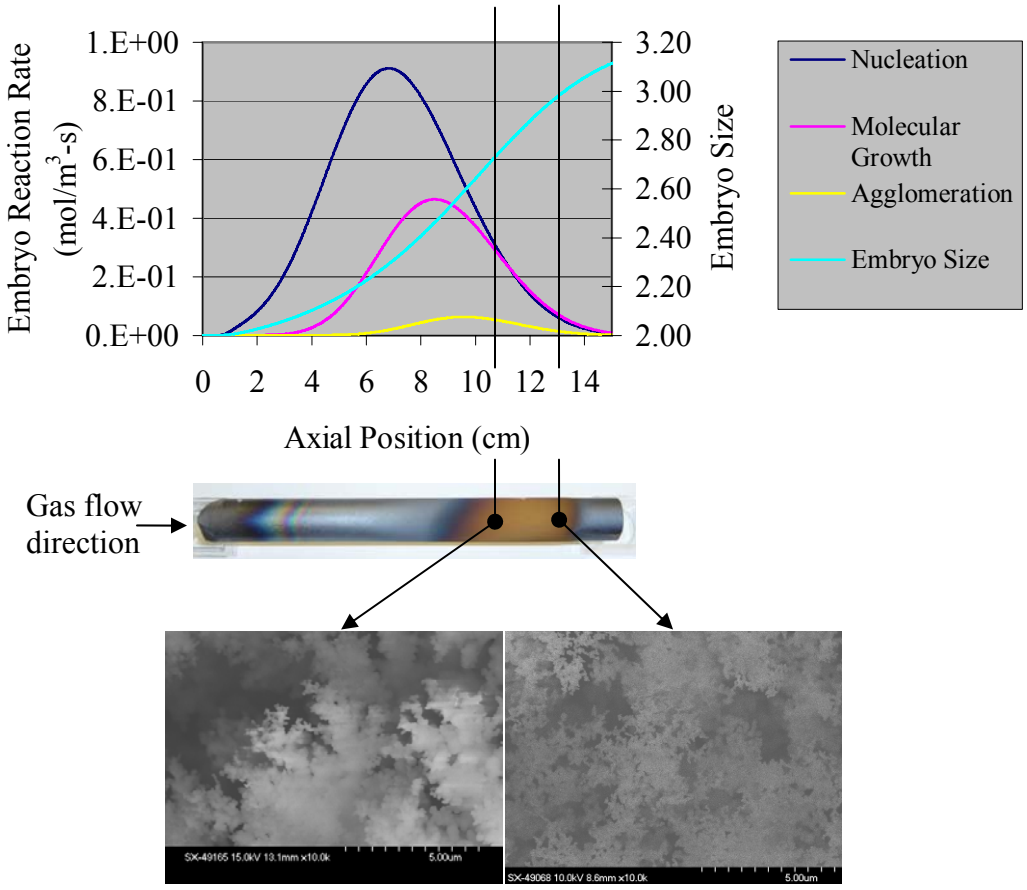

Figure 7.8. Predicted embryo growth mode rates as a function of axial position with SEM micrographs of selected areas shown for comparison for specimen AFCI-SiC-10.

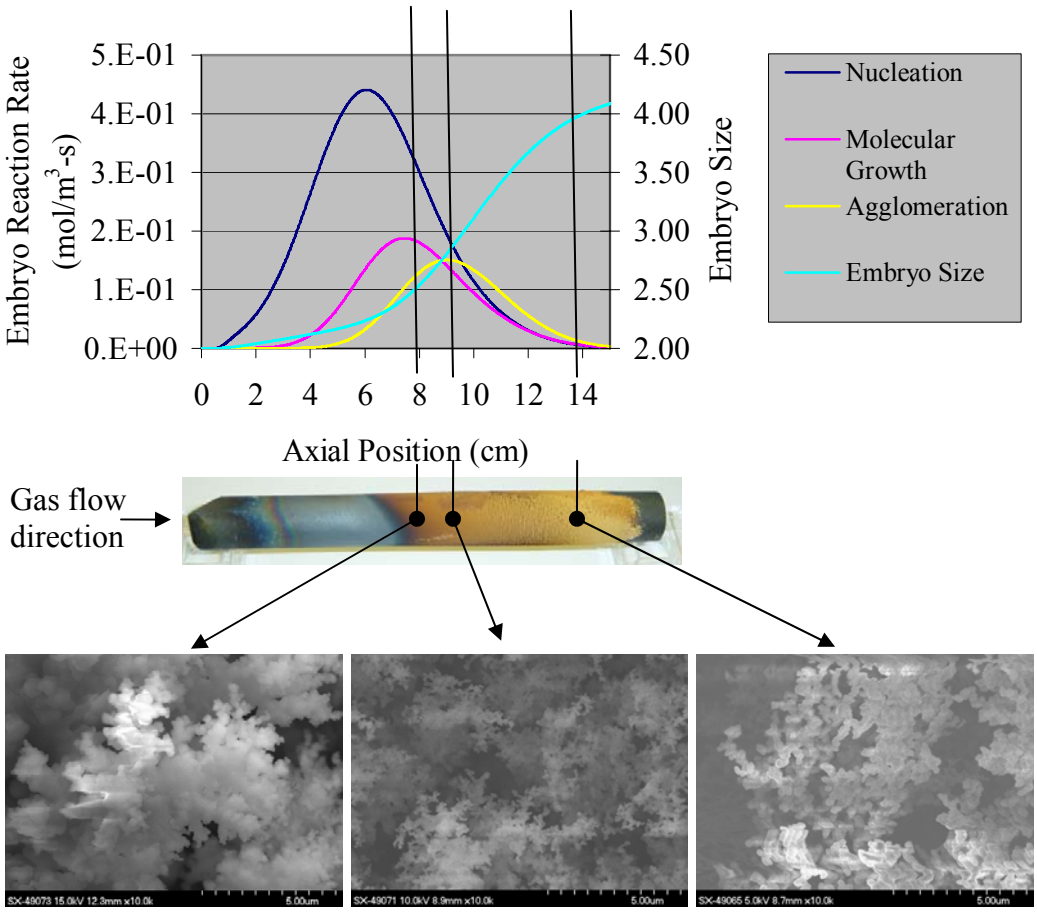

Figure 7.9. Predicted embryo growth mode rates as a function of axial position with SEM micrographs of selected areas shown for comparison for specimen AFCI-SiC-1.

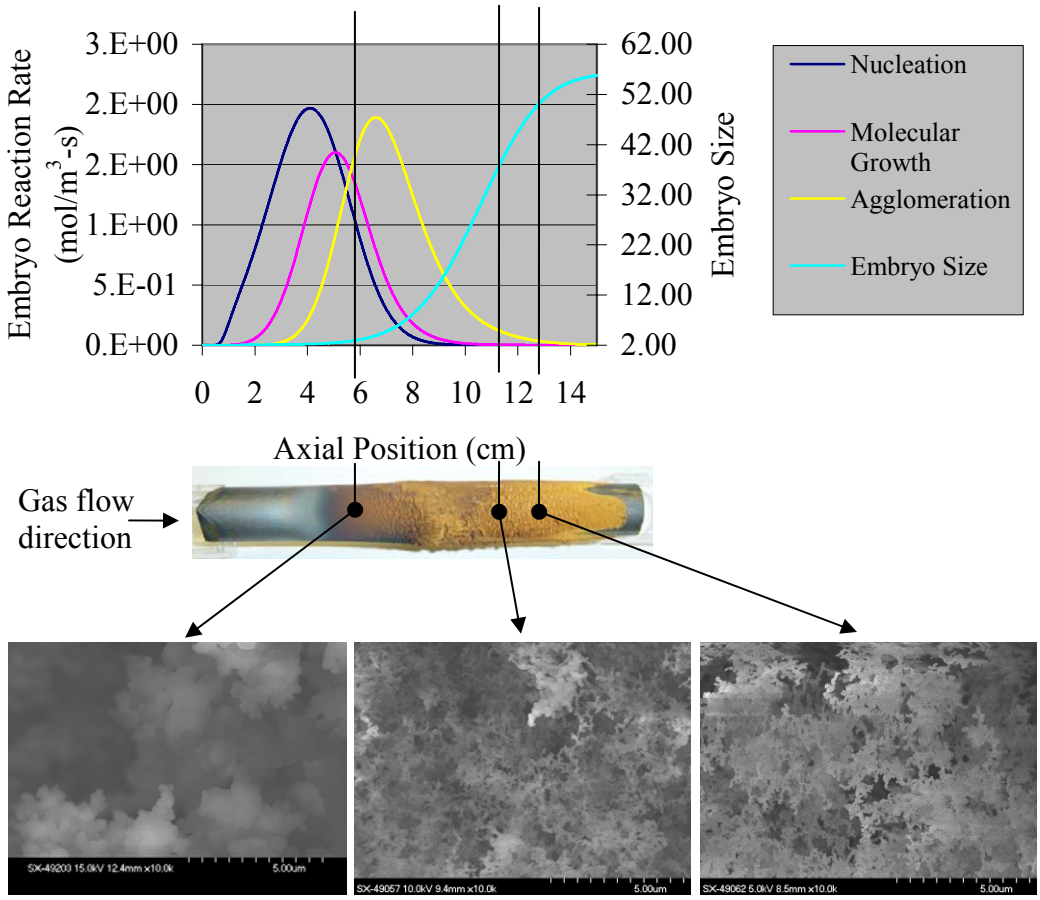

Figure 7.10. Predicted embryo growth mode rates as a function of axial position with SEM micrographs of selected areas shown for comparison for specimen AFCI-SiC-4.

Vita

James Henry (Jim) Miller was born September 30, 1969 in Oak Ridge Tennessee. Jim grew up in Oak Ridge and graduated from Oak Ridge High School in 1987. After high school he attended the University of Tennessee, Knoxville where he graduated with a Bachelor of Science degree in Mechanical Engineering in 1992. Jim then went to work at Oak Ridge National Laboratory as a development engineer in 1993. He also continued his education part time and graduated with a Master of Science degree in Metallurgical Engineering in 1995 and a Doctor of Philosophy degree in Materials Science & Engineering in 2006, both from the University of Tennessee, Knoxville.